3-2020

Design and Analysis of a Disk-oriented Engine Combustor

Bennett M. Staton

Design and Analysis of a Disk-Oriented Engine Combustor

THESIS

Bennett M. Staton, Second Lieutenant, USAF

AFIT-ENY-MS-20-M-281

DEPARTMENT OF THE AIR FORCE
AIR UNIVERSITY

AIR FORCE INSTITUTE OF TECHNOLOGY

Wright-Patterson Air Force Base, Ohio

AFIT-ENY-MS-20-M-281

DESIGN AND ANALYSIS OF A DISK-ORIENTED ENGINE COMBUSTOR

THESIS

Presented to the Faculty

Department of Aeronautics and Astronautics

Graduate School of Engineering and Management

Air Force Institute of Technology

Air University

Air Education and Training Command

in Partial Fulfillment of the Requirements for the

Degree of Master of Science

Bennett M. Staton, B.S.

Second Lieutenant, USAF

March 2020

AFIT-ENY-MS-20-M-281

DESIGN AND ANALYSIS OF A DISK-ORIENTED ENGINE COMBUSTOR

Bennett M. Staton, B.S.
Second Lieutenant, USAF

Committee Membership:

Major Brian T. Bohan, PhD
Chairman

Marc D. Polanka, PhD
Member

Major Levi M. Thomas, PhD
Member

Abstract

In a novel approach to gas-turbine power production, an engine was designed and analyzed to use both a single-stage centrifugal compressor and single-stage radial in-flow turbine configured back-to-back. This air path reduced the axial length of the engine up to 60%, providing additional modularity in a gas-turbine engine that could be used to improve mobility of ground-based power units or increase the survivability of aircraft through the use of distributive propulsion. This increased modularity was made possible by the use of a circumferential flow combustor that substantially decreased the axial length of the burner and negated the need to return compressor radial flow to the axial direction, as found in conventional combustion approaches. The Disk-Oriented Engine was designed to incorporate swirling inlet flow from a centrifugal compressor and exhaust directly into a radial in-flow turbine, while still maintaining the initial swirl pattern out of the compressor. The configuration of the combustion cavity was evaluated through computational fluid dynamics. An iterative design approach was used to achieve desired flow characteristics and combustion dynamics through geometry shaping and placement of air supply holes. The result of this design process was a computational combustor model that accepted swirling inlet flow, dispersed that air and fuel about a unique u-bend circumferential combustion cavity, and exhausted in the radial direction to feed a radial in-flow turbine. Sustained combustion was simulated at design conditions with a 3% total pressure loss in the combustor and a turbine inlet pattern factor of 0.24, indicating that such a design could operate as a gas-turbine engine, while reducing axial length up to 60% compared to traditional systems of similar size and performance. Computational results were compared to experimental tests on fuel-air swirl injectors, providing qualitative and quantitative insight into the stability of the flame anchoring system. From this design, a full-scale physical model of the Disk-Oriented Engine Combustor was designed and built for combustion analysis and characterization.

Acknowledgements

Over the course of this Master's Degree program, I have once again realized the truth behind the words of Thomas Paine:

What we obtain too cheap, we esteem too lightly; it is dearness only that gives everything its value. The harder the conflict, the more glorious the triumph.

While this program brought forward difficulties and troubles that have made me a better man in the end, in no way did I reach this point without the help of countless individuals. First off, I would like to thank my advisor, Maj Brian Bohan, and the rest of my committee, Dr. Marc Polanka and Maj Levi Thomas, for the meetings and out-of-office hours that those individuals made available to help shape my research endeavor. I would also like to thank other students working in the AFIT COAL lab, including 2d Lt Daniel Holobeny and 2d Lt Ricky Macias, for their contributions to this project and flexibility in testing schedules.

Much of my computational research was aided by the Linux network technical support provided by Mr. Dave Doak, while the experimental data acquisition and reduction was a result of collaboration and guidance from Dr. Larry Goss of ISSI. These two individuals proved to be extremely valuable in the computational and experimental aspects of this research. This project relied heavily on the time-intensive process of model fabrication, and I would like to thank Mr. Brian Crabtree, Mr. Chris Harkless, Mr. Joe Owings, Mr. Dan Ryan, and Mr. Dean Harshman of the AFIT Model Shop for their indispensable design input and ongoing support to help manufacture research hardware. I would also like to thank Mr. Ben Doane and Mr. Travis Shelton of the AFIT AniMaL lab for their 3D printing support, and Mr. James Nees of AFRL for his help to heat treat hardware. Technical support from the AFIT ENY lab technicians, Mr. Jamie Smith, Mr. Mike Ranft, Mr. Josh DeWitt, and Mr. Keith Long, was extremely valuable in the setup and operation of lab entities.

Finally, I would like to thank all of my friends and family that supported me throughout this journey. My biggest supporter in all of this has been my wife, who I want to thank for everything over the last 18 months. Between classes, exams, and research, she was always there for me. Her willingness to listen as I attempted to teach her about gas turbine engine design was endlessly impressive.

Bennett M. Staton

Table of Contents

Page

List of Figures

Figure Page

Figure Page

List of Tables

List of Abbreviations

Abbreviation		Page
CFD	Computational Fluid Dynamics	7
HGC	High-G Combustors	18
ITB	Inner-Turbine Burner	18
UCC	Ultra-Compact Combustor	19
IGV	Inlet Guide Vane	19
CC	Circumferential Cavity	19
RQL	Rich-burn Quick-quench Lean-burn	19
PZ	Primary Zone	19
OD	Outer Diameter	19
PF	Pattern Factor	23
TVC	Trapped-Vortex Combustor	24
SHC	Short Helical Combustor	26
RIT	Radial Inflow Turbine	32
AFIT	Air Force Institute of Technology	34
GUI	Graphical User Interface	34
RANS	Reynolds-Averaged Navier-Stokes	37
LES	Large Eddy Simulation	37
DNS	Direct Numerical Simulation	37
PDE	Partial Differential Equation	38
SST	Shear Stress Transport	38
GRIMech	Gas Research Institute Mechanism	39
PDF	Probability Density Function	40

Abbreviation		Page
PIV	Particle Image Velocimetry	40
ISSI	Innovative Scientific Solutions Incorporated	41
CAD	Computer-Aided Design	42
T-Rex	Anisotropic Tetrahedral Extrusion	57
PDE	Partial Differential Equation	60
BCs	Boundary Conditions	67
COAL Lab	Combustion Optimization and Analysis Laser Laboratory	68
PCA	Parametric Cycle Analysis	73
EPA	Engine Performance Analysis	73
SLS	Sea-Level-Static	73
CPR	Compressor pressure ratio	73
TSFC	Thrust-Specific Fuel Consumption	74
AFRL	Air Force Research Laboratory	80
RT	Rig-Ready Test Geometry	81
IN 718	Inconel 718	82
SS 321	Stainless Steel 321	82
SS 316	Stainless Steel 316	82
EDM	Electrical Discharge Machining	84
AFRL	Air Force Research Laboratory	86
LPG	Liquid Propane Gas	90
CW	Continuous Wave	92
ST	Swirler Test Geometry	103
CNC	Computer Numerical Control	128

List of Symbols

Symbol		Page
y	Normal Wall Distance (m)	37
u_τ	Friction Velocity (m/s)	37
ν	Kinematic Viscosity (m^2/s)	37
ν_t	Turbulent Viscosity (m^2/s)	38
k	Turbulent Kinetic Energy (J)	38
ϵ	Turbulent Dissipation (m^2/s^3)	38
ω	Turbulent Dissipation Rate (m^2/s^4)	38
Φ	Equivalence Ratio	46
ρ	Density ($\frac{Kg}{m^3}$)	70
K	Coefficient of Thermal Conductivity ($\frac{W}{m\ K}$)	70
V_r	Radial Velocity Component (m/s)	71
V_θ	Circumferential Velocity Component (m/s)	71
Φ_{global}	Global Equivalence Ratio	72
$(a/f)_{stoich}$	Stoichiometric Air to Fuel Ratio	72
T_{t4}	Turbine Inlet Temperature (K)	73
A_3	Compressor Exit Area (m^2)	76
$\dot{m}_{fuel}$	Mass Flow Rate Fuel ($\frac{kg}{s}$)	78
ΔT	Change in Temperature (K)	134
ΔP	Total Pressure Loss (%)	136
T_{res}	Residence Time (s)	142

DESIGN AND ANALYSIS OF A DISK-ORIENTED ENGINE COMBUSTOR

I. Introduction

1.1 Motivation

The gas turbine engine has been utilized heavily in aircraft as a means of propulsion since its inception in the late 1930's. Jet propulsion pervaded the market rapidly, boasting a power-to-weight ratio three times greater than that of its reciprocating counterpart [1], but early turbojet engines were highly inefficient. Over the last 80 years, the engineering community has improved on both the efficiency and power-to-weight ratio of gas turbine power production systems at the expense of engine axial length. In large-scale thrust applications, this axial length is dedicated to compress the incoming air to high overall pressure ratios, increasing the thermal efficiency of the engine. Conversely, small-scale thrust applications do not require this high pressure rise, but demand similar combustion performance to high-thrust, high-performance engines. This fact is a result of the standard burn time of a hydrocarbon fuel, known as residence time; all engines must provide sufficient residence time within the combustor for complete combustion to occur.

Of interest to the aeropropulsion community is a means of reducing the axial length of small scale engines that produce less than 1000 N of thrust. A reduction in axial length would provide previously unavailable modularity to thrust and power production. On an aircraft powered by engine thrust, a reduction in axial length provides more room for payload in an existing engine's volume. From a power production view, a reduction in axial length of an engine could reduce the overall length

of a gas turbine electric generator. This length savings would be realized in an increased mobility of ground-based generators, and mobile gas turbine auxiliary power systems are of interest to the military for their "high specific power, easy cold weather starting, low noise, low vibration, low exhaust smoke and multifuel capabilities" [2]. A representative length savings for a generator powered by an engine with reduced axial length is shown in Figure 1, where the axial length of an entire electric generation system powered by a PT6A turboshaft engine can be reduced to a length shorter than the turboshaft engine itself.

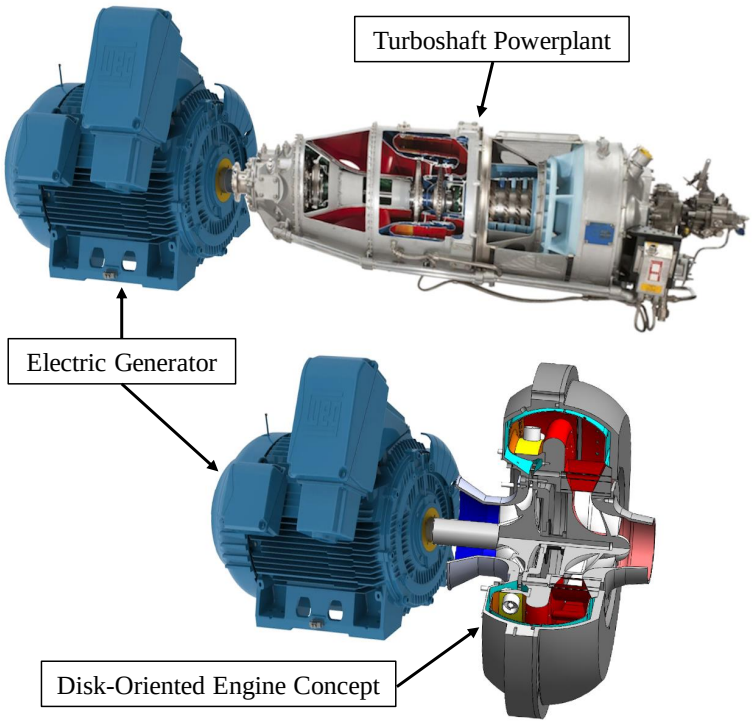

Figure 1. Representation of Disk-Oriented Engine length savings as a power plant for mobile ground power. For comparison, a representative electric generator [3] and modern turboshaft engine [4] are shown.

Another benefit of power production in a reduced axial length could be realized in supplying power for a distributed turbo-electric propulsion system in an aircraft. An example of distributed electric propulsion is shown in Figure 2 with the Airbus E-Thrust concept aircraft [5]. In this design, mechanical power created by the gas

turbine engine is converted to electrical power for thrust production by multiple fans. From a survivability standpoint, spreading the thrust to multiple electric motors rather than one jet engine provides redundancy in case one thrust point fails. This could increase survivability of both manned and unmanned vehicles that currently rely on single-engine power production. An engine with reduced axial length could provide power to such a system, allowing for the fixture of power production engines to aircraft locations that otherwise would not fit a traditional gas turbine engine.

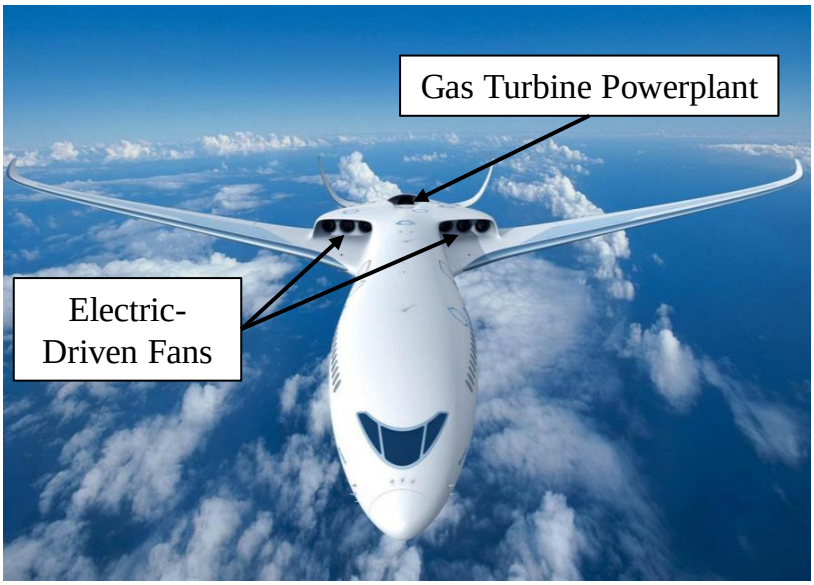

Figure 2. Airbus E-Thrust concept aircraft, displaying a potential use for distributed electric propulsion [5].

The focus of the present research was to reduce the axial length of a thrust-producing gas turbine engine by two means: 1) lessen the shaft length between turbomachinery with a back-to-back configuration of a centrifugal compressor and radial in-flow turbine, and 2) combust in a u-bend that combines these radial paths while increasing residence time through the use of bulk swirl in the combustor. Figure 3 displays the Disk-Oriented Engine concept. Additionally, a cutaway exhibits the novel combustor flow path, joining the centrifugal compressor to the radial in-flow turbine. It blends several concepts previously studied to reduce combustor axial length, and

the residence time requirement is achieved with bulk swirl in the combustor. This swirl is supplied by the compressor, it increases the path length a particle travels before exiting the combustor, and it reduces the turning requirement of the nozzle guide vane at the turbine inlet. The residence time increase achievable by combustion in a swirling fashion was suggested in ultra-compact combustion studies at the Air Force Institute of Technology [6], and the present research intends to take those length savings a step further by applying the combustion concept to power a new turbomachinery configuration with reduced length.

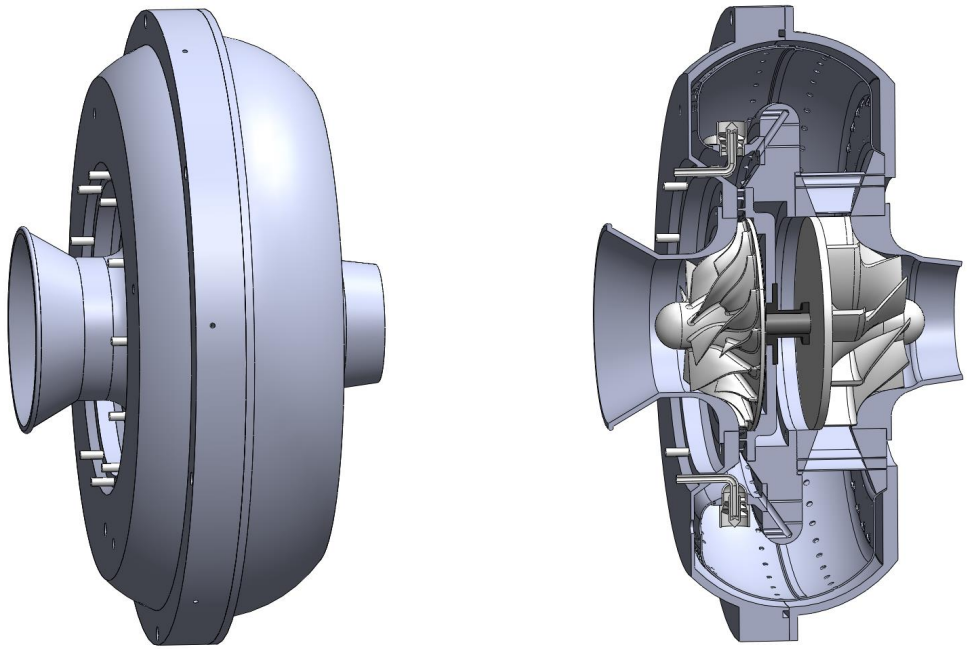

Figure 3. Configuration and cutaway of Disk-Oriented Engine concept.

1.2 Objectives

The primary focus of the present research was to design a combustor geometry capable of operating in a swirled configuration about radially oriented turbomachinery. Completion of this goal was supported by multiple objectives including an engine cycle analysis, computational modeling, experimental comparison of select components,

and physical hardware fabrication. Each of these specific objectives are detailed to set the focus of the present research:

1. Perform an engine cycle analysis to determine operating conditions, station parameters, and sizing requirements for an engine operating at the target constraints: 668 N (150 lbf) of thrust at a compressor pressure ratio of 4.0.

2. Computationally investigate the combustion performance of various three-dimensional combustor geometries to determine a suitable design for sustained combustion at the target operating conditions.

    - Develop a fuel injection system appropriate for the flow path unique to a Disk-Oriented Engine, capable of anchoring a stable flame across the operating envelope, and adaptable between gaseous propane and future liquid jet fuel injection.

3. Compare velocity profiles and flame stability of focused experimental testing to CFD results to better understand the real-world operation of this design prior to full-engine tests.

4. Design a combustor geometry that is manufacturable, survivable, and testable at atmospheric and elevated conditions.

The following chapters present background information relevant to these objectives, provide a plan for answering the questions inherent in each objective, and analyze findings to support the present research's accomplishment of the objectives. Since many of these project goals revolve around the blank-page creation of a new gas turbine engine and its combustor, it is important to outline the constraints that guided this research.

1.3 Constraints

Since the Disk-Oriented Engine was intended to be a proof of concept for circumferential combustion coupled with radially configured turbomachinery, the cycle constraints were fairly limited. The project was intended to reduce axial length for small scale gas turbines, producing less than 1000 N of thrust, meaning that the engine would operate on single-stage compression and power extraction. With a target thrust of 668 N (150 lbf), engines of similar size indicated that the compressor would operate with a pressure ratio of approximately 4.0, and a turbine inlet temperature of 1300 K was assumed feasible with minimal secondary air used for turbine and bearing coolant. Since the Disk-Oriented Engine was designed to trade axial length for radial diameter, a maximum engine diameter of 0.5 m was set to limit the width of the engine. Based on these constraints, an engine cycle was selected and a combustor was designed to fall within the design space while complying with the objectives previously stated.

II. Background and Theory

To better understand how a Disk-Oriented Engine Combustor can be designed to maintain stable and efficient combustion with an estimated length savings of up to 60%, theory and research in the field of compact-combustion must first be reviewed. In this chapter, Section 2.1 outlines the combustor design fundamentals that are important to consider when applying combustion concepts to a new design. Section 2.2 lists research done in the compact-combustion field that is applicable to the theory behind a Disk-Oriented Engine, as well as its design. To better illustrate the design requirements dictated by the turbomachinery, Section 2.3 explains the fundamentals of radial turbomachinery applicable to the compressor and turbine stators integrated into the combustor. These findings set the stage for the initial design, but in order to do preliminary iterative tests on Disk-Oriented Engine Combustor designs, computational fluid dynamics (CFD) was employed for its ability to test prototypes in a cost-effective manner. Section 2.4 explains the theory behind the CFD model used. Finally, Section 2.5 presents the theory behind Particle Image Velocimetry as it applies to experimetal testing for the Disk-Oriented Engine.

2.1 Combustor Design Fundamentals

For insight on compact combustion and how it can be implemented into a Disk-Oriented Engine, combustion fundamentals are be reviewed so that the intricacies of combusting flow can be referenced to explain design choices. The particular fundamentals of interest include chemical kinetics of reacting gases (Section 2.1.1) that govern the rates at which combustion events occur, turbulent premixed flame structures that will be present in the combustion chamber (Section 2.1.2), and fuel/air introduction schemes, such as air swirlers (Section 2.1.3).

2.1.1 Chemical Kinetics

At a basic level, combustion is the oxidation of some fuel (such as propane in the case of the Disk-Oriented Engine), and this oxidation reaction occurs at some finite rate for given conditions. An understanding of these rates and how conditions effect them can be used to improve combustion stability and efficiency. Reactions are often expressed in global form, and an example of which is propane combusting in air to produce CO_2, H_2O, and N_2 directly. Global reactions are useful in determining macro scale values such as stoichiometric fuel-to-air ratios, but they do not govern the reaction rates. Such a global reaction is made up of many individual elementary reactions; the speed of these elementary reactions drives the global combustion reaction.

Turns [7] explains that elementary reaction rates are driven by collision frequency, consisting of an energy factor (fraction of collisions occurring with an energy above the activation energy) and a steric factor (the geometry involved in a collision between two particles). The physical values of these factors rely on many variables and are complicated to calculate, so the reaction rate is often expressed by an empirical Arrhenius form:

$$k_{bimolec}(T) = A_{Arrhenius} e^{\frac{E_A}{R_U T}} \tag{1}$$

where $A_{Arrhenius}$ is the frequency factor based on collision theory and the exponential term is the energy factor, consisting of the activation energy (E_A), universal gas constant (R_u) and temperature (T). This Arrhenius equation applies to bimolecular collisions, neglecting dissociation, and is primarily a function of temperature [7]. The frequency factor is also a function of pressure, as a high-pressure gas experiences high-frequency collisions, driving up the reaction rate. Coefficients for the Arrhenius equations are empirical and have been tabulated for many elementary reactions. Equations of this form make up the reaction chemistry model in Fluent (discussed in-depth in Section 2.4). Applying these reaction rates on a global scale, the time

taken for reactions to occur is the chemical time: a driving function in flame stability and combustion efficiency.

Chemical time (τ_{chem}) is the amount of time a particular reaction takes to progress. This is a function of the initial molar concentration of the species reacting ($[\mathrm{A}]_0$) and the reaction rate coefficient. The chemical time is then dependent on the amount of species reacting, and is highly influenced by the temperature and pressure of the gas. A simple example of chemical time for a bimolecular reaction between generic species, A and B, is shown in Equation 2 [7].

$$\tau_{chem} = \frac{ln(e + (1-e)([\mathrm{A}]_0/[\mathrm{B}]_0)}{([\mathrm{B}]_0 - [\mathrm{A}]_0)k_{bimolec}} \tag{2}$$

Analysis of these chemical times on a global scale often takes a different form. Turns [7] noted that these reactions are modeled by a reduced chemical mechanism that omits many of the unimportant species and combines elementary reactions into a system of global reactions. This mechanism models the system in a computationally efficient manner that takes into account only important aspects to recreate a desired reaction. The methods used to reduce the system are often case specific, so it is important to use a combustion model made for flows similar to those of interest [7]. The selection of a reduced combustion model was important in CFD analysis of the Disk-Oriented Engine Combustor, as a mechanism applicable to the anticipated flow conditions was needed to properly model the combustion chemistry. The combustion model is laid out in-depth in Section 2.4.

The chemical time is important to compact combustion, as the reaction must take place in a short axial distance, or flow time (τ_{flow}) when distance is divided by a velocity. This time requirement can be expressed as a ratio known as the Damköhler number (Da in Equation 3) [7]. The ratio of these two parameters is important, as it

indicates whether the reaction has enough time to complete within a flow structure.

$$Da = \frac{\tau_{flow}}{\tau_{chem}} \tag{3}$$

Damköhler numbers much larger than one have more time for the reaction to complete than is required, while those much less than one will likely not progress and lead to flame extinction. This flow time is not to be confused with the residence time, or the amount of time a fuel particle remains in the combustion chamber. Residence time is a function of the path length followed by a given particle and the speed at which it moves along this path [8]. Both flow and residence times are important characteristics of complete and stable combustion, but residence time is a collection of many flow times. Each flow time is the amount of time a particular flow structure impacts a reaction; the frequency and length of these flow times increase dramatically in turbulent combustion.

2.1.2 Turbulent Premixed Flames

One way of decreasing chemical time is to burn in a turbulent flow regime. This turbulence increases mixing, creating a premixed zone prior to the flame front, and eddies at the flame front increase the surface area of the reaction zone. Turns [7] defines three different turbulent flame regimes: wrinkled laminar, distributed-reaction and flamelets-in-eddies. The regime defines how the flame front forms and is determined by the turbulent Damköhler Number (Equation 4). The flow time scale is represented by the integral length scale (ℓ_0) over the turbulent fluctuating velocity (v'_{rms}), and the chemical time is estimated by the laminar flame thickness (δ_L) over the laminar flame speed (S_L).

$$Da = \frac{\ell_0/v'_{rms}}{\delta_L/S_L} = \left(\frac{\ell_0}{\delta_L}\right)\left(\frac{S_L}{v'_{rms}}\right) \tag{4}$$

The laminar flame speed and length are used because they are much easier to measure than their turbulent equivalent, and they give a representation of how a laminar flame propagates with the given gas properties. This laminar assumption can be corrected by the turbulent terms to account for turbulent mixing. Turns [7] also explains that, while turbulence increases mixing, the turbulent Da correlation explains that for a constant length scale ratio ($\frac{\ell_0}{\delta_L}$), Da is inversely proportional to turbulence intensity ($\frac{v'_{rms}}{S_L}$). This decrease in Da is a result of shorter relative flow times associated with high turbulence, and thus, the flame does not propagate as well as laminar flames. There is a trade-off between the enhanced mixing and decreased burning that must be weighed. Fundamentally, high turbulence is desired in the mixing region of the Disk-Oriented Engine Combustor, but the Damköler requirement dictated that the flame must burn at lower turbulence levels. These requirements place much of the primary zone combustion success on the fuel and air introduction process.

2.1.3 Fuel-Air Introduction

The fuel-air introduction step in combustor design is crucial in setting up the turbulent premixed flame structure required to rapidly mix the reactants and burn in a limited residence time. Burning in a turbulent premixed regime creates a stable flame, defined by Turns as, "one that is anchored at a desired location and is resistance to flashback, liftoff, and blowoff over the device's operating range" [7]. This definition was important in the design of a Disk-Oriented Engine Combustor, as the flame would need to satisfy these criteria across the entire operating envelope. The implementation of such an anchoring point depended on how the fuel was introduced to mix with the air; Turns listed several methods such as low-velocity bypass ports, refractory burner tiles, bluff-body flame holders, swirl or jet-induced recirculating flows, and rapid

changes in flow area that result in recirculating, separated flows [7]. Since many modern combustors introduce primary zone air through the use of swirling annular jets [9], and the inlet conditions of the Disk-Oriented Engine Combustor allowed for swirl air introduction, swirl-induced recirculating flows were focused on in this design.

The purpose of an air-swirl introduction mechanism with gaseous fuels is to optimally mix fuel and air with swirled air, while a swirler can also be used to atomize and distribute liquid fuels [10]. Mixing is enhanced by the vortex-breakdown-induced recirculation zone shown in Figure 4. Introducing air with sufficient swirl causes a flow reversal immediately downstream of the injector, and this pattern increases turbulence to enhance mixing [9]. The vortex core also provides an anchor point for the flame to hold off of the injector surface.

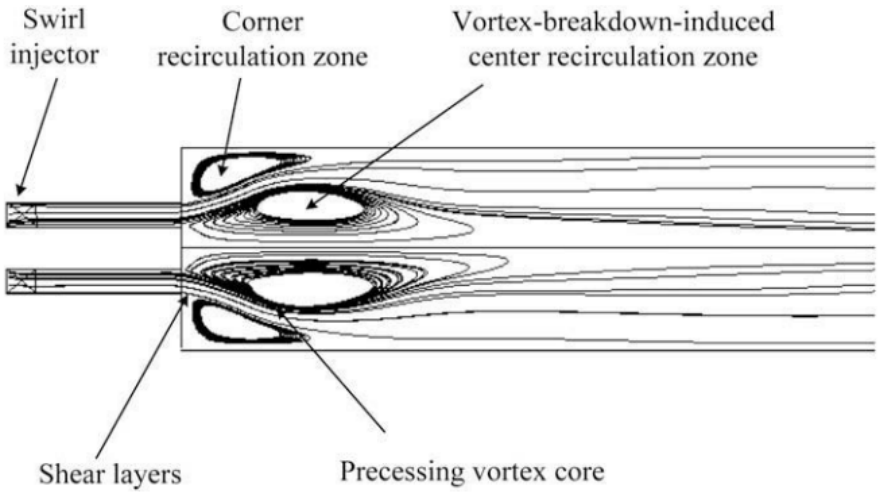

Figure 4. Swirl injector diagram, showing recirculation regions [10].

Swirl injectors generally fall into two categories, radial and axial, which are differentiated in the way air is introduced to the mechanism prior to swirling [10]. Figure 5 compares the two, showing that an axial swirler introduces air parallel to the incoming fuel and swirls with turning vanes. The radial swirler flows air tangential to the fuel, swirling primarily with the introduction geometry. Studies by Cowell and Smith

[11] comparing the performance of the two swirl types showed that radial swirlers facilitated lower-emission combustion and increased recirculation zone strength in comparison to axial swirlers, but a longer premixing length was required for radial swirled flow. Although radial swirl injectors presented benefits in the combustion process, complexities in air introduction for a radial swirler forced the Disk-Oriented Engine Combustor to focus on axial swirl injector design as the primary fuel-air introduction system.

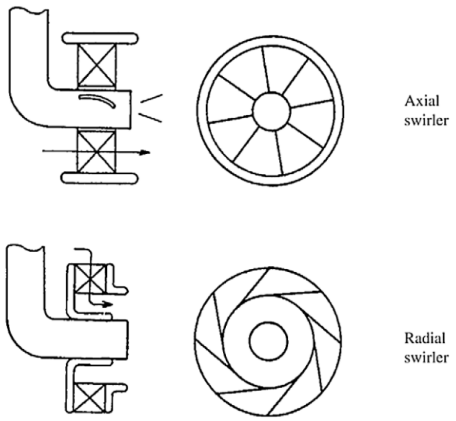

Figure 5. Radial and axial swirl injector comparison [12].

The swirl number (S) characterizes the swirl obtained by the physical hardware in the swirler and was important in designing the swirlers for the Disk-Oriented Engine. Fundamentally, the swirl number is defined as the axial flux of tangential momentum over the axial momentum flux at a characteristic radius, and S can be estimated using Equation 5 [10],

$$S = \frac{\int_{R_h}^{R_n} \bar{V}_\theta \bar{V}_y r^2 dr}{\int_{R_h}^{R_n} R_h \bar{V}_y^2 r dr}, \tag{5}$$

where $\bar{V}_\theta$ is the swirler tangential velocity, $\bar{V}_y$ is the swirler axial velocity, and the radius (r) is integrated from the vane hub radius (R_h) to the vane tip radius (R_n). For initial design purposes, S can be estimated based on the swirler vane angle (ϕ) and the ratio of center body to inlet duct radii (R_h/R_n) as shown in equation 6.

Equation 6 assumes flat, thin swirler vanes with uniform axial inlet flow [10].

$$S = \frac{2}{3}\left[\frac{1-(R_h/R_n)^3}{1-(R_h/R_n)^2}\right] tan\phi \tag{6}$$

To better understand the impact of swirl number on combustion processes, Yilmaz [13] conducted numerical analysis on methane combustion with various swirl numbers using Fluent. Figure 6 shows streamlines of a swirling jet issuing into a quiescent combustion chamber, varying swirl number ($0.0 < S < 0.6$). In all cases, there was a recirculation zone (highlighted in blue) outside of the jet caused by the shear layer between the fast moving jet and the zero-velocity surroundings. As the swirl number increased, a secondary recirculation formed, similar to that predicted by Huang and Yang [10] in Figure 4. This additional recirculation zone created turbulent mixing and a region for stable combustion to occur [13].

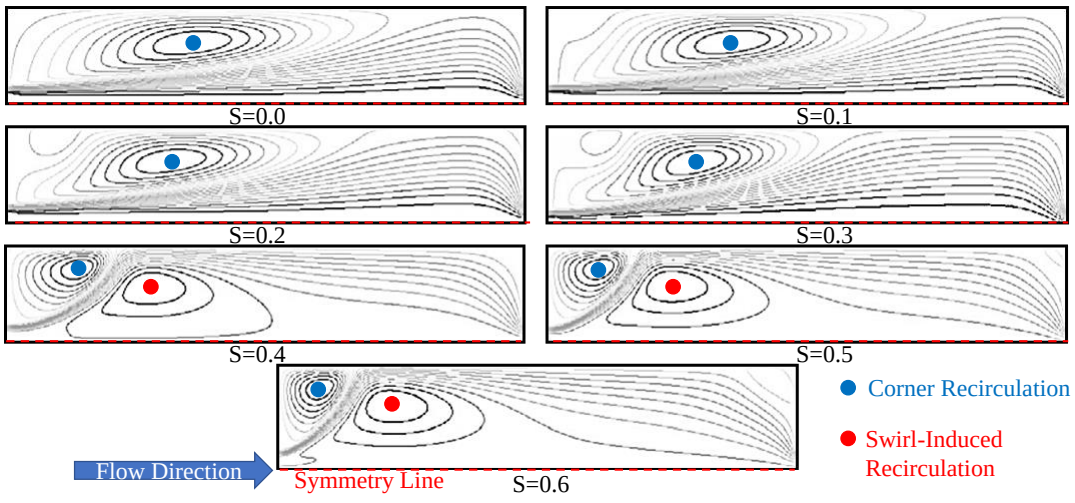

Figure 6. Isobars along axisymmetric swirling jet centerline, adapted from [13].

Stable combustion in this recirculation zone impacted the exit temperature profiles, as shown in Figure 7. Primarily, the combustion process was brought axially closer to the jet exit, thus allowing the combustion process to begin at an earlier

location. This drove up the temperature near the centerline and radially outward in Figures 7a and b. Yilmaz also suggested the exit plane temperatures for high swirl cases were lower because higher swirl created facilitated mixing, and better mixing of the non-reacted air and combustion products resulted in lower temperatures [13]. Another possible explanation for this phenomenon would be an increase in heat transfer within the system. Since the reactions occur in a shorter axial distance with high swirl, there is a larger gradient as the products move through the combustion chamber. Additional heat transfer to the surroundings would result in lower temperatures on the exit plane.

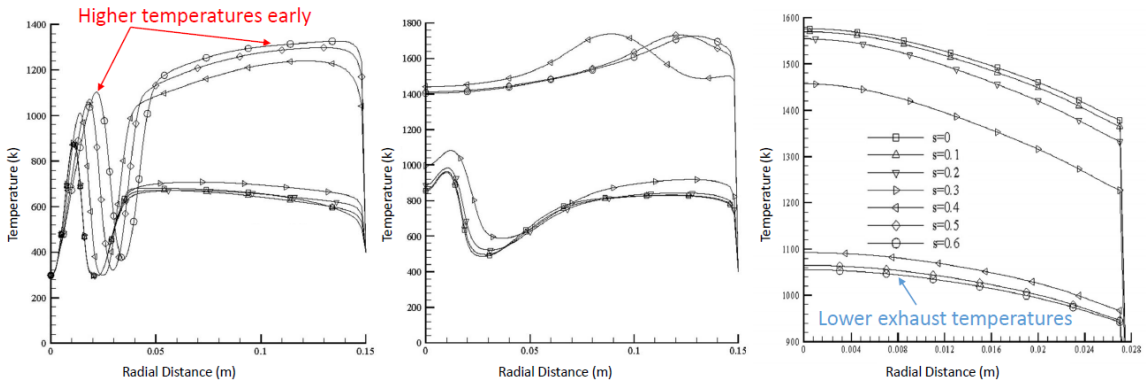

Figure 7. Temperature plotted against radial location for various swirl numbers at different downstream locations, adapted from [13].

2.2 Compact Combustion

Compact combustion, as applied to an Ultra-Compact Combustor, is the use of swirled flow to 1) reduce the chemical time of a reaction and 2) increase the residence time of the flow path. By influencing these two parameters, efficient combustion can be achieved in a shorter axial length. Section 2.2.1 discusses the physics resulting in reduced chemical time and increased residence time associated with compact combustion. Multiple attempts have been made to implement this in various ways, but

those applicable to a Disk-Oriented Engine are centrifugal loading, trapped-vortex, short helical combustors, and reverse flow combustors; these are detailed in Sections 2.2.2, 2.2.3, 2.2.4, and 2.2.5, respectively.

2.2.1 Physics of Centrifugal Loading in Combustion

Lewis [14] presented the first discussion about the benefits of centrifugal loading in combustion, stating that there was a buoyancy effect created in the loading process that increased flame speed and improved combustion. In this experiment, propane and air were premixed in a tube (as shown in Figure 8) that was then rotated like a helicopter blade at various speeds to achieve different circumferential loads. The reaction was ignited at one end of the tube, and flame speed was tracked using the ionization probes. Conducted for various loading conditions, this experiment found that turbulent flame speeds increased with loads between 500 and 3500 times the force of gravity. Lewis speculated that this increase in flame speed was due to a bubble velocity, that was proportional to the square root of the centrifugal load. This bubble velocity was simply added to the known turbulent flame speed to act as a correction to account for the increase in flame propagation rates seen in the experiment.

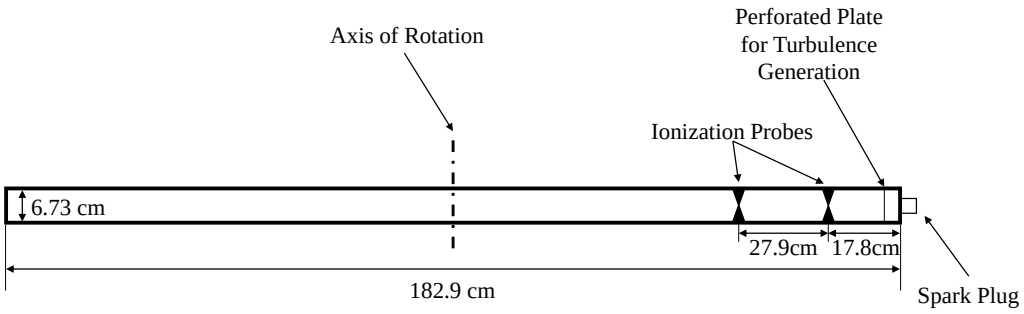

Figure 8. Lewis' centrifugally loaded combustion experiment, adapted from [14].

Lewis explained that centrifugal loading created a density variation between heavy fuels and lighter air particles, where the air was forced radially inward through the fuel

by a buoyant force that enhanced flame propagation. While benefits of circumferential loading pointed out in this experiment led to its use in future combustor designs, additional work was required to better explain the physics behind increases in flame speed, beyond buoyant affects.

To further investigate the physics behind this phenomenon, Briones *et al.* [15] created CFD models that replicated Lewis' experiment. A propane-air mixture was ignited at five different loading conditions (1, 395, 1000, 2000, and 3000*g_e), and the flame front was analyzed using a time-accurate model. Flame propagation at 1*g_e was slow, but the next three loading conditions had similar flame fronts, shown in Figure 9. The convex shape near the unburned mixture did not touch the walls, allowing unburned gases to reach the corrugated flame front, increasing flame surface area and thus propagation speed. The three modes of flame propagation in this case were Rayleigh-Taylor instabilities, thermal expansion, and turbulent flame speed.

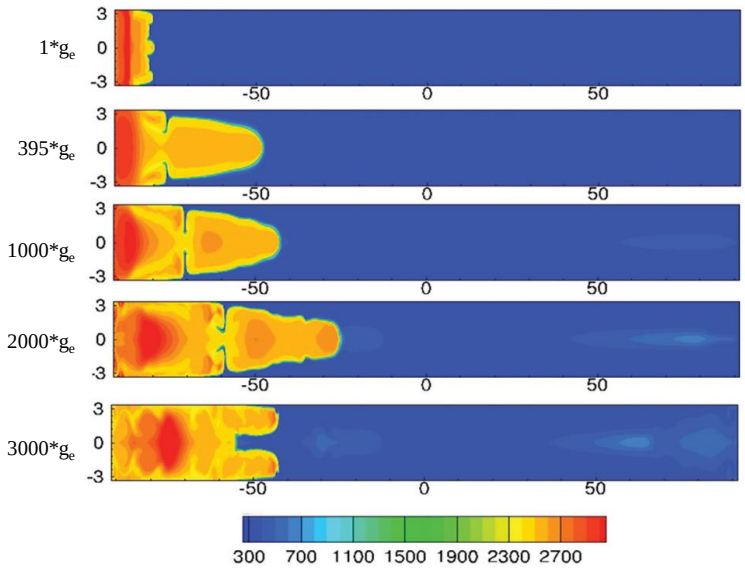

Figure 9. Comparison of flame fronts for various loading conditions, captured 8 ms after ignition. Contours show temperature (K), and dimensions mark distance (cm) [15].

Briones *et al.* suggested that the Rayleigh-Taylor instabilities were caused by weak wave interaction with the flame front that generated fluctuating eddies, corrugating

the flame front [15]. This corrugation increased the surface area of the flame front, and the larger surface area resulted in faster flame propagation for a constant reaction rate. Creation of these Rayleigh-Taylor instabilities in an advanced combustor design would lead to an increase in flame surface area and, consequently, flame speed. Since the increase in Rayleigh-Taylor instabilities were the driving factor behind increased flame speeds, Briones *et al.* proved that there were more complex flow features increasing flame speeds than the buoyant effect suggested by Lewis. The benefits behind circumferentially loading the combustion process all act to decrease the chemical time of the reaction, a key necessity for efficient combustion in limited residence times.

Briones *et al.* [15] also suggested that the upper limit for loading benefit was between 2000 and 3000*g_e, lower than the 3500*g_e suggested by Lewis. A limitation of over-loading the centrifugal forces was that the flame propagated at such a high rate that relatively cool reactants were introduced too rapidly at the flame front, locally quenching the flame as seen in Figure 9 [15]. This information indicates how important heat transfer is to the combustion process, not only from a macro scale of combustion interacting with the walls, but also on a micro scale where reactants enter a flame front. If reactants are forced to enter at a rate exceeding the chemical reaction rate, local quenching may occur. These two works set the foundation for both the physics and the limitations of circumferentially loaded combustion, which lead to the design of high-swirl Ultra-Compact Combustors.

2.2.2 Centrifugally Loaded Combustion

Centrifugally loaded combustors, also referred to as high-g combustors (HGC), were first suggested for practical use by Sirignano *et al.* [16] as an inner-turbine burner (ITB) in a constant-temperature engine cycle. This cycle provides increased enthalpy between the high and low-pressure turbines that can be extracted as increased work by

the low-pressure turbine stage. Implementation of an ITB required a burner designed with limited axial length, limiting the increased distance between turbine stages. This ITB concept was implemented by Zelina *et al.* [17], who created an Ultra-Compact Combustor (UCC) that consisted of a core flow section that integrated both the compressor stators and the turbine inlet guide vanes (IGV). Around the circumference of this core flow section was a circumferential cavity (CC) in which the rich burn of the rich-burn quick-quench lean-burn (RQL) combustion cycle was completed.

Burning in the CC was done in the circumferential direction, rather than the traditional axial direction, to increase residence time in a short axial length and to take advantage of the benefits of circumferentially loaded combustion discussed in Section 2.2.1. The CC served as an effective primary zone (PZ) for the initial burn and also as a flame stabilization zone before products migrated into the core flow. Zelina *et al.*'s tests showed that centrifugal loading kept fuel and air in the CC longer, thus increasing the residence time and combustion efficiency. Hot gas migration of the CC was found to be a highly turbulent process, resulting in increased mixing prior to the lean-burn in the core flow. From these experiments, Zelina *et al.* [17] estimated that a UCC could achieve a 66% reduction in length utilizing this circumferential swirl technique. Although this experiment was designed to be used as an ITB, the realization of a possible 66% reduction in combustor length sparked research to implement centrifugally loaded combustion in main burner applications.

In an effort to apply centrifugal loading in a fighter-scale main combustor, Bohan and Polanka [18] began numerical research on an HGC with a square CC cross-section, circumferentially wrapped around axial core flow. Air was introduced about the outer diameter (OD) of the cavity at 35° tangent to the circumferential cavity. The tangential introduction forced a circumferential swirl about the core flow, replicating the

circumferential loading seen by Zelina *et al.* [17]. Circumferential loading conditions, as introduced previously in Section 2.2.1, were targeted in these experiments using Equation 7 [17]

$$F_c = \frac{U_{tan}^2}{g_e * r_{cav}} \tag{7}$$

where F_c is the dimensionless circumferential acceleration parameter found using the circumferential acceleration of a tangential velocity (U_{tan}) about a radius (r_{cav}), normalized by Earth's gravitational acceleration (g_e). Any F_c would represent a load when multiplied by a fluid particle's weight, or an acceleration if multiplied by g_e. This was especially useful when comparing to previous research that presented information in terms of gravitational acceleration. The tangential velocity was calculated using Equation 8 [17] from the cavity mass flow rate ($\dot{m}$), density (ρ) and exit area (A_{exit}) by continuity, and the introduction angle from tangent (β).

$$U_{tan} = \frac{\dot{m}_{cav}}{\rho_{cav} A_{exit}} \frac{1}{tan\beta} \tag{8}$$

These two equations define the test parameters necessary to match circumferential loading in experiments in order to compare to previous research on HGC applications. Bohan and Polanka [18] determined that the circumferential swirl increased residence time within a shorter axial distance, resulting in nearly complete combustion before the entrance into the turbine section. One issue pointed out for implementation in a gas turbine cycle was that a compressor would need to be designed to feed both the CC and the core air, both of which flow nearly perpendicular to one-another. This notion influenced the design of the Disk-Oriented Engine, as it does not have a core flow and all air is fed to the circumferential cavity. The need for separate core and CC air introduction would be negated by such a design, but following experimentation of the AFIT UCC continued with a core-flow design.

Later iterations of the UCC at AFIT, designed initially by Conrad *et al.* [19], introduced CC swirl via the front air driver plate (Figure 10). Cottle *et al.* [20] iterated on this with 48 holes on the front face, each 0.493 cm in diameter and angled at 55° from axial flow and 10° radially outboard. Fuel was injected from the OD radially inward, utilizing shear as the method for mixing. This configuration resulted in a layer of fuel on the OD that was not mixing with the air.

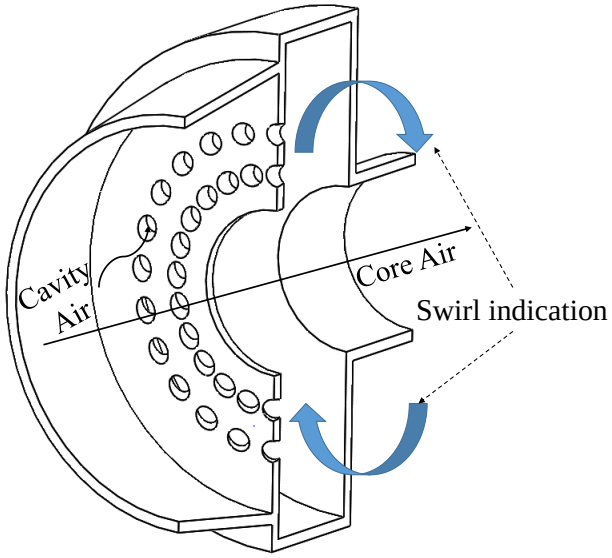

Figure 10. Diagram of Cottle combustor assembly, showing air driver holes and swirl direction, adapted from [6].

A solution to this problem, investigated by DeMarco *et al.* [6], was to introduce more air to the OD of the cavity with a six-step ring that forced additional mixing and created recirculating mixing zones at each backwards-facing step. The step feature created a rapid separation of the flow, resulting in a low-pressure region behind the step and a vortex that rolled along the span of the step. This vortex then acted as both a flame holder and a mixing feature that enhanced combustion efficiency and stability in the CC of the UCC. The step and hole geometries served as a initial baseline for hole placement and CC structure in the design of the Disk-Oriented Engine Combustor.

The stepped-ring design was further explored by DeMarco *et al.* [21], who introduced a twelve-step outer ring with alternating fuel/air steps and fuel only steps to improve mixing by creating recirculation regions. With less momentum introduced than fuel and air steps, the fuel only steps functioned as much stronger flame holders and mixing zones for stable combustion. Tests of back-plate (opposite the air driver plate) fuel injection were also conducted, resulting in a 10% increase in exit temperatures.

A critical issue with the AFIT UCC was a product of combining a circumferential combustion cavity with an axial core bypass the hot products did not migrate across the cool core. This phenomenon was investigated [6, 18, 22] with little success in mitigating the flow migration issue. To visualize this OD hot-spot, Figure 11a provides an exit temperature profile typcical of AFIT UCC experimentation, while the opposing (Figure 11b) provides an exemplar exit profile captured by Bohan *et al.* [23] in testing UCC applied to JetCat small engines. Since this exit profile supplies directly to the turbine face, peak temperatures are desired with a slight OD skew from mid-span of the turbine for maximum power extraction [23].

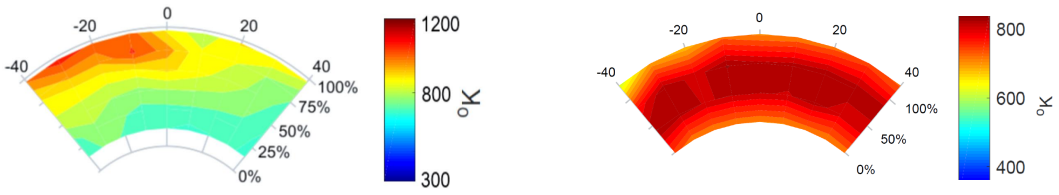

(a) Exit profile typical of AFIT UCC [6]

(b) Desired exit temperature profile [23]

Figure 11. Example of two exit temperature profiles, showcasing hotspots seen in AFIT UCC operation.

Another determining factor for turbine survivability is the uniformity of temperatures that it is exposed to. Localized hot spots one position of the turbine rotor will cause extreme heating, and can lead to catastrophic failure of the rotating hard-

ware. One way of determining the temperature uniformity on the combustor plane is pattern factor (PF), defined by Mattingly *et al.* [9]. Equation 9 presents pattern factor as a function of maximum combustor exit temperature (T_{t4max}), average exit temperature (T_{t4avg}), and compressor exit temperature (T_{t3}). Traditional combustors operate with pattern factors between 0.2 and 0.45, setting the bounds for target PF in the Disk-Oriented Engine [24].

$$PF = \frac{T_{t4max} - T_{t4avg}}{T_{t4avg} - T_{t3}} \tag{9}$$

DeMarco *et al.* [21] also noted that combustion was limited to bulk cavity velocities between 3.6 and 9.5 m/s (18-125*g_e), well below the expected maximum discussed in Section 2.2.1. Chemiluminescence tracking of the OH radical done by Rathsack *et al.* [8] showed that the lowest air flow rates introduced to the CC resulted in the most uniform flame profile at all twelve step locations. This visual data corroborated DeMarco *et al.*'s findings about the benefits of low circumferential loading, thus leading to the discovery that improved combustion as a result of circumferential swirl in the UCC was a function of increased residence time, not centrifugal loading as predicted by Lewis and Briones [14, 15].

The limits seen by both DeMarco *et al.* and Rathsack *et al.* [21, 8] were taken into consideration in the design process, but the swirl of the Disk-Oriented Engine Combustor was dictated by the compressor stator exit conditions. With a larger radius than previous AFIT UCC iterations, the Disk-Oriented Engine Combustor would also experience higher circumferential loads than tests by Rathsack *et al.* and DeMarco *et al.* for the same tangential velocities, as defined by Equation 7.

2.2.3 Trapped Vortex Combustion

Another method for compact combustion development is the trapped-vortex combustor (TVC), which utilizes swirl differently than an HGC to create a stable flame. As shown in Figure 12, the bulk-swirl maintained by an HGC has an axis of rotation parallel with the core flow, while a TVC creates swirling motion about the center line with an axis of rotation tangent to the circumference outer diameter. In a TVC, a cavity is recessed from the axial flow that traps a vortical structure. Fuel is introduced within this structure, and the stable vortex core provides both mixing and a flame anchor for combustion to occur inside and out of the cavity [25].

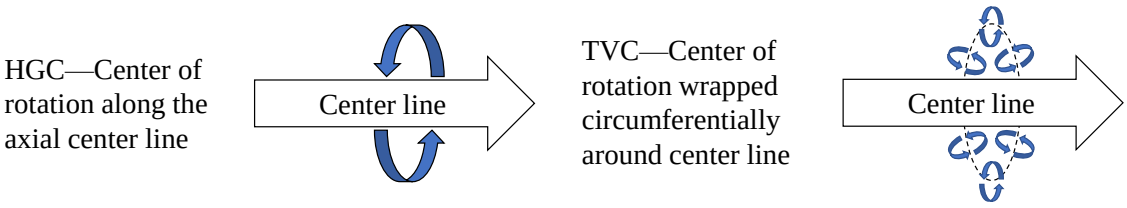

Figure 12. Comparison of HGC and TVC flow patterns, adapted from [26].

The idea for flame stabilization within a recessed cavity was based on a drag-reduction practice tested by Mair [27], where disks were mounted aft of a blunt body to create trapped vortices which reduced pressure drag. Little and Whipkey [28] took this information and applied it to combustion, finding that the configuration resulting in minimum drag seen by Mair corresponded to the most stable recirculation zone, and thus the most stable combustion. This stands to reason, as high pressure-drag aft of a blunt body is a result of unsteady separation, but the introduction of a stable vortex rather than an unsteady region provided a place for stable combustion to anchor. Hsu *et al.* [29] ran tests on a TVC, as shown in Figure 13, with varying cavity length (H). This design created a vortex initiated by separation off of the forebody and sustained it with fuel and air introduction from the afterbody in the direction of swirl.

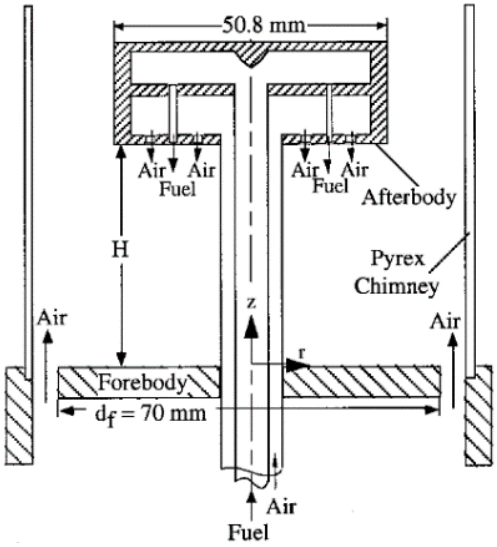

Figure 13. TVC setup tested by Hsu *et al.* [29].

Since TVCs have shown higher lean blow-out velocities than other bluff-body stabilizers (such as v-gutters) [30], UCC applications of TVCs have been limited to flame holders. Zelina *et al.* [17] introduced a cavity-in-cavity feature as a part of their HGC/TVC combined system (Figure 14c), where the trapped-vortex flame holders resided in channels about the circumference. In these channels, two different methods of air introduction were tested (Figure 14a and b). These radially-offset holes introduced mass to enhance the swirl created by the flow over the cavity alone. Lean blow-out tests showed that air introduced from both holes (Figure 14a) caused blow-out at a higher equivalence ratio than other tests. This was believed to be a result of too much mass entering the confined area, preventing the formation of a stable vortex [31]. While it was important to introduce enough mass to maintain swirl, too much momentum introduced tangent to the vortex, especially near the open end of the cavity, caused vortical breakdown and possibly prevented entrainment of reactants from the circumferential cavity. Without the cavity-to-cavity exchange of fuel and air reactants for hot products, the trapped-vortex could not serve as an efficient flame holder.

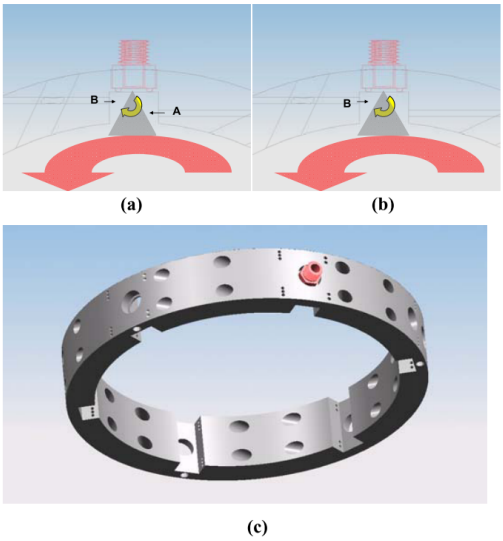

Figure 14. Cavity-in-cavity design, combining HGC and TVC [31].

Both the afterbody fuel and air injection in Hsu *et al.*'s tests [29] and the radially-offset air introduction in Zelina *et al.*'s design [31] served as a basis for utilizing a trapped-vortex in the Disk-Oriented Engine. Without a core flow over the open end of the cavity as seen in both of these, the vortical setup needed to be different. Swirl was maintained by the placement of jets that forced momentum to swirl in a desired way without physical hardware, but the same principles of vortex-core stabilization and hot-gas exchange with the main combustion volume applied.

2.2.4 Short Helical Combustors

A third method for reducing combustor axial length is the short helical combustor (SHC), introduced by Ariatabar *et al.* [32]. This geometry takes advantage of the increased residence time seen in the HGC (Section 2.2.2) by introducing a circumferential swirl about the axis of the engine. This design was applied to a traditional annular combustor, but instead of turning the compressor flow axial as a conventional combustor would, the SHC maintains some swirl as shown in Figure 15. This swirl does not introduce circumferential loading as seen in an HGC. Since a circumferen-

tial component is maintained prior to fuel introduction, the burner nozzles were also tilted into the direction of the flow. The effect of this design is a helical flow pattern that swirls circumferentially about the engine center line while migrating axially toward the turbine section. The benefit of this design was two-fold: 1) a trigonometric axial length savings due to increased residence time in a circumferential direction, and 2) a reduction in the turning angle of the nozzle guide vane, thus reducing losses through the first-stage high-pressure turbine. A combustor length savings of 15-30% was estimated by this method [32].

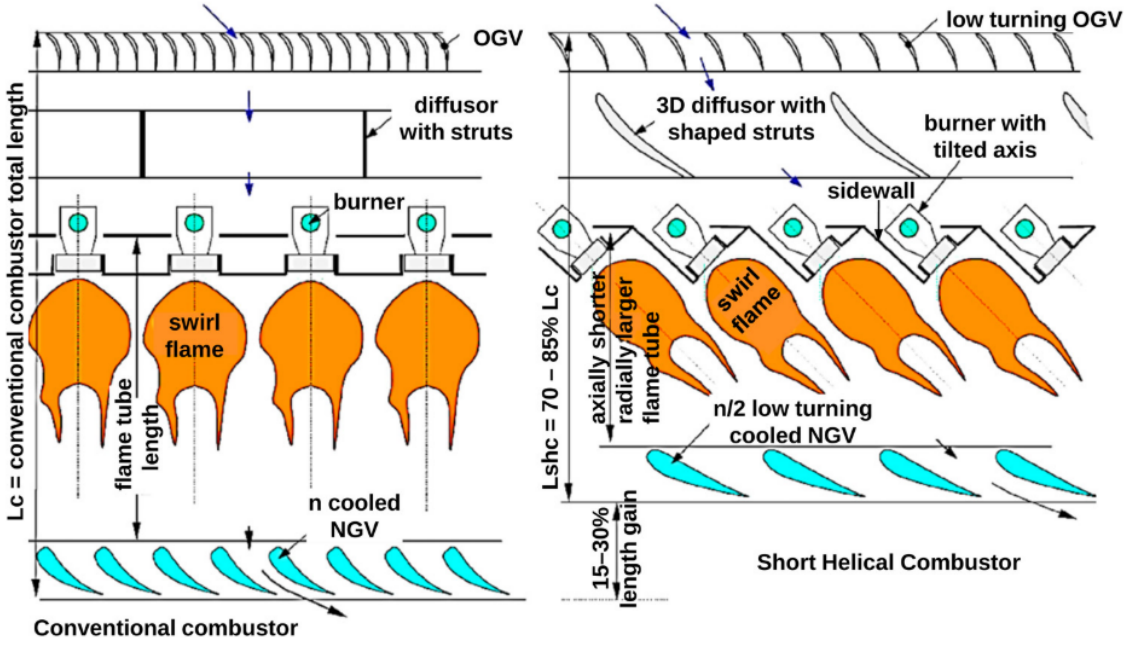

Figure 15. Comparison of traditional annular combustor configuration compared to a short helical combustor [32].

While this implementation of compact-combustion was not the basis for the Disk-Oriented Engine design, as it was not designed to circumferentially load the combustion process, some elements transfer between the two. Both take advantage of the compressor swirl to enhance combustion while reducing the turning load on the turbine inlet guide vane.

2.2.5 Reverse-Flow Combustors

Another compact-combustion approach is the reverse flow combustor, as shown in Figure 16. The flow reversal provides a longer path length for complete combustion within a shortened axial length by turning the flow back on itself multiple times between the compressor and turbine [33]. Reverse flow combustion is not typical of large scale gas turbine engines, as turning the flow path produces total pressure losses, and therefore inefficiencies. Aviation applications, such as turboprop and turbo-shaft engines, utilize reverse flow combustors, accepting this pressure loss penalty. Since these engines are primarily designed to extract power to create torque instead of thrust, this pressure loss impacts performance less than it would a turbojet.

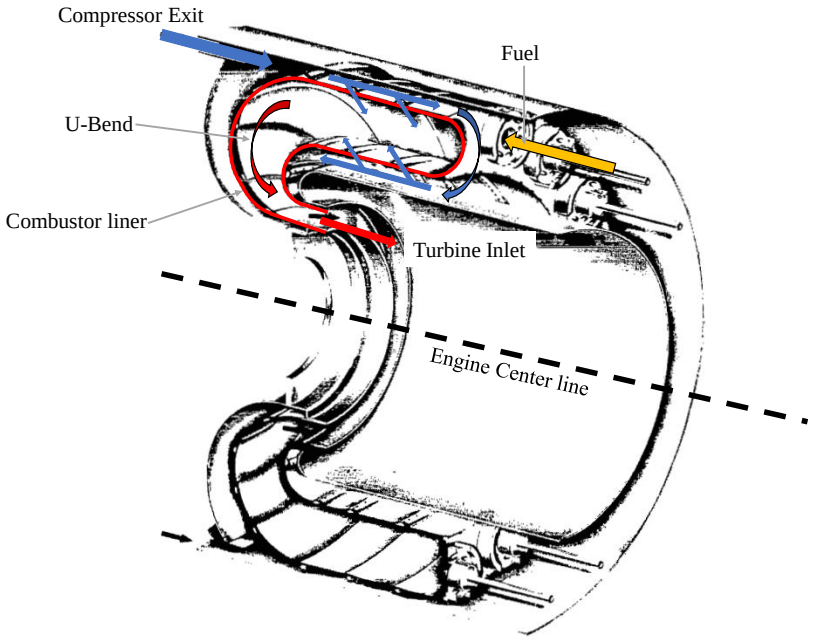

Figure 16. Reverse flow combustor layout, adapted from [33].

As seen in Figure 16, air enters a reverse flow combustor stage from the left, passes through the liner from both the top and bottom (as denoted with blue arrows into the liner), and mixes with the fuel in this pseudo primary zone. Much of the combustion is completed in the highly-turbulent fuel introduction zone, with some secondary

burning being accomplished in the U-bend before entering the turbine. While the overall flow pattern shown here could not be replicated in the Disk-Oriented Engine, elements such as combusting flow reversal proved to be useful in the design.

2.3 Radial Turbomachinery

To experience the full length savings of a Disk-Oriented Engine, the combustor was designed to accept swirling flow from a centrifugal compressor and prepare exhaust products for a radial in-flow turbine. Figure 17 shows the flow pattern of air through a Disk-Oriented Engine, depicting how the combustor design provides a linkage between radial compressor and turbine. Burning in this U-bend configuration allows for a direct coupling of the radial compressor and turbine, without having to turn the flow for an axial combustor. The direct connection between the compressor and turbine require that they spin in the same direction, at the same speed, and the Disk-Oriented Engine was designed to facilitate this flow requirement. This flow condition was created using stator vanes for both the compressor and turbine, which are incorporated directly into the design of the combustor. The feed and exhaust conditions of the combustor are then products of the rotating machinery, which dictate the stator angles producing the swirl in and out of the burner. Velocity triangles control theses angles and are dictated by the compression requirements of the cycle and the turbine speeds required to meet this work output.

2.3.1 Centrifugal Compressors

While axial compressors are generally more efficient for large scale engines [1], multiple factors make axial compression an inappropriate means of supplying air to a Disk-Oriented Engine Combustor. Centrifugal compressors can also achieve a higher pressure ratio across a single stage, are more stall resistant, and are less sensitive to tip losses in small-scale engines than their axial counterpart [1]. One downside to radial

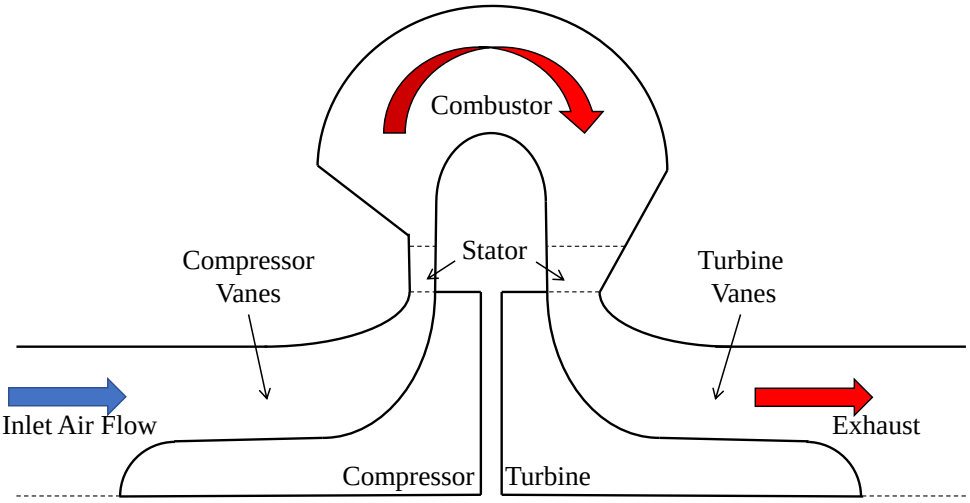

Figure 17. Flow path diagram through turbomachinery of a Disk-Oriented Engine.

compressors is the additional stage requirement to turn radial flow axially, increasing losses through the compression process, but a Disk-Oriented Engine relieves some of this turning requirement by accepting radial flow without turning it axially after compression.

Figure 18a depicts a typical centrifugal compressor, outlining the spin direction of the compressor rotor. The velocity triangles for such a compressor are shown in Figure 18b. In these figures, the compressor stations numbers 1, 2, and 3 refer to the impeller inlet, the impeller-stator interface, and the stator exit, respectively. The velocities, U_{tip} and V, refer to the rotor tip velocity and fluid velocity, respectively, and the subscripts are indicative of the location at the rotor-stator interface. The relative subscript (R) denotes the vector represents a fluid velocity from the rotating reference frame, and the lower case letters v and w are the tangential and radial components of the V velocity. While all of these values could be evaluated if necessary from the engine cycle, the angle (α_2) and velocity at station 2 were of interest at the combustor boundary of the Disk-Oriented Engine. Following the method outlined in Mattingly *et al.* [1], a sample α_2 and V_2 were solved using the following general assumptions:

1. Compressor inlet Mach number (M_1) = 0.5 (generally $M_1 < 0.6$)
2. Ratio of specific heats (γ) = 1.4
3. Specific gas constant (R) = 287 $\frac{J}{kg*K}$
4. Compressor inlet temperature (T_1) = 288.15 K (standard day SLS)
5. Slip factor (ϵ) $\approx$ 0.9
6. U_t = 450 m/s (approximate maximum for light weight alloy compressors)
7. w_2 = Inlet axial velocity (u_1)

Based on the definition of Mach number, the exit radial velocity for this compressor would be 170 m/s by Equation 10.

$$w_1 = u_1 = M_1\sqrt{\gamma R\ T_1} \tag{10}$$

Tangential velocity could then be found by the definition of slip factor as presented by Mattingly *et al.* [1] in Equation 11, where v_2 = 408 m/s.

$$\epsilon = \frac{U_t}{v_2} \tag{11}$$

Applying the trigonometric properties of these two values, v_2 and w_2, in Figure 18b, it can be shown that the compressor rotor exit conditions for the example rotor are V_2 = 442 m/s at $\alpha_2 = 22.87°$. With known information about the cycle, this process could be applied to find compressor exit conditions for the Disk-Oriented Engine without development of a specific compressor rotor.

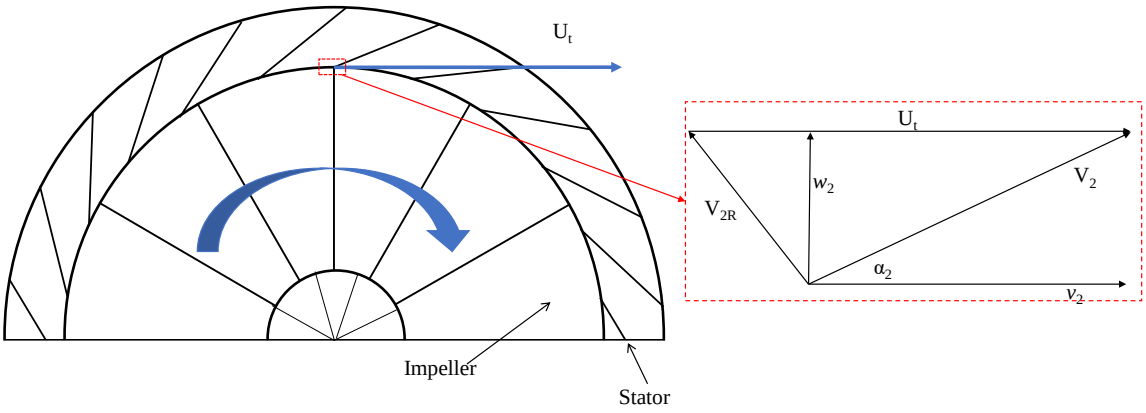

(a) Rotational View b) Exit Velocity Triangles

Figure 18. Centrifugal compressor diagram with velocity triangles. Adapted from [1].

2.3.2 Radial Inflow Turbines

The use of a radial in flow turbine (RIT) in a Disk-Oriented Engine application serves two purposes. When compared to an axial turbine, a radial turbine can extract the same amount of power as two axial stages, resulting in weight savings [34]. The second, and most advantageous benefit of an RIT is its direct coupling with the flow orientation of a Disk-Oriented Engine Combustor.

Although a particular turbine would not be designed for the present research, the basic concept of velocity triangles for an RIT would provide an appropriate starting point for the exit angle of incorporated turbine stators. Aungier's Turbine Aerodynamics text [35] provides an iterative design technique for determining radial in-flow turbine stator size and orientation. Following this design process, the bounds suggested for the ratio of radii (r_2/r_3), as shown in Figure 19, are 1.1 to 1.7 with a stipulation that the airfoil setting angle (γ_3) be greater than 5°. While additional steps for design iteration were presented by the text, these simple bounds were declared sufficient for preliminary design of stators without a known turbine rotor.

To relate the setting angle to the ratio of radii, the law of cosines was employed

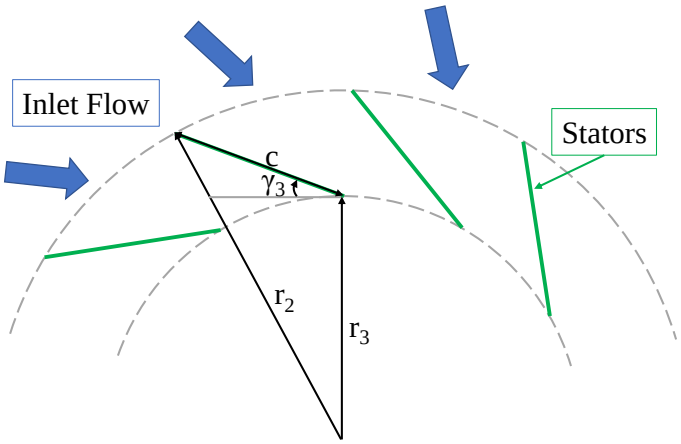

Figure 19. Radial in-flow turbine stator nomenclature, viewing the face of the turbine as if it were rotating clock-wise. Adapted from [35].

in Equation 12:

$$r_2^2 = c^2 + r_3^2 - 2 * c * r_3 * cos(90^\circ + \gamma_3), \tag{12}$$

where c is the mean-line cord length. Rearranging this expression, Equation 13 shows γ_3 as a function of r_2/r_3 if r_3 and c are known.

$$\gamma_3 = -acos\left(\frac{(r_2/r_3)^2 - (c/r_3)^2 - 1}{2 * (c/r_3)}\right) - 90^\circ \tag{13}$$

If r_3 and c are assumed to be 8.06 cm and 6.12 cm, respectively (these lengths are representative of the chosen design, used for demonstration purposes), then the bounds for γ_3 can be estimated to $-14^\circ < \gamma_3 < 30^\circ$ if $1.1 < r_2/r_3 < 1.7$. Since a restraint was placed on setting angle in the text, the bounds for setting angle of the stator vane in the Disk-Oriented Engine were $5^\circ < \gamma_3 < 30^\circ$. With rough bounds for stator placement angles, all other facets of stator design (number, profile, inlet incidence) were designed iteratively, taking advantage of the cost effective analysis possible with CFD.

2.4 Computational Fluid Dynamics

To facilitate rapid prototyping of this novel Disk-Oriented Engine design, computational fluid dynamics (CFD) was employed for its ability to predict flows computationally without the expense of cutting metal for each iteration. Since the disk UCC was designed to operate at temperatures exceeding 1000 K, it was built out of stainless-steel and inconel, and prototyping in these materials would be cost-prohibitive. Prior to computational modeling, it was important to research a CFD solver (Section 2.4.1), conjugate heat transfer (Section 2.4.2), various turbulence models (Section 2.4.3), and a combustion model (Section 2.4.4) to predict the flow physics as closely as possible.

2.4.1 Solver Selection

For computations on the Disk-Oriented Engine, ANSYS Fluent version 17.2 was used for multiple reasons. Primarily, Fluent is a commercial code that was readily available at the Air Force Institute of Technology (AFIT), and the inherent robustness of commercial codes such as Fluent meant that it applied to a variety of applications. Also, like most commercial CFD codes, Fluent operates in a Graphical User Interface (GUI), that allowed for ease of use in implementation [36]. Fluent also supports three-dimensional flows, multi-phase flows, turbulence models, conjugate heat transfer, species transport and reacting flows [37]. It was for these reasons that Fluent was implemented in multiple combustion studies at AFIT; a thesis by Bills [38] and a dissertation by Bohan [26] served as the basis more many settings used in this experimentation. Briones [39] also used Fluent in research on UCC combustion, recommending that the partially-premixed combustion model would replicate the combination of premixed and non-premixed flames found in centrifugal combustion.

Fluent offers two different ways to approach solving the mass, momentum, and energy conservation equations: density- and pressure-based solvers. A density-based solver computes the velocity profiles using full continuity and momentum equations, while a the pressure-based solves for a pressure correction equation that is derived from those same momentum and continuity equations. The benefit to solving this pressure correction, as opposed to the entire momentum/continuity equations, is that there is a reduction in computation time. The partially-premixed combustion model also dictates the use of a pressure-based solver [37].

2.4.2 Conjugate Heat Transfer

Bills [38] explained that conjugate heat transfer is a way of accounting for the transfer of thermal energy across a boundary between a multi-state interface (*i.e.* fluid-solid interfaces), and Bills incorporated conjugate heat transfer in two-dimensions to better understand combustion interactions with surrounding walls. While thermal modeling of a system can done assuming an adiabatic boundary condition, Bohan [26] showed that the lack of thermal diffusion has an affect on temperatures at the surface, which could impact reaction quenching at a flame front.

Figure 20 shows the difference between an adiabatic model (Figure 20a) and a conjugate heat transfer model (Figure 20b). Although all fluid and combustion conditions between these two figures are identical, heat transfer into the surface allowed for heat dissipation and reduced the abundance of hot-spots on the metal surface. Figure 21 shows how this difference in wall modeling can impact the quenching of a reaction front as it approaches the wall. In the adiabatic case, the temperature contours show near-adiabatic flame temperatures for the propane burning all the way up to the wall. This was indicative of a flame anchoring to the surface of the wall, while heat transfer into the wall would likely locally quench this reaction. The conjugate

figure shows a decrease in temperature at the wall, indicating local quenching of the flame that will likely have an impact on both the metal temperature and the reaction propagation rate [26].

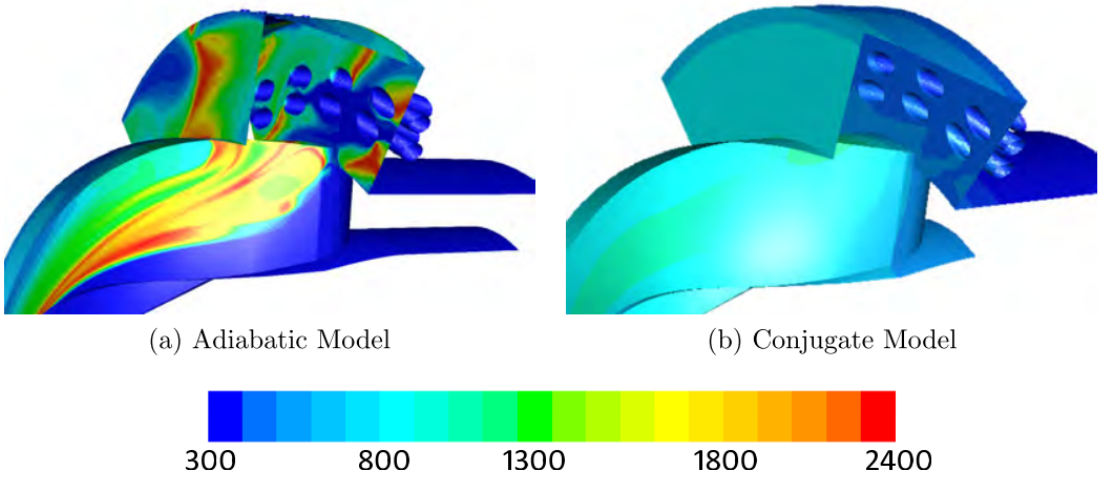

Figure 20. Contours of temperature [K], comparing adiabatic and conjugate heat transfer boundary conditions on a UCC cavity-vane section [26].

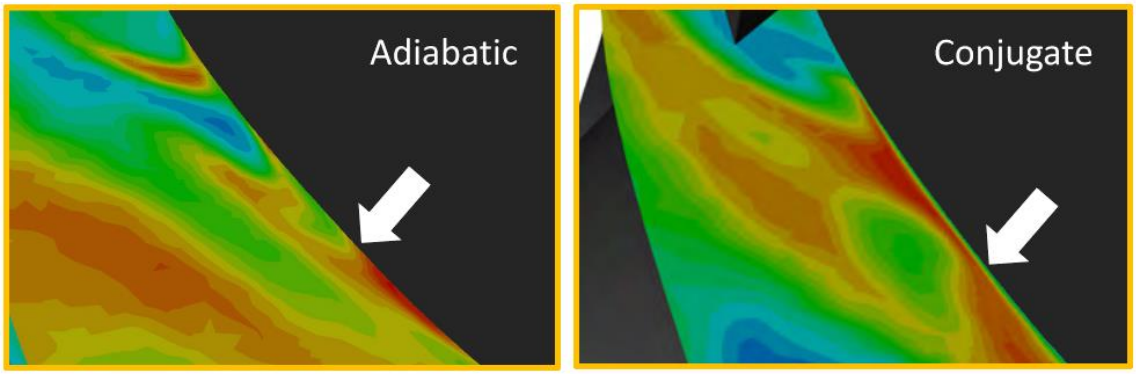

Figure 21. Contours of temperature [K], showing quenching in a conjugate heat transfer model, but not the adiabatic model [26].

Patankar [40] explained, to solve for properties at this interface, the heat transfer as convection in the fluid must be matched to the conduction in the solid. The accuracy of this solution is highly dependent on the temperature field, as conduction at the interface is directly proportional to the temperature gradient at the wall by Fourier's law [41]. This temperature profile, and the accompanying velocity profile,

change drastically in turbulent flows. The conjugate heat transfer solved in CFD is then highly dependent on the model used to approximate the turbulent velocity profile.

2.4.3 Turbulence Model

Cummings [36] explained that most modern turbulence modeling approaches fall under Reynolds-Averaged Navier-Stokes (RANS), Large Eddy Simulations (LES) and Direct Numerical Simulation (DNS). DNS attempts to solve the Navier-Stokes equation set directly over all turbulent scales and requires grid resolution magnitudes larger than that feasible for large-scale modeling of a Disk-Oriented Engine Combustor. LES solves those same equations for the largest of these eddies directly, but models the smaller turbulent scales. This method is useful for separated flows, where the computing power allows for appropriate span wise grid resolution to solve for those large-scale turbulent eddies. RANS approaches use empirical data to model all scales of turbulence in a steady, time-averaged flow. Since turbulence is modeled on all scales, the grid requirements are much less demanding than those for DNS and LES, but RANS approaches struggles to account for separated, unsteady flows [36].

The grid resolution is dependent on the spacing near the wall required to properly model turbulence in the boundary layer. This resolution is often expressed as a dimensionless wall spacing (y^+), a function of normal distance from the wall (y), friction velocity (u_τ) and viscosity (ν), as defined in Equation 14 [36].

$$y^+ = \frac{y u_\tau}{\nu} \tag{14}$$

Fluent [42] uses two primary methods in approximating turbulence in the near-wall region of a RANS model: direct simulation and wall functions. Simulating the turbulence to the wall requires grid resolution within the viscous sublayer ($y^+ < 5$) and

the first grid point is often required near $y^+ \approx 1$. This high-resolution grid practice often increases the computational requirements greatly, but it can provide accurate turbulent solutions near the wall. Utilizing wall functions, the turbulence is modeled between the fully-turbulent boundary layer and the wall, requiring the first cell to be located within the log-law region ($30 < y^+ < 300$) [42]. While wall functions do not use the full RANS model all the way to the wall as direct simulation does, they require lower grid resolution and are often more stable.

RANS models are often differentiated by the value of turbulent viscosity [36], ν_t, which is a constant applied to the rate of strain of the fluid to estimate the deviatoric Reynolds Stress [43]. This is the closure method for the RANS model, and the value of ν_t is often based on experiment and varies for flow conditions. Cummings [36] presented two popular ways of applying this RANS turbulent viscosity: the Jones-Launder $k-\epsilon$ model and the Launder-Spalding $k-\omega$ model. They are named for the partial differential equation (PDE) variables used in the model, which include turbulent kinetic energy (k), turbulent dissipation (ϵ) and turbulent dissipation rate (ω) [36].

A combination of these two models, the Menter shear stress transport (SST) model [44], combines the advantages of each in a single turbulence model and is the basis for the Fluent $k-\omega$ SST model [37]. The $k-\omega$ model is more effective for wall-bounded flows, especially in the viscous sublayer region of the boundary layer, as its simplicity leads to stability that does not require damping functions seen in the $k-\epsilon$ model [45]. Away from the wall, in the wake region of the boundary layer outside of the log-law layer, the $k-\omega$ model is sensitive to the viscous dissipation rates in the free stream. The $k-\epsilon$ model is not as sensitive to these rates and is therefore more appropriate for free-shear turbulence away from the wall [46]. The Menter SST model [44] transitions between these two models outside of the log-law layer, modifying eddy viscosity to

"account for the transport of the principle turbulent shear stress" [44]. Since elements of both wall bounded turbulence and free-shear turbulence were expected with little separated flow, the Menter SST model ($k-\omega$ SST in Fluent) was used to model turbulence in early Disk-Oriented Engine Combustor computations.

With the introduction of fuel-air swirlers and a dump diffuser in later, more complex geometries, the turbulence modeling approach shifted for Disk-Oriented Engine Combustor analysis. Turbulent characteristics were modeled using a $k-\epsilon$ realizable turbulence model with enhanced wall treatment, as used in previous UCC research by Cottle *et al.* [47]. Since areas of high shear were expected in both the dump diffuser and the fuel-air swirlers, it was anticipated that the $k-\epsilon$ model would be appropriate for this research. Enhanced wall treatment allowed for less strict grid requirements ($30 < y^{+}_{\text{wall}} < 300$), as the model exploits the turbulent and laminar laws-of-the-wall and is valid throughout the logarithmic near-wall region [42]. These two models provided turbulent predictions that not only account for the impact of turbulence on heat transfer and total pressure loss, but also the impact of mixing in the reaction model.

2.4.4 Combustion Model

Shown in research done by Briones *et al.* [39], the combustion process in a UCC contains both premixed and non-premixed combustion, and the Fluent partially premixed combustion model is a combination of these two models [37]. Previous UCC combustion modeling by Bohan [26] and Cottle [48] used partially-premixed combustion with flamelet generated manifolds. The combustion reactions in this model are based on the Gas Research Institute Mechanism (GRIMech), developed by the University of California at Berkeley, Stanford University, the University of Texas, and SRI International. The GRIMech is a chemical reaction mechanism, containing

a list of 325 chemical reactions and rate constant coefficients for 53 species, used in the Chemkin program to simulate hydrocarbon combustion [49]. Fluent used this Chemikin model to reduce the full GRIMech and create a reaction probability density function (PDF) that contains the 20 most prevalent species and the 32 most frequent reactions in the propane-air combustion process [37]. This PDF is then used to predict species interaction throughout the simulation, providing flame information based on the turbulent premixed and non-premixed flame speeds tabulated by the Chemkin model.

2.5 Particle Image Velocimetry

Focused experimental testing on components of the Disk-Oriented Engine Combustor required a fluid measurement technique that was both accurate and comparable to computational results. Particle Image Velocimetry (PIV) provides a non-intrusive, "...accurate [and] quantitative measurement of fluid velocity vectors at a very large number of points simultaneously" [50]. Using PIV, two-dimensional or three-dimensional velocities could be measured in a particular flow field (*i.e.* above fuel-air swirl injectors) which could then be compared directly to computational results on the same region. PIV measures velocities by seeding a fluid with illuminated particles and tracking those particles with a high-speed camera. Adrian [50] explained that commercially available two-dimensional particle tracking systems for PIV typically include a seed illuminated by a double-pulsed Nd:Yag laser, where the laser is refracted into a planar sheet, and the seed movement is captured by a high-speed, cross-correlation PIV camera [50]. Figure 22 shows an example of such a setup used for single-camera, two-dimensional velocity measurements. A similar setup was used by LeBay *et. al.* [51] for flow visualization in AFIT UCC testing, where a Dantec PIV system tracked silicon carbide seed, chosen for its low density and small diameter (0.1-2.5 μm).

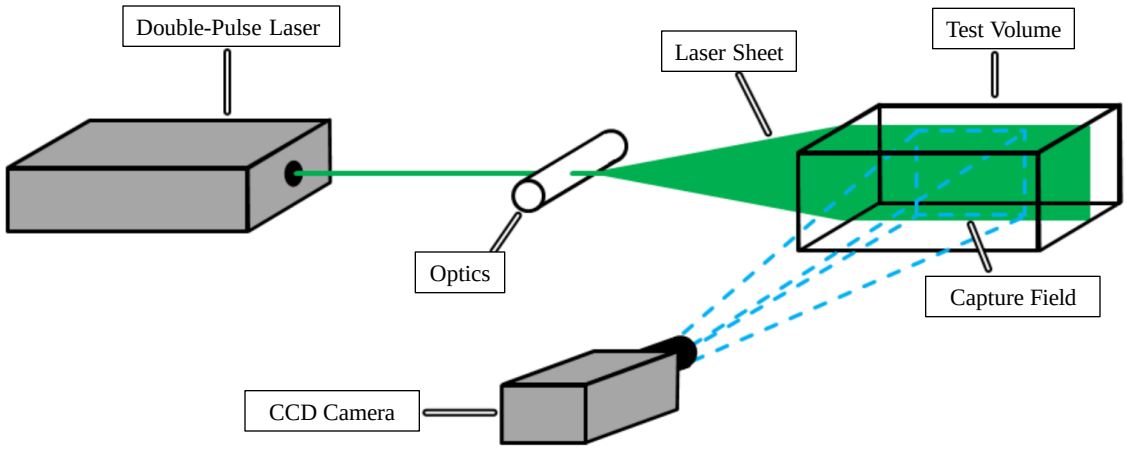

Figure 22. Example PIV setup [52].

In PIV, high-speed imagery from a double-pulse laser produces two independent images of particle locations. An auto-correlation of intensities between the two images provides the distance a particle traveled between laser pulses. Adrian [50] explained that these images are divided into equivalent grids and an auto-correlation is applied to a Fourier transform of average image intensity in these gridded cells, known as interrogation spots [50]. From this auto-correlation, average velocity vectors for each interrogation spot can be calculated to develop a velocity field over the image area. Similar to UCC research done by Bohan [26], Dr. Larry Goss of Innovative Scientific Solutions Incorporated (ISSI) provided expertise in data collection and reduction with his PIV analysis program called DPIVB.

III. Methodology

To determine if the design of a Disk-Oriented Engine would be feasible and could operate in a sustained condition, analysis was conducted to aide the design process and showcase the viability of such designs. Various methods were employed to aide in the design of a Disk-Oriented Engine Combustor. Section 3.1 outlines the iterative nature of the geometry design and how that design progressed through computational analysis. Initial design concepts were analyzed computationally in ANSYS Fluent, allowing for rapid and cost effective analysis of various designs. The development and solution methodology for computational analysis is outlined in Sections 3.2 and 3.3. Section 3.4 explains the engine cycle selection process for determining test conditions in both computational and experimental analysis. Following extensive computational analysis and design iterations, a full-scale model was then fabricated for experiment; experimental setup is outlined in Section 3.5.

3.1 Geometry Design Progression

The computer model of the Disk-Oriented Engine was created in the computer-aided design (CAD) program, SolidWorks 2019. The primary design iterations of the Disk-Oriented Engine Combustor were based on the circumferential cavity tested previously at AFIT [6, 8, 19, 20], and subsequent designs were based on findings through computational modeling of those geometries. The nomenclature for design progression in Chapters III and IV follows a version numbering system, stepping through Versions One through Three (V1-V3). A comprehensive list of these design versions is listed in Table C-1, Appendix C. These computational geometries eventually led to a rig-ready test geometry, that would be designed from lessons learned in computational analysis on geometries V1 through V3.

3.1.1 Version 1 Geometry

Previous UCC experimentation at AFIT utilized a circumferential-cavity (labeled at the bottom of Figure 23) with dimensions 2.54 cm axial by 2.54 cm radial, and these were the base dimensions for the Disk-Oriented Engine Combustor primary zone (PZ) as shown in Figure 24. The front and back side PZ air introduction holes of the Version 1 Disk-Oriented Engine Combustor were staggered 1.27 cm radially to introduce a trapped-vortex like swirl (shown in red arrows, Figure 24) that would provide stable, efficient combustion as discussed in Section 2.2.3. Primary zone holes were designed to imitate the design tested by Cottle [20], who introduced air through 48, 0.493 cm holes with a 55° tangential component to force centrifugal loading and a 10° radially outboard angle to keep the swirl in the primary zone. The combination of the radially-offset holes to create a TVC and the tangential component to induce centrifugal loading were intended to introduce a helical-like spiral that mixed reactants and burned in a multi-axis fashion around the CC.

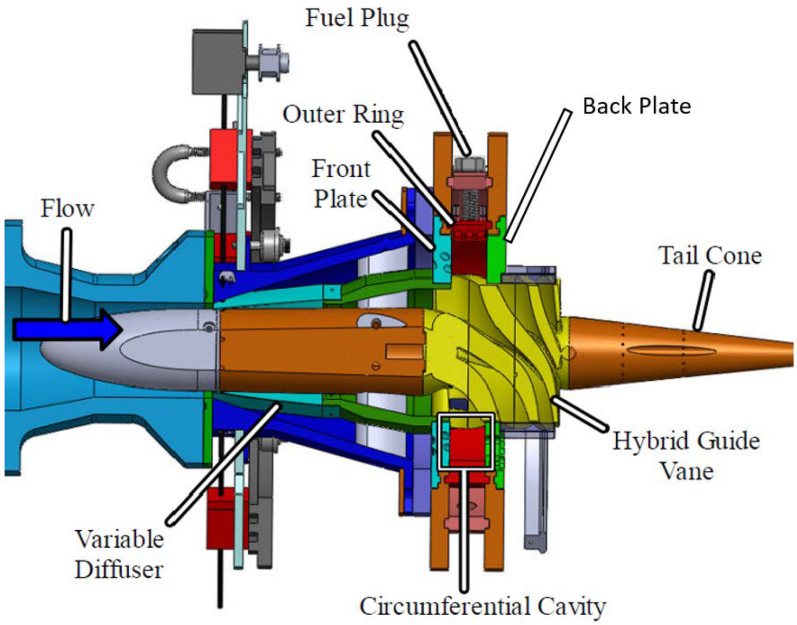

Figure 23. DeMarco *et al.*'s experimental setup, showcasing CC location and sizing [21].

Since the AFIT UCC utilized a hybrid guide vane (yellow body, Figure 23) with core flow, routing a percentage of the air mass flow around the CC, there was no secondary zone (SZ) or dilution built into the design. The lean burn in this design was accomplished in the interaction with the core flow, resulting in the hot outer region discussed in Section 2.2.2. To mitigate this flow migration issue, the Disk-Oriented Engine was designed with the SZ and dilution zone built into the CC, with the intent of a uniform temperature entering the radial in-flow turbine face.

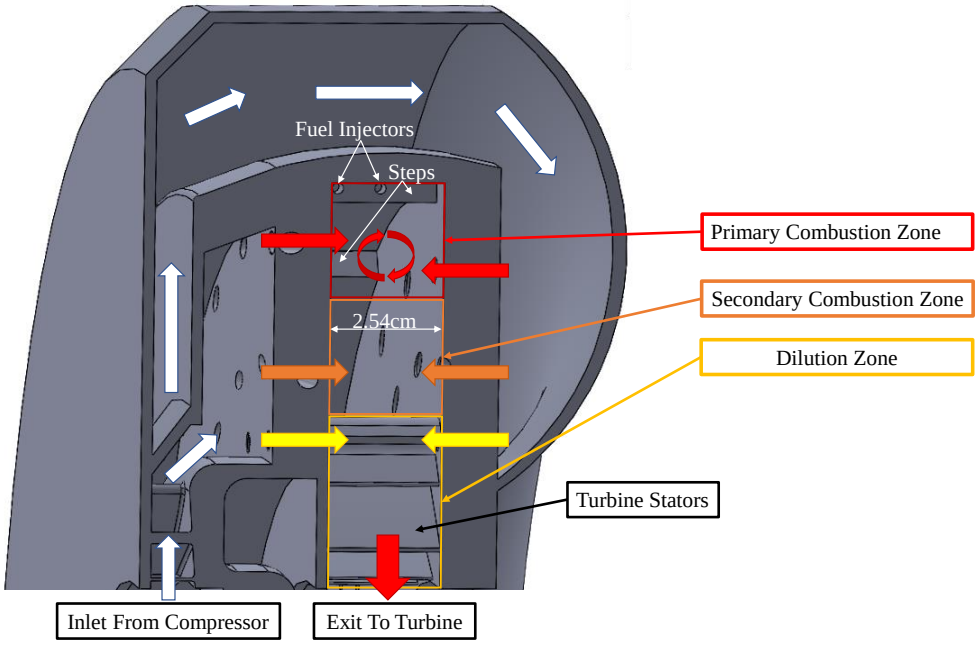

Figure 24. Disk-Oriented Engine flow path outline depicting inlet distributions, combustion zones, and exit path.

As seen in Figure 24, the axial depth of 2.54 cm was maintained throughout the CC, and the SZ was assumed to be the same radial size as the PZ, marked by the introduction of secondary air. These secondary air holes were designed with the same diameter as the PZ holes and angled at 65° tangent from axial to further accelerate the air before the turbine stators. The dilution holes served two purposes: air was introduced in the turbine inlet guide vanes (design discussed in depth in Results:

Section 4.2.4) to cool combustion products in preparation for rotating hardware, and the air created a cooling film on the underside of the guide vane to keep material temperatures lower and maintain the integrity of the guide vanes. The dilution zone was assumed 50% radially larger than the PZ to allow for dilution air to interact completely with combusted products and for any unfinished reactions to be completed before the radial in-flow turbine (RIT) inlet. The result was an 8.89 cm radial CC, with a volume of 1780 cm^2.

To feed the circumferential combustion cavity, air partitioning was a driving function behind subsequent iterations of Version 1. Figure 24 shows how air that entered radially from the compressor was split between the front and back faces of the CC. The idea was to create a pseudo-plenum that supplied equal pressure to the front and back sides, allowing for equal air mass flow introduction. Air that entered from the compressor stators was partitioned by the splitter in the front plenum, as shown by the white arrows. The red, orange, and yellow arrows indicate PZ, SZ, and dilution air introduction before the exit to the turbine. Hole sizing and placement, along with splitter design were iterated extensively, as pressure distributions were impacted by design when a true plenum was not reached.

Fuel was injected in the recirculation zone of a backwards-facing step, as shown in Figure 24. A scaled version of the twelve-step ring designed by DeMarco *et al.* (Figure 25) [6] was used, as it provided stable combustion in a similarly-sized CC. Fuel injectors in the Disk-Oriented Engine Combustor were sized and located just as they had been in DeMarco *et al.*'s fuel-only steps, omitting the air-fuel alternating steps. This location assumed that the compressor-side of the CC would see the most air with an air injector located at the radially-outboard location, and the fuel from this point would have the longest residence time in the trapped-vortex orientation before entering the secondary zone.

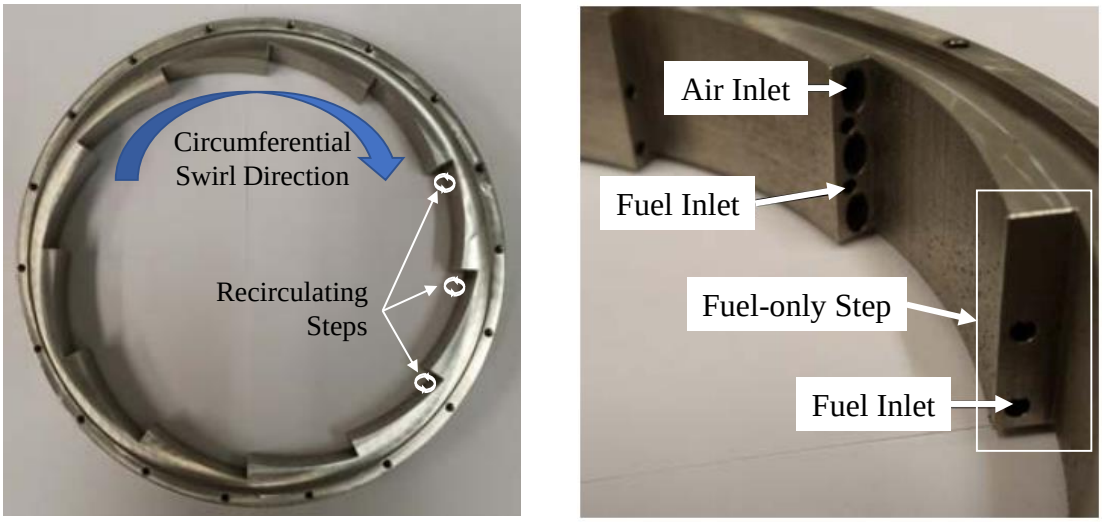

a) 12-step ring

b) Step-face injection scheme

Figure 25. AFIT UCC 12-step ring, adapted from [6].

Computational analysis of Version 1 indicated that complete combustion could not be sustained at max power conditions with such a geometry. Figure 26a shows equivalence ratio (Φ), as defined by Equation 15, on a plane at the axial-center of the circumferential cavity.

$$\Phi = \frac{(a/f)_{stoich}}{(a/f)} \tag{15}$$

The local air-to-fuel ratio was found by the sum of N_2 and O_2 mass fractions over the sum of all hydrocarbon mass fractions. Literature shows that flames are most stable near stoichiometric ratios, with the max temperature produced in slightly rich conditions ($\Phi \approx 1.05$) [7]. Figure 26a shows throughout much of the primary zone in Version 1, the mixture was fuel rich ($1.0 < \Phi < 1.5$) and unable to sustain combustion. At the interface between the PZ and SZ, high mass flow rates of air entering the combustion cavity created a gradient in equivalence ratio that included near-stoichiometric fuel-to-air ratios, but combustion was once again not sustained at this point.

In addition to fuel-rich conditions in the PZ, circumferential loading within the CC were too high to maintain combustion. Figure 26b shows circumferentially-averaged normalized centrifugal acceleration (F_c) against CC span. In Figure 26a, the PZ and SZ are highlighted to span the CC in the horizontal direction, and the radial span is plotted horizontally on Figure 26b to coincide. Indicative of circumferential loading, without the mass term, F_c was defined as centrifugal acceleration over Earth's gravitational acceleration in Equation 7. It was apparent that the load throughout Figure 26 was much higher than both the $3500 * g_e$ limit predicted by Lewis [14] and the 125*g_e maximum suggested by DeMarco *et al.* [6]. The peak centrifugal loading on this plane was 290,000*g_e, over 8000% larger than Lewis' region of estimated benefit. While circumferential loading was noticeably lower in the PZ than the SZ, it was magnitudes greater than that which could sustain combustion. The Version 2 designs would take this loading into account, attempting to reduce tangential velocity throughout the CC.

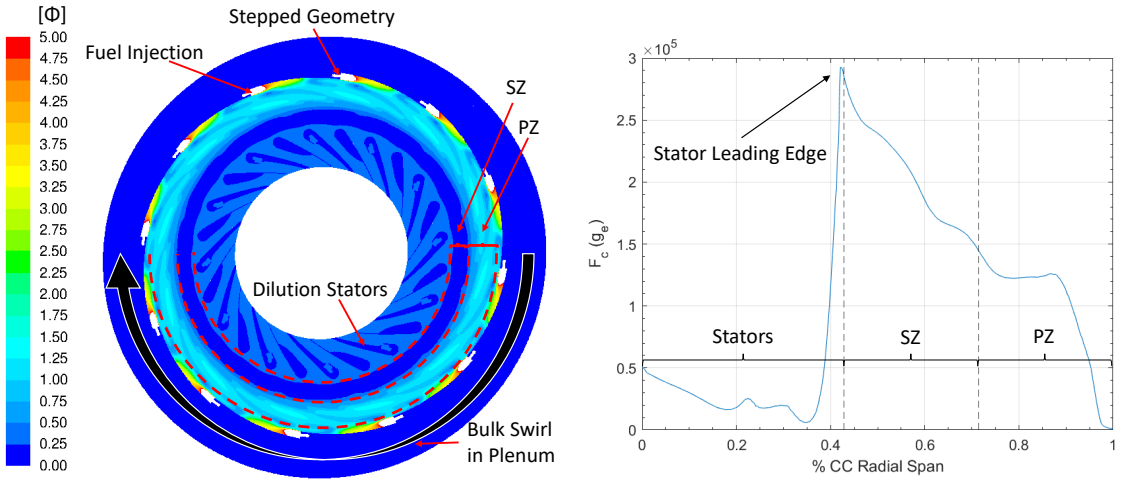

a) Equivalence ratio on CC centerline

b) Circumferentially-averaged centrifugal loading on CC center plane

Figure 26. Version 1 computational results.

3.1.2 Version 2 Geometry

The primary objective of the Version 2 geometry was to decrease the velocity in the circumferential cavity by increasing the CC volume, allowing for a more complete combustion process before products exit the cavity. As shown in Figure 27, the PZ in Version 2 was doubled both radially and axially to allow for more volume to develop a trapped vortex. A larger vortex would, in theory, create a larger surface area to burn on the edge of the vortex, and the increase in radial offset of the front and back PZ holes, from 1.27 cm to 3.81 cm, created more torque and a tighter core for complete mixing. The circumferential component of the PZ holes was removed to reduce centrifugal loading in the PZ, and the steps were removed as they would not create a stable recirculation zone without PZ circumferential flow. The fuel holes were also found to be too small in the Version 1 design for the mass flow rate of fuel being applied, adding to the circumferential load. Version 2 then saw an increase in the fuel hole diameter to reduce the jet injection velocity, while the fuel was introduced in a manner to be sheared by the outer-most PZ air holes.

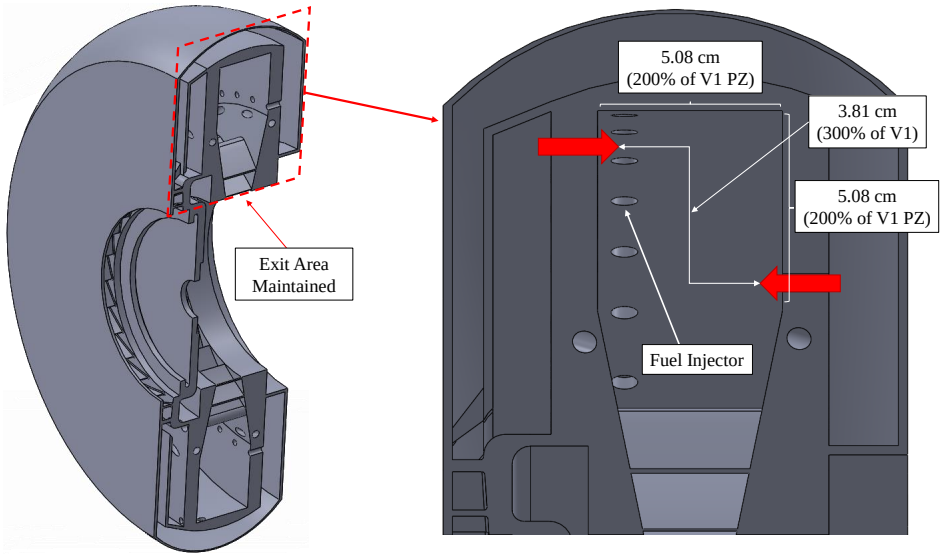

Figure 27. Version 2 Disk-Oriented Engine Combustor, outlining changes from V1.

Figure 28 shows some computational results from Version 2 analysis to understand the impact of the aforementioned changes. In the same side view orientation of the circumferential cavity shown in Figure 27, Figure 28a shows velocity vectors within the CC. One primary zone vortex, created by design with the radially-offset injection holes, is shown by the rotating fluid along with two secondary zone recirculations created by the front-side SZ holes. The shape and speed of this PZ vortex showcases the benefit of expanding the CC volume. With a larger volume, this vortex was larger, slower, and more sustained than that seen in Version 1. The combination of these three benefits created an environment in the CC that facilitated a strong primary burn, as intended.

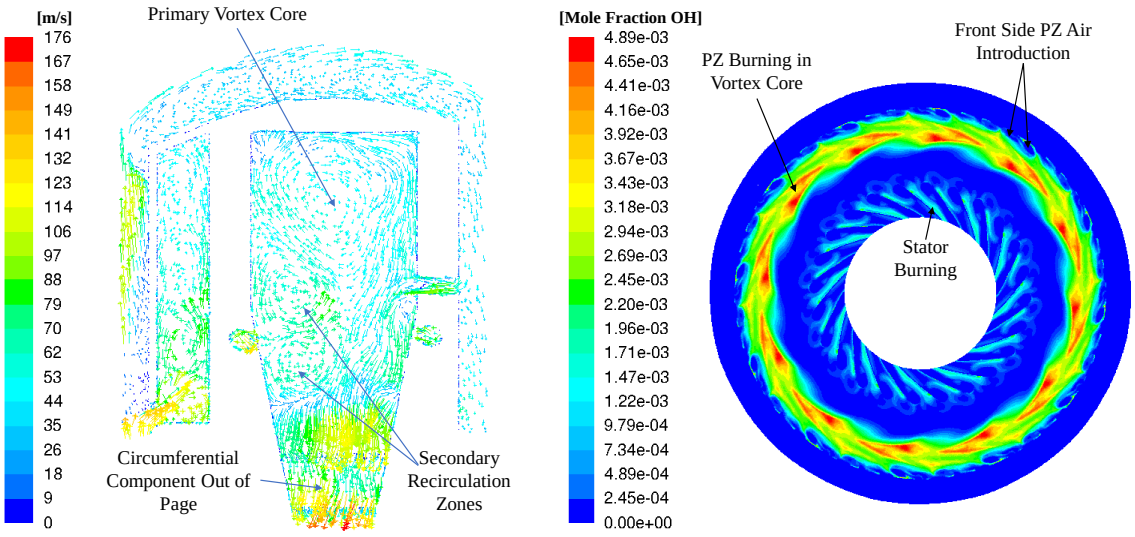

(a) Velocity vectors on radial-axial plane

(b) OH species contours on radial-circumferential plane

Figure 28. Version 2 computational results.

The strength of this PZ burn can be seen in Figure 28b, which shows species contours of OH indicating reaction front locations. The bulk of the burning species were located in the PZ vortex core about the entire CC. One major issue with this result was the bright pattern on the inner diameter suggesting combustion and heat release in the dilution-stator section. Additional heat release in this region could over

stress the thin cane-shaped stators, possibly causing material failure. While the bulk of the reactions occurred in the desired zone, any heat release in the stator section was deemed unacceptable and greater CC volume would be required to provide an increase in residence time, ensuring complete combustion before flow enters rotating hardware.

While the Version 2 results indicated that bulk-swirling combustion could be sustained for a combustor fitting the performance requirements of a Disk-Oriented Engine, combustion in the stators required changes be made to the design to ensure complete combustion occurred in the designated primary and secondary combustion zones. On the positive end, Version 2 showed that bulk-swirling air could be accepted in the diffuser and swirled once again in the combustion cavity. It is important to note that CC swirl in Version 2 was driven by the air injection holes, not necessarily maintained from the compressor. Version 3 then focused on utilizing the existing swirl, rather than forcing bulk swirl through discrete holes. Version 2 never established a defined SZ, as air introduced in this region was so fast and cool that it quenched any reaction that could be progressed with air injection. The Version 3 design increased the volume and decreased the mass flow of air entering the SZ to allow this secondary reaction to progress.

3.1.3 Version 3 Geometry

With the appearance of OH indicating combustion reactions still occurring in the stator vanes, it was determined that a third version would require more volume to allow for complete combustion before the dilution stages. While this could be achieved by simply scaling up Version 2, in the same process used between Versions 1 and 2, further radial scaling of the combustor was expected to negate the benefits of axial length reduction. Figure 29a shows a half-body cut of the full Version 3 combustor

for comparison to previous iterations. To increase the combustor volume within its current radial and axial dimensions, the front side of the combustion chamber was extended axially 3.45 cm, assuming this to be the complete compressor rotor depth, in addition to the 0.97 cm previously assumed for the compressor tip height. This increase allowed for use of volume that would otherwise be empty in a fully-operating version of the Disk-Oriented Engine Combustor inside of an engine casing. Figure 29b illustrates that the inlet and exit conditions remain the same as Version 2 (shown in Figure 27), allowing for the same reduced shaft length anticipated by the Disk-Oriented Engine orientation, while the geometry is noticeably different from Versions 1 and 2. Air enters through a dump diffuser before being divided between PZ, SZ and dilution feeds. Figure 30 shows how air was partitioned throughout the Version 3 combustor. Since the combustion liner created air injection points that more closely resembled orifices than jets, the V3 design would require substantial iteration to balance pressure and distribute the air as desired.

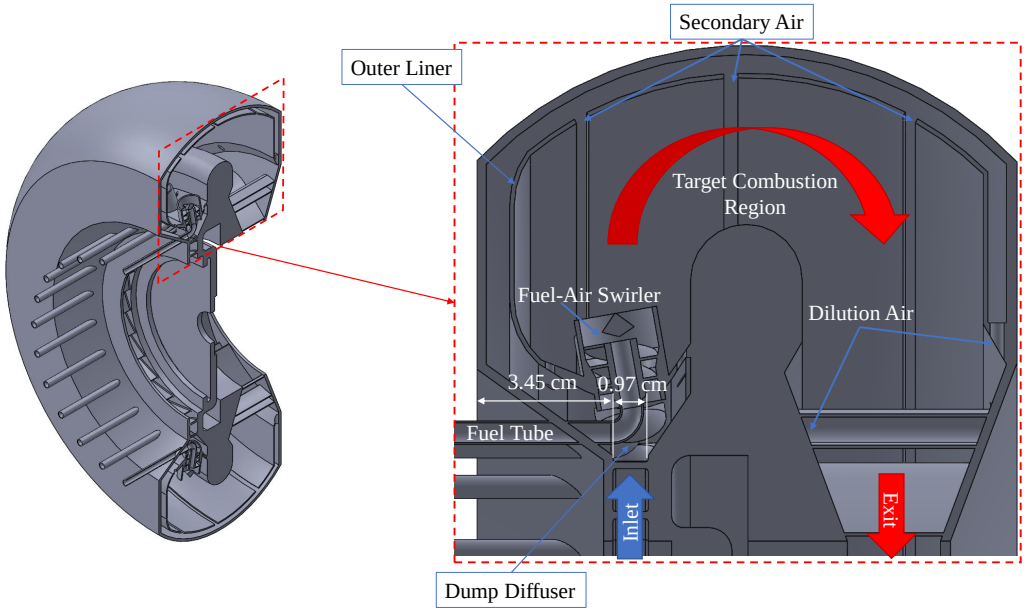

(a) Half-Body Cutaway

(b) Feature Description

Figure 29. Version 3 Disk-Oriented Engine Combustor, outlining changes from V2.

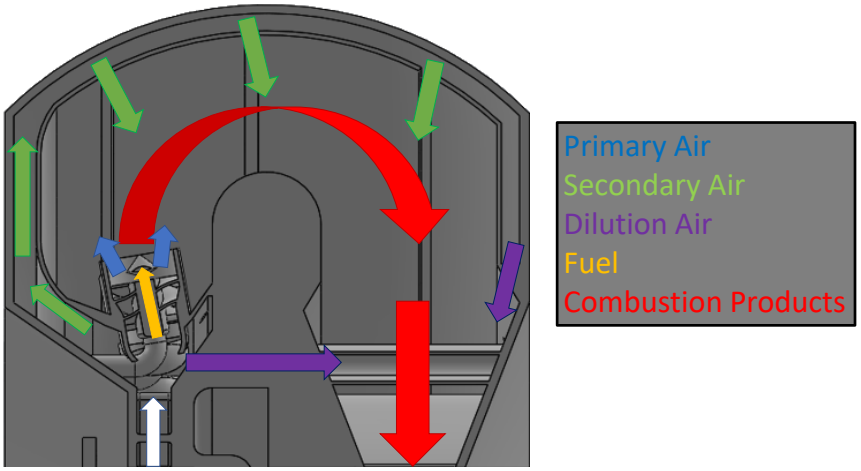

Figure 30. Version 3 flow diagram and air allocation.

With the increase in volume and change in air partitioning strategy, the need for and ability to create a trapped vortex within the combustion chamber was lost. The intent of the change in shape was to allow the combustion reactions to occur in the u-bend shape, much like a reverse flow combustor as seen in Section 2.2.5. The bulk circumferential swirl created by the compressor would still be maintained, but jets were not established as seen in Versions 1 and 2 to force additional circumferential loading in the combustion cavity.

Without a trapped vortex in the PZ, there would be little means of flame stabilization and fuel-air mixing. A fuel-air swirl injector, visible as a cutaway in Figure 29b, was iteratively designed to create regions of strong recirculation that would increase mixing and promote stable flame holding. This mechanism was designed based on principles discussed in Section 2.1.3, with air swirled about a co-axially introduced fuel jet, and this design is explained further in Section 4.1.

To better understand the changes in size and shape between Versions 1, 2 and 3, Figure 31 compares an iteration of the Disk-Oriented Engine from each of the three aforementioned versions. These geometries are scaled relative to one-another, and the similarity in inlet and exit conditions can be easily noticed. While the outer radius

varied slightly between all geometries, the size of the combustion cavity increased 720% between Versions 1 and 3. It was this increase in volume, and therefore residence time, that allowed for a more complete burn in the computational model of Version 3 than previous design iterations.

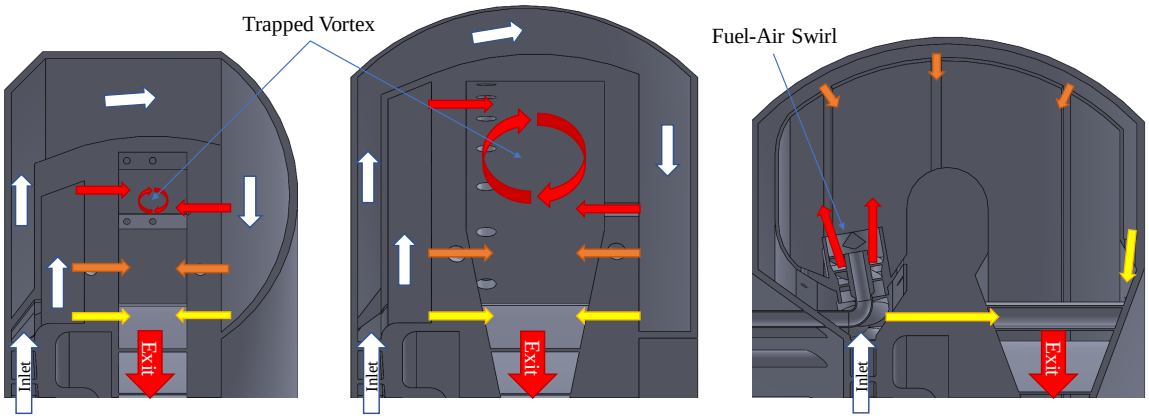

(a) Version 1-6 (b) Version 2-6 (c) Version 3-5

Figure 31. Comparison of three Disk-Oriented Engine Geometries.

Since the primary objective of the Disk-Oriented Engine was to reduce axial engine length by burning in a circumferential pattern, it is important to understand the impact changes from Version 1 to 3 had on axial length. Increasing the combustion cavity volume in Version 2 also increased axial length 18% from Version 1. Likewise, the re-designed flow path of Version 3 increased axial length of the combustor 13 % compared to Version 2. Much of this lost axial length was due to a 3.45 cm expansion on the compressor side, increasing combustor volume in an axial length already in use by other engine features. Accounting for this efficient use of existing space, the axial length of the combustor alone decreased 13% from Version 2 to 3, resulting in a combustor axial length increase of only 5% from Version 1 to Version 3. This small increase was required to preserve length savings on the order of 60% when comparing this V3 Disk-Oriented Engine to a traditional axial gas turbine combustor with similar performance.

3.2 Numerical Grid Development

Numerical grids were created in Pointwise 18.0-R1 to represent a sector of the physical, three-dimensional geometry of a Disk-Oriented Engine Combustor in computational space. Section 3.2.1 shows the generalized domain that was analyzed computationally along with the methods required to create an appropriate grid for the flow condition. The grid practices that differ between intended turbulence models are compared in Section 3.2.2. Sections 3.2.3 and 3.2.4 explain the necessity of convergence and grid independence, respectively, as well as the methodology for proving each was satisfied by the grids employed.

3.2.1 Computational Domain

Computational domains for all iterations of the Disk-Oriented Engine shared features common with the 30° sector shown in Figure 32. Since every feature in the geometry was a multiple of twelve, the computational domain was reduced to $1/12^{th}$ of the full annulus; every geometry maintained periodicity on 30° intervals and was gridded with the same periodic boundary process. Each version shared the same inlet and exit conditions, resulting in similar domain shapes for each design analyzed. The grids constructed by overlaying connectors on an imported initial graphics exchange specification (.igs) computer aided design database file. These database files were exported from SolidWorks Part (.sldprt) files designed in the manner described in Section 3.1. Connectors in these domains were placed with an average nodal spacing of 0.089 cm, and spacing was altered as needed to accurately capture curvature seen in the geometry. With the introduction of the swirlers in Version 3, the average spacing changed to 0.051 cm on the swirler faces to adequately capture the small features of the geometry.

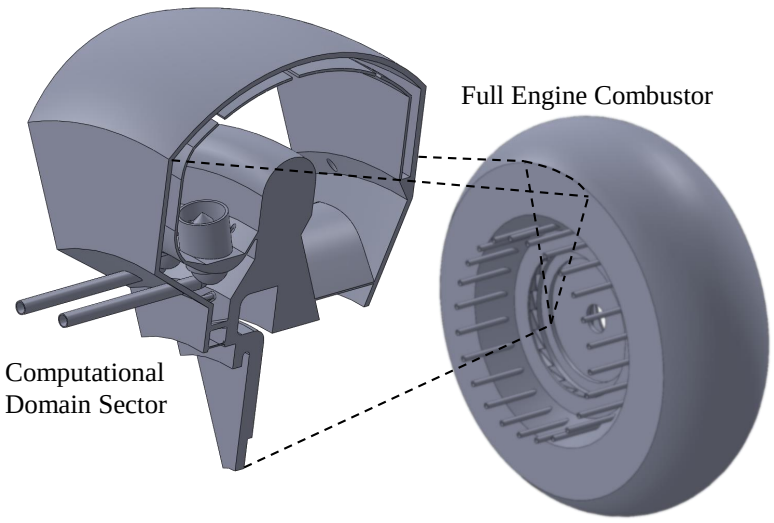

Figure 32. 30° **periodic computational model taken from the complete V3 combustor.**

Fluent accounts for the sector geometry using periodic boundaries, labeled in Figure 33. The periodic boundary acts as an inlet and exit, assuming that whatever leaves one end of the domain enters through the other periodic boundary. All fluid entering through a periodic boundary is assumed to have the properties and kinematics as the same fluid that exited the other boundary. To ease the computational burden when fluid passes through one boundary and into the other, the periodic faces must be matched. This means that all cells and nodes are identically placed on both periodic faces. The match was accomplished using Pointwise's periodic boundary tool to rotate one face about the engine center line. The baseline

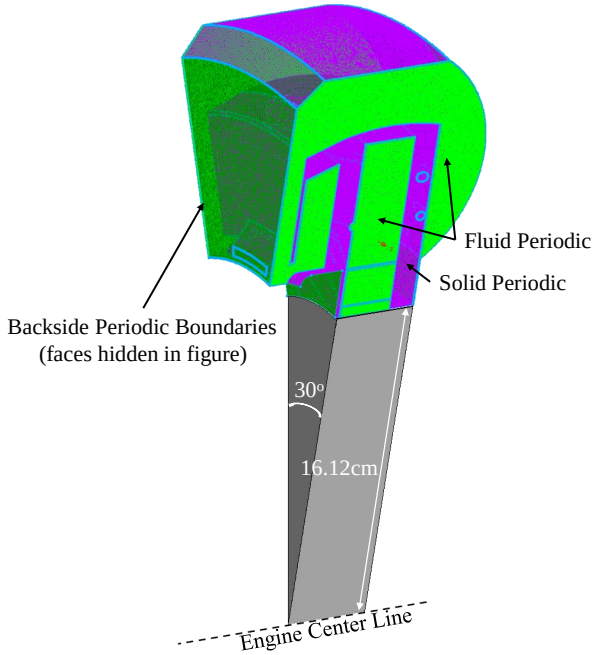

Figure 33. Version 2 domain showcasing periodic boundary.

assumption in this process is that all features about the entire combustor are periodic throughout, but work by Rathsack *et al.* [8] showed visual evidence that there were unsteady, circumferential variations about the combustion cavity of the AFIT UCC. Despite this, the Disk-Oriented Engine was modeled as a sector, acknowledging that circumferential unsteadiness may be a factor in full annulus experimentation.

The match boundary condition was an important feature at the periodic sides (Figure 34), allowing for the volume structures leading up to those boundaries to be built as they would if they were building into the next sector. This meant that the periodic boundaries were required to match whatever wall spacing was used throughout the volume. The initial spacing between the wall and first cell of $1.27 * 10^{-3}$ mm at the fluid-solid interaction wall was unique to the grids built for $k - \omega$ turbulence modeling, and it was important that these same wall conditions were applied to the two-dimensional domain on the periodic boundary. Changes in turbulence modeling approaches eventually removed the small initial spacing requirement on the periodic boundary, but the match condition was applied throughout all geometries.

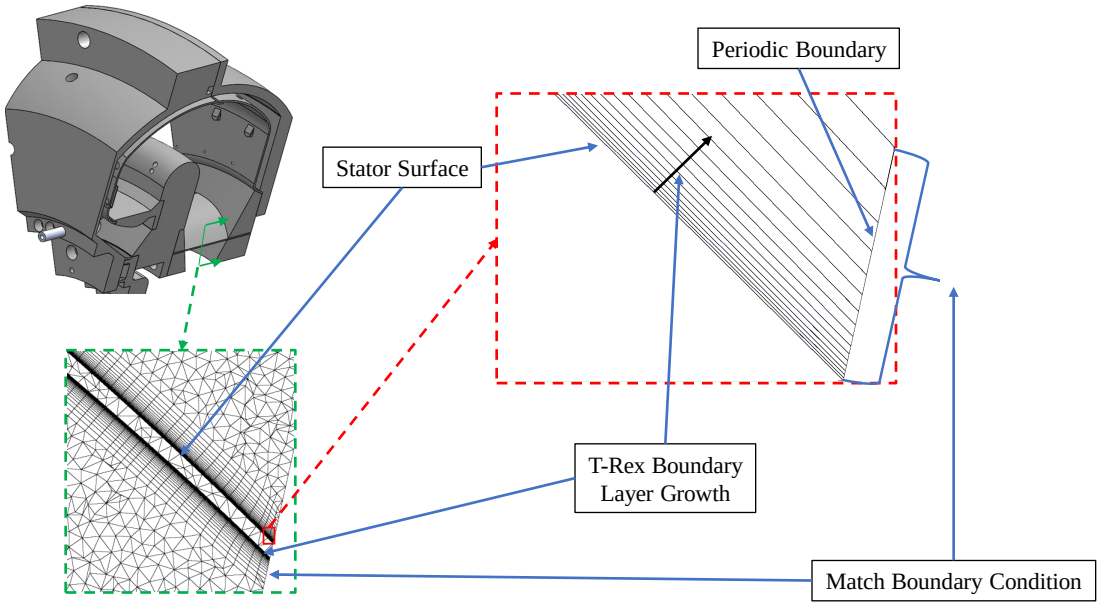

Figure 34. Match boundary condition on the periodic face.

3.2.2 Wall Spacing for Turbulence Models

While many of the methods discussed in Section 3.2.1 applied to all iterations of the Disk-Oriented Engine, the turbulence modeling approach adapted over time. Per the discussion in Section 2.4.3, the $k-\omega$ SST turbulence model was used for its advantages in predicting shear stress at the wall and providing a switch between $k-\omega$ and $k-\epsilon$ models in regions where each is better suited. Since the $k-\omega$ SST model requires the first grid point to be within the viscous sublayer, $y^+ \approx 1$ at the wall was targeted throughout the geometry. To resolve this fine in the boundary layer, a hybrid structured-unstructured grid was required. The structured nature gives greater control over growth rates, while an unstructured grid simplifies the creation of a domain to fill volumes with complex geometries.

Figure 35 shows an example of this hybrid griding process, known as anisotropic tetrahedral extrusion (T-Rex) in Pointwise. To achieve a first-cell wall spacing within the viscous sublayer, the T-Rex function was started with an initial spacing of $1.27 * 10^{-3}$ cm, and grew at a rate of 1.2 for 15 layers. The growth rate was based on that used by Bohan [26] for testing UCCs in a similar fashion, and the number of layers was chosen to allow a smooth transition between the high aspect ratio cells in the structured grid and the tetrahedral cells outside of the boundary layer. Note that the hybrid mesh was only used on the fluid side of the fluid-solid interface, as a boundary layer would not develop within the solid and did not require the fine resolution necessary for turbulence modeling. The T-Rex function was applied to all fluid-solid interfaces, as the velocity profile was crucial for accurate friction and heat transfer measurements. On the periodic boundaries, the T-Rex was applied in a two-dimensional fashion to those same fluid-solid connector interfaces. CFD results analyzing Version 1 showed that the average y^+ at the wall was approximately 1.05, suggesting that the average first cell off the wall was within the viscous sub layer.

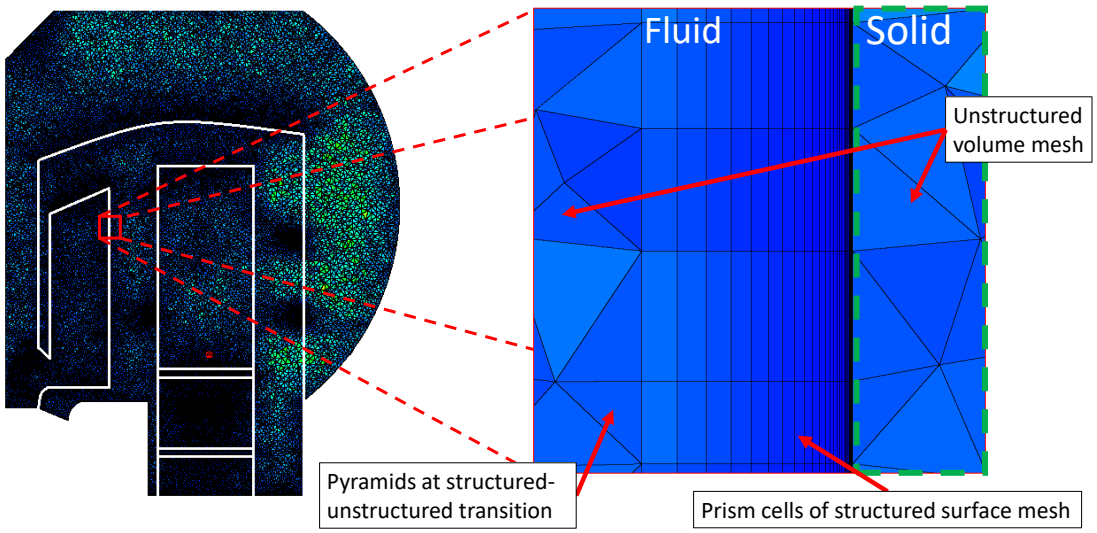

Figure 35. Cut plane of grid volume in Version 1, highlighting the T-rex boundary layer growth at the fluid-metal interface.

With the introduction of a dump diffuser in Version 3, the high velocity gradients due to separation in such a feature provided difficulty in creating a hybrid boundary layer grid that would account for these steep gradients without being overly refined. Figure 36 compares the grids between Versions 1 and 3, before and after the introduction of the dump diffuser. Applying the same practices discussed previously for Versions 1 and 2 to this dump-diffuser style inlet for Version 3 resulted in numerical instabilities in the turbulence model. It was speculated that this was simply because the wall spacing requirements for $k-\omega$ SST were not being fulfilled, resulting in unstable solution attempts. To combat this, the $k-\epsilon$ model with enhanced wall functions was introduced. As discussed in Section 2.4.3, the $k-\epsilon$ turbulence model is inherently more stable, having a less restrictive requirement on wall spacing than the $k-\omega$ model.

Grid design for the $k-\epsilon$ turbulence model was far less intensive than that previously described for the $k-\omega$ model. With a target wall spacing of $(30 < y^{+} < 300)$, the volume could be made entirely of tetrahedrons with a wall-function mesh at the

surface [42], eliminating the computationally intensive process of creating a T-Rex mesh at the surfaces as seen in the comparison between the two meshes in Figure 36. Another direct comparison between the two structures is shown in Figure 37, where the wall was gridded without the hybrid grid seen in Figure 35. Since an initial spacing and growth are not specified, the volume mesh is based entirely on the connector spacing and boundary decay as defined by the practices in Section 3.2.1.

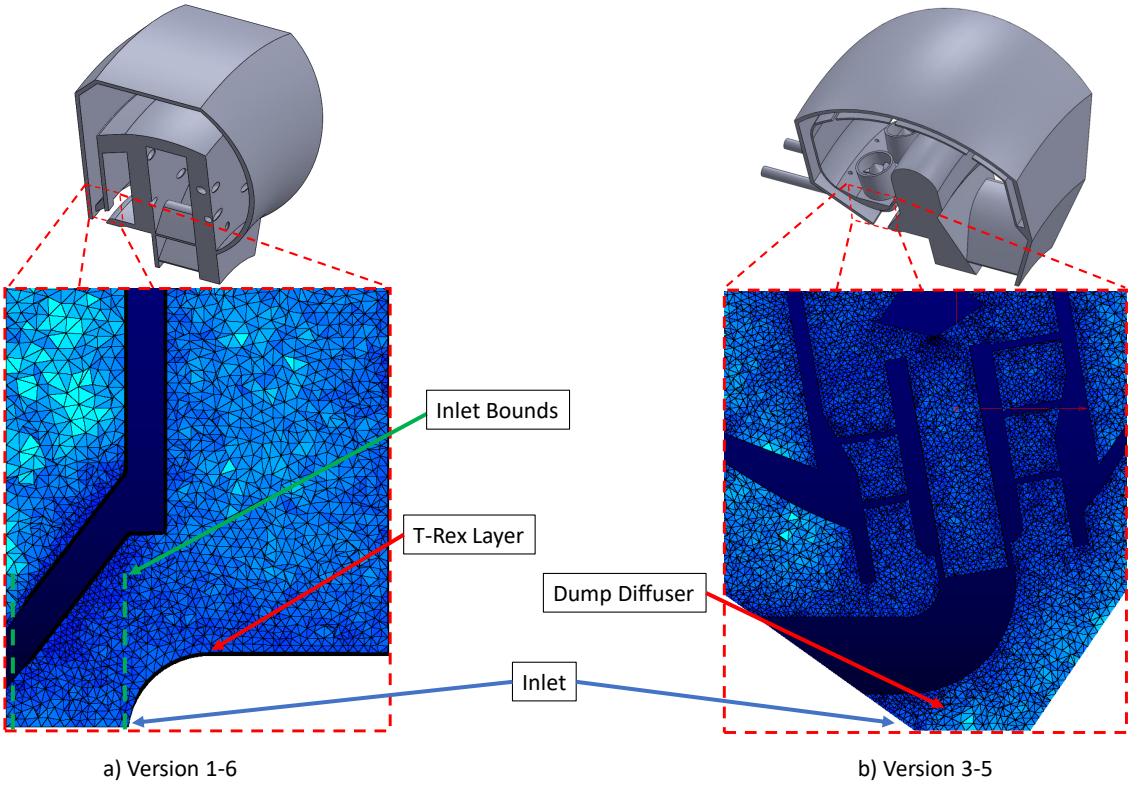

Figure 36. Comparison of hybrid and unstructured mesh inlets.

Moving away from the wall, Figure 37 shows the boundary decay in both the fluid and solid of a Version 3 grid. The solid cells are seen to grow much quicker off the wall than the fluid cells did. The boundary decay for all grids tested was 0.92 in the fluid and 0.8 in the solid. These decay rates were the same throughout the model, resulting in uniform changes that did not require special attention in the griding

process. The swirlers in Version 3 created a free-shear flow that dominated much of the combusting fluid; the $k-\epsilon$ turbulence model with enhanced wall functions did not require fine structures to resolve turbulent gradients within such a shear flow. The $k-\epsilon$ model was the better of the RANS models at simulating these features, as discussed in Section 2.4.3.

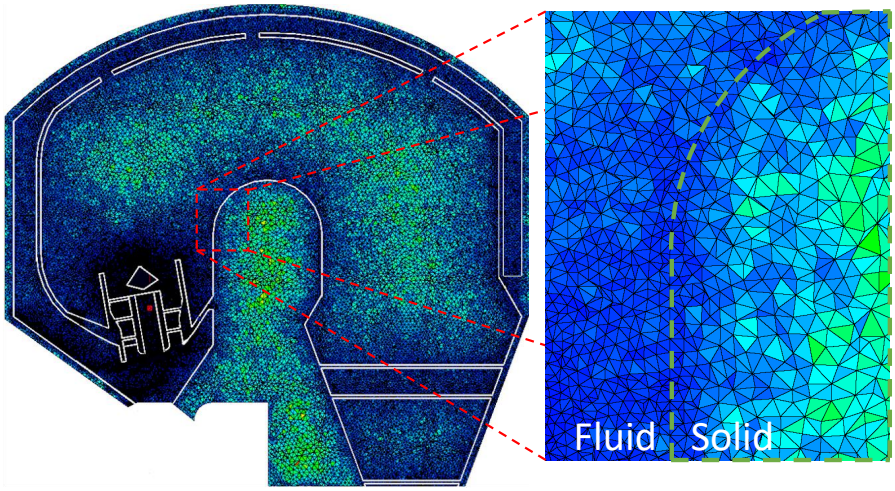

Figure 37. Cut plane of grid volume in Version 3, highlighting the grid structure at the fluid-metal interface without a structured boundary layer.

3.2.3 Convergence

Cummings *et al.* [36] explained that in any iterative solution method to a differential equation set, the end condition is a desired steady-state solution, and the solution must then be iterated until the solution converges on a steady-state value. While steady-state is generally excepted as a constant value in time, it is unlikely that a combusting fluid model will ever settle on one solution, as the combustion process is inherently unsteady. Cummings *et al.* also provided a method for checking for convergence based upon the residuals. A residual is the value of the difference between the discretization of the partial differential equation (PDE) and the actual PDE at a given step in time.

Literature suggests that residuals will approach zero as the solution converges, but in engineering uses the solution is considered converged when the residual is three to four orders of magnitude smaller than initial values. Figure 38 shows an example scaled residual plot from the Disk-Oriented Engine Combustor analysis, and it is apparent that the target of a three to four order reduction was not reached, as that would only be seen in plotting absolute residual values. It can also be shown that these residual values have converged to a non-zero, steady value. With the convergence of these residual values, it is unlikely that they would further reduce with more iterations to the absolute zero value discussed by Cummings *et al.* [36]. For this reason, another measure of convergence was required to determine if steady-state solutions were achieved.

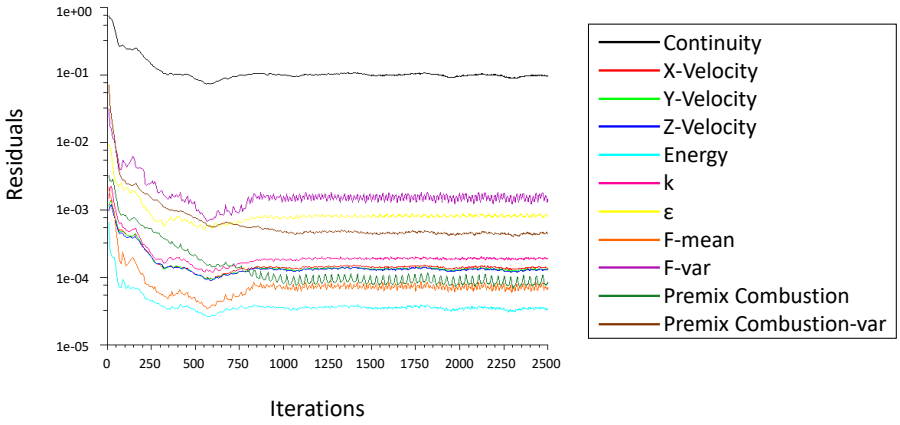

Figure 38. Convergence monitoring with scaled residuals.

Another check for convergence used previously in UCC CFD analysis was an iteration history of surface monitors such as temperature. Bohan [26] tracked area-averaged temperature on the combustor exit and declared convergence once temperature minimally fluctuated about an average value. This temperature monitor was an indication of the combustion process and how it was changing over iteration history. Pressure on the inlet boundary was an additional surface monitor implemented for

testing the Disk-Oriented Engine Combustor. Since the pressure within the combustion cavity was controlled by back pressuring the exit as a turbine would, the inlet pressure fluctuated as a function of the combustion process. While fluctuations in exit temperature history plots were dampened by the specific heat of the air, pressure measurements acted as a responsive measure to changes in combustion.

Figure 39 plots an iteration based history of both inlet pressure and exit temperature, where values are seen to converge on a steady value at approximately 1000 iterations. After the settling of the surface monitors, the simulation continued for an additional 1500 iterations to allow for an iteration independence check to prove the steadiness of the solution.

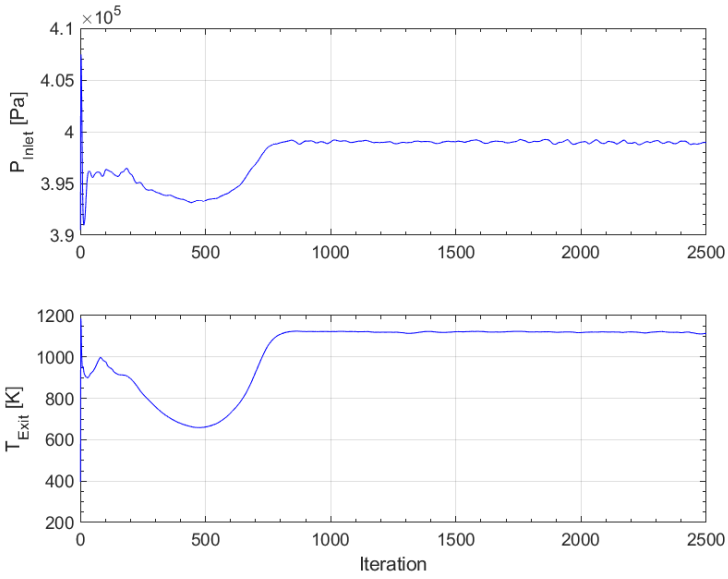

Figure 39. Convergence monitoring with surface monitors.

To better understand if this solution had converged to a steady value on the inlet and exit boundaries, Figure 40 plots temperature and pressure from 1000 to 2500 iterations. On this scale, it is apparent that the solution is fluctuating in an unsteady nature, and the pressure plot shows this unsteadiness with more frequent fluctuations than the temperature plot. Each of the peaks in the pressure fluctuations were

assumed to be an independent sample, with the largest turbulent flow oscillations creating the greatest pressure changes on the inlet face. To properly determine if the data had converged, the fluid properties tracked were required to be statistically stationary over this converged region. While turbulent oscillations and statistically stationary are terms traditionally used to describe time-accurate data, the same concept was applied to this data set. Each iteration was assumed to be a time step, but in reality each iteration was an undefined time step in solution history.

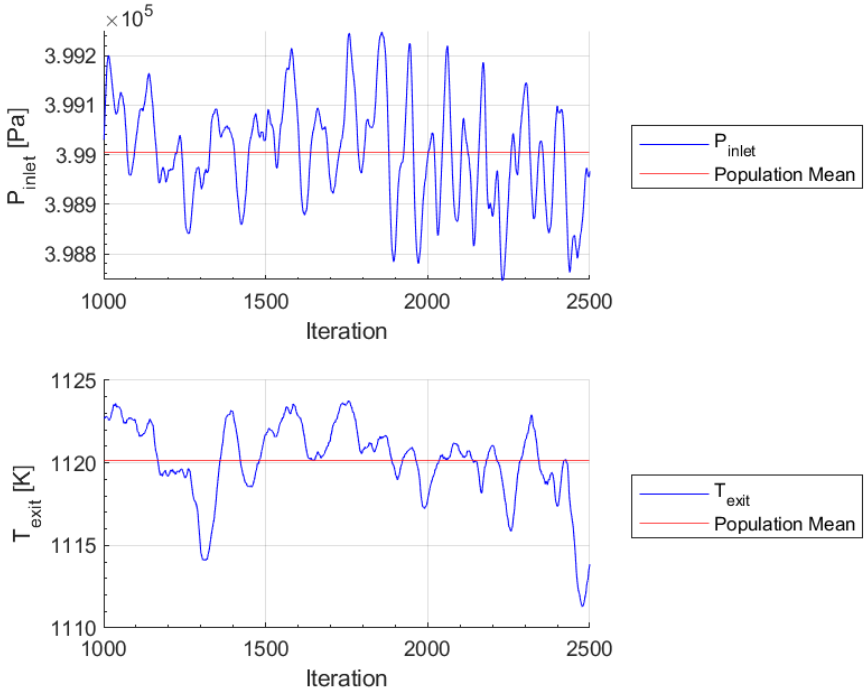

Figure 40. Surface monitor history plots, zoomed on converged iterations.

Figure 41 separates the data set of 1000-2500 iterations into seven separate samples. Since each oscillation was assumed to reflect the largest turbulent time scale, each one would then be an independent sample. These oscillations occurred approximately every 100 iterations, so an independent sample was assumed to be over 200 iterations. This approach to independent sampling resulted in seven samples of 214 iterations, and the statistics of each is presented in Figure 41. Each data point is a sample mean centered within its respective sample, and the horizontal error bars

mark the width of each sample. Vertical error bars are used to indicate the standard deviation of each sample, while the red lines mark the statistics of the entire data set.

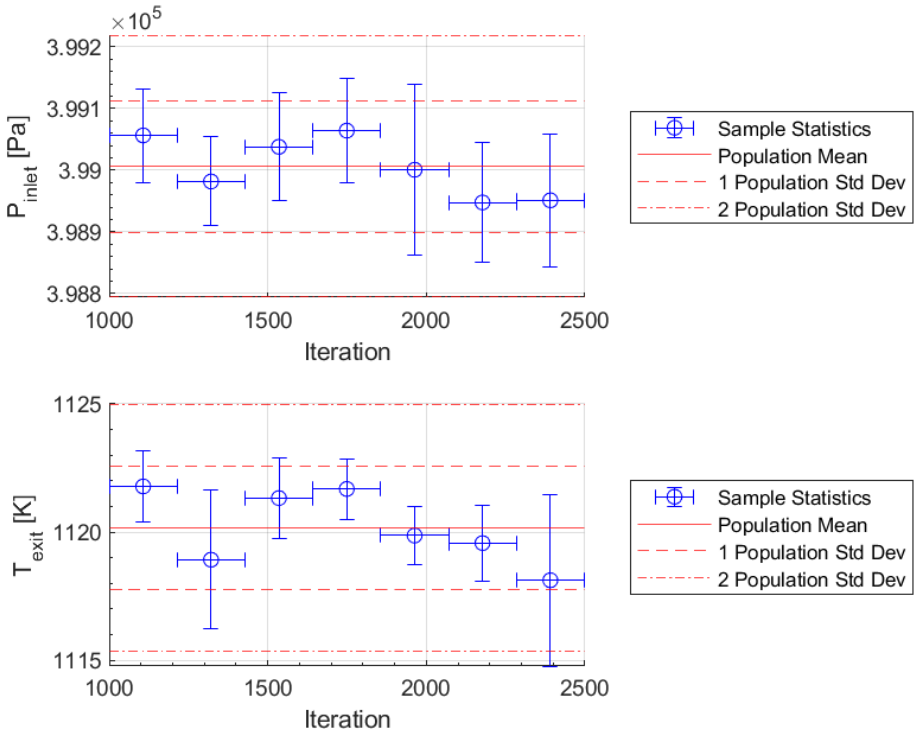

Figure 41. Convergence statistics on independent samples.

The sample means fell within one standard deviation of the population mean, and individual sample standard deviations fell near the population standard deviation. An exception to this case is the lower standard deviation of the last temperature sample, which fall outside of two standard deviations of the population mean. This point may suggest a statistical outlier in the data set, but the relative closeness of the pressure sample mean to the population mean suggests that this point is statistically stationary with all others in the population. Temporal accuracy on 1000-2500 iterations was assumed to be the standard deviation, resulting in computational iteration uncertainty of 0.03% of the average in pressure ($\pm 0.001 * 10^5$ Pa) and 0.23% in temperature (± 2.5 K). Based on this analysis, all models of Disk-Oriented Engine

Combustor iterations were run to at least 2500 iterations, and surface monitors were visually inspected to ensure convergence was satisfied.

3.2.4 Grid Independence

A grid sensitivity study, frequently referred to as a grid independence check, was required to ensure that the solution produced within the computational domain was unaffected by the size and distribution of cells. Cummings *et al.* [36] suggested performing this sensitivity study by incrementally increasing the number of cells within a fixed geometry and comparing the results using surface monitors over the solution history. The use of certain monitors was cautioned, in that an area-averaged approach could result in damping of grid dependencies if they resulted in steep gradients in localized regions [36]. Although use of area-averaged surface monitors could miss these gradients, they gave an overall picture of combustor performance that were directly comparable between grids. The monitors of choice for the Disk-Oriented Engine were the area-averaged inlet pressure and exit temperature. The selection of these properties were discussed in detail as convergence monitors in Section 3.2.3.

For analysis on the Disk-Oriented Engine Combustor, a target grid size was chosen (approximately 23 million cells) and all following domains were constructed to best match this size. It was important that grid scaling for an independence study was done in such a manner as to reflect the griding practices outlined in Section 3.2 with similar relative sizing between neighboring cells, while increasing the total cell density. This was achieved by changing the spacing of nodes on each connector, thus allowing cells to scale accordingly on domains and in the volume. Since it was computationally intensive to run multiple grids of the same geometry for domains over 20 million cells, the sensitivity study was done on one configuration and assumed applicable to all others. This assumption was backed by the consistency of grid development between

geometries, the similarity of fluid and reaction modeling between versions, and the use of single-version grid independence studies in other UCC works [23].

The grid independence study for the Disk-Oriented Engine Combustor was conducted on a Version 3 grid, with a target size of 23 million cells. Figure 42 shows a similar plot to that shown previously in Figure 39, where inlet pressure and exit temperature were tracked over the solution history. In Figure 42, this solution history is tracked for three separate grids: one representative of the 23M cell target, a coarse grid with 20% less cells, and a fine grid with 30% more cells. As the solution converged, each solution collapses around one value, and these three separate values neighbor one-another.

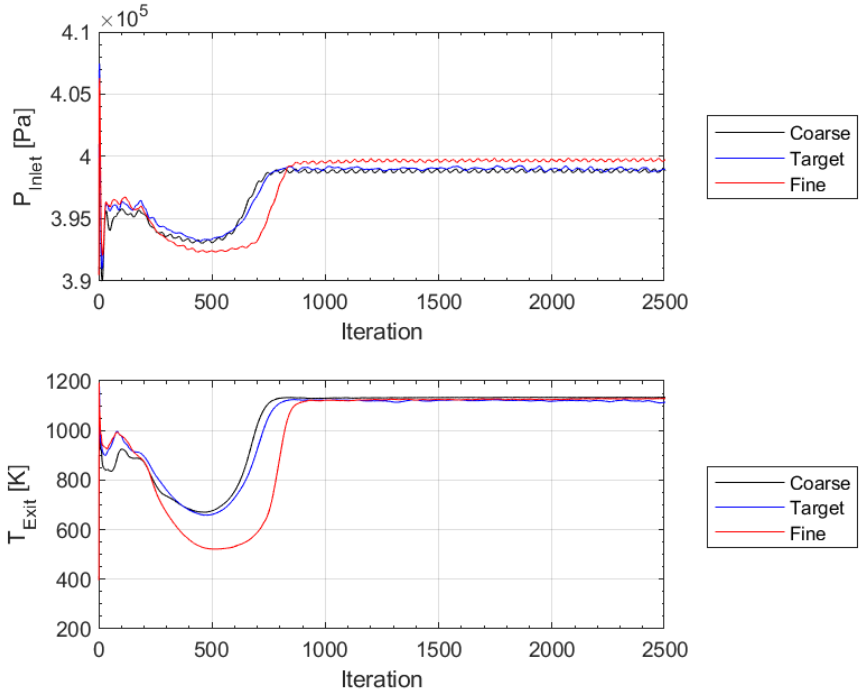

Figure 42. Grid independence comparison over solution history.

As outlined in Table 1, all of the refined grids were within 0.23% in temperature and 0.71% in pressure, and the fine grid was assumed to be the most correct with the highest fidelity. Despite early deviations, the three solutions in Figure 42 converged

on the same steady-state values. The pressure and temperature data presented in Table 1 are iteration-averaged to capture the pseudo-transient nature of combustion reactions, and the averaging process was on the same 1000-2500 iteration interval used to determine convergence in Section 3.2.3. Since these values are within 1% of one another, and variation within that 1% can be declared statistically insignificant, it was assumed that all grids constructed for the Disk-Oriented Engine within the bounds of 19-29 million cells were independent of grid sizing. Grids continued to target 23 million cells to balance fidelity with computational expense.

Table 1. Grid independence test results on converged solution.

	Cell Count	**Pressure [Pa]**	**% Diff**	**Temperature [K]**	**% Diff**
Coarse	18.7M	398800	0.23	1133	0.71
Target	23.1M	399000	0.18	1120	0.44
Fine	29.5M	399700	-	1125	-

3.3 CFD Solver Setup

To realize the benefits of preliminary testing through computational fluid dynamics, it was necessary to choose settings that best approximate the expected characteristics of the physical flow. The computational power available was important for modeling such physics, and the machine specifications available for this research are outlined in Section 3.3.1. The solver settings attempting to best approximate the reality of the system are discussed in Section 3.3.2, with an in-depth settings outline in Appendix A. Finally, the boundary conditions (BCs) assumed for the equation set to be solved by Fluent are presented in Section 3.3.3.

3.3.1 Computer Specifications

All CFD pre-processing, solving, and post-processing were completed on an HP Z820 desktop machine dedicated to computational analysis in the AFIT Combustion Optimization and Analysis Laser Laboratory (COAL Lab). This machine ran a Linux based operating system on two Intel Xeon E5-2690v2 processors, each containing ten physical cores with two threads per core. The system then has 40 logical cores available for parallel processing in Fluent. Visual displays for pre- and post-processing graphics in Pointwise and Fluent were handled by the NVIDIA Quadro K6000 graphics card. System memory was supplied by 256 GB of 8-channel, ECC DDR3 RAM, which had proven sufficient in handling cases with complex chemistry and grid sizes up to 66 M cells (approximately 210 GB) [48]. Since target grids for Disk-Oriented Engine Combustor research were not larger than 30 M cell, this machine could perform all necessary computations at AFIT without the need of the high-performance computing center.

3.3.2 Solver Settings

The setup of Fluent CFD cases were based upon the previous research and techniques outlined in Section 2.4. A pressure-based solution method was implemented, compliant with the requirements for the partially-premixed combustion model utilized in previous UCC combustion analysis [15]. The solution was assumed steady-state, but a pseudo-transient solution approach was utilized to reduce convergence requirements and speed up convergence [26]. Coupled boundary conditions were used at the fluid-solid interface to enable conjugate heat transfer and eliminate guessing of temperatures at these locations, as Fluent could solve for the temperature based on heat flux. This BC selection also allowed Fluent to solve regions of quenching associated with partially-premixed combustion modeling. The turbulence models were selected

between $k-\epsilon$ and $k-\omega$ SST based upon the inlet characteristics, as outlined in Section 3.2.2. A detailed walk-through of these settings are outlined in Appendix A, including screenshots from Fluent.

3.3.3 Boundary Conditions

To solve the highly non-linear PDEs that govern flow through a Disk-Oriented Engine combustor section, Fluent required boundary conditions that specify constant values or rates at domain boundaries. Figure 43 shows an image of how these boundary conditions are implemented on the Version 3 computational domain. Each boundary type is colored to differentiate it from others, and the parameters for all walled boundaries are specified in the figure.

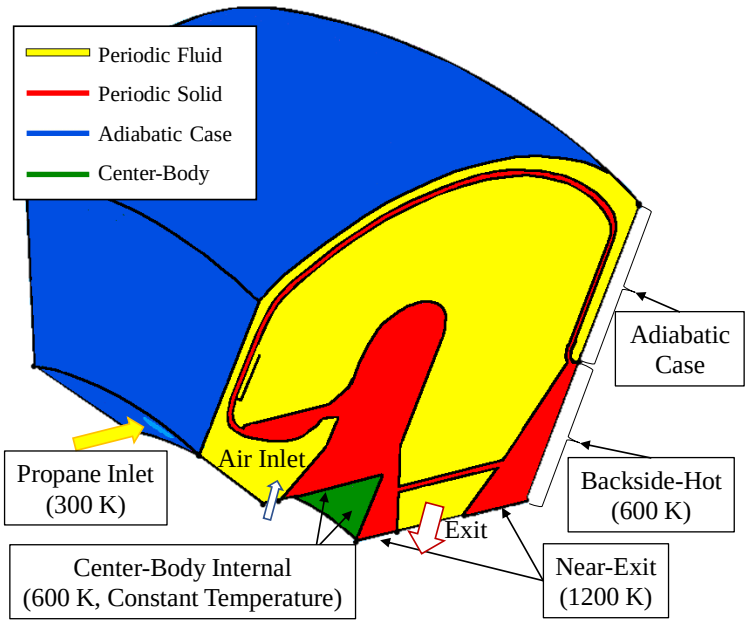

Figure 43. Boundary conditions on the 30° computational domain.

Fluid-metal interfacing surfaces (not shown) were set to allow conjugate heat transfer between the solid and fluid, and the solid block was treated as one piece of steel for simplicity. While an actual Disk-Oriented Engine would contain multiple types of steel alloys, to include stainless steel and Inconel, the properties of steel

were readily available in Fluent and reasonable enough for representation of physical hardware. Table 2 presents the actual densities (ρ) and thermal conductivities (K) for the Fluent model, as well as different metals used to construct the geometry in the physical domain. Errors in K suggest that the rate at which the metal moves energy from the fluid-metal interfaces may contain error, but this high percentage was likely not indicative of the magnitude of the error in heat transfer at the surface. Conductivity errors would alter the temperature at the surface directly, but would not impact the heat transfer coefficient, and the value of the heat transfer coefficient drives the energy transfer in this convection problem. Regardless of error in thermal conductivity, it was anticipated that a conjugate heat transfer model with steel would provide more accurate combustion analysis results than an adiabatic model, per the data presented in Section 2.4.2.

Table 2. Material (Stainless Steel, SS, and Inconel, IN) comparison to Fluent steel model; ρ is density and K is the coefficient of thermal conductivity [53].

	Fluent	**SS 316**	**SS 321**	**IN 718**
ρ $[\frac{Kg}{m^3}]$	8030	7888	7916	8193
K $[\frac{W}{mK}]$	16.27	13.50	20.94*	23.02**
Comparative Error, K	(-)	21%	22%	29%

*above 810 K **at 1030 K

The upper-exterior, or outer casing, was assumed to be an adiabatic surface, as preliminary tests showed that the bypass plenum moved heat at a rate too rapid to allow conduction to the outer surface. The circumference near the exit was assumed to be 1200 K to approach the 1300 K target turbine inlet temperature. Surfaces heated by the combustion process but uncooled by dilution air were assumed to be 600 K.

The inlet conditions, both fuel and air, were set as mass flow inlets to target the mass flows required for the selected cycle, as shown in Table 3. Since the air mass flow was given for the design condition, the settings would need to be $1/12^{th}$ of 1.139 kg/s, or 0.0949 kg/s of air. This air would be introduced with a bulk swirl by the compressor and maintained through the stator section, so the direction was set based on a stator angle of 22.87° up from tangent. This resulted in an inlet air velocity with a radial component (V_r) of 0.389 times the velocity magnitude (V), and a circumferential component (V_θ) of 0.921*V, as seen in Figure 44. Inlet turbulence for both in-flow conditions was assumed to be 2%, with a length scale based upon the smallest radius of the inlet, as seen in Table 3. The temperature for the fuel was based on unheated, ambient temperature fuel entering the system, while the air inlet temperature was based on the heat added by the compression process.

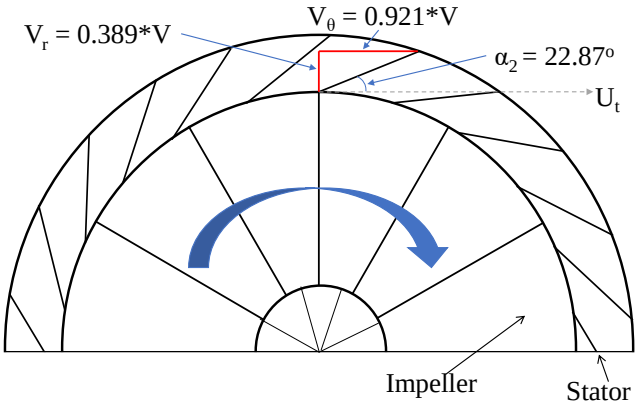

Figure 44. Inlet angles defined by the compressor geometry. Angle derivation explained in Section 2.3.1.

Table 3. Settings for mass flow inlets.

	$\dot{m}$ [kg/s]	Turbulence (Intensity, Scale)	Temperature [K]
Air Inlet	0.0949	2%, 0.965 cm	470
Fuel Inlet	0.00189	2%, 0.305 cm	300

The fuel mass flow rate was set to match the global equivalence ratio, Φ_{global}, of 0.31 used in one of the UCC studies by DeMarco *et al.* [6]. This equivalence ratio is based on the stoichiometric air-to-fuel ratio, $(a/f)_{stoich}$, over the air-to-fuel in the system. To apply this for a mass flow rate of fuel, the stoichiometric balance was found by Equation 16 [7].

$$C_3H_8 + 5(O_2 + 3.76N_2) \rightarrow 4H_2O + 2CO_2 \tag{16}$$

These molar coefficients were then applied to the definition of air-to-fuel ratio for a constant volume system (Equation 17). With the value for stoichiometric air-to-fuel known, it was applied to a rearranged Equation 15 and solved for fuel in Equation 18 [7]. The resulting design condition fuel flow rate was 0.0227 kg/s, or 0.00189 kg/s for a 30° sector.

$$(a/f)_{stoich} = \frac{\dot{m}_{air}}{\dot{m}_{fuel}} = \frac{5(4.76mol) * 28.85g/mol}{1mol * 44.1g/mol} = 15.57 \tag{17}$$

$$\dot{m}_{fuel} = \frac{\dot{m}_{air} * \Phi_{global}}{(a/f)_{stoich}} \tag{18}$$

The combustion exit condition was set as a pressure outlet boundary, allowing for a constant pressure to be set on that surface and fluid to move across the boundary. Since the mass flow inlet for the combustor inlet did not allow for a pressure to be set, the exit condition was used to simulate the back pressure of a turbine and force an inlet pressure equal to the compressor operating pressure. For an overall pressure ratio of four at static sea level conditions, the overall operating pressure in Fluent was set to 405300 Pa, and the exit was held at -20265 Pa gauge pressure. This 5% reduction in static pressure from the expected inlet to the exit accounted for the static pressure lost between the two and could be controlled to dial in a more precise

inlet pressure if necessary, depending on engine conditions. Since this combustor exit boundary was an outlet condition, the temperature and turbulence settings were left default as they would only control fluid re-entering the domain.

3.4 Engine Cycle

Engine cycle selection was an important step in combustor design. An engine cycle was chosen to meet performance specifications, and this information provided boundary conditions for computational analysis of the combustor. While the cycle could be analyzed by hand, computer software was used to enhance the process and provide cycle information at on- and off-design conditions. For the present research, supplemental programs included with Mattingly *et al.*'s [9] text were used for cycle analysis. The AEDsys 4.100 engine cycle analysis software suite includes all the necessary physics models to perform preliminary parametric cycle analysis (PCA) and engine performance analysis (EPA), as well as some preliminary turbomachinery design tools that were not used in the present research. Sections 3.4.1, 3.4.2, and 3.4.3 focus on the PCA, sizing, and EPA procedures utilized in developing an engine cycle for the Disk-Oriented Engine.

3.4.1 Parametric Cycle Analysis

Engine performance was targeted to produce at least 668 N (150 lbf) of thrust at sea-level-static (SLS) conditions utilizing a single-stage centrifugal compressor. While centrifugal compressors can create compressor pressure ratios (CPR) as high as 7:1, rotors made from light weight alloys often cannot exceed CPRs of 4.0 [1]. The ONX program, part of the AEDsys package, was used to run parametric cycle analysis with various CPRs from 2.5 to 5 and turbine inlet temperatures (T_{t4}) from 1000 to 1500 K. Modern combustors can operate with $T_{t4} > 2000$ K [1], but a lack

of significant secondary air for turbine cooling and a desire to maintain relatively low thrust-specific fuel consumption (TSFC) resulted in cycle temperatures on the lower end of the modern scale, yet consistent with other small, uncooled gas turbine engines. Figure 45 shows this parametric study as a carpet plot, with specific thrust plotted on the x-axis and TSFC plotted on the y-axis. CPR and T_{t4} were varied as they are the most impactful independent variables in an engine cycle, while specific thrust and TSFC provided insight on cycle performance [1].

In order to select a cycle from the plot in Figure 45, comparisons were made to other small engines, including the JetCat P400-PRO, P500-PRO-GL, and the P550-PRO-GL. These engines were chosen because their specifications were readily available [54], and they operated with similar CPRs and performance characteristics to the desired Disk-Oriented Engine cycle. Table 4 outlines specifications for the various JetCat engines, and this information was used to place these engines on Figure 45.

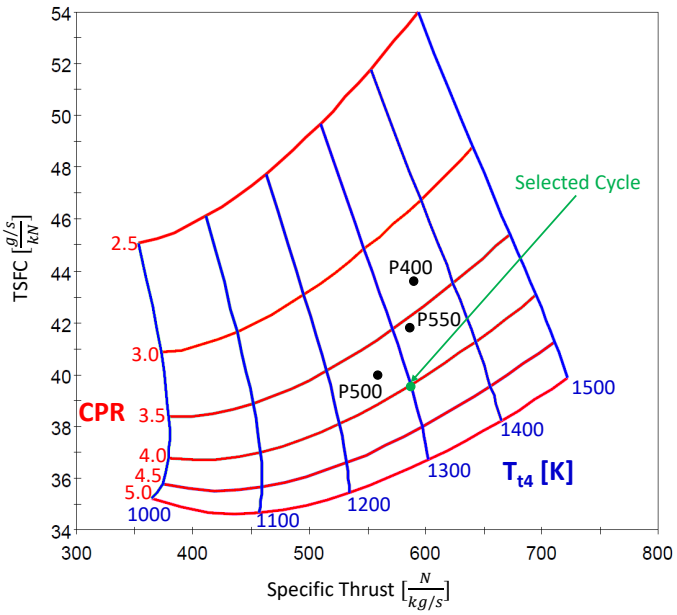

Figure 45. Carpet plot of various engine cycles, varying T_{t4} and CPR at SLS conditions. JetCat engines are plotted by actual TSFC and Specific Thrust and not relevant to carpeted lines.

While these engines do not coincide with the temperature and pressure data plotted, they do give insight into performance of similarly-sized engines. Specific thrust and TSFC would likely need to be comparable to these engines for viable engine operation in a flight-ready Disk-Oriented Engine configuration. Selecting a CPR of 4 reduced the TSFC by $6 - 16\%$ compared to the JetCat engines. A turbine inlet temperature of 1300 K was thought to be sustainable with Inconel single-body manufacturing and 4% secondary-air cooling, and specific thrust at this temperature was within 1% of both the P400 and P550 engines. The selected cycle would create 587 $\frac{N}{kg/s}$ specific thrust at 39.6 $\frac{g/s}{kN}$ specific fuel consumption, as noted by the green marker in Figure 45. Table 4 also compares the selected Disk-Oriented Engine cycle parameters to those of the listed JetCat engines.

Table 4. JetCat engine performance specifications [54] compared to the Disk-Oriented Engine cycle.

	CPR	**Thrust** $[N]$	$\dot{m}_{air}$ $[kg/s]$	**TSFC** $[\frac{g/s}{kN}]$
P400-PRO	3.8	397	0.67	43.6
P500-PRO-GL	3.6	492	0.90	41.9
P550-PRO-GL	3.8	550	0.93	40.0
Disk-Oriented Engine	4.0	668	1.14	39.6

3.4.2 Design Condition and Sizing

Parametric cycle analysis yielded thrust specific performance approximations for a selected cycle, but these figures constituted a rubber engine with no definite size. Scaling was required to fit the engine to desired design specifications. Dividing the desired thrust (668 N) by the cycle's specific thrust (587 $\frac{N}{kg/s}$) produced an air mass flow rate of 1.138 $\frac{kg}{s}$. With this information, AEDsys was used to calculate engine

parameters at each station, including station areas. Since the combustor would be wrapped around the exit of a centrifugal compressor, the compressor exit area (A_3) was critical in the design of the Disk-Oriented Engine. AEDsys estimated $A_3 = 0.0025m^2$, but this was for an assumed axial compressor. While cycle analysis would present the same areas for axial and centrifugal compressors, AEDsys reported the effective flow area required to achieve such a pressure rise. In an axial compression system, the effective and actual areas are identical as the fluid has been turned axial by the last stator row. The same would be true if a centrifugal compressor forced air only in the radial direction at Station 3, but the Disk-Oriented Engine maintained the bulk swirl imparted by the compressor. The required A_3 was the effective area, adjusted by the trigonometric relation of the circumferential inlet velocity, as shown in Equation 19, where α_2 is the compressor exit tangency angle as shown in Figure 44.

$$A_3 = \frac{A_{3,eff}}{\sin(\alpha_2)} = \frac{0.0025m^2}{\sin(22.87°)} = 0.0064m^2 \tag{19}$$

A compressor to fit this 0.0064 m^2 exit area had two major degrees of freedom in the design, impeller diameter and tip height, and these would be required to set the combustor inlet. Research into commercially available turbochargers for relative sizing discovered a turbocharger compression system capable of operating at the mass flow rate and CPR required for the Disk-Oriented Engine selected cycle. The Garret Motion INC. GTX5544R GEN II turbocharger operates on the compressor map shown in Figure 46 [55]. The design point for the Disk-Oriented Engine cycle is shown, adjusting for the corrected mass flow rate, and this point is within the stable operation islands of the compressor and would not likely stall. The GTX5544R GEN II operates with an outer diameter of 14.4 cm, and the compressor would operate at an efficiency of 70% if used on the selected cycle with a speed between 65500 and 69000 RPM. In

order to move the design cycle closer to the compressor optimum operability line, the compressor would have to be scaled up in application with the Disk-Oriented Engine.

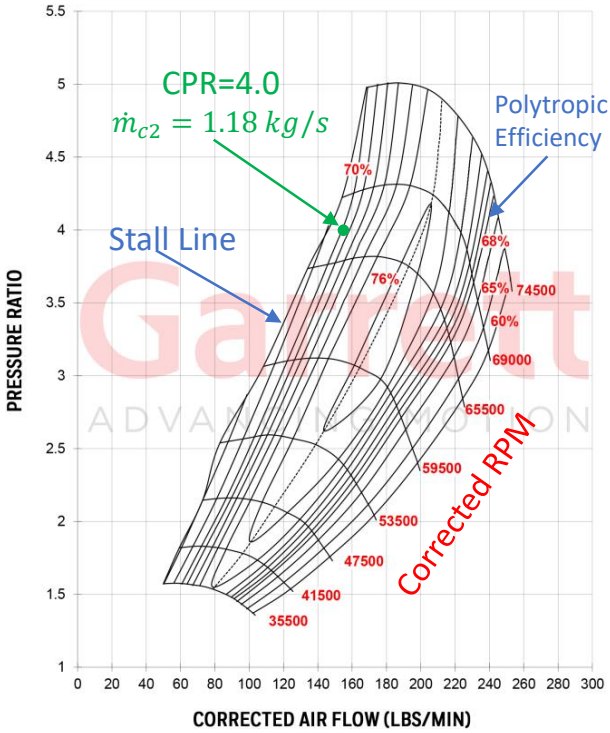

Figure 46. Compressor map of Garrett GTX5544R GEN II turbocharger, adapted from [55].

The present research assumed that the compressor diameter would have to be scaled 12% to a diameter of 16.1 cm, with the diameter of Station 3 measuring 20.8 cm. This measurement includes a stator section that added an additional 30% to the 16.1 cm disk diameter to increase the static pressure of the fluid expelled by the impeller. Since the target A_3 was 0.0064 m^2, this diameter allowed for a tip height of 0.97 cm. These dimensions set the inlet of the computational domain as a 0.97 cm opening about a 20.8 cm diameter. Without performing extensive turbine design analysis, the sizing of the combustion exit was less refined. A nominal exit angle was chosen based on the calculations in Section 2.3.2 to maintain the engine bulk swirl, but the area was reduced to a 2.54 cm opening at the same 20.8 cm diameter,

accelerating the exhaust products to near sonic Mach numbers. This dimension will be updated as needed in a later phase of the Disk-Oriented Engine design, once the turbomachinery is designed.

It is important to note the assumptions made in the cycle performance analysis that resulted in the parameters used in the present study. Compressor polytropic efficiency was assumed to be 76%, as that was the highest efficiency island shown in the compressor map of a similarly sized compressor. The turbine was assumed to operate on a similar polytropic efficiency, rounded to 80% as there was little information on the efficiency of radial-in flow turbines operating in this class. The turbine of the GTX5544R GEN II claims to operate at a maximum efficiency of 74%, but a custom-designed RIT was assumed to operate with slightly higher efficiency. AEDsys allowed for cooling air to be bled off the compressor to cool the turbine, and a modest 4% secondary air of the 1.138 kg/s was assumed sufficient to force fuel across the bearings for lubrication purposes and to extract bearing heat as a phase change. This secondary air exchange is similar to that used by JetCat engines, discussed in depth by Bohan [26]. Pressure loss across the combustor for initial estimates was assumed to be 5%, based upon modern axial combustion systems [1], and all other AEDsys settings were left default. The design condition cycle results are included in Appendix B, for engine operation at SLS, full-power conditions. It is important to note that the AEDsys program estimated the mass flow rate of fuel ($\dot{m}_{fuel}$) at design condition to be $0.0265 kg/s$, while equivalence ratio analysis based on previous experimentation (Section 3.3.3) estimated a required fuel flow rate of $0.0227 kg/s$, a difference of 15%. For comparison to previous research, the fuel flow rate determined by equivalence ratio was used for design condition analysis. The AEDsys estimated 100% conditions were also run for comparison with off-design settings, with results presented in Section 4.3.

3.4.3 Off-Design Parameters

To analyze the Disk-Oriented Engine at conditions other than the design point, AEDsys provided engine parameters at conditions other than the design point. Combustion analysis at off-design conditions required these boundary conditions on the combustor, as they would change with throttle settings or flight conditions. The chosen conditions were 80% and 30% throttle, assuming 80% to be closer to a cruise condition and 30% as idle: it was the lowest converged engine solution, as shown in Table B-3. Beyond this point, the pressure supplied at the turbine inlet could not sustain the power balance between the compressor and turbine. Figure 47 provides performance information at off-design conditions based on the data from Table B-3. This plot shows how TSFC decreases with increased thrust settings, where TSFC is a function of both fuel flow changing at various conditions and decreasing thrust production. Ideally, the engine would achieve its best TSFC at the design point, and would be less efficient off-design. The 80% and 30% throttle conditions are shown, and those points evidently operate at higher TSFC levels.

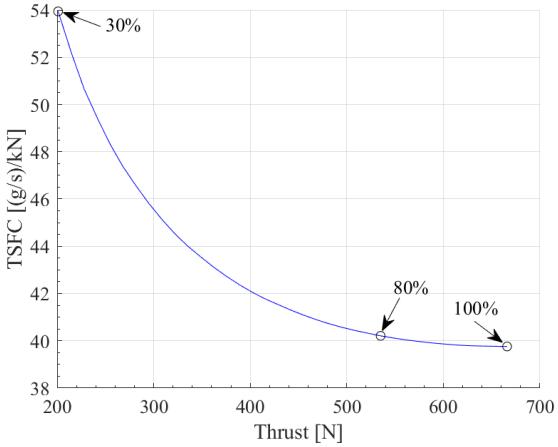

Figure 47. Throttle hook plot at SLS conditions for various throttle settings.

The off-design performance analysis outputs for the 80% and 30% throttle cases are shown in Tables B-4 and B-5. Boundary conditions at these cases are listed in Table 5, compared to the settings of the 100% condition. These fluid properties were used in conjunction with other boundary conditions outlined in Section 3.3.3 for all off-design analysis of the Disk-Oriented Engine.

Table 5. Station parameters for on- and off-design cases.

Throttle	**Thrust [N]**	P_3 **[kPa]**	T_3 **[K]**	$\dot{m}_{air}$ **[kg/s]**	$\dot{m}_{fuel}$ **[kg/s]**
100%	668	355.3	471.4	1.14	0.0265
80%	535	313.2	450.8	1.10	0.0218
30%	201	182.8	370.2	0.70	0.0111

3.5 Experimental Setup

From the information learned through the iterative computational design process, a full scale model was fabricated to be tested in the AFIT COAL lab at low flow rates or at an Air Force Research Laboratory (AFRL) facility at engine representative conditions. Real-world tests would provide two key factors not available in CFD analysis alone: 1) validation of the CFD model used to calculate global combustor performance, and 2) facilitation of tests with turbomachinery that were too computationally expensive for the available resources. A physical model of the Disk-Oriented Engine would allow for on- and off-design tests once the combustion had been characterized. After the model was designed for fabrication, as shown in Section 3.5.1, the swirler hardware was tested for verification of computational modeling techniques (Section 3.5.2).

3.5.1 Model Fabrication

Before experimental testing of the Disk-Oriented Engine Combustor, aspects of the desired computational design needed to be changed. The computations utilized walls that were overly complex to manufacture as a single piece; as such the Version 3 design needed to be broken up into separate, manufacturable sections to build a physical model that would perform similarly to the computational model. Figure 48 showcases changes made between the V3 computational model (Figure 48a) and the fabrication model (48b) which was partitioned and manufacturable.

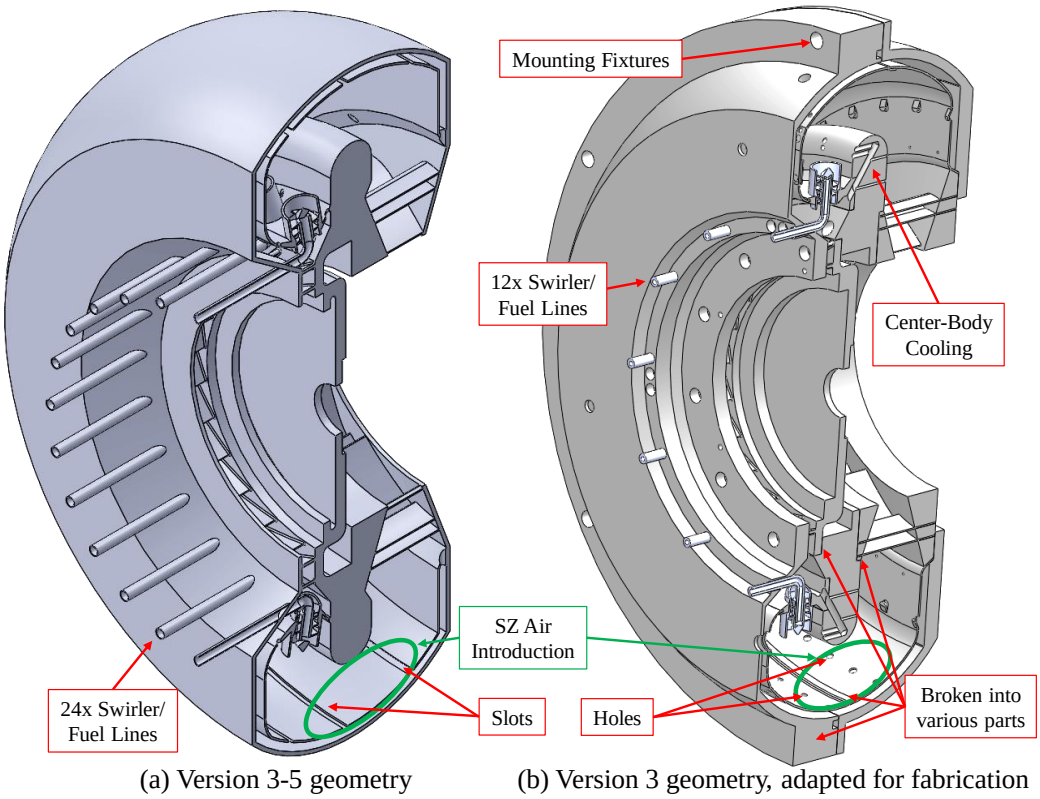

Figure 48. Comparison of Version 3 design to the fabricated model.

The fabrication model was dubbed the rig-ready test (RT) model, and required multiple iterations analyzed in CFD to achieve desired computational combustion characteristics. A great number of those iterations involved SZ hole placement. As Figure 48 shows, the SZ air introduction was changed from floating-wall slots to manufacturable holes. Utilizing slots in the 1.6 mm thick liner geometry produced many issues, to include a connection gap between slotted sections. Heat stresses in these separated pieces of material would likely induce crimping and buckling, and the liner would need to be made in fewer, larger pieces to maintain structural integrity under heat load. Figure 49 displays the final liner design, consisting of only two separate pieces that utilize holes instead of slots to create secondary recirculation zones in the combustion cavity. Additional differences can be seen between the V3 and RT geometries in Figure 48, such as the number of fuel injectors and center body

cooling. These additional design changes resulted from computational analysis on the RT geometry. Development of such features are discussed in Section 4.2, as they were developed based on computational results on the rig-ready test geometry.

The RT model in Figure 48b was broken up and colored to show various parts in Figure 50, and this cutaway illustrates the partitions required to make this assembly machinable. Table 6 explains the part numbers in Figures 50 and 51 and lists the materials used to machine each part. Inlet components (Parts 1 and 2) were expected to see little temperature rise above atmospheric conditions, so they were designed to be Aluminum 6061-T6511. The feed adapter (Part 1) connected the engine to an existing forced air supply, but would not be incorporated to a standalone engine. All parts in direct contact with heat generation were machined or printed in a high-temperature nickel alloy, Inconel 718 (IN 718), with the exception of the combustion liner. The liner was metal spun at Lewark Metal Spinning, which required a more malleable stainless steel 321 (SS 321). Any part that contacted an Inconel part was machined out of stainless steel 316 (SS 316), as it has better temperature characteristics than aluminum and was cheaper and easier to machine than IN 718. Since the design was a full annulus with an intricate combustion cavity wrapped about the engine center line, many of the sections could not be machined as one piece and would require clam shell assembly of the pressurized combustion chamber. This clam-shell technique was primarily used in the outer casing (Parts 4 and 12) and the combustion liner (Parts 5 and 11).

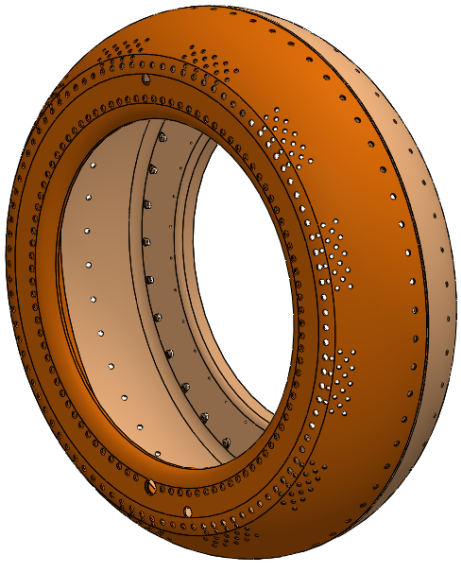

Figure 49. Combustion liner assembly.

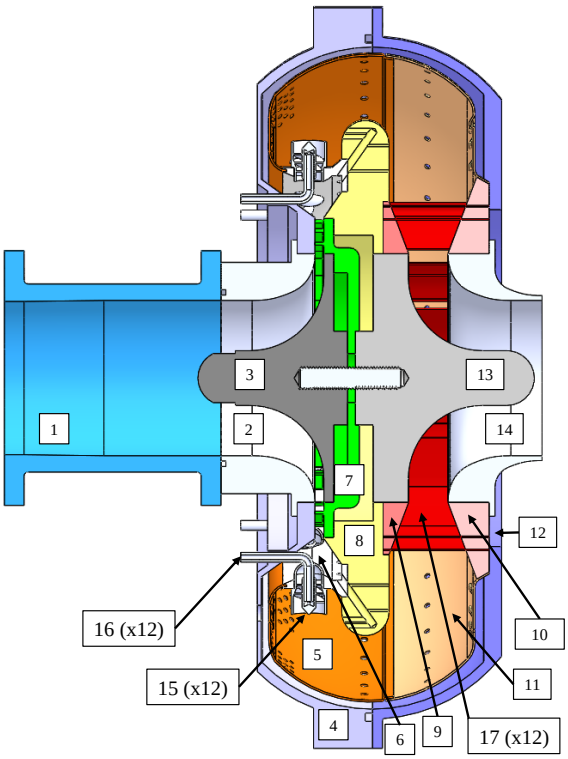

Figure 50. Cutaway of RT model, parts numbered according to Table 6.

Table 6. Model part numbers coordinating to parts in Figures 50 and 51.

	Part	Material		Part	Material
1	Feed Adapter	Al T6511	10	Back Turbine Plate	IN 718
2	Inlet Housing	Al T6511	11	Back Liner	SS 321
3	Compressor Plug	SS 316	12	Back Outer Casing	SS 316
4	Front Outer Casing	SS 316	13	Turbine Plug	SS 316
5	Front Liner	SS 321	14	Exit Housing	SS 316
6	Fuel Introduction Body	IN 718	15	Fuel-Air Swirler (x12)	IN 718
7	Compressor Stator	SS 316	16	Fuel Tubes (x12)	SS 316
8	Center Body	IN 718	17	Turbine Stators (x12)	IN 718
9	Front Turbine Plate	IN 718			

Figure 51 shows how each part of the Disk-Oriented Engine disassembles into its individual parts. This helps to make sense of the assembly process, as there are multiple sections that would function as one solid piece if machining such a design would be possible. For example, the turbine stator section (Parts 9, 10, and 17) were welded together as one piece of Inconel, but had to be cut as different pieces. Figure 52 shows how the cane-shaped stators fit into the surrounding plates to be welded into place.

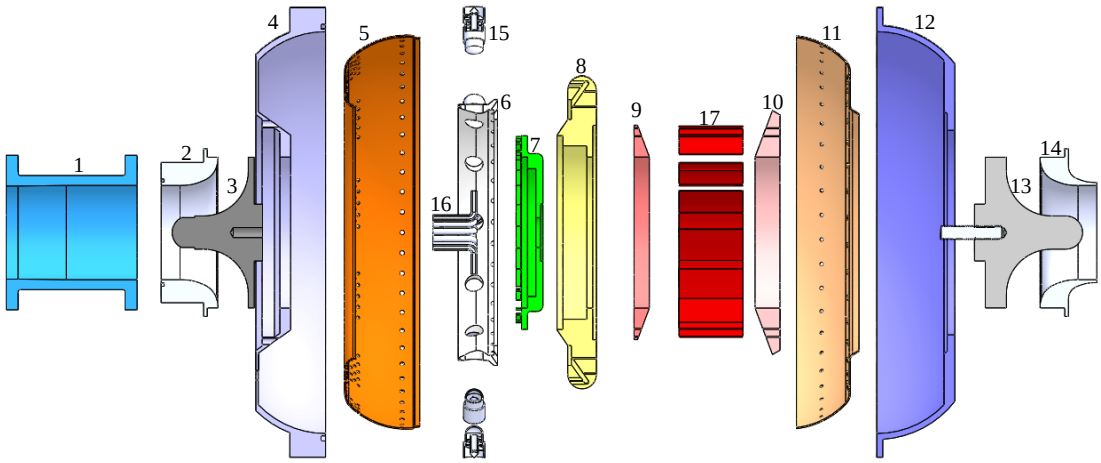

Figure 51. Exploded view of RT model.

Both the stators (Part 17) and the mounting slots (Parts 9 and 10) were cut by wire electrical discharge machining (EDM) from blocks of IN 718. The chamfered contours in the front and back mounting plates (Parts 9 and 10) were lathe machined prior to the EDM cutting process. It is important to note that size and hardness of these mounting plates (Parts 9 and 10) pushed the capability of AFIT Model Shop's largest lathe, requiring frequent tooling replacement and slow cutting speeds. For these reasons, the profile of the center body (Part 8) was machined in the five-axis mill at the AFIT Model Shop. This was a much slower process than lathe machining would have provided but was necessary due to machine limitations.

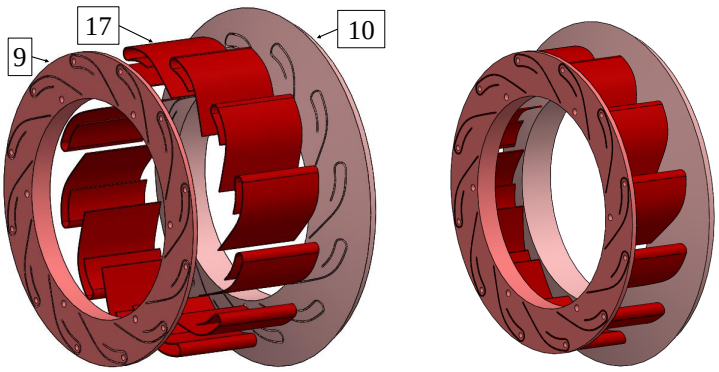

(a) Disassembled (b) Assembled

Figure 52. Turbine stator assembly.

With the exception of the turbine stators and the fuel swirlers being welded to their respective mounting bodies, all other parts in the assembly were planned to connect via machine screws. This method worked well for the majority of the design, except for the mounting of the combustion liner. With future adaptations expected, these liner joints were not permanently welded. Since the liner was only 1.6 mm thick and sustained extreme temperatures in excess of 1000 K in CFD analysis, it was anticipated that even silvered machine screws would seize after repeated runs and the combustor would be locked in the current configuration. The final solution was to secure the liner in the open joints of fixed parts, as seen in Figure 53. The front liner (Part 5) was contoured to fit into a slot on the front of the fuel body, fixing it in the radial direction. The back liner (Part 11) was compressed between the back turbine plate and the outer casing, freezing it in both the radial and axial directions. The front liner was axially fixed by the anchor point between the front and back liners at their clam-shell intersection. The front liner was beaded to allow for concentric mating of the parts, and dimples were placed on both edges to prevent separation of the clam-shell liner. Since both the inside and outside of the liner were within the pressurized outer casing, and CFD showed a pressure drop from outside to inside, it was unlikely that outward pressure would be enough to separate this concentric joint.

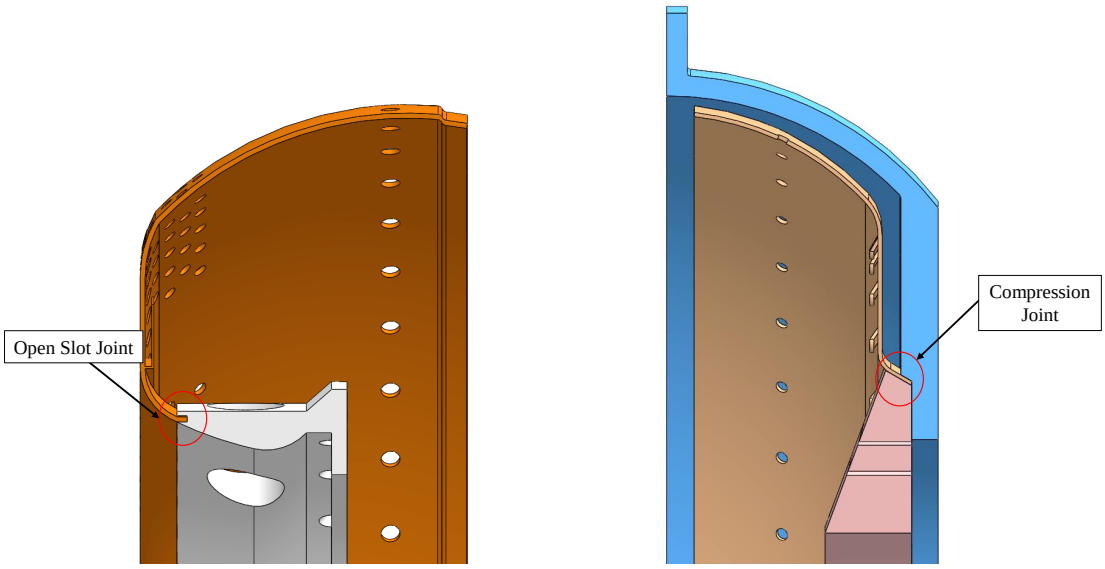

a) Front liner junction with Fuel Body

b) Back liner junction with Turbine Plate and Outer Casing

Figure 53. Combustion liner anchoring scheme.

Shown as-delivered from the metal spinning process in Figure 54a, the combustion liner was formed in two pieces that fit concentrically at the intersecting junction. Since the part was spun and stretched from 1.6 mm stainless steel sheet, locations of high curvature experienced thinning and absorbed many stresses from the forming process. To relieve these stresses, the parts were heat treated according to Table 7 in an oven available at the Air Force Research Laboratory (AFRL), as shown in Figure 55. Lewark Metal Spinning suggested that the parts undergo a stress relief heating, as well as an anneal process to soften the metal for further machining. The oxidation incurred through this treatment process resulted in the discolored metal in Figure 54b.

The oven shown in Figure 55 has a heating section 48 cm wide, 45 cm tall, and 91 cm deep, ample enough to fit both sections of the combustion liner, in nearly any orientation. The two halves were treated while connected to provide support about the circumference that would help prevent warping at the interface of the two sections.

(a) As delivered from metal spinner

(b) Post heat-treatment process

Figure 54. Spun combustion liner, prior to machining of air-injection holes.

To relieve the stress and anneal the metal, technical data suggested that stainless steel type 321 anneals between 1255 K and 1366 K, but a stress relieving anneal falls in the range of 700 K to 1088 K without causing the intergranular corrosion seen in a higher-temperature anneal [56]. The peak temperature was set for 1144 K, 5% greater than the upper limit of the stress-relieving anneal range to ensure that the metal would be within the desired temperature range for much of the cool-down process. Based on previous use of the AFRL oven, the heating chamber cooled below the 700 K lower bound 10-12 hours after oven shutdown, as it took this long to naturally convect the heat from the system. This meant that the combustion liner was exposed to heat-treatment temperatures for up to 12 hours, relieving internal stresses and annealing the metal.

Table 7. Heat-treatment oven settings for combustion liner.

Condition	**Oven Setting**	**Duration**
Ambient Start	Power Off (293 K)	(-)
Heating	274.5 K/hr	3.1 hr
Hold	1144 K	1.17 hr
Cooling	Power Off	$<$ 700 K within 12 hr

(a) Heat-treatment oven

(b) Combustion liner in oven

Figure 55. Oven used to heat-treat combustion liner.

3.5.2 Swirler Testing

A fuel-air swirl injector was iteratively designed using computational results. The design process is presented in Section 4.1. The goal of this swirler was to induce turbulent mixing of the fuel and air and create a stable flame anchor point in the primary reaction zone. To help validate the Section 4.1 CFD results and flame stabilization scheme, a full scale model of the fuel-air swirler (Part 15, Figure 50) was printed at AFIT in Inconel 718 to be tested experimentally. Experimental validation of the swirler CFD results was a secondary objective of the present research, as it was critical to gauge the accuracy of the numerical approximations paramount to the Disk-Oriented Engine Combustor design.

A metal model allowed for reacting flow measurements, characterizing the mixing and flame stabilization of the fuel introduction system. Additionally, a metal model provided insight into the manufacturability of the swirler before printing all twelve required for the Disk-Oriented Engine. Figure 56 shows the model used to test the

swirler geometry. Annotated are the fuel and air inlet lines, where fuel is introduced into the plenum which feeds the swirling fins concentric about the fuel injection line fed from a separate source.

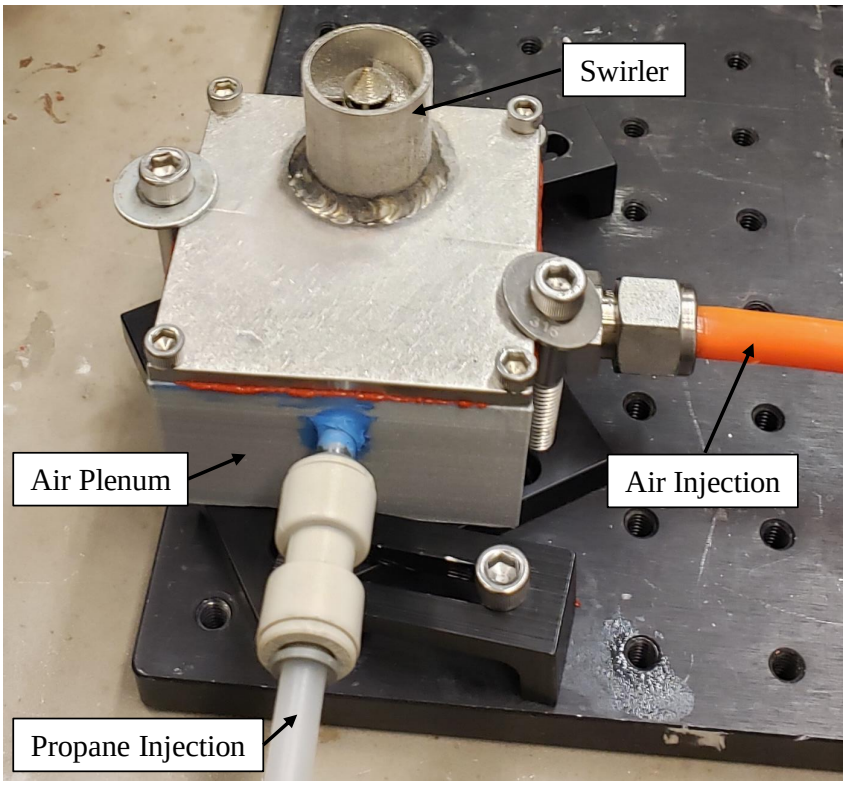

Figure 56. Fuel-air swirler model.

As discussed in Section 2.1.3, the swirled fuel-air injection system was chosen to provide ample mixing for combustion and flame stabilization in a short length. The expected exit profile is reiterated in Figure 57, overlaid on the Disk-Oriented Engine swirler. This diagram shows how air enters from a plenum and intersects the four swirl vanes about the swirler. Each of these vanes sweeps 180° about the swirler, inducing the swirl required to maintain the recirculation pockets outlined in Figure 57. A recirculation body was introduced to provide additional pressure drop in the center, as well as fuel dispersal into the swirled air. The outer diameter of the swirler also tapers with length, to slow the axial velocity of the air without changing the

swirler inlet area. All of these features make this swirler appear different than those more traditional fuel-air swirl injectors and are discussed at length in Section 4.1.

Existing facilities in the AFIT COAL Lab were suitable for atmospheric pressure tests of the fuel-air swirlers for the Disk-Oriented Engine. As shown in Figure 58, fuel and air supplies in the COAL lab were routed to supply sufficient mass flow rates of propane and air to operate a single swirler across the operating envelope of the Disk-Oriented Engine. An Ingersoll Rand H50A-SD 50 hp compressor supplied air to a dryer for removal of condensation prior to entering the lab and feeding the 1.9 cm air line. Mass flow rates were measured by FT2 Fox Thermal Instruments flow meters and controlled by a Flowserve Maxflo 3 valve. Manufacturer calibration rated the flow meter to ±1%. For reacting flow cases, ignition was achieved using an ethylene torch, controlled by a digital MKS-647C flow controller. Ethylene was stored as a gas in the fuel farm with propane, as shown in Figure 58. The igniter was pre-existing from UCC experiments [6, 8], and it was designed to produce an ethylene-air torch by electrically sparking a mixture of 23.0 SLPM of air and 3.5 SLPM of ethylene with an automotive spark plug.

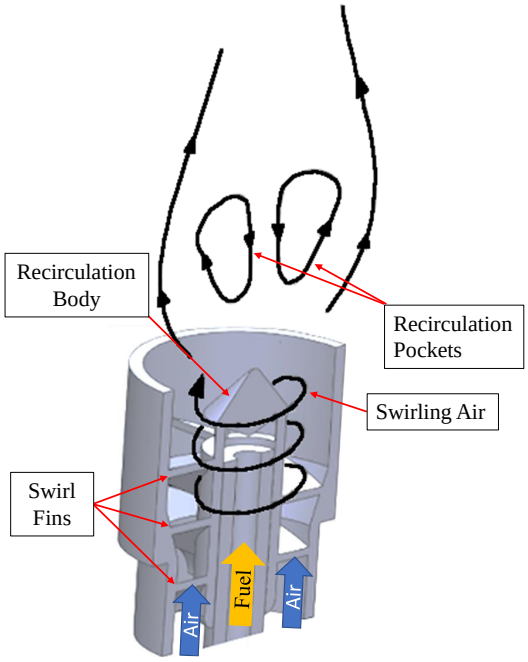

Figure 57. Cutaway of fuel-air swirler with pathlines adapted from [7].

Propane was supplied by four 568 liter (150 gal) liquid propane gas (LPG) cylinders, stored in an external fuel farm. Two Zimmerman LPG electric heaters vaporized the liquid propane prior to entering the COAL Lab, where it was controlled by an Al-

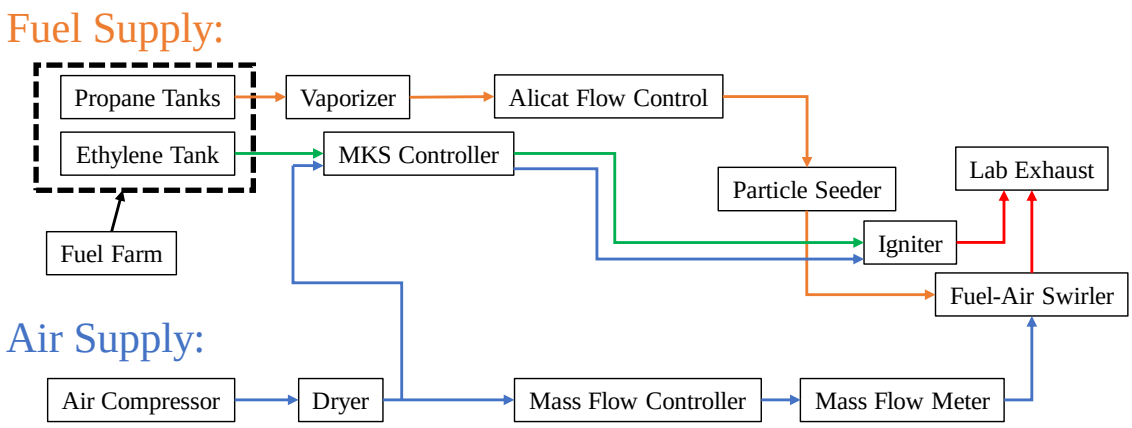

Figure 58. COAL Lab fuel and air supply diagram.

icat MCR-250SLPM-D-40X55 mass flow controller. For visualization purposes, this propane was fed through a seeder (Figure 59) that introduced silicon carbide seed into the fuel. Figure 60 shows how the fuel and air supplies connect to the swirler, where propane feeds the concentric fuel line directly and air fills a plenum beneath the swirler vanes. Fuel and air exiting the swirler was then vented by the lab exhaust, pulling approximately 0.24 kg/s mass flow out of the test section.

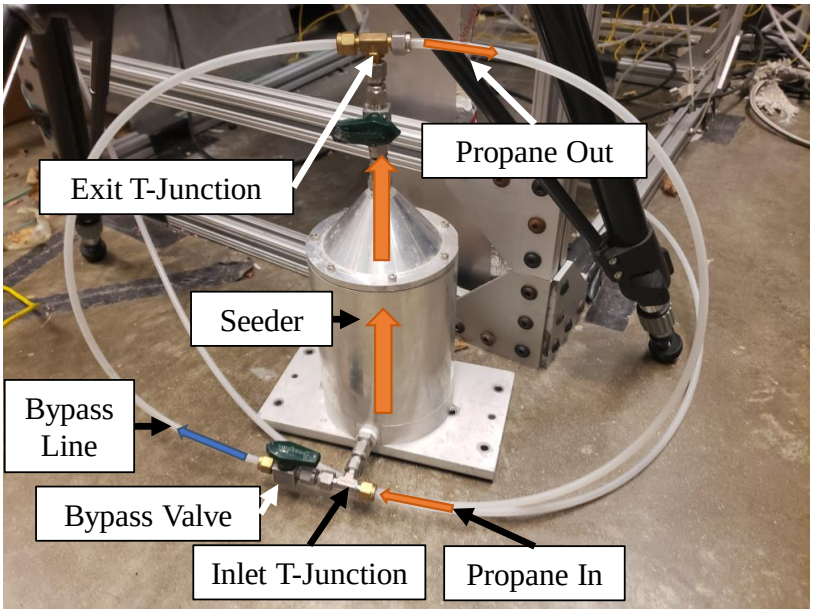

Figure 59. Seeder used to introduce silicone carbide seed into propane supply.

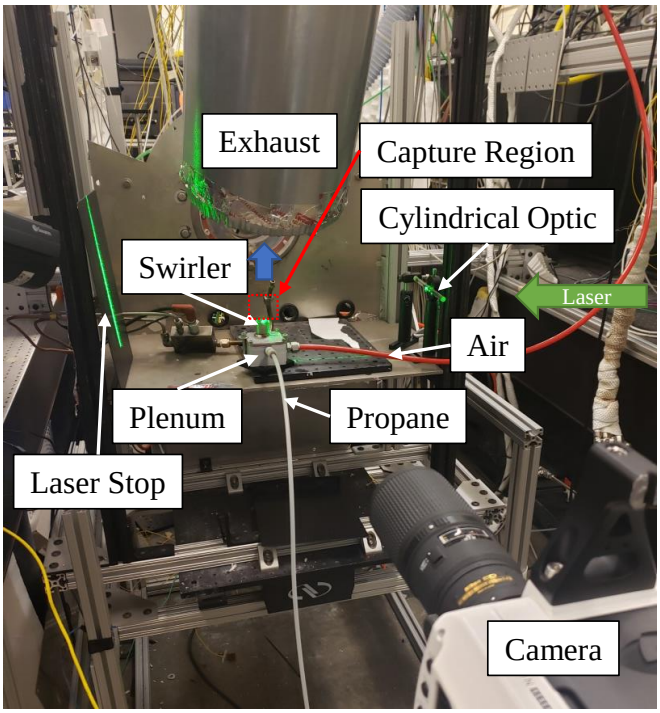

Figure 60. Swirler experimental test section.

Particle illumination for PIV was supplied by a Coherent Verdi V-12, continuous wave (CW) solid-state laser. This 532 nm laser, shown in Figure 61, was capable of outputting a continuous beam up to 12 watts. A high-power CW laser was chosen over a pulsed laser to reduce complexity in timing between the laser and camera. The Phantom v16 high-speed camera was capable of recording at a high enough frame rate to produce independent images for auto-correlation analysis. Images were recorded at 49,000 frames/second with a 3 μs exposure time and a 512x512 pixel resolution. Figure 62 diagrams the laser setup, showing the location of the laser, test section, and camera. Note that the laser sheet created by the glass rod spreads out of the page in Figure 62.

In addition to PIV, visual tests were conducted to compare combustion stability at various operating conditions. For flame holding tests of reacting flow on the same swirler used for PIV tests, still-frame images were capture with a Cannon PowerShot-

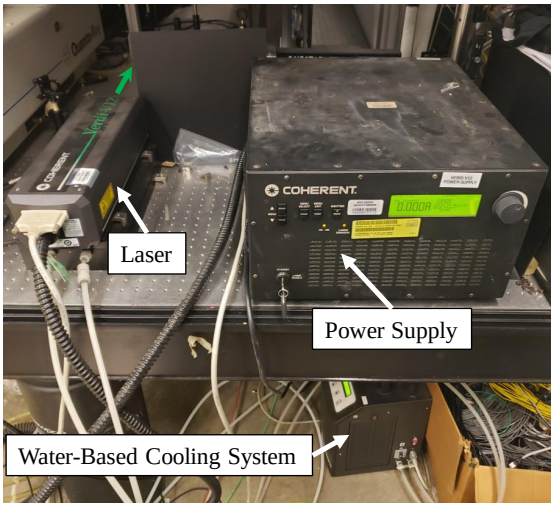

Figure 61. Verdi V-12 CW Laser.

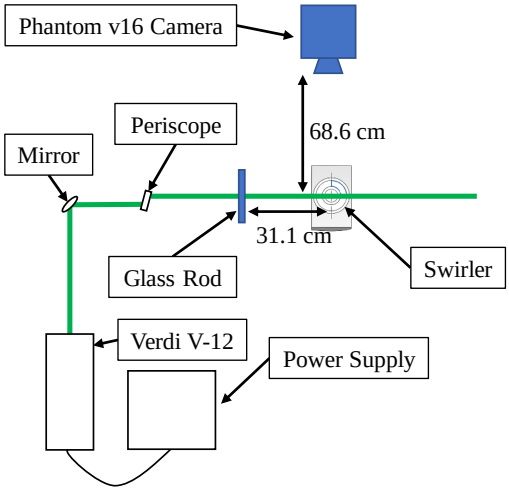

Figure 62. Laser and camera setup.

SX540-HS DSLR camera, and a Phantom v16 camera was used for high-speed image capture at 10,000 frames/second. The still frame images provided a visual comparison between different flow conditions, while the high-speed camera recorded monochromatic images of flame intensities to better visualize blow out conditions. The relative position of these cameras to the test section can be seen in Figure 63a. Unlike in PIV tests, the combustion reactions radiated in the visual spectrum, allowing for visualization of the flow structures without seeding the fuel. For the Phantom v16 to capture the flame, exposure time was increased from 3 μs to 70 μs as the flame did not radiate as intensely as illuminated seed particles. Figure 63b shows the setup of the test section for reference, including the ethylene igniter that appears to be in the plane of the swirler exit, but it was rotated along the marked motion path to ignite the swirler and removed from the flow for testing.

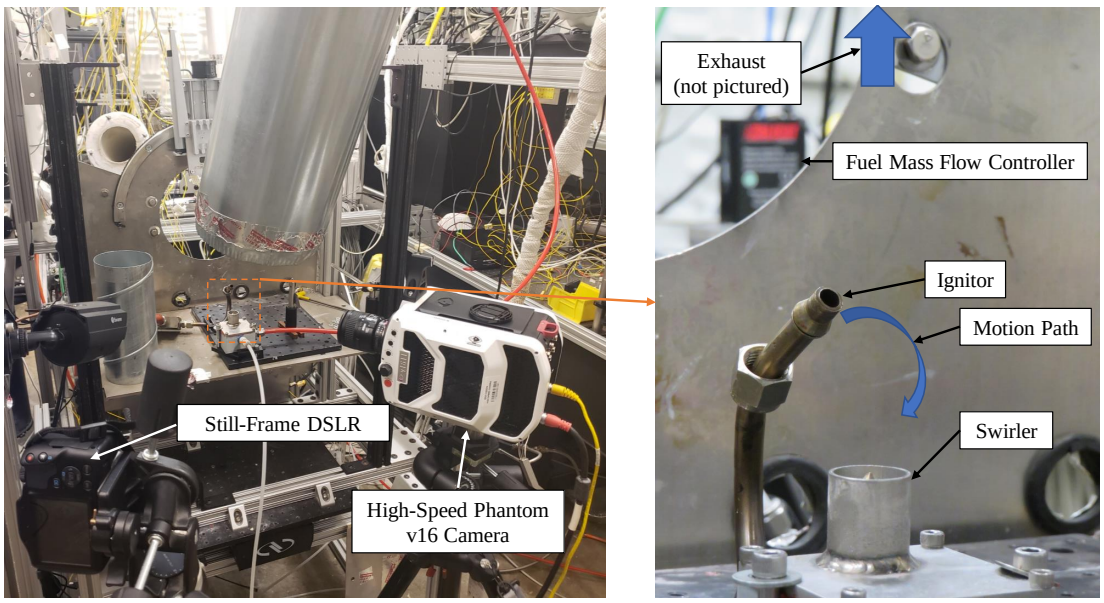

(a) Reacting Diagnostic Setup

(b) Reacting Swirler Setup

Figure 63. Setup for visual inspection of reacting cases.

IV. Results

The results section of the present work outlines the achievement of several objectives. With a known cycle and size developed for the Disk-Oriented Engine (Objective 1) in Section 3.4.1, this chapter presents results from various designs that aided decision making towards an end configuration, including the design of a combustor showing sustained combustion (Objective 2) and the development of a fuel-air injector operable across the entire operating envelope. Also presented is the comparison of computational and experimental swirler analysis (Objective 3) and the performance characteristics of the final design at various operating conditions (Objective 4).

While 48 different adaptations of the Disk-Oriented Engine Combustor were designed and analyzed computationally, only major findings and adaptations that lead directly to the final design are presented in this chapter. Versions 1 and 2 are discussed in Sections 3.1.1 and 3.1.2, respectively, so the following results focus on Version 3 (V3) and rig-ready test (RT) adaptations that led to the development of full-scale physical hardware, ready for experimental tests. Rather than stepping chronologically from the V3-1 geometry through to the final RT-14 (no plate) geometry and mentioning all of the changes that came with each step, the following sections present results specific to regions in the combustor, from the diffuser to the nozzle guide vanes. For this reason, certain geometries (*i.e.* V3-5e and RT-10) will be shown multiple times from different design viewpoints. A comprehensive list of all design versions with descriptions is provided for reference in Table C-1, Appendix C.

Starting from the forward dome of the combustion chamber, Section 4.1 outlines the swirler-specific analysis that developed the end state of the swirled fuel-air injection system. Section 4.2 steps through the key adaptations, designed to ensure functionality and manufacturability of the final computational geometry, which is presented in Section 4.3. Section 4.4 displays the parts that have been manufactured

for the real-world model, developed from the final Rig-Ready Test Geometry. Finally, Section 4.5 presents experimental results of reacting and non-reacting jets produced by the representative swirler experiments.

Before presenting a discussion on results, it is important to orient the reader to geometries and positions that are frequently called to characterize the combustor. Shown in Figure 64 are the axes most often referred to in discussing the Disk-Oriented Engine, highlighting the radial, axial, and circumferential direction vectors. This nomenclature was chosen to reflect the same used in discussion of the AFIT UCC, where this research was derived from. With a standard orientation determined, it is important to show the most common planes for presenting CFD results of the Disk-Oriented Engine, starting with the combustion cavity views.

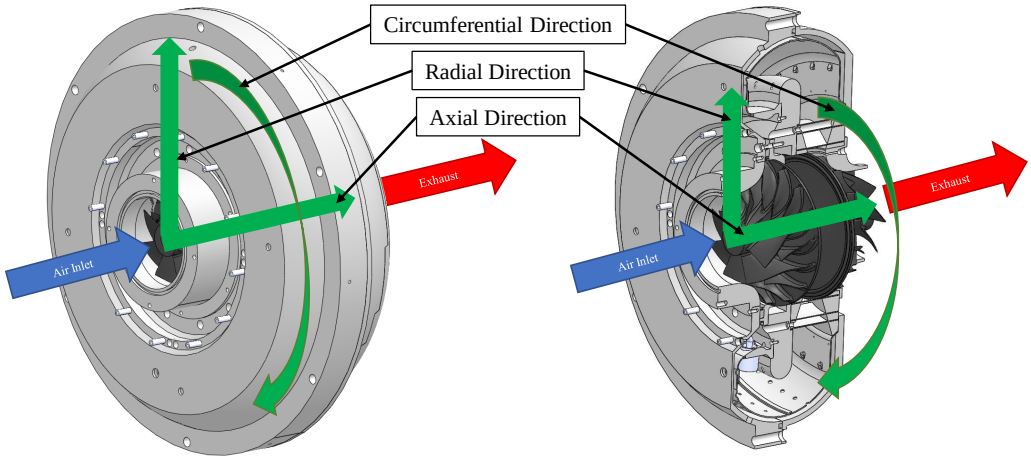

(a) Disk- Oriented UCC (b) Cutaway of Disk- Oriented UCC

Figure 64. Axis orientation of a Disk-Oriented Engine.

Figure 65 shows one of the most common views used to display figures of the combustion cavity. This presents a radial-axial planar view of the entire combustion zone, from inlet to exit, and is frequently used at cut-planes of cooling or flame anchoring. Figures on this plane can show the entirety of the U-bend combustion zone, but lack a critical component of a Disk-Oriented Engine Combustor: the circumferential swirl.

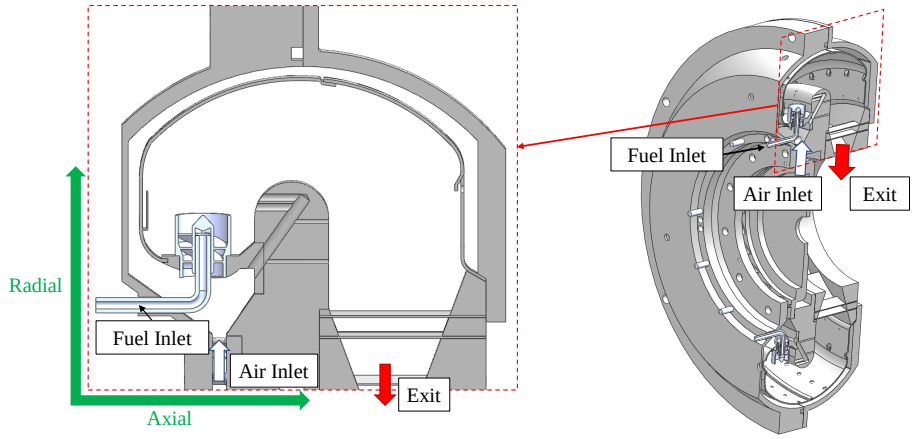

Figure 65. Radial-axial combustion cavity plane orientation.

To better understand how swirl impacts the combustion process, two common views are shown in the radial-circumferential plane. Figure 66 shows the two most common planes in this orientation, with example results on those surfaces. The foremost plane intersects the swirler, and this gives insight into the impact of swirl within the primary zone. The later plane cuts the mid-span of the stator vanes, showing how flow interacts with the unique cooling scheme used in these blades. A combination of both of these views is used throughout the results discussion.

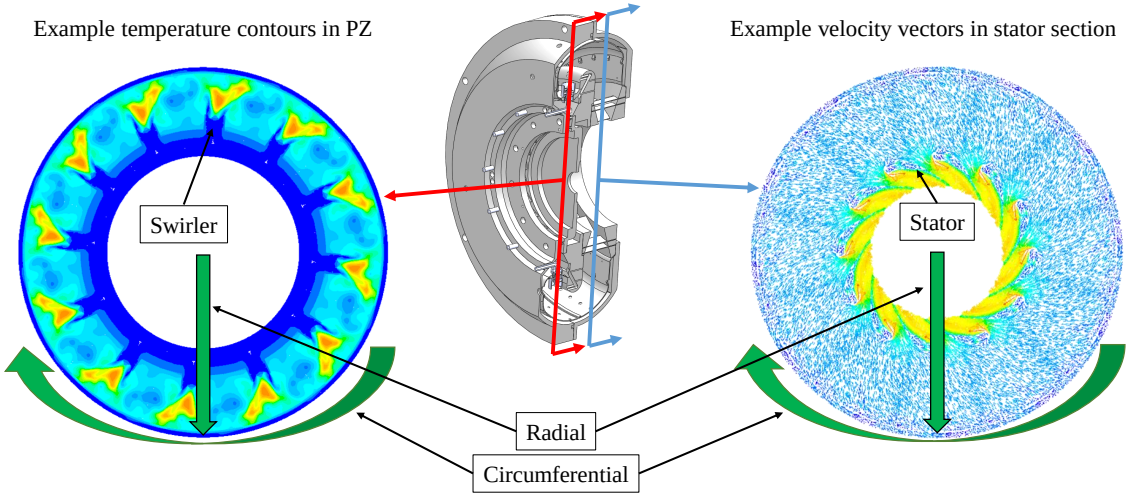

Figure 66. Radial-circumferential plane orientation.

The final frequently discussed view is the combustor exit plane, as it provides insight into turbine inlet properties. Most frequently, a temperature contour is presented from this view, as shown in Figure 67. Here, an isometric view of the combustor is shown with an arrow indicating the viewing vector for the exit plane. An example temperature contour plot is overlaid for orientation purposes; the axial and circumferential directions are pointed out as well. Key features on this exit plane are the turbine rotor hub and tip sides, as noted in Figure 67. The location of the rotor hub and tip are important in the discussion of favorable exit profiles, and these locations are referenced frequently.

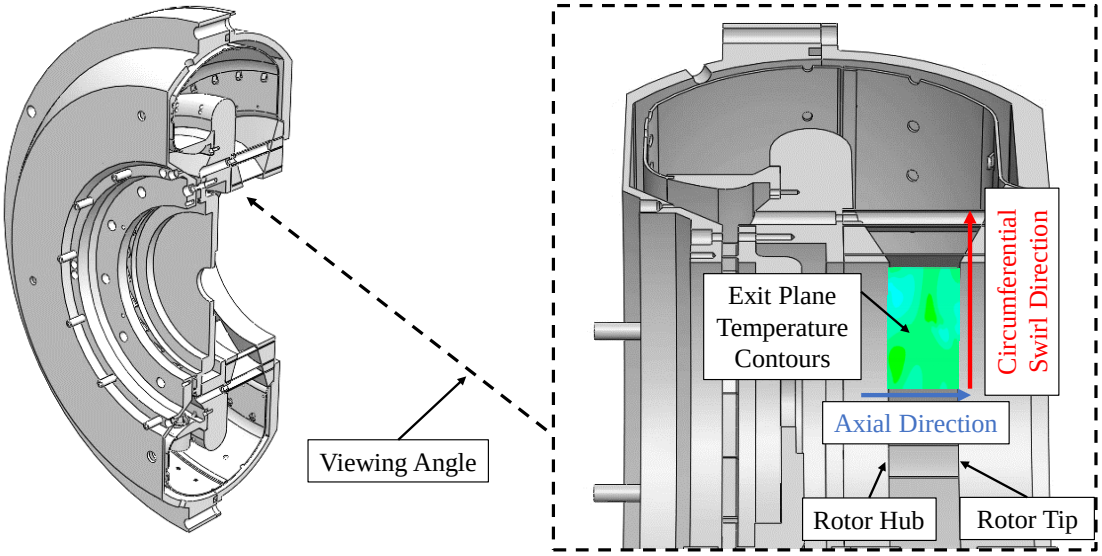

Figure 67. Exit plane orientation.

4.1 Swirler Computational Design

A component of Objective 2 for the present research was to develop a fuel injection system appropriate for the Disk-Oriented Engine's unique flow path. With the evolution of the Version 3 design of the Disk-Oriented Engine Combustor to increase the combustor volume compared to Versions 1 and 2, the flow path from inlet to exit

was also different. A different fuel introduction and flame stabilization scheme was required to ensure reaction anchoring in the PZ, as the V3 combustor would not use the helical trapped-vortex designed discussed in Sections 3.1.1 and 3.1.2. Bluff-body flame stabilization was the first attempt to create a flame anchor in the PZ, where air would stagnate on a dome (shown in Figure 68) and form velocity shear layers as air moved about the plate. Figure 68 illustrates how slots were used to allow air to flow around this plate, creating recirculation zones in the wake of the shear layers.

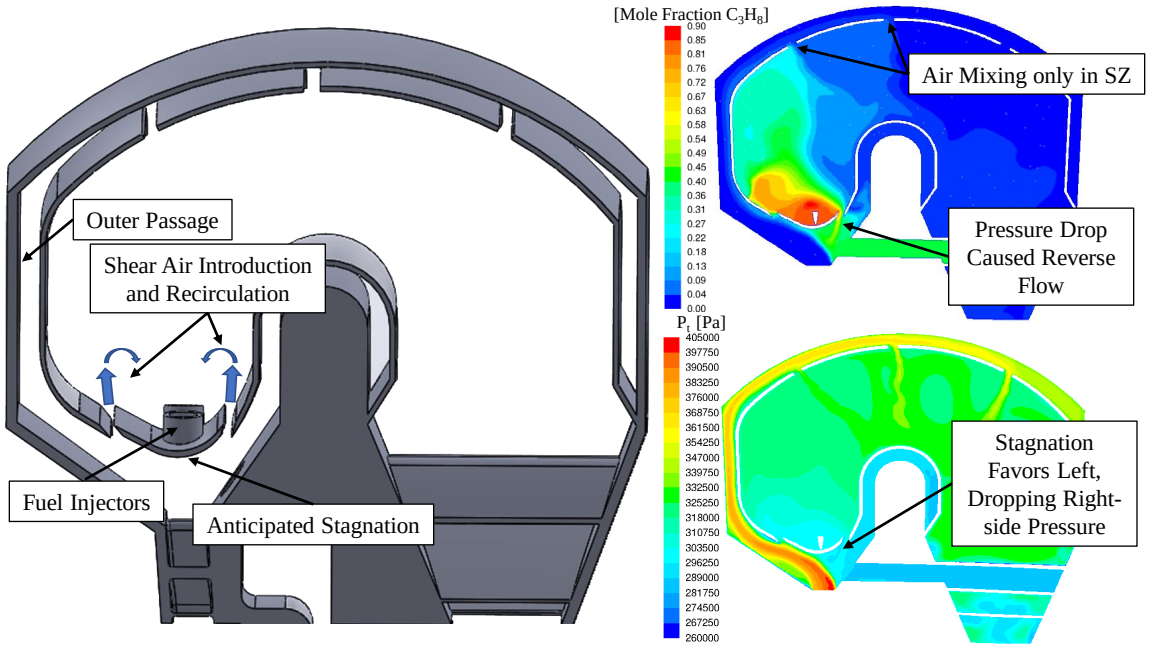

Figure 68. V3-2 fuel injection scheme, resulting in reverse flow into the diffuser. Mole fraction contours of propane are plotted to show how fuel mixes with air in the PZ; gauge total pressure contours are shown for causal representation of reversed-flow out of PZ.

Also shown in Figure 68 are propane mole fraction and gauge total pressure contours to illustrate the results of this fuel introduction system. Propane is seen in high quantities throughout the PZ, with little dissipation before interacting with SZ air jets. This indicated that there was not enough air entering through the PZ slots to sustain combustion. Apparent in the propane mole fraction contours is the presence of propane within the diffuser, as it had flowed backwards through the right-side air

introduction slot. The cause of this flow reversal is shown in the total pressure plot, where the stagnation point favored the bypass duct around the PZ, rather than stagnating directly on the forward dome. The high velocity of air moving through the outer passage in this plot caused a pressure drop in the diffuser, allowing propane molecules to flow into the dilution air supply. Both the reverse flow and high concentration of propane were addressed in subsequent iterations. A more reliable and turbulent fuel injection system was designed for this forward dome, which illustrates the iterative design nature of the fuel-air swirl injector.

Although fuel-air swirlers traditionally have a flat vane design [10], where vanes are spaced around the swirler annulus with a given swirl vane angle (ϕ) as shown in Figure 69a, the present research created a new design that involved sweeping the vanes about the swirler annulus like the design shown in Figure 69b. The angle swept by each fin about the swirler controlled both the swirl imparted on the flow and the pressure behind the swirler as a flow blockage. Controlling the blockage of the vanes was important for this design, as any hole located on the forward dome would see near-stagnation pressures and flow would favor a path with least resistance over any bypass flow around the PZ. By changing the sweep of these vanes during the design process, the velocity and swirl number through the air-fuel swirl injectors were moderately controllable.

The initial design of the swirl injector was based on the provided expression in Equation 6, assuming a flat vane structure at a given angle (ϕ) with uniform inlet flow. While these conditions would not be satisfied by the swept vane design of the present swirlers, this was a starting point for design. It was anticipated, based on previous research discussed in Section 2.1.3, that a high swirl number ($S > 0.6$) and rich local equivalence ratio ($\Phi_{PZ} > 1.0$) would provide conditions necessary to maintain the turbulent combustion process in the primary combustion zone. The

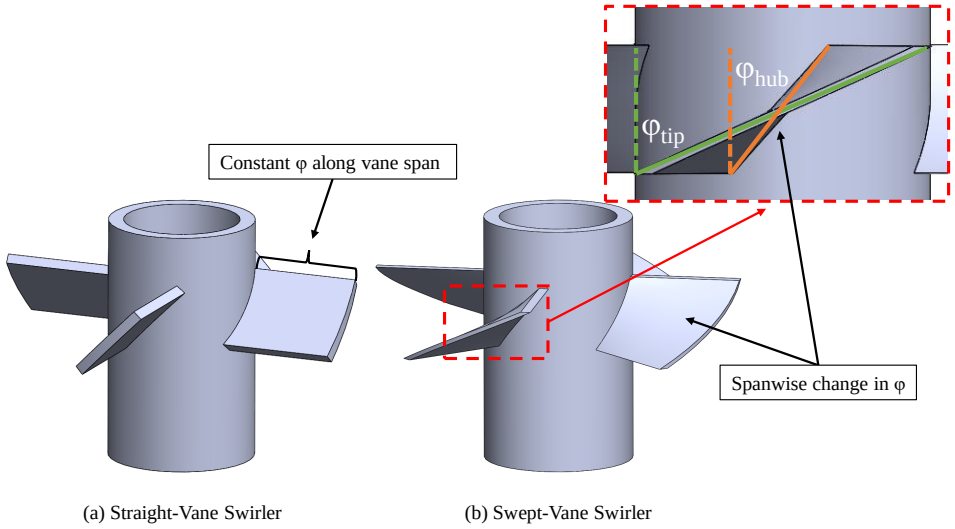

Figure 69. Swirler geometry cutaway, showcasing straight and swept vanes.

initial swirler was designed to operate at a swirl number 67% higher than the $S = 0.6$ case discussed in the literature [13], with the expectation that the flat vane and axial inlet flow assumptions in Equation 6 could not be satisfied with a bulk swirl entering the PZ swirlers.

Targeting a swirl number of 1.6 by Equation 6, the V3-3 swirler was designed with a vane angle of 62.7° and a radius ratio of $\frac{r_h}{r_n} = 0.60$. Dimensions of the V3-3 swirler are displayed in Figure 70, with four vanes sweeping 180° about the concentric fuel line. The initial swirler design was tilted 23° from radial to accept swirling flow from the compressor exit. The sweep and tilt variables are listed in Table 8, along with mass flow rates, swirl numbers, and equivalence ratios from each varying swirler geometries. Tilt and sweep were changed in coordination with analysis to provide appropriate swirl and equivalence ratio for stable flame anchoring above the swirler exit. Swirl numbers were calculated using Equation 5 from a velocity vector field output at the exit of each swirler. These (x,y,z) velocity vector fields were reduced to S using the MATLAB script found in Appendix D that includes all coordinate transformations necessary to apply Equation 5.

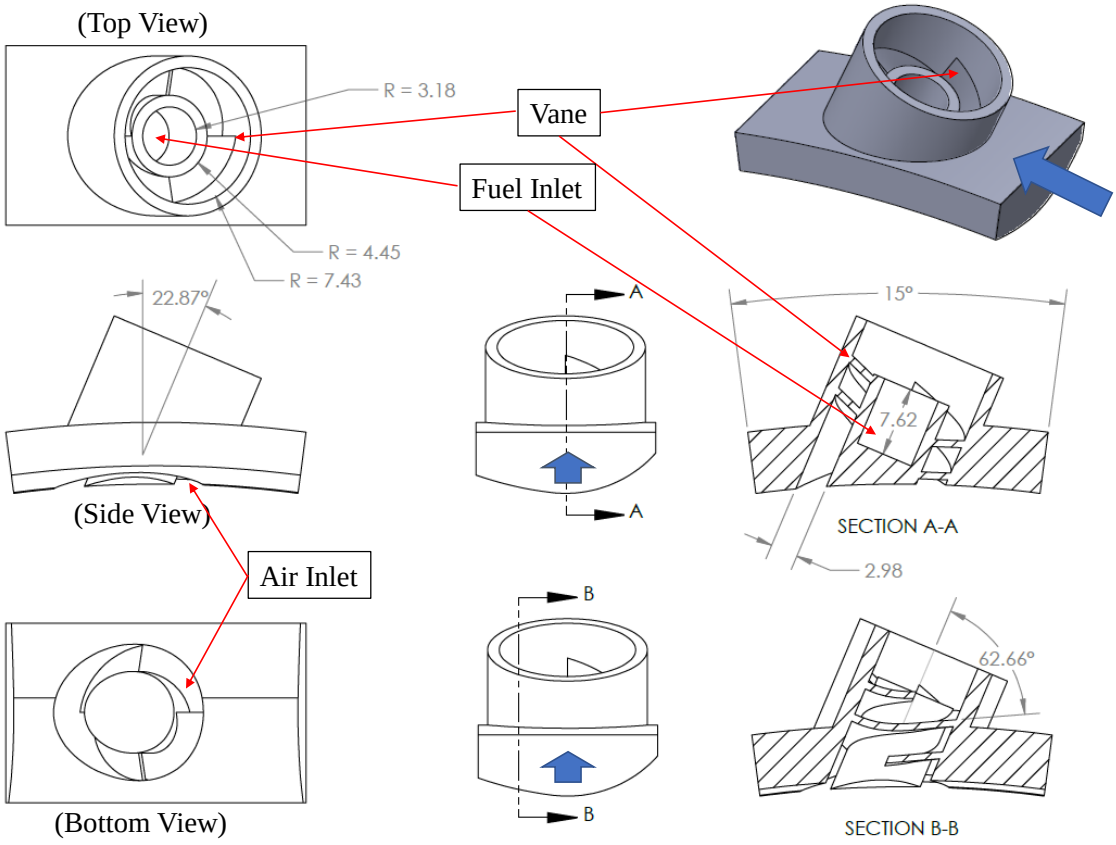

Figure 70. Version 3-3 swirler, displaying dimensions [mm] and cutaway views that are relevant to discussion on other swirler geometries.

Fuel was controlled as an input to the system, but the air into the PZ was dependent on swirler design and total pressure distribution in the diffuser; air supply then influenced the local equivalence ratio differently in each design. An important note is that Φ_{global} was overestimated in all designs prior to V3-5, as shown by the fuel flow rates in Table 8. An error in the fuel-to-air stoichiometric balance created an overestimation of Φ by a factor of 4.76 in early analysis, but all designs tested after V3-5 included updated fuel flows. For direct comparison, the actual value of Φ_{PZ} is presented in Table 8 where designs prior to V3-5 erroneously supplied 4.76 times more fuel than desired. Therefore, many of the efforts made in swirler design were to increase the airflow through the swirler geometry.

Table 8. Details of swirler evolution. Parameters were evaluated for an individual swirler.

	Tilt [°]	**Sweep** [°]	**S**	$\dot{m}_{fuel}$ **[kg/s]**	$\dot{m}_{swirl}$ **[kg/s]**	Φ_{PZ}
V3-3	23	180	0.96	0.00450	0.0070	9.97
ST-1	23	180	1.05	0.00450	0.0012	59.28
ST-2	23	90	0.90	0.00450	-0.0004	(-)
ST-3	45	90	1.53	0.00450	0.0082	8.57
V3-4	45	90	1.36	0.00450	0.0044	15.90
V3-4b	45	135	2.01	0.00450	0.0191	3.67
V3-5	45	180	0.67	0.00094	0.0124	1.19
V3-5e	0	180	1.03	0.00094	0.0161	0.91

Figure 71 shows a pressure plots and velocity vectors resulting from analysis on the Version 3-3 swirler geometry. Just as the V3-2 design in Figure 68, the stagnation pressure favored the left side of the forward dome. This resulted in a total pressure deficit on the other side of the forward dome and reverse flow through the dilution zone. The swirled fuel injection system prevented the reverse flow of propane out of the PZ that was seen in Version 3-2, but the flow from the stator section to the diffuser was not desired in this design. To learn from this design, three separate swirlers were tested without the SZ of the combustor, reducing the computational domain significantly.

By reducing the computational domain to a single swirler, the swirler-test (ST) model sped up the computational process for faster analysis of various swirler design iterations. Figure 72 shows the 15° periodic sector of the primary combustion zone, including a single swirler for analysis. Based on pressure data from the full domain Version 3-3 analysis, the bounds of both the PZ and bypass duct were estimated as constant-pressure outlets, and the mass flow inlets supplied half of the fuel and air mass flow as 30° models. Three different swirl geometries (shown in Figure 73) were

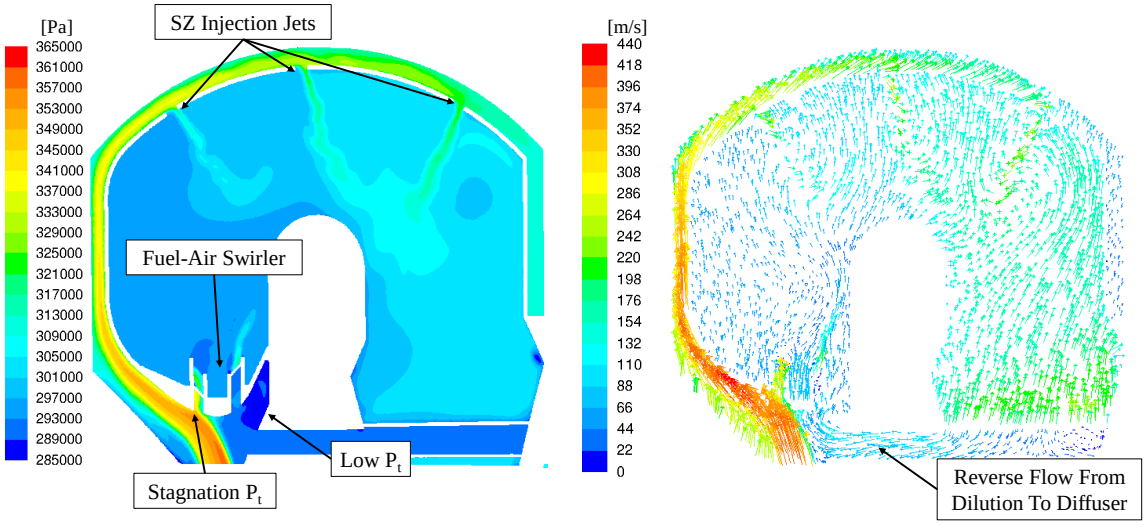

(a) Gauge total pressure

(b) Velocity vectors

Figure 71. V3-3 fuel injection scheme, resulting in reverse flow through dilution holes. Total pressure contours represent gauge pressures from 101325 Pa.

analyzed through this process, varying both tilt angle and sweep angle to force Φ_{PZ} closer to 1.0. As noted in Table 8, swirl numbers in these designs varied between 0.9 and 1.5, with the equivalence ratio decreasing from 59.3 to 8.6 from ST-1 to ST-3. This reduction in Φ_{PZ} was helped more by an increase in tilt than vane sweep angle, as tilting the swirler into the direction of the bulk swirl reduced turn requirements on high-momentum flow in the diffuser. While the reduction in Φ_{PZ} was significant, it was not enough to provide a sustainable fuel-air-ratio in the primary zone. Further design iteration was required to stabilize PZ flame anchoring.

An outlier in this data, as shown by the negative mass flow rate of air through the swirler in Table 8 for the ST-2 design, ST-2 created a condition that allowed for reverse flow of fuel in the swirler. This meant that the reduction in vane sweep also reduced back pressure on the swirler, allowing for air and fuel to escape the PZ through one of the swept air supply passages as shown in Figure 74 where path lines released from the fuel injector flow into the diffuser rather than the PZ. Knowing this, a 90° sweep would likely be susceptible to reverse flow at off -design conditions with

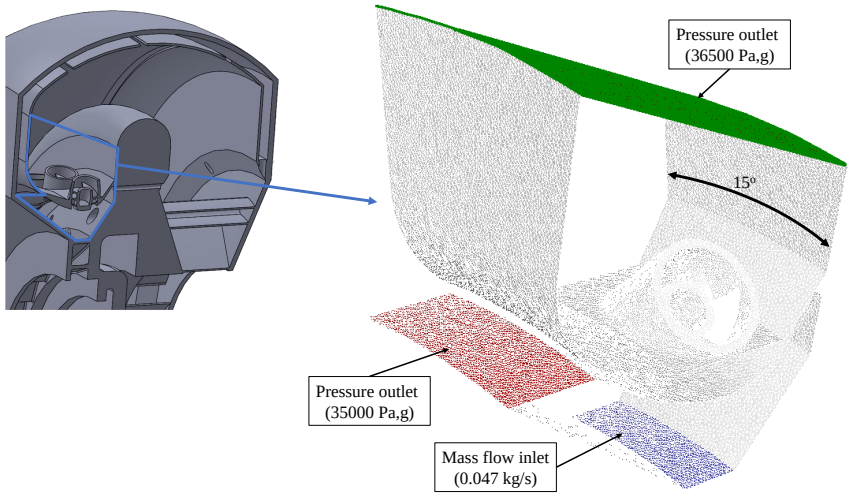

Figure 72. Swirler Test (ST) domain, encompassing a single swirler within a 15° periodic sector. Gauge pressure is based on 101.3 kPa operation pressure, averaged from results at these locations in the V3-3 design.

less stagnation pressure on the swirler inlet. The 90° sweep was kept for ST-3 and V3-4, as it also reduced the equivalence ratio in the PZ, but the design would later revert to a 180° for the back pressure benefits already discussed.

Taking the lessons learned from single-swirler interrogations, Version 3-4 incorporated a swirler with 45° tilt and 90° vane sweep. This design was implemented to compare the reduced domain ST results to that of the full 30° periodic domain. Table 8 shows how transferring the 45° tilt and 90° sweep from the ST design to the full 30° domain increased the equivalence ratio by 86% and decreased S 11%, all due to a reduction in mass flux through the swirler. Figures 75a and b show how the change in design between V3-3 and V3-4 had little impact on swirler induced recirculation in the PZ, resulting in high bulk swirl throughout the volume. To decrease Φ_{PZ} and create the recirculations characteristic of a swirl injector, the length of the swirler body was extended into the diffuser section; a longer length created more uniform inlet air contacting the vanes, and the extension into the diffuser acted as a scoop to force bulk-swirling diffuser air into the fuel-air swirl injector. This change

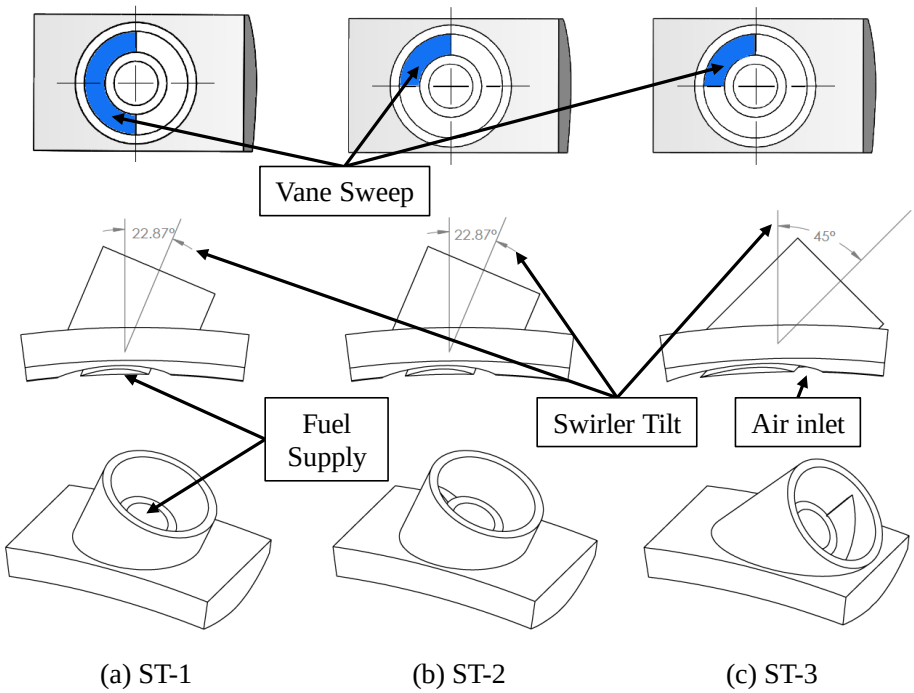

Figure 73. Swirler test geometry comparison, highlighting key features of the single swirler on a 15° periodic domain.

in geometry created the swirl recirculation pockets seen in Figure 75, providing a low velocity, turbulent structure for stable flame anchoring, but more importantly this design change increased the air flow through the swirler and therefore Φ_{PZ} by 77%. While this was too rich to burn in the primary combustion zone, it was also at this point that the global equivalence ratio was recognized to be set too high, and the fuel introduced into the system was reduced by a factor of 4.76 to account for the known error in fuel-to-air ratio. A reduction this great would likely create a system that was too lean in the PZ if the V3-4b design was kept, so the sweep of the vanes was once again increased to 180° to reduce air in the swirler.

While an increase in swirler vane sweep angle was thought to also increase the swirl number, as more sweep about the geometry would result in greater rotational torque imparted on the fluid, Table 8 shows that the opposite occurred. Between Versions 3-4b and 3-5, S decreased 67%. This was due to a 35% reduction in air mass

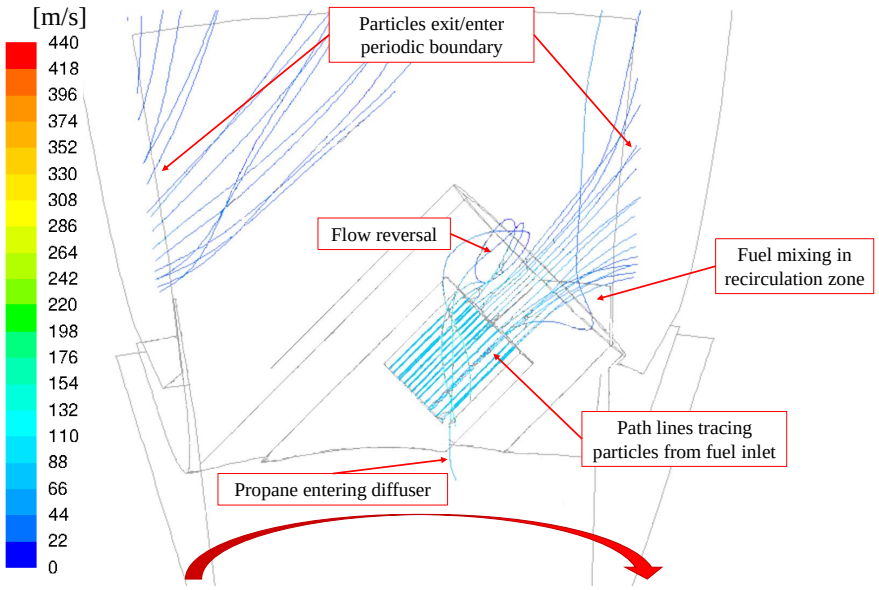

Figure 74. Pathlines issuing from fuel inlet on the ST-2 geometry, colored by velocity magnitude and showing flow reversal of fuel into the diffuser.

flow through the system, with momentum flux being a key factor in determining S through Equation 5. This decrease in S was not a negative result, as this was the first iteration to model a stable flame on the swirler exit, as shown in Figure 76a. Here, temperature contours through the center of the swirler indicated stable flame anchoring above the swirler, with reactions initiating on the swirling shear layers and heat release positioned away from the swirler inlet face. Since the PZ had a rich equivalence ratio with greater residence time requirements for complete combustion, the highest heat release is further from the swirler exit. The peak location shown in Figure 76a was thought to be a result of heat release from the other swirler in the domain, showcasing the impact of bulk swirl within the PZ. Since the interior of the swirler jet was being influenced by the center body location, the final step of swirler-focused iteration was to analyze the impact of swirler orientation in the radial-axial plane and point the swirler towards the combustion liner to better use this volume.

Figure 76b shows the impact of rotating the swirler in the radial-axial plane. Temperature contours highlight the location of highest heat release, now located

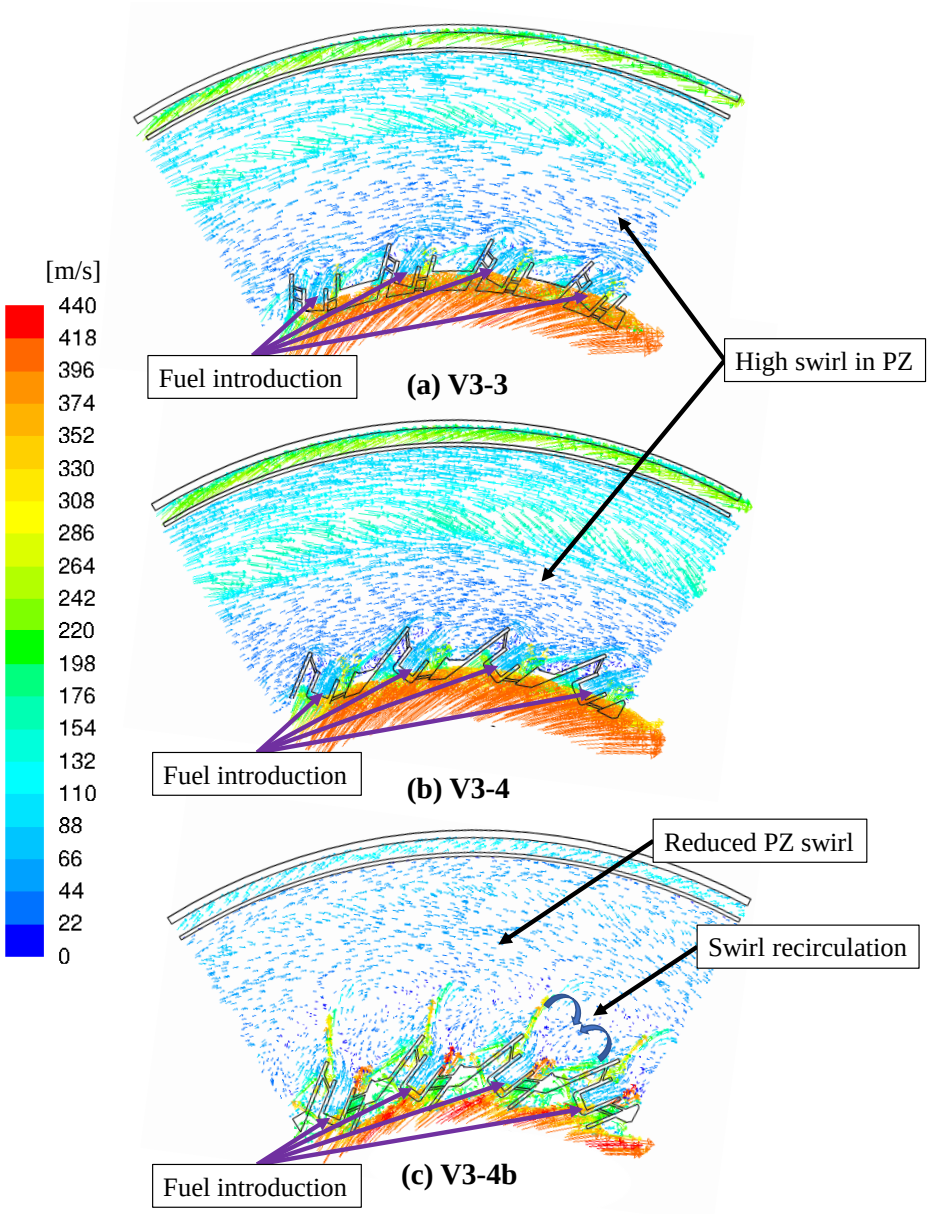

Figure 75. V3-3 through V3-4b fuel injector comparison with velocity vectors, highlighting swirler exit profiles and swirler interaction.

closer to the swirler exit than in the V3-5 design (Figure 76a). This change used the PZ volume effectively, creating a more uniform temperature profile throughout the entirety of the PZ than seen in V3-5. This tight flame anchor above the swirler was thought to be a result of two factors: the 54% increase in swirl number that increased recirculation intensity, and the removal of swirler tilt as shown in Figure 77.

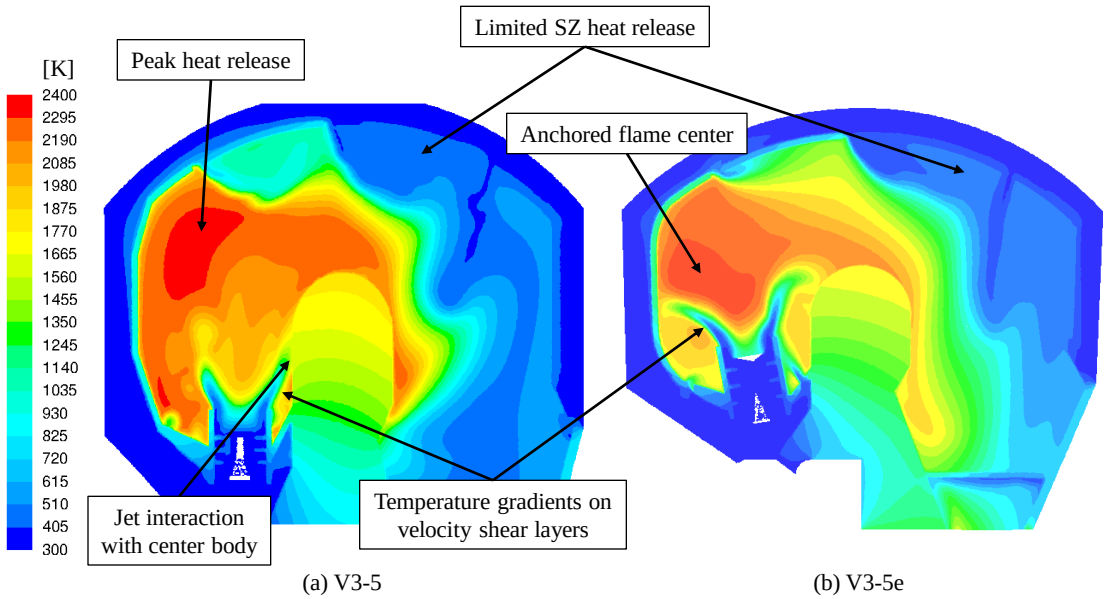

Figure 76. Temperature contours through the swirler geometry for Versions 3-5 and 3-5e.

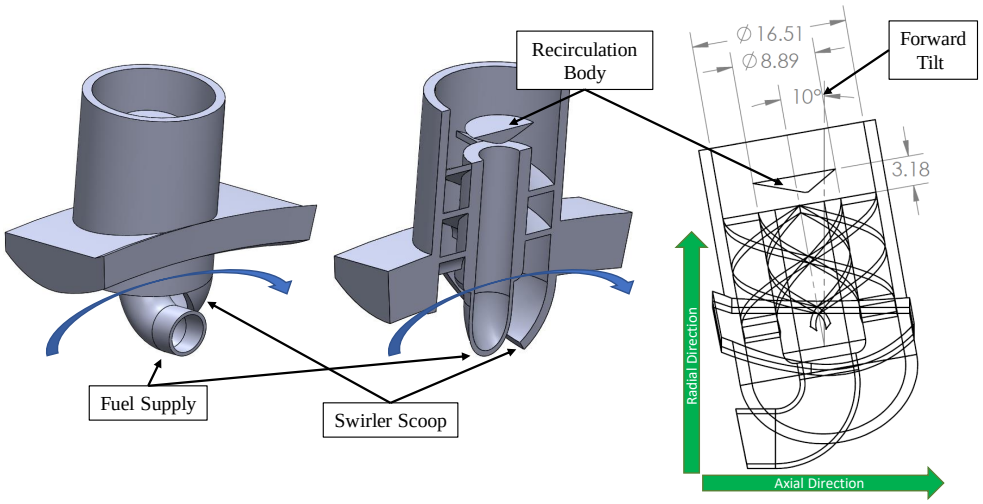

Figure 77. V3-5e swirler geometry, showcasing axial tilt to better utilize PZ volume and swirler dimensions [mm].

Based on impact of bulk swirl in the PZ, where swirler peak heat release was forced on top of its neighboring swirler, it was thought that swirler tilt imparted high bulk swirl within the PZ. While this fact was good for the amount of time a

particle remained in the primary combustion zone, the downward forcing of these swirler reactions indicated that products released in the PZ were not exiting over the center body with enough radial velocity to reach the upper portions of the SZ. To address this issue, the swirlers were tilted radially outboard (as shown in Figure 77) to remove much of this PZ bulk swirl, and the introduction of swirling air through SZ liner holes provided the bulk swirl for secondary combustion and exhaust purposes. The 45° scoop introduced in V3-4b was retained, as this was necessary to force bulk-swirled air from the compressor through the radial swirlers, but air was turned within this scoop to a radial injection configuration. While the temperature contours in Figure 76 suggests that increasing the radial component of velocity did not increase SZ combustion as intended, the impact of increased S created a more desirable flame anchor point, so the radial swirler configuration was kept for future iterations.

The result of the iteratively designed fuel-air swirl injector was the geometry shown in Figure 78. Note the capsule-like recirculation body that was not discussed; it was introduced to force gaseous propane outboard into the swirled air, simulating the conical spray pattern of a liquid fuel injector that would likely be used in further application of the Disk-Oriented Engine.

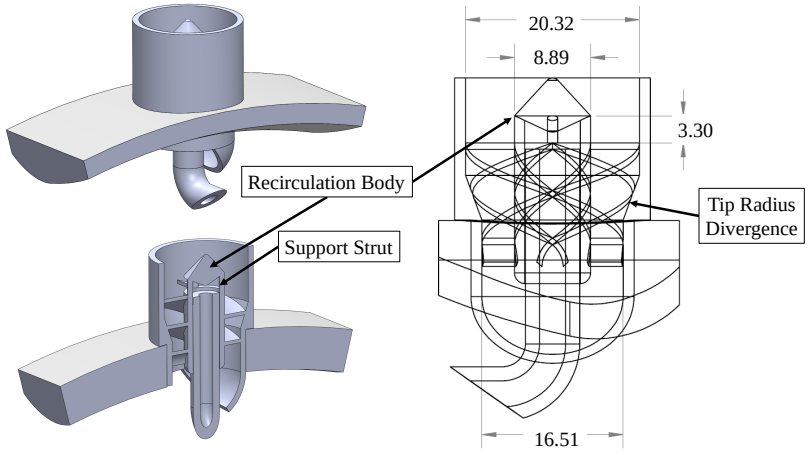

Figure 78. Final swirler geometry (dimensions in mm), used for rig-ready test analysis and experimental swirl testing.

This swirler operated at $S = 0.79$ and $\Phi_{PZ} = 1.3$ at the design condition, installed on the final design geometry. Changing hole placement in future designs impacted these values, but computational analysis suggested that they would hold stable flames at reasonable values ($0.6 < S < 1.6$ and $0.9 < \Phi_{PZ} < 1.2$), and their success was qualitatively accessed based on temperature contours for future iterations. This swirler, including its presented dimensions, were used in the atmospheric experimentation of the swirler design.

4.2 Combustor Geometry Design

With a rough design for Version 3 geometries created from lessons learned in Versions 1 and 2, it was important to outline specific design choices that led from a generalized CFD geometry to a design that would be fabricated for experimental testing. This sections presents results as they pertained to design changes leading up to the final rig-ready test geometry. Rather than progressing chronologically from Version 3-5 to the RT-14 (no plate) design and detailing each change, this section focuses on development of different regions of the combustor: swirler placement in the PZ, liner coolant and SZ air supply, center body cooling techniques, turbine nozzle guide vane design, and dilution introduction to shape exit temperature profiles.

4.2.1 Number of Swirlers

The Disk-Oriented Engine combustor was originally designed with twenty-four swirlers equally spaced about the combustor annulus. Such a high number was chosen initially to ensure that the jets produced by each swirler would interact with those surrounding. Prior to cutting metal on a design, it was thought that this many swirlers more than enough to ensure stable flame holding throughout the PZ, and the system could operate with fewer to reduce weight and complexity. To investigate

this, a computational study was done to compare the impact swirler density had on combustion. The same geometry (RT-4) was analyzed with twelve and twenty-four swirlers. A two-fold reduction in the number of swirlers would mean that twice the mass flow rate of fuel would be supplied to each swirler, requiring twice the mass flow rate of air to maintain the same swirler equivalence ratio. Rather than design and iterate upon the swirler inlet dimensions to obtain this increase in air mass flow, the same swirler geometry was used for both twelve and twenty-four swirler configurations for a direct comparison of the impact number swirlers had on combustion in a constant geometry.

If the diffuser acted as a plenum, the air through each of the swirlers would double as the number of swirlers was halved, but computational analysis revealed that the mass flow rate of air through a single swirler increased only 3%. Since the air supply to the combustion section of the Disk-Oriented Engine Combustor was not a plenum, air followed the path of least resistance and forced an additional 24% of the total air to enter the SZ, bypassing the PZ entirely. The twelve-swirler configuration saw little change in swirler air supply, holding swirl number approximately constant, but the equivalence ratio in the primary zone increased 78%. This increase in fuel concentration caused the flame structure to change, as shown by the temperature contours in Figure 79.

These contours were taken on the radial-axial plane through the center of the swirler geometry. Primary zone swirl was observed in each design, where the bulk-swirl side of the swirler jet extended further into the PZ than its opposing side. Since the 12-swirler configuration introduced the swirled fuel-air mixture at a higher equivalence ratio, the primary reaction no longer anchored to the same spot. Instead, the reaction in Figure 79b encompassed more of the volume and a longer distance than reactions in Figure 79a. This spreading of the flame front was necessary to ensure

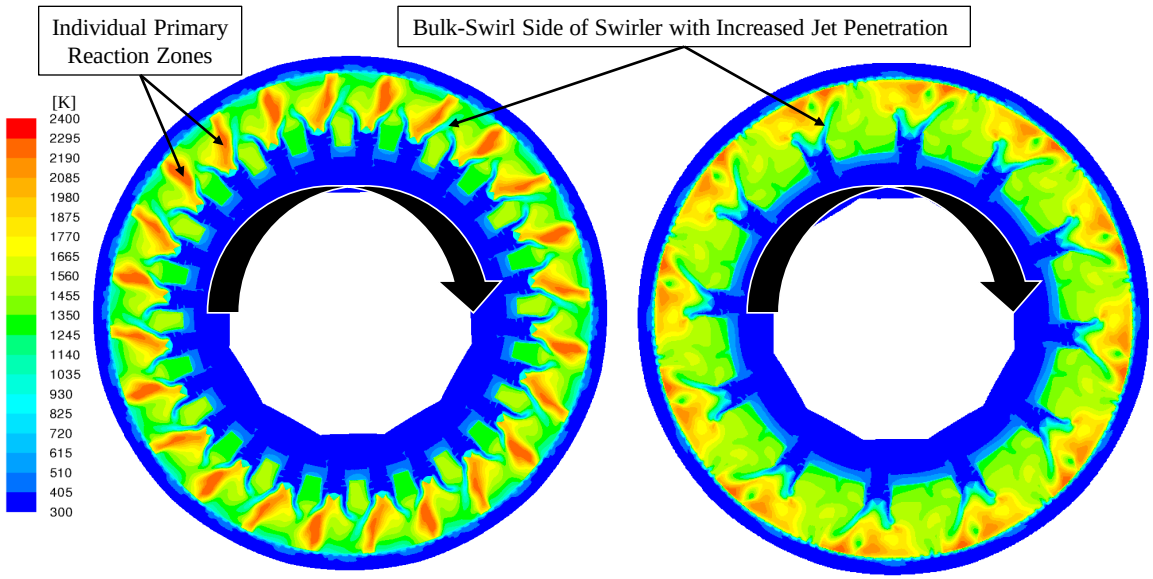

(a) 24-Swirler Configuration (b) 12-Swirler Configuration

Figure 79. Temperature contours comparing number of swirlers on the radial-circumferential plane.

swirler jet interaction at an increased distance, but the spreading flame front would also require a longer residence time to burn than the compact flames over the 24-swirler configuration. Based on this fact alone, the 12-swirler configuration seemed to be less beneficial than the 24-swirler configuration, but there were additional advantages to reducing the number of swirlers not shown in Figure 79.

Some of the benefits of reducing the number of swirlers is shown in Figure 80, which presents a comparison of the same configurations on the radial-axial plane. This shows that the increase in Φ for individual swirlers strengthened the flame anchor in the recirculation and mixing zones, resulting in flame stabilization directly above the swirler; this removed the reaction front off the wall as seen in Figure 80a. Additionally, the 24% increase in bypass air that supplied the secondary zone is seen in Figure 80b with temperature reductions associated with jet penetration. While these SZ jets extinguish any lean burn that occurred outside of the PZ in this design, the additional bypass air provided by reducing the number of swirlers was used differently

in subsequent designs to cool the combustion liner above the swirler and to increase the bulk-swirl residence time within the PZ. Ultimately, the 12-swirler adaptation was kept for its reduction in complexity for manufacturing and reallocation of air to the bypass liner; Section 4.2.2 outlines how the additional bypass air was allocated to influence combustion in the primary and secondary zones.

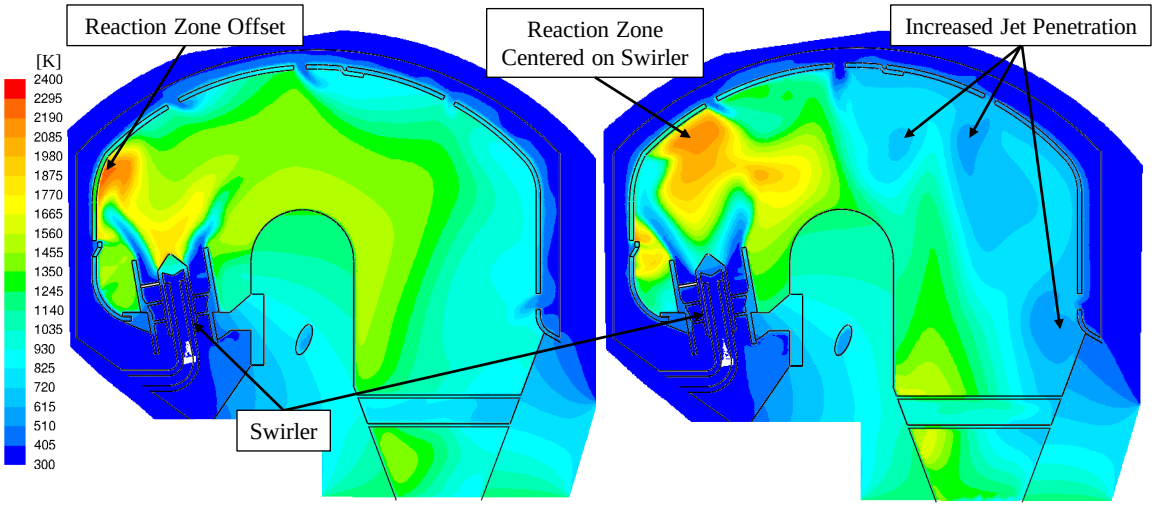

(a) 24-Swirler Configuration (b) 12-Swirler Configuration

Figure 80. Temperature contours comparing number of swirlers on the radial-axial plane.

While computational analysis showed that the 12-swirler configuration could sustain combusting in the PZ with enough interaction between swirlers, experimental testing on this design may show a need for a greater number of swirlers. Although not tested in this computational study in order to maintain the 30° periodic nature of the domain, an intermediate number of swirlers between 12 and 24 may be optimal to ensure proper swirler interaction. For this reason, an experimental investigation into the proper number of swirlers may by necessary if desired PZ combustion characteristics are not achieved in testing.

4.2.2 Liner Coolant Scheme Development

Demonstrated by the successful flame anchoring of the fuel-air swirl injector in Figure 76, the high heat release in the primary combustion zone required additional cooling for the combustion liner in addition to convective cooling with bypass air on the backside. Figure 81 shows a blown-up view of the Version 3-5e PZ, highlighting the high gas temperatures throughout the volume and at the liner surface. With this geometry the front side of the combustion liner was only cooled by back-side convective heat transfer, but temperatures on the computational surface exceeded 1300 K in this analysis. For survival purposes of the real-world liner built in SS 321, peak temperatures on this surface would need to be suppressed below 1000 K. The only location where the liner was predicted to see temperature relief in Figure 81 was after the first SZ air injection slot. Air injected at this location had an appropriate momentum compared to the hot gases to set up film cooling along the surface. Film cooling similar to this was the target for the following design iterations on the combustion liner surface.

Moving from Version 3 designs to the rig-ready test (RT) geometries called for a change in SZ injection geometries. The simple slot (highlighted in Figure 81) that had been modeled for grid simplicity purposes would be replaced with manufacturable rows of holes. While the size and number of these holes was iterated on between RT-1 and RT-14, the initial design consisted of 156 holes in the first two SZ rows and 78 in the third cooling row, all with a diameter of 4.7 mm. The resulting total area of the SZ injection holes was 67.6 cm^2, a 53% reduction from the area produced using slots. This reduction in area redistributed total pressure throughout the diffuser and bypass air supply, but this was acceptable as more air would be needed at the liner front face for film cooling.

The initial attempt to create film cooling on the front liner surface was to use plane

holes, but the injection velocities were too great such that they formed jets rather than films. The solution to this problem was the use of discrete scooped-louvers, as shown in Figure 82a. The scooped-louver was designed to inject the mass flow supplied by a similarly shaped hole into the PZ, but the louvered arm would force the cool air into a fan shape that attached to the surface. The scooped-louver was also designed as a manufacturable alternative to a slot that would perform similarly to produce coolant sheets rather than jets.

While this design did force air to attach to the surface, interaction with the swirler jet created a recirculation zone near the louvered arm. Figure 82b shows temperature contours of this design, where air supplied by the cooling hole facilitated combustion in this recirculation pocket. Air introduced on this front face would need to be shielded from mixing with the swirler jet to prevent combustion from anchoring to this surface. In addition to the scooped-louvers on the front face, Figure 82 shows an area of high temperature directly above the swirler at the liner surface. While combustion on top of the swirler was desired, the direct impingement of the flame on the liner at this position would exceed metal failure temperatures. For this reason, a fourth row of cooling jets was placed on the upper PZ to cool this section of the liner.

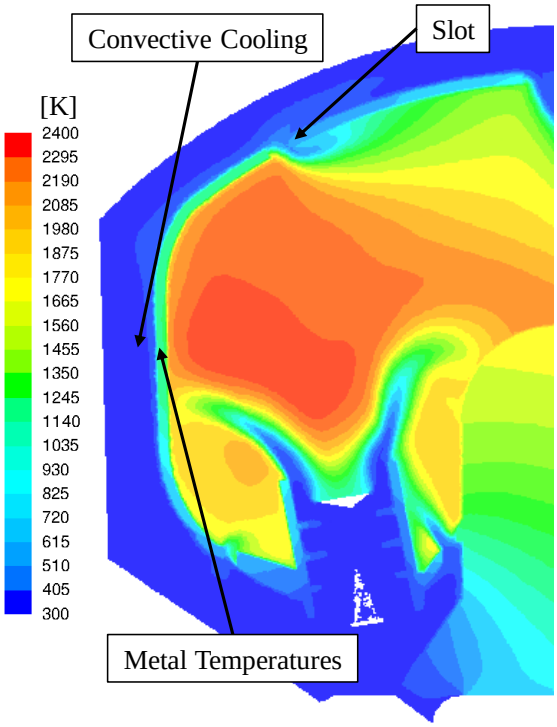

Figure 81. V3-5e temperature contours, focusing on PZ.

Figure 83a shows the design intended to reduce the liner surface temperature in

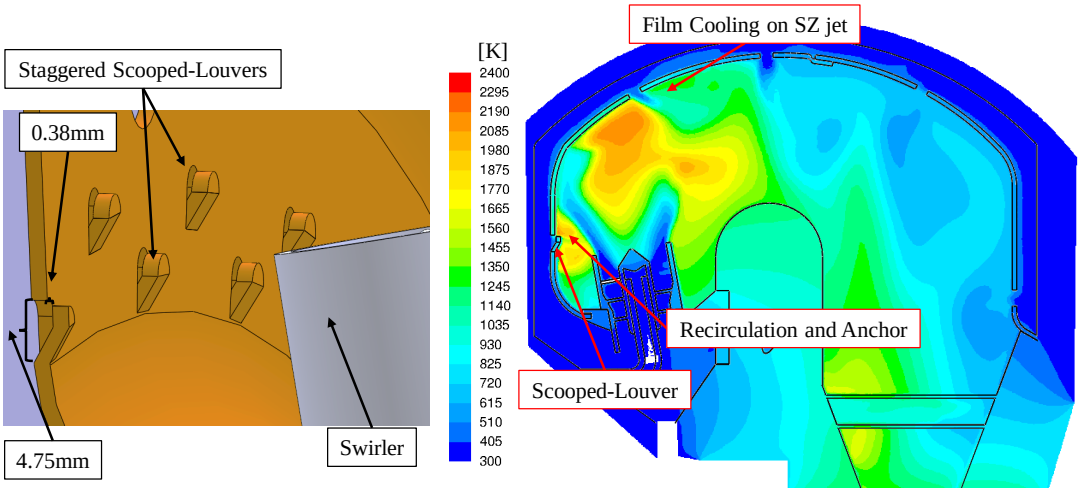

(a) Scooped-Louver Geometry

(b) Temperature Contours

Figure 82. RT-4 liner cooling geometry and temperature results.

the PZ. The scooped-louver rows were stacked, rather than staggered, to create a film shielding affect. The intent was that the first row would provide a fan of coolant air that protected the second row from mixing with the fuel and combusting at the surface. The temperature contours in Figure 83b show that the result did not match the intent. Reaction fronts anchored to both rows of scooped-louvers, increasing temperature at the surface. One takeaway from this geometry was the success the additional SZ jet had in pushing the swirler-anchored heat release from the liner surface. Temperature peaks near the base of this jet indicate combustion occurring at the jet shear layers, a problem that would be addressed in subsequent designs. The swirler's forward tilt from previous designs was also removed so that the radial distance from the exit to liner surface was increased, and the swirler now sat directly below the SZ injection jets highlighted in Figure 83b.

Although the scooped-louver was used for dilution cooling purposes on the back-side of the SZ, the analysis on RT-4 and RT-7 suggested that the design was incapable of preventing flame anchor on the liner surface. The solution was to create an im-

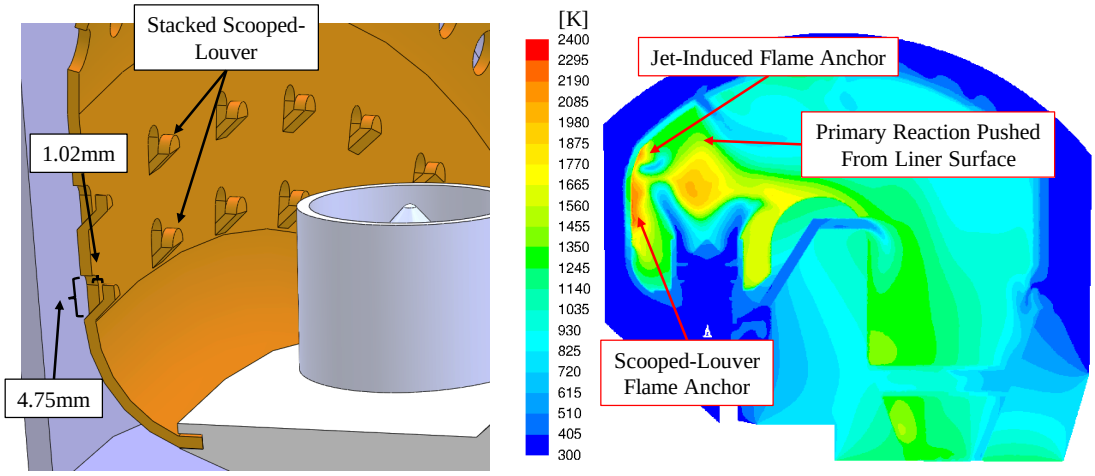

(a) Stacked Scooped-Louvers

(b) Temperature Contours

Figure 83. RT-7 liner cooling geometry and temperature results.

pingement cooling plate to create the same cooling sheet as the scooped-louver, while protecting the coolant from reacting. Figure 84a shows this geometry, where air was supplied by plane holes with an equivalent area to the scooped-louvers to minimize the change in total pressure supplied to the other SZ injection holes. Temperature contours in Figure 84b showcase the effectiveness of this cooling scheme. There was no longer a reaction anchoring to the exit of the coolant supply. The impact of this design was not necessarily a film cooling sheet that attached itself to the liner surface, but rather an air spillage over the impingement plate that interacted with the swirler jet. This momentum injection forced the primary swirl jet away from the liner surface, removing the localized reactions rather than cooling the surface from neighboring reactions.

Rig-Ready Test 13 focused on heat release above the swirl injector exit, where jet injection caused reaction anchoring in Figure 84. The intent of this design was to create a buffer of air directly above the swirler exit, preventing direct interaction between the flame front and the liner surface. The result of iterating between RT-10

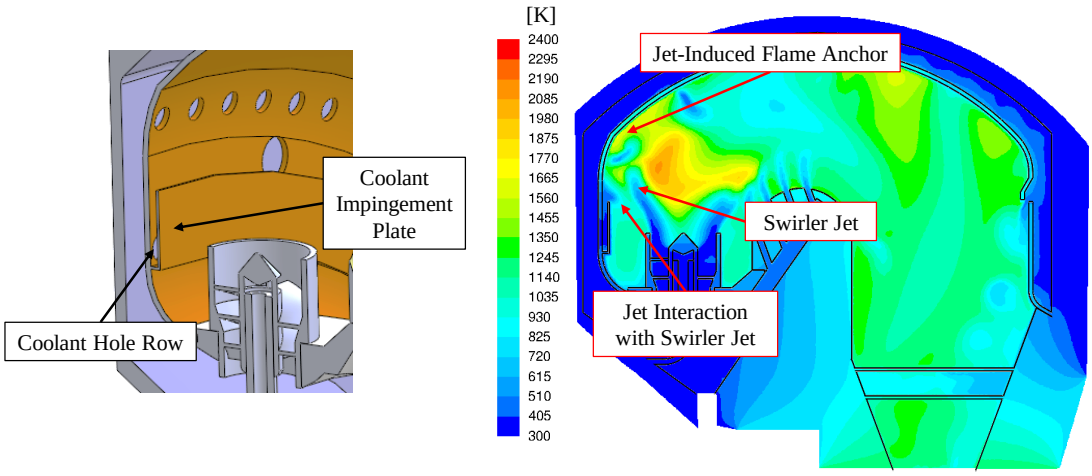

(a) Impingement Cooling Plate

(b) Temperature Contours

Figure 84. RT-10 liner cooling geometry and temperature results.

and RT-13 was a cluster of 18 staggered holes above the swirler, as shown in Figure 85. Temperature contours are presented on the solid surface to indicate what metal temperature ranges would be on the combustion liner. Note that the scale is different than the standard 300-2400 K scale used to discuss reaction fronts, as this scale provides greater contrast between metal temperatures throughout the domain. The peak metal temperature on the PZ liner was 1150 K, highlighted in Figure 85. This peak was below the initial PZ cooling jet, indicating that the impingement cooling scheme was insufficient in this configuration to prevent flame anchoring on the shear layer of the coolant jets. The final iteration of the liner design targeted this peak temperature zone shown in Figure 85.

As previously discussed, the benefit of the impingement cooling plate was not from a film cooling stance, but rather a jet momentum interaction. Since the coolant air forced the swirler jet away from the liner and had a positive impact on heat transfer to the surface, RT-14(no plate) removed the impingement plate completely and replaced it with plane holes. These holes were located to interact with the swirler

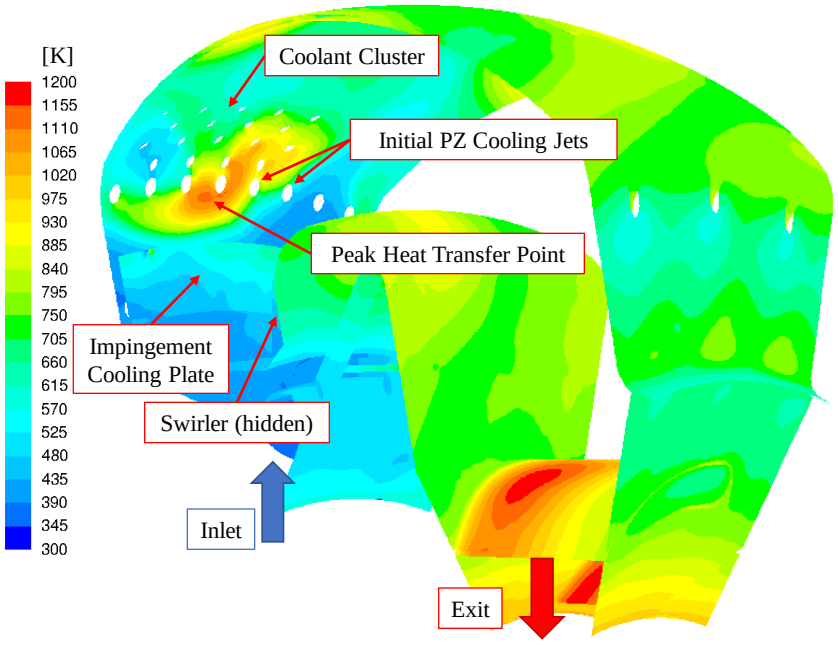

Figure 85. RT-13 liner cooling geometry and temperature results.

jet, just as in Figure 85, but instead these issued as jets rather than a sheet. Figure 86 shows the impact these jets had on temperature distribution throughout the PZ. Effectively, the jets pushed the anchored swirler flame off of the liner, forcing primary combustion to occur in the U-bend path of the Disk-Oriented Engine Combustor. Another impact of the RT-14 (no plate) design was an increase in area of the final SZ injection holes. Air introduced in this region facilitated the oxidation of CO into CO_2, releasing substantial amounts of heat outside of the PZ. The heat released in this upper SZ was more abundant than in RT-13 analysis, indicating that the air distribution in RT-14 (no plate) was sufficient for complete combustion; air supplied to both the PZ and SZ were adequate to continue with this design.

Although the RT-14 (no plate) design was the final iteration of the Disk-Oriented Engine Combustor, the following sections show the iterative nature of this design from aspects besides liner coolant. The non-plenum air supply in the diffuser and bypass duct proved challenging throughout the design process, making individual changes

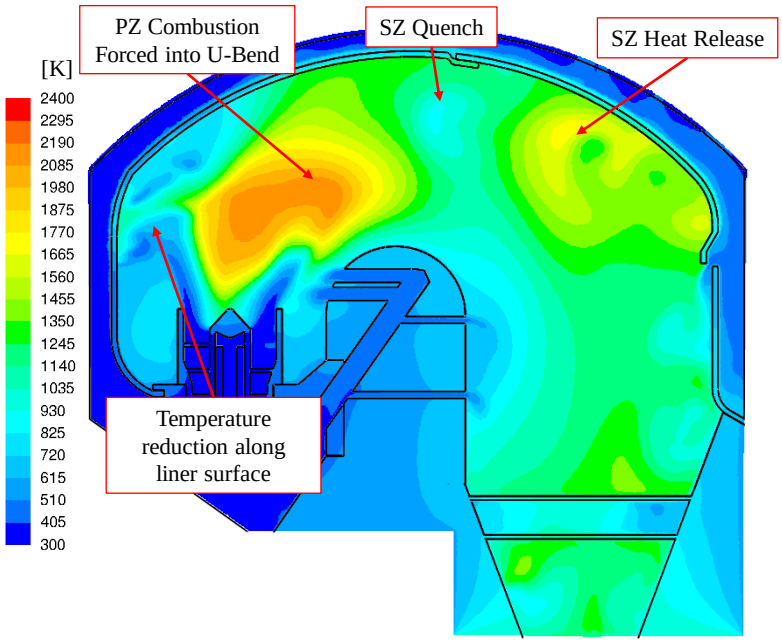

Figure 86. RT-14 (no plate) temperature results.

more variable across the entire domain. For this reason, adaptations to various parts (*i.e.* liner coolant, center body coolant, stator design) were not made one after another according to their location in the geometry, but the results are presented according to feature location.

Based on this liner development process, Figure 87 shows the clam-shell liner (Parts 5 and 11) prior to hole machining. A blue-light scan of the liner geometry, produced by AFRL, was used to develop the CAD model shown in Figure 87b. The holes were then oriented on the scans of the parts to ensure the final product would match the design analyzed computationally in RT-14 (no plate). Once these holes were stamped, the liner was complete.

4.2.3 Center-Body Cooling Development

With sustained flame fronts anchoring to the fuel-air swirl injectors in the primary zone, heating of the surrounding metals on the combustion liner and center body presented issues for real-world implementation of such a combustor design. Figure

(a) Liner prior to hole machining (b) Liner with holes

Figure 87. Liner (Parts 5 and 11) awaiting holes to be machined in the patterns shown.

88 shows temperature contours on the radial-axial cut plane of the RT-1 geometry, and heat created by the combustion process was penetrating most of the center body. Heat transfer through this Inconel part presented issues, as it directly connected to other stainless steel parts and hardware that were not designed to operate at such elevated temperature conditions. It was apparent from this information that a cooling scheme would be required to increase the survivability of the structure forming the U-bend combustion path.

Figure 89 depicts the initial design of this cooling concept, where a combustion liner would be created about the center body to cool the solid on the inside of the U-bend combustion path. This coolant chamber would provide internal cooling to the liner, but film cooling along the inner liner was not used as any holes in this inner liner would give diffuser air a preferential flow path, drawing from the SZ bypass air on the outer liner. With the manufacturing process of the outer liner expected to be expensive and lengthy, the production of an inner liner for the center body was not feasible for this design. Other alternatives to a liner coolant scheme were then explored.

To create a machinable cooling system, it was determined that discrete holes drilled into the center body would be much easier to manufacture than a liner-type

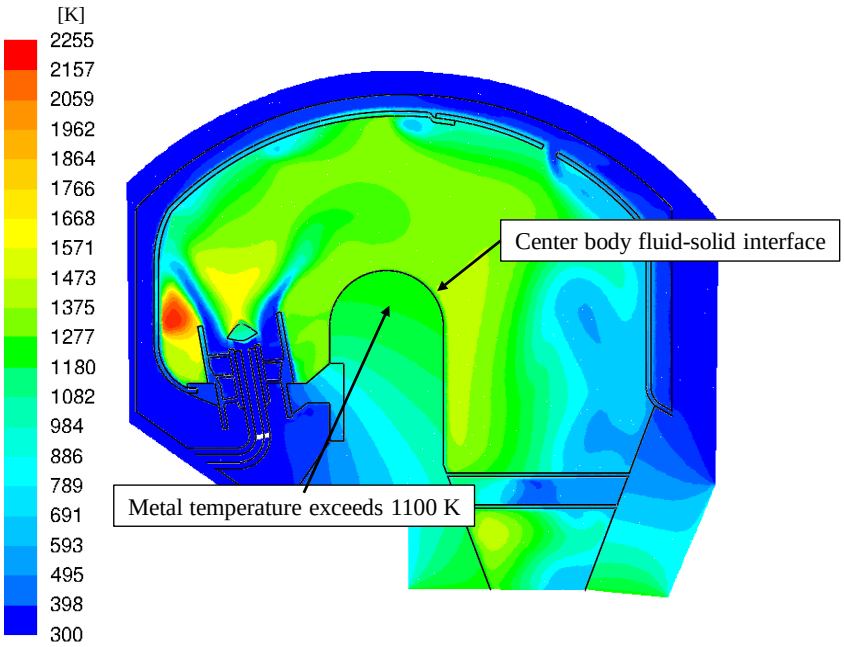

Figure 88. Temperature contours on swirler cut plane of RT-1, showing center body heating.

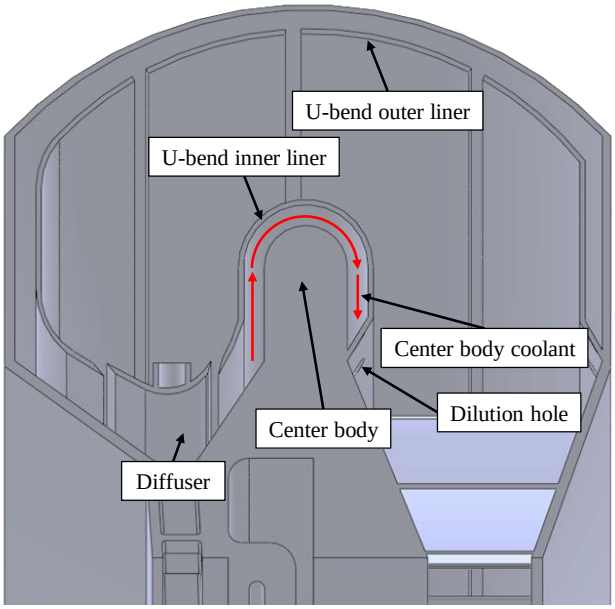

Figure 89. Version 3-2 center body cooling scheme.

cooling system, as holes could be manufactured in-house by the AFIT model shop. Figure 90a shows the cooling scheme implemented in RT-2, where dilution air would be extracted from the stator dilution supply to cool the center body. To coerce fluid

into the cooling path, the coolant hole was angled 20° from perpendicular, and the stator dilution exit diameter was reduced by half. This reduced the mass flow through the stator, and drove air through the center body coolant hole. This cooling design provided insufficient heat transfer paths for the high metal temperatures, as seen in Figure 90b. Here the metal temperature exceeded 1300 K near the U-bend, above the 1000 K target maximum in the center body. Additional heat transfer paths were believed to be a possible solution to this problem.

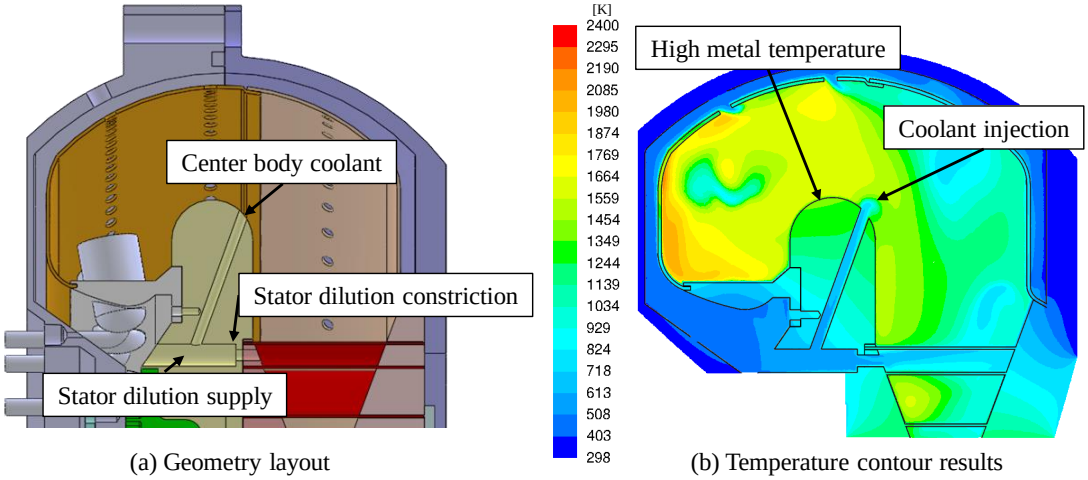

(a) Geometry layout (b) Temperature contour results

Figure 90. Center body cooling scheme for RT-3.

To increase the number of internal heat transfer paths within the center body, RT-4 utilized three coolant injection holes that branched from the stator dilution air supply. These holes were sized similarly to the hole in RT-3, with the intent that cooling air would be supplied to the center body every 10° about the annulus, rather than every 30° in a twelve-hole setup. Although not shown expressly in the model, Figure 91 shows the presence of three branched cooling holes, supplied by a single stator dilution air supply still spaced every 30°. The cut planes below show temperature contours on the radial-axial plane through each coolant hole. The only hole explicitly visible in these is the center hole, where the other two are branched from this location and out-of-plane from these contours. Once again, the internal coolant

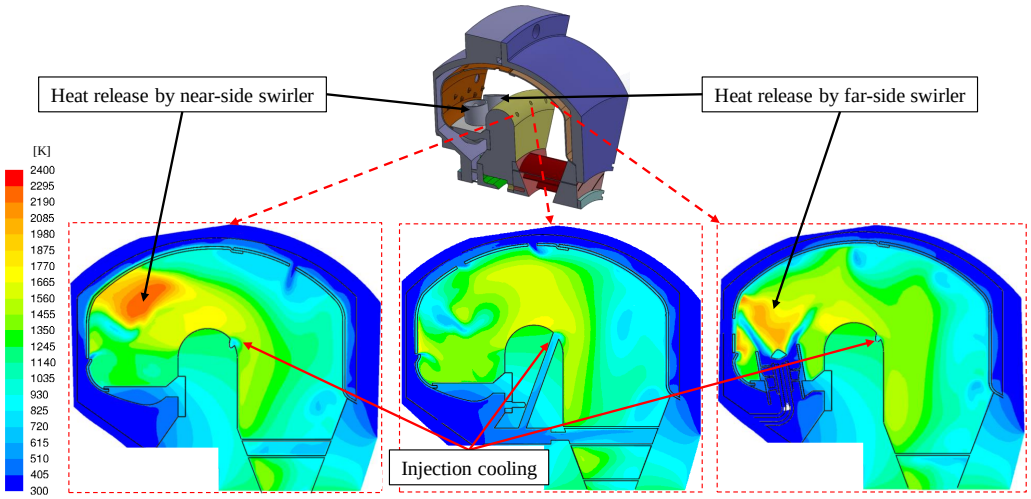

Figure 91. Center body cooling results for RT-4, including position diagram.

provided heat transfer paths, reducing the temperature of the metal surrounding the coolant holes, but this was insufficient to reduce the metal temperatures significantly.

The subsequent iteration to the center body cooling problem was implemented in RT-6, where instead of 36 drilled holes branching from 12 discrete supplies, each hole was individually supplied by the high total pressure zone in the diffuser, shown in Figure 92. In this setup, the holes would no longer be straight, but would turn axially prior to the center body surface, as shown in Figure 93a. The goal of this design was to create an air-buffer between the hot surface temperatures near the U-bend and the rest of the center body. This would complicate manufacturing, where two holes would be machined from opposite directions.

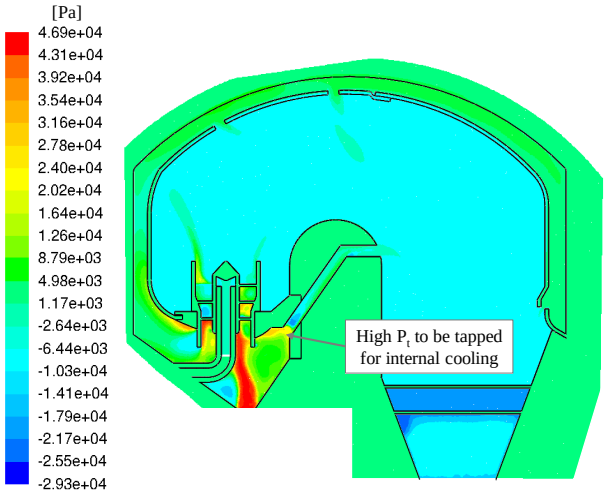

Figure 92. Gauge total pressure contours for RT-6, showcasing local high pressure used to supply internal cooling.

Figure 93b shows temperature contours of RT-6, highlighting the benefits of such a cooling scheme. Metal temperatures within this design were lower than those shown in RT-4 analysis (Figure 91), and the coolant hole created a clear divide between the hot upper section and the cooler internal section of the center body. Note that the jet injects further into the SZ than RT-4 jets, allowing for increased air introduction with the remaining reactive species. This created heat release pockets on the back side of the center body, as shown in Figure 93, that increased local temperature after the primary zone. While supplying air to the back side of the center body was beneficial to continue reactions in the volume outside of the PZ, additional iteration of the combustion liner would be necessary to force reactions to occur in upper sections of the U-bend path. Figure 93b also shows heat release near the upper surface of the center body that had yet to be addressed. This was caused by vortex flame anchoring outside of the swirler, causing reactions to attach to the surface of the center body. To cool the metal at the surface, this anchor point would need to be removed.

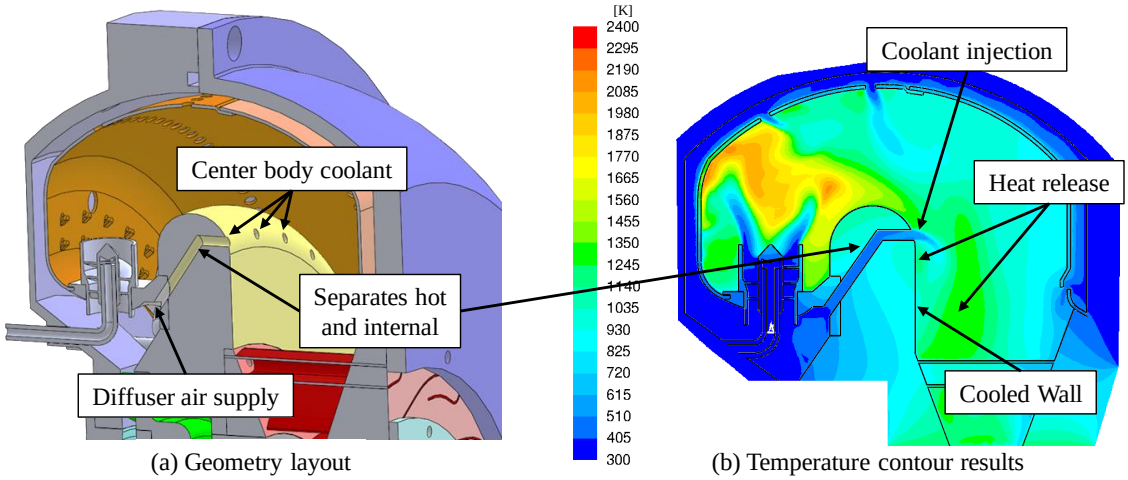

(a) Geometry layout (b) Temperature contour results

Figure 93. Center body cooling results for RT-6.

To combat flame anchoring to the surface of the center body, front side jet injection was introduced as shown in Figure 94a. This concept increased the air supply hole diameter 50% to increase the amount of air supplied to the coolant holes, and five

1.9 mm holes were drilled into the center body as shown. This hole configuration was patterned 48 times about the center body to provide coolant injection at and between the swirlers. The largest benefit to this design, as seen in Figure 94a, was the reduction in temperature above the surface of the center body. The jet injection effectively pushed the spreading swirled air off of the surface, preventing an anchor from forming. Figure 94b clearly shows a reduction in metal temperature below 1000 K, so this design would provide ample cooling within the center body. Machinability of such a feature was anticipated to be difficult, as many drill bits would break drilling 240x1.9 mm diameter holes in Inconel 718. The AFIT model shop wire EDM burner was also not suitable for this project, as the angle of the holes created a clearance issue in the machine. To proceed with manufacturing, holes would have to be relocated to fit in the available EDM machine.

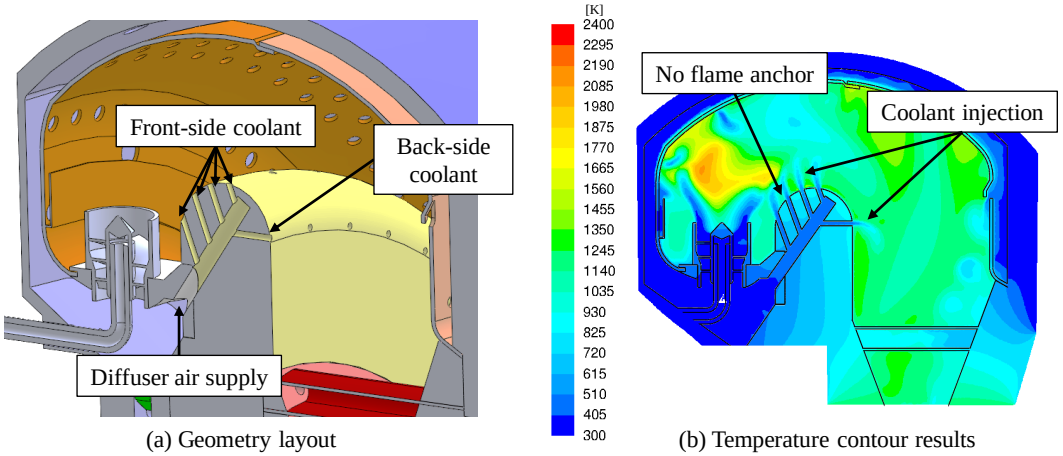

(a) Geometry layout (b) Temperature contour results

Figure 94. Center body cooling results for RT-10.

Since the angles of the coolant holes created a problem for manufacturing, the solution was to design holes without the angle. The 34 cm diameter center body would fit in the AFIT Model Shop hole burner, and perpendicular holes could therefore be burned out of the material. These surface-normal holes are shown in Figure 95a, where their diameters were chosen to roughly match the effective area of the five-hole design shown in Figure 94. The result was a four-hole design, with two 3.0 mm diameter holes

on the front side and two 1.5 mm holes on the back side, patterned 36 times about the center body. This provided one jet positioned at each swirler and two coolant injections between the swirlers. Figure 95b shows the impact this configuration had on flame recirculation near the surface of the center body. Although regions of high temperature were closer to the surface than in RT-10, the jet interaction between the coolant and swirler created enough separation to prevent reactions from anchoring to the surface. Based on these results, this coolant scheme was used for the physical model to ensure survivability of the center body.

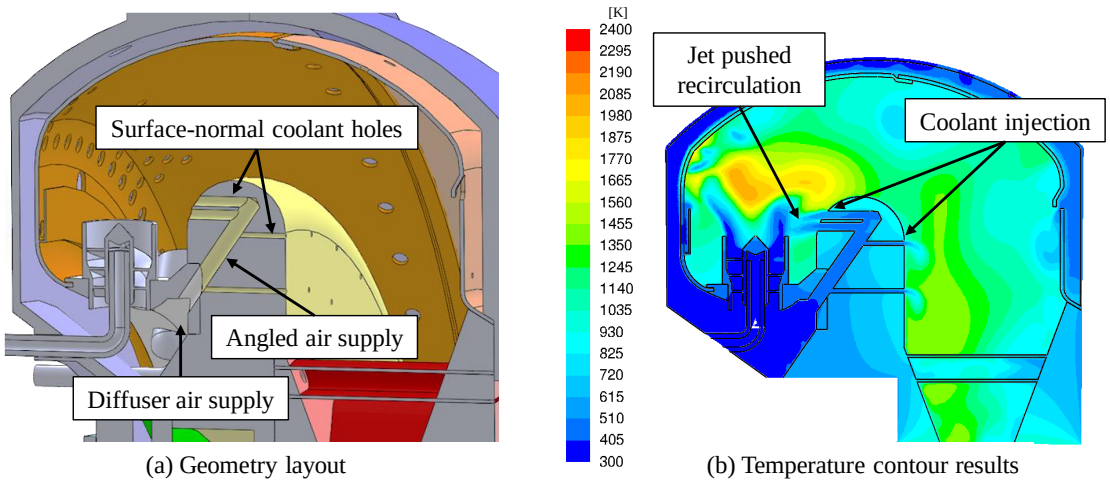

(a) Geometry layout (b) Temperature contour results

Figure 95. Center body cooling results for RT-12.

Figure 96 shows the center body geometry (Part 8) in its machining process. In this photo, the profile of the part had already been machined in a five-axis computer numerical control (CNC) machine in the AFIT Model Shop. Stator dilution and center body coolant supply holes were also drilled using the CNC machine, but the 144 coolant jet holes were burned using 3.0 and 2.0 mm EDM probes. Figure 96 shows the center body on a machine, prior to the EDM process. Once these holes were burned, the center body piece was complete and ready to join the assembly.

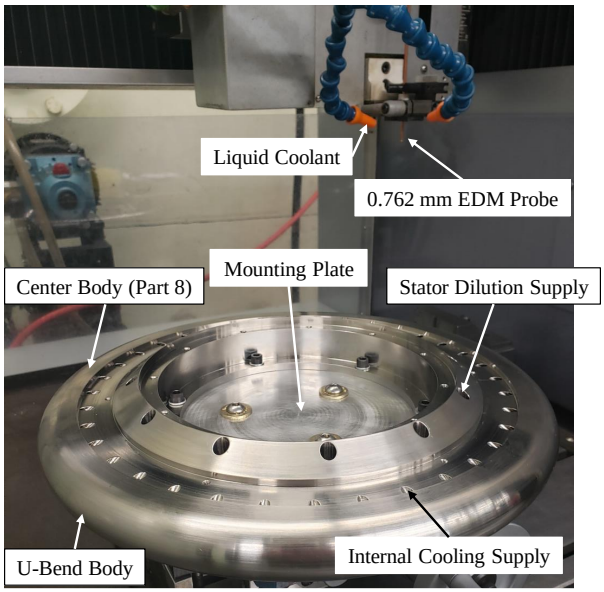

Figure 96. Center body machining, where coolant jets were being burned on the AFIT Model Shop's EDM machine.

4.2.4 Stator Vane Shaping Process

The stators designed for the Disk-Oriented Engine were another feature unique to this design. Although a particular radial in-flow turbine had yet to be designed for this project, stators were incorporated as they would utilize compressor air for cooling and dilution and would therefore impact the air mass flow distribution throughout the combustor. The Version 1 vane profile is shown in Figure 97, and this shape was formed to meet incoming flow with little incidence, maintain a slight camber, and exhaust at a 31° exit angle for the turbine. The airfoil setting angle (γ_3), as defined in Section 2.3.2, was chosen to be 20° based on an example presented by the Augnier Turbine Design text [35] and the bounds previously assumed in Section 2.3.2. Since a turbine rotor had yet to be designed, this angle, as well as the assumed 16.1 cm turbine rotor diameter, would likely be changed in future iterations. Figure 98 showcases the zero-incidence this profile saw in combustor Versions 1 and 2, but a difference in combustion cavity bulk swirl in Version 3 produced a different velocity profile in the turbine stator section.

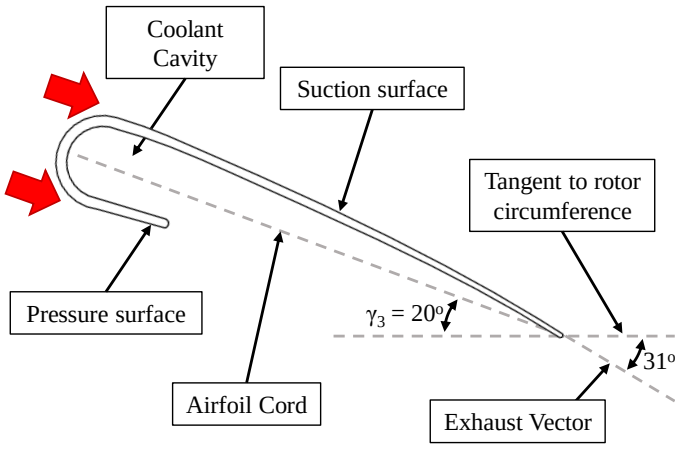

Figure 97. Version 1 turbine stator profile.

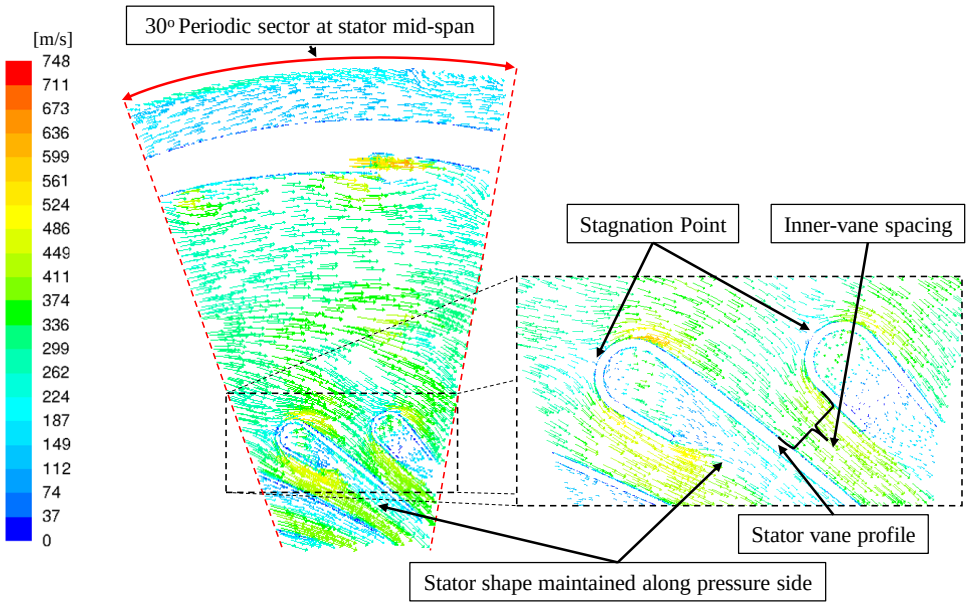

Figure 98. Velocity vectors of Version 2-2 on the stator mid-span, showcasing the Versions 1 and 2 stator profile.

Version 3-2, shown in Figure 99, experienced separation over the suction surface of the stator vane, effectively blocking the passage at the mid-span. To combat this, the vanes were re-designed with less incidence angle to this bulk circumferential swirl, and the new stator profile is shown in Figure 100a. To maintain the 59° exit angle, camber was added to the vane, increasing the suction surface length 32%, thus

constricting the inner-vane passage distance to zero area. This required a reduction in the number of stators within the combustor in order to maintain adequate spacing between individual stator vanes, where spacing is defined in Figure 98. A reduction of blade count from twenty-four to twelve created an inner-vane spacing of 1.5 cm, only 6% smaller than the Version 1 and 2 stator passage. All remaining Version 3 and Rig-Ready Test designs contained twelve stators, as opposed to the twenty-four stator design used in Versions 1 and 2. The use of twelve vanes maintained the 30° periodic sector used for computational analysis.

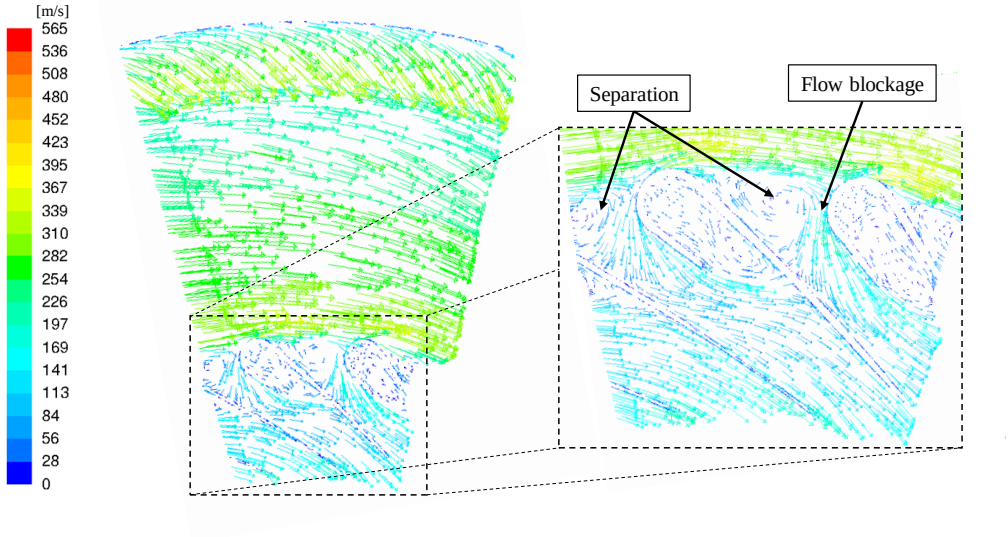

Figure 99. Velocity vectors of Version 3-2 on the stator mid-span, showing separation in Version 3 flow patterns.

The stator profile shown in Figure 100a was the final design implemented into the Disk-Oriented Engine Combustor. Figure 101 shows the twelve individual vanes (Part 17), as well as their front (Part 9) and back (Part 10) mounting plates. The stators and their negatives were cut using an EDM machine, as described in Sections 3.5.1. Once the stators and brackets were machined, they were laser welded together in the orientation previously shown in Figure 52. After welding, this sub-assembly was ready to join the Disk-Oriented Engine assembly, preparing the combustion exhaust

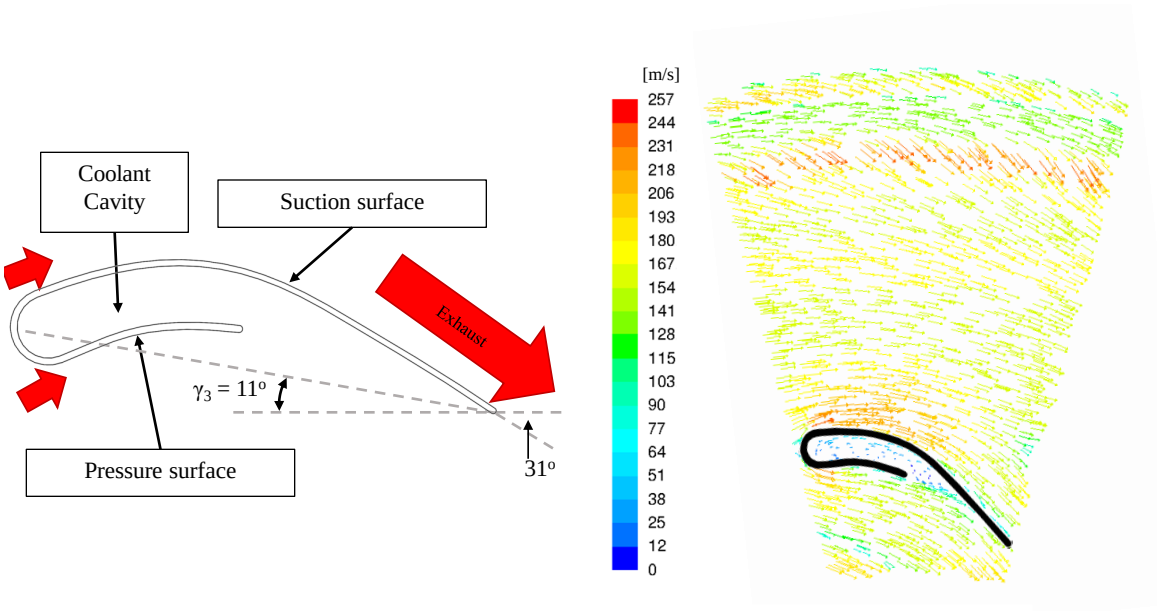

(a) Stator profile

(b) Velocity vectors at mid span

Figure 100. Version 3 adapted turbine stator profile.

gases for the turbine rotor interface.

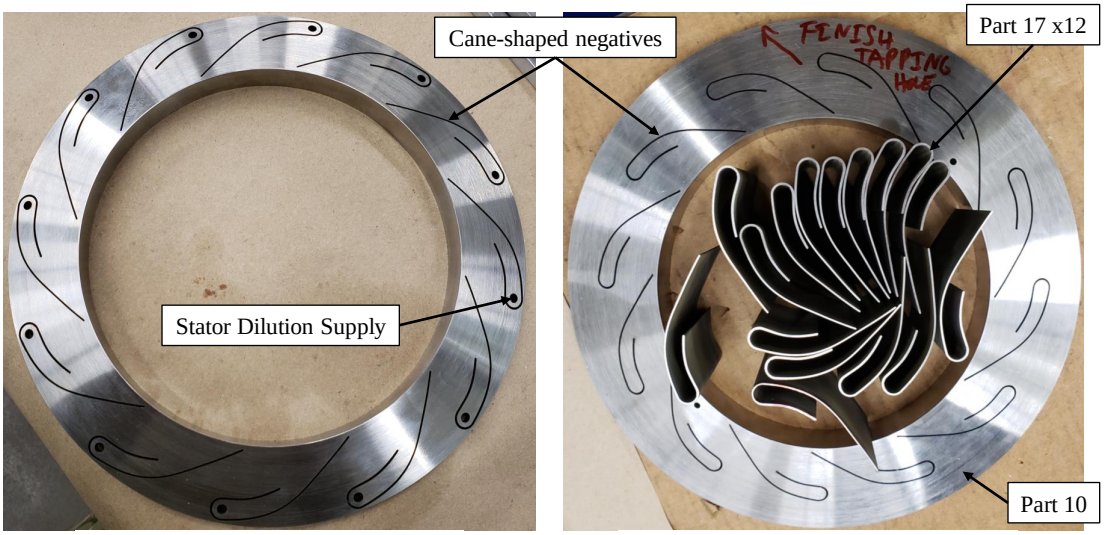

(a) Stator front mounting plate (Part 9)

(b) Stator rear mounting plate (Part 10) and 12xStators (Part 17)

Figure 101. Stator hardware, ready for welding prior to assembly. Parts were welded in accordance with Figure 52.

4.2.5 Combustor Exit Profile

In the design of the secondary air introduction and center body cooling methods, outlined in Sections 4.2.2 and 4.2.3, respectively, turbine rotor inlet profiles were scrutinized to emulate the desired profile presented in Section 2.3.2. Dilution air was introduced, as shown in Figure 102, to help cool the inner and outer walls of the U-bend combustion path as it returned the flow radially-inward for power extraction. Implementation of such a system was expected to push the hottest products to the mid-span of the turbine, cooling the hub and tip to maintain structural integrity. Air supply to each of these hole locations was once again a pressure balance throughout the entire combustor, where distribution of total pressure throughout the diffuser and bypass duct controlled the mass flow rate of air through all of the liner and center body holes.

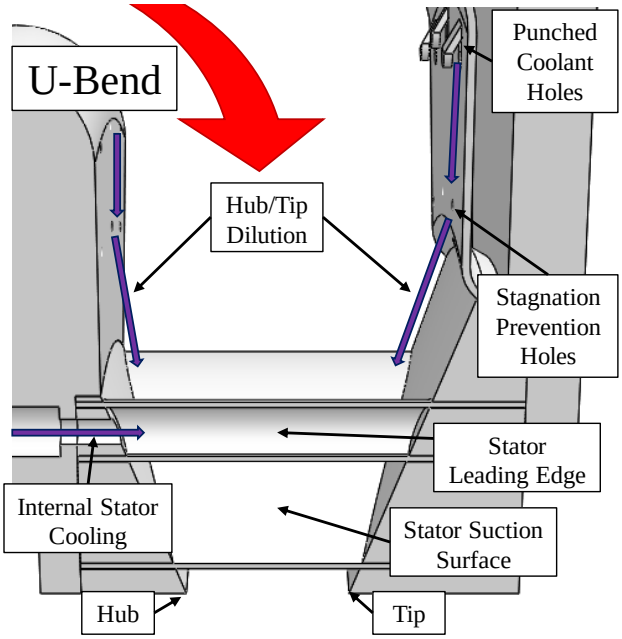

Figure 102. Illustration of dilution air introduction prior to the turbine stators.

Since changes in the PZ and SZ air supply would change the distribution of air through dilution holes, the dilution zone was developed in tandem with the liner hole

placement to impact the exit profile. For this reason, the changes in geometry for Versions RT-10 through RT-14 (no plate) are not presented in this section, as they were introduced in Sections 4.2.2 and 4.2.3. Figure 103 shows the impact each of these designs had on the combustor exit profile. The data is presented as circumferentially-averaged temperature profiles from the turbine hub (Axial Location 0) to tip (Axial Location 1.0); these lines allow direct comparisons to be made between iterations. Marked on Figure 103 with squares, RT-12, which was the end result of the center body design study, showed the worst temperature profile of those plotted. The RT-12 design introduced the most air along the back side of the center body, allowing for oxidation of carbon-monoxide to occur within the stator, creating a peak in exit temperature at the 20% span location. Analysis of this trend showed that additional air would need to be introduced by the SZ liner holes to make the center body cooling scheme viable.

Aside from RT-12, many of these contours (RT-10, RT-11, RT-13, and RT-14) follow a similar pattern: a nearly linear decrease from turbine hub to tip with a change in temperature (ΔT) less than 200 K across the turbine blade span. While this change in temperature across the span was acceptable, a peak closer to the 60% span was desired with as little ΔT as possible at the hub and tip. By removing the front-liner cooling plate from RT-14, the air distribution changed in such a way as to push the hot products to the mid-span and cool the hub and tip, as shown in red on Figure 103. The RT-14 (no plate) configuration achieved an average turbine inlet total temperature (T_{t4avg}) of 1182 K that was 9% lower than the cycle requirement of 1300 K at the 100% thrust settings. To better understand this deviation from the cycle required temperature, Section 4.3 compares the design engine cycle ($\Phi = 0.31$) performance to the performance of the Disk-Oriented Engine Combustor at various conditions across the operating envelope.

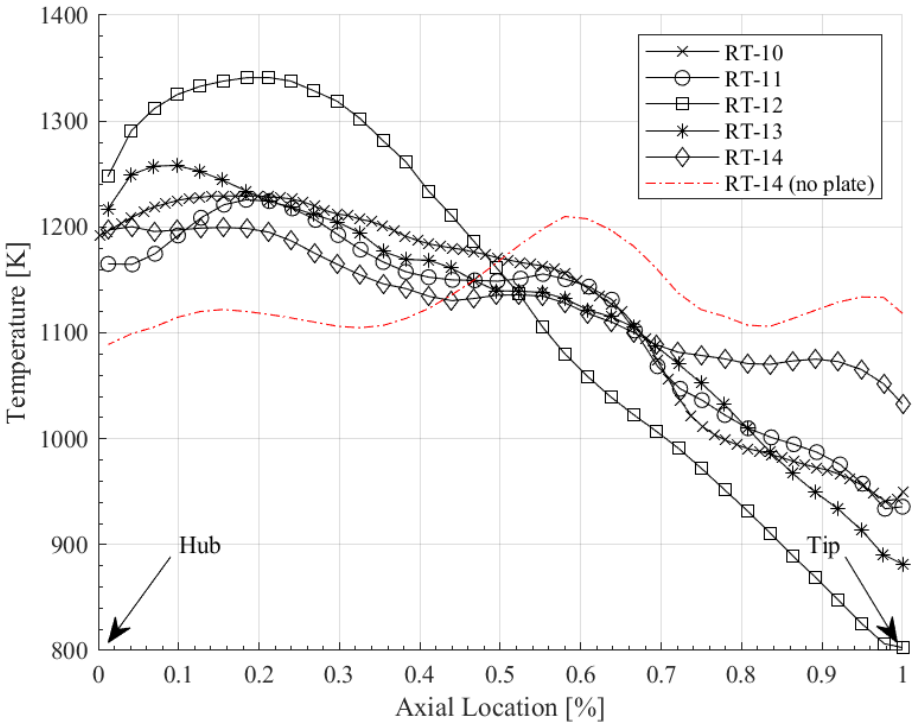

Figure 103. Comparison of circumferentially-averaged temperature profiles on the combustor exit for six RT geometries.

4.3 Final Geometry Computational Results

With a final design geometry selected, it was important to understand the impact of off-design operation. The computational model of the final Disk-Oriented Engine was analyzed on- and off-design, displaying sustained combustion at 100%, 80%, and idle (30%) thrust conditions. Properties at these three conditions were determined by cycle analysis (Section 3.4), and the results were compared to a fourth condition selected outside of the cycle, with $\phi = 0.31$, CPR = 4.0. This additional condition is referred to as the design case, as it was used for the analysis of all geometries previously discussed. This design case was selected to isolate the effects of equivalence ratio at elevated pressures for discussion, and it differed from the 100% thrust condition with a Φ reduction from 0.36 to 0.31. Specific results for each of these conditions are

displayed in Table 9, and those values are discussed in depth throughout this section. To characterize the combustion process, flow paths and pressure distributions are presented, while flame stabilization, reaction positioning, and temperature profiles are discussed in depth to show sustainability of such a novel combustion approach.

Table 9. Final design result comparison for varying design conditions.

	Cycle Targets			CFD Results			
	100%	**80 %**	**30 %**	**Design**	**100 %**	**80 %**	**30 %**
Φ_{global}	0.36	0.31	0.25	0.31	0.36	0.31	0.25
Pattern Factor (PF)	(-)	(-)	(-)	0.24	0.27	0.23	0.29
$\mathbf{PF}_{avg}$	(-)	(-)	(-)	0.22	0.24	0.15	0.14
$\mathbf{T}_{t4}$ **[K]**	1300	1195	981	1182	1298	1183	980
$\Delta\mathbf{P}_{diffuser}$ [%]	(-)	(-)	(-)	8.85	8.82	12.20	15.34
$\Delta\mathbf{P}_{combustor}$ [%]	5% assumed loss			3.46	3.48	3.95	4.21
Swirl Number (S)	(-)	(-)	(-)	0.79	0.79	0.77	0.40

In Figure 104 total pressure peaked on the stagnation zone of the forward dome, and the swirl injectors were located at this point to ensure the PZ was supplied with enough mass flow of air to sustain combustion. The velocity vectors in Figure 105 show how air moved following the dump diffuser. In the bypass duct, an attempt was made to maintain pressure about the outside of the liner, providing all secondary and dilution holes with similar jet introduction velocities. While there was some total pressure drop across the air supply holes about the cavity, none were as expensive as the pressure loss within the dump diffuser. It was anticipated that this pressure loss was caused by the intense velocity shear layer between the separated flow out of the dump diffuser and the slower-moving flow near the diffuser walls. Area-averaged surface comparisons of total pressure at the inlet and exit of the diffuser showed a 8.85% loss of inlet total pressure (ΔP) by the forward dome, but the remainder of

the combustor only experienced a 3.46% loss between the forward combustion dome and the domain exit of the stator section. Pressure loss values for other operating conditions are presented in Table 9, showing how performance degraded at the non-design condition, but combustor pressure loss remained below 4%.

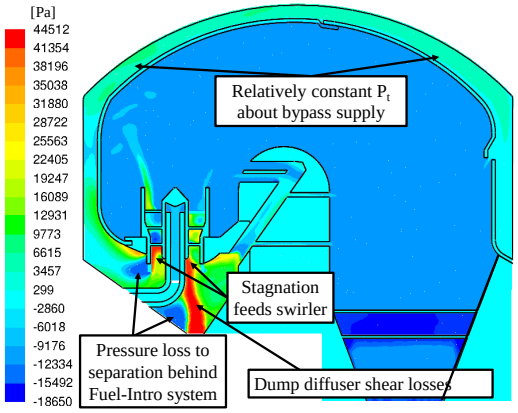

Figure 104. Gauge total pressure (from 405 kPa) on radial-axial plane ($\phi = 0.31$).

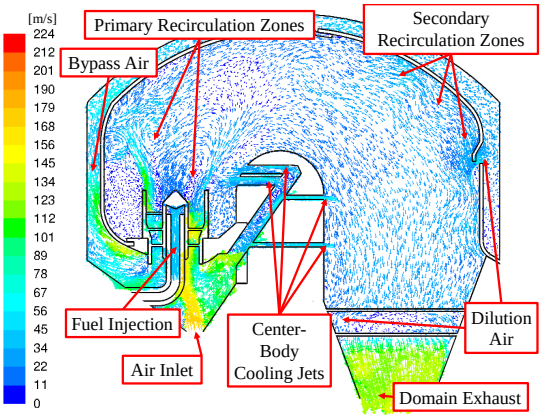

Figure 105. Velocity vectors on radial-axial plane at the design condition ($\phi = 0.31$).

To better understand how the pressure distributions of Figure 104 impacted combustion characteristics, Figure 105 highlights the key features apparent in a velocity vector field of the combustion cavity. Air entered the dump diffuser with velocities greater than 170 m/s and impacted the forward dome of the combustion cavity. From this stagnation point, air supply followed one of three paths: through the air-fuel swirl injectors at the stagnation point and into the primary zone, left into the bypass duct to feed the secondary and dilution jets, or right into the center-body cooling jets and stator internal cooling. While the swirler created the most recirculation zones for mixing and flame holding, air supplied to the bypass duct maintained bulk circumferential swirl (out of the page in Figure 105), and this swirling flow created secondary recirculation zones in the U-bend chamber where reactions could occur. Jet induced shear layers and recirculations in the SZ worked harmoniously with the bulk circumferential swirl to increase mixing and residence time in the U-bend combustion cavity.

Jet injections, as seen in Figures 106 and 107, are shown as an iso-surface of constant total pressure at 399 kPa, issuing into the combustion cavity. The contours on the surface show the reaction progress variable, indicative of the completeness of the partially-premixed combustion process at that position, where progress variable increases from 0.0 where only air or propane is present to 1.0 when completely reacted to form CO_2 and H_2O. Gradients in this contour indicated the presence of a reaction front, and the largest of these gradients were found on the strong recirculation zones surrounding the air-fuel swirler. To better show the impact of swirl on the PZ, Figure 107 shows the same iso-surface as Figure 106 from a different view point. Looking down on the primary combustion zone, it was apparent that the iso-surface issuing from the fuel-air swirler maintained high total pressure longer on the near side than the opposing side, indicating that the bulk swirl within the combustion cavity (out-of-the-page in Figure 106) had an impact on how the issuing jet maintained pressure and momentum. With higher total pressure on the swirl side, the jet had more energy to enhance mixing for an efficient burn. Reactions also occured on liner coolant jets in the SZ, forcing remaining products to react outside of the PZ. It is important to note that these iso-surfaces in Figures 106 and 107 are not all-inclusive of the reaction fronts within the circumferential combustor. Since these reactions are not directly tied to a certain total pressure, the iso-surfaces serve best as indications of jet penetration.

Contours of temperature about the annulus in Figure 108 show how each flame-holding swirler would interact with the adjacent swirler for all twelve periodic sectors. While the jet spread angle was not wide enough for swirlers to intersect directly, bulk swirl introduced by the SZ jets imparted circumferential force on the flame to allow interaction with its clockwise neighbor. Swirl-jet interaction ensured stable flame holding about the annulus, as surrounding anchored flames can ignite nearby fuel-

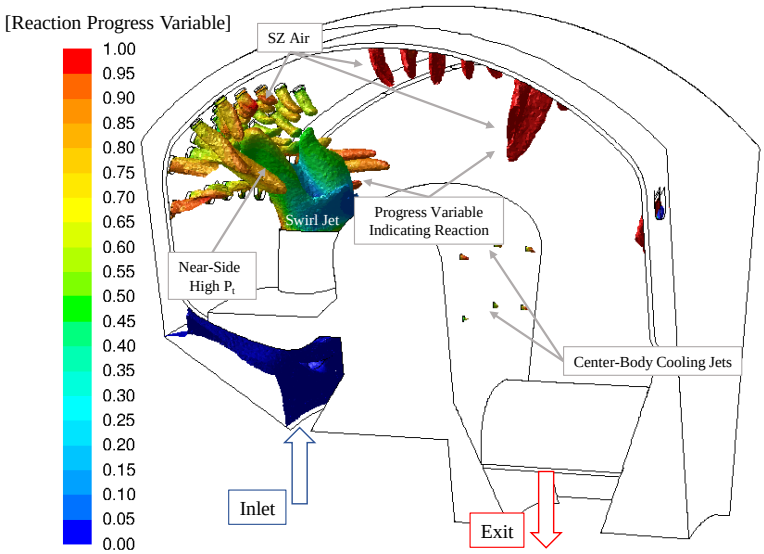

Figure 106. An iso-surface of total pressure (399 kPa) shows jet penetration into the combustion cavity and is colored by reaction progress variable to illustrate reaction completeness.

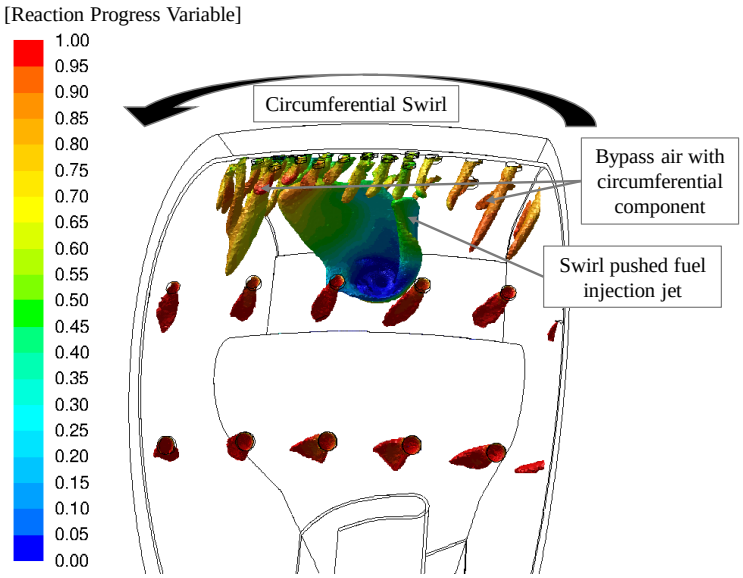

Figure 107. An iso-surface of total pressure (399 kPa), colored by reaction progress variable, shows impact of swirl on mixing jets within the PZ. View is oriented to look down on the 30° periodic sector of the combustor.

air injectors that may flame out. Each 90° sector in Figure 108 represents a different operating conditions and how swirler interaction changes at these conditions. Note the similarity in flame structure between all cases, suggesting similar PZ burns occured

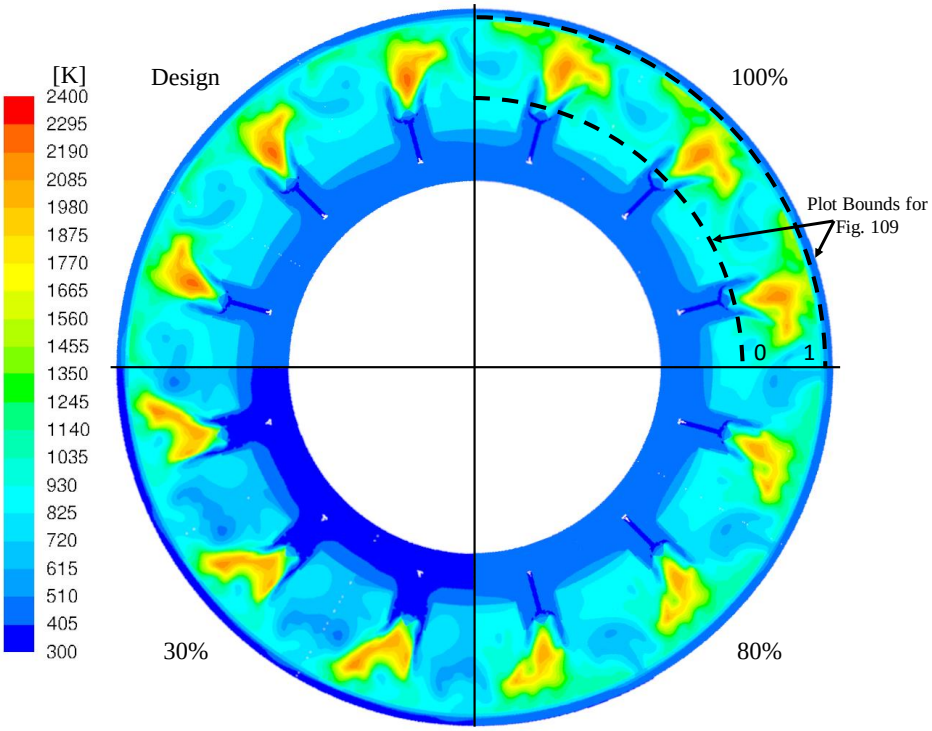

Figure 108. Temperature contours about the annulus, cutting the center of the swirl injectors. Each of the four conditions tested are represented by a 90° sector of the annulus containing three repeated swirlers.

across the operating envelope. Swirl in Figure 108 also enforces the idea that the PZ flame anchor preferred the near side of the jet, as previously noted in Figure 106.

Captured at 250 radial locations on the same plane as Figure 108, Figure 109 shows circumferentially-averaged centrifugal acceleration (F_c) and temperature across the radius (r) of the PZ, from the swirler exit to the top of the PZ liner. The vertical axis is normalized distance, representing the 4.9 cm PZ radius as a percentage from zero to one. Centrifugal acceleration is defined by Equation 7, and it was normalized by Earth's gravitational acceleration (g_e).

Circumferential acceleration is plotted for comparison with previous UCC studies which focused on loading normalized by g_e, and temperature is plotted to show the increase in heat release as a result of increased mixing and burning on shear layers. Starting at the top of the swirler, both the acceleration and temperature increased

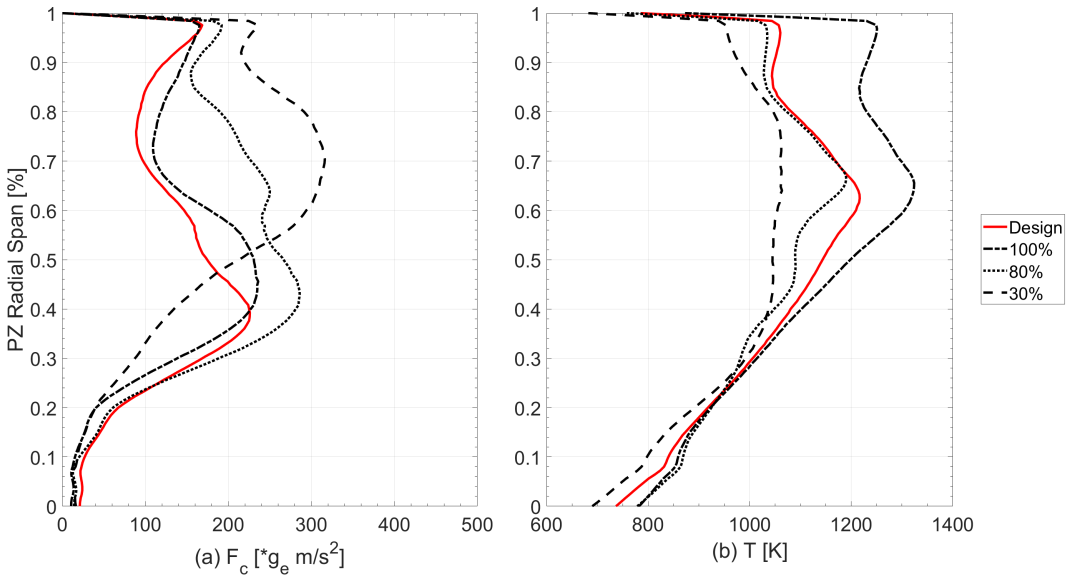

Figure 109. Plots of circumferentially-averaged tangential acceleration and temperature at four engine conditions, averaged on 250 radial arcs from the swirler exit to the PZ upper liner.

to a maximum value before decreasing as they approached the liner surface at 1.0. At the three highest operating conditions (Design, 100% thrust, and 80% thrust) the acceleration and temperature plots are nearly identical, where peak loading occurred around $r = 0.4$ due to the swirl injector, and temperature peaked at ($0.6 < r < 0.7$) after the reaction anchored above the swirler began to release heat. Note that circumferential acceleration was non-zero throughout the PZ, indicating that there was a bulk-swirl presence throughout the entire radius of the PZ.

Acceleration and temperature in the PZ of the 30% case were different, with peak F_c and T located in the same region ($0.6 < r < 0.8$). Table 9 shows that swirl number decreased 49% between the 100% and 30% thrust cases. This reduction in swirl of the injector reduced the circumferential velocity exiting the swirler, thus reducing the acceleration at $r = 0.4$. The 30% thrust line in Figure 109b does not peak in the same fashion seen in other cases, indicating that the heat release throughout the PZ was a longer process. This lengthened heat release zone is also seen in the 30% contours

of Figure 108, where the temperature released in the PZ was not as tightly anchored to the swirler as in other cases. This suggests that bulk swirl had a bigger impact on combustion performance nearing the idle condition, as the fuel-air swirler became less dominant.

DeMarco *et al.* [6] suggested the impact of bulk-swirl combustion was benefited more by an increase in residence time than circumferential load, and the peak UCC temperatures resided at centrifugal accelerations between 18-125*g_e m/s^2. While the specific circumferential accelerations that applied to previous UCC studies may not be applicable to a geometry with different cross-sectional areas and flame holding features, the concept of increased residence time by circumferential swirl did apply to the Disk-Oriented Engine. Residence time of a fluid particle from the swirler exit to turbine rotor inlet in the Disk-Oriented Engine Combustor was estimated to be 10 milliseconds. This estimation was based on an average residence time calculated from 32 path lines (shown in Figure 110) that emanated from the swirler exit. Along these lines, total residence time (T_{res}) was simply the integral shown in Equation 20,

$$T_{res} = \int \frac{1}{|V|} dx, \tag{20}$$

where the inverse of velocity was integrated along the path lines for finite distances (dx). This 10 ms residence time at the design condition indicated that the bulk swirl increased the residence time 67% from an equivalent non-swirled path. The equivalent, non-swirling residence time was calculated on a path through the combustor that traversed the U-bend at a single circumferential angle, assuming similar velocities to the swirling case. This residence time increase due to swirl caused particles to travel between 60° and 120° (two-four stator vane passages) circumferentially before exiting, helping to validate the compact combustion advantages assumed by DeMarco *et al.* [6], where swirl increased the distance traveled by a single particle.

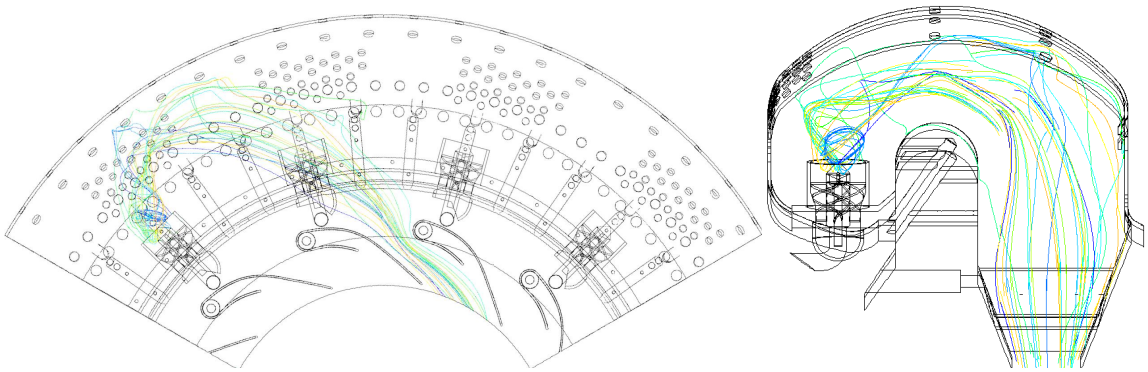

(a) Radial-circumferential view across 4x 30º sectors (b) Radial-axial view, single sector

Figure 110. Pathlines, colored to distinguish individual lines, showing fluid paths through the combustion chamber for 100% thrust.

To compare combustion performance about the U-bend path for all engine conditions, Figure 111 shows temperature contours on the radial-axial plane through the center of the swirl injectors. Evident in these figures is the similarity in flame holding. All conditions in Figure 111 display nearly identical flame anchor shapes with similar temperatures being released in the PZ. As expected, Table 9 indicates that the exit temperatures vary between the engine settings, and Figure 111 displays the impact SZ reactions has on additional heat release leading to varying temperatures at the combustor exit (T_{t4}). The 100% thrust case displayed the highest exit temperature (T_{t4} = 1298 K), and Figure 111b displays the highest SZ temperatures of all conditions. The design (Φ = 0.31) and 80% thrust cases reached a nearly identical T_{t4} with similar SZ temperature profiles in Figures 111a and c, and this was a result of identical global equivalence ratios at these conditions. The 30% thrust case produced the lowest T_{t4}, with Figure 111d displaying the lowest SZ temperature of all cases analyzed. Based on temperature distributions staying relatively consistent across the entire operating envelope, as evident in Figures 108 and 111, the final computational model, RT-14 (no plate), was declared sufficient to sustain stable combustion for real-world tests.

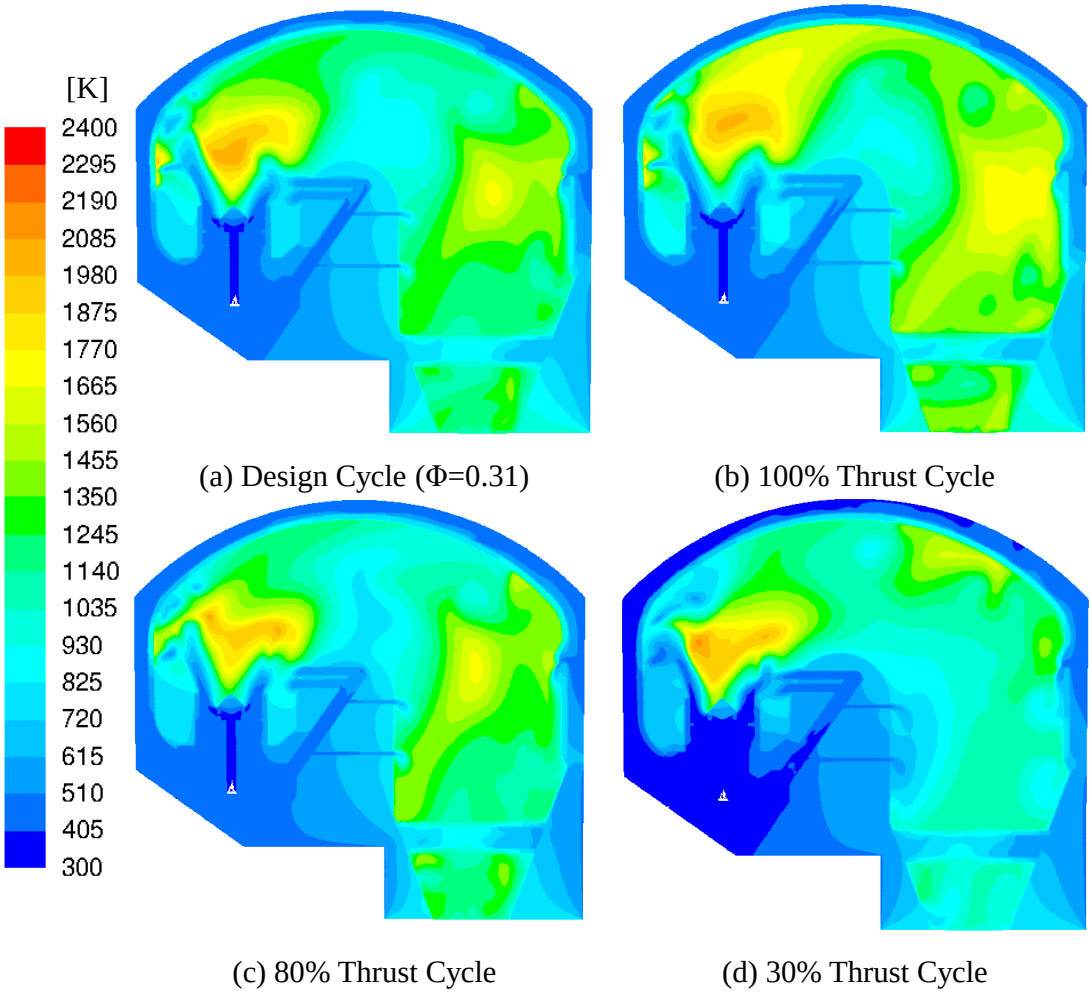

Figure 111. Temperature contours on the solid surface of the RT-14 (no plate) geometry.

With a realized increase in combustion residence time due to bulk circumferential swirl, the success of the temperature dilution scheme was evaluated for progression into the experimental phase of analysis. Temperature profiles on the exit to the turbine were important, knowing that the turbine would not survive unsteady, non-uniform temperatures. Dilution air supplied to either side of the turbine stator span, as shown in Figure 102, attempted to force a peak temperature band at the center span of the turbine rotor, with cooler flow hitting the hub and tip regions. Cooling the combustor exit in this way was expected to negate the hot gas migration issues

seen in previous AFIT UCC applications [6, 18, 22] where hot gases remained at the OD without mixing with the cooler flow that bypassed the combustion process. In application, Figure 112 shows how the cooling scheme of the Disk-Oriented Engine was less effective along the center body side of the exit plane. It is apparent in the contours of Figure 112a that the reactions on the back side of the center-body in Figure 111a, b, and c stayed attached through the stators and elevated the exit temperatures along the hub of the rotor. Ideally, the contours would mirror about the center (axial location of 0.5) with the hottest fluids at the mid span. Figure 112b presents this same temperature information as circumferentially-averaged temperatures, taken across the 2.54 cm axial span of the turbine rotor face and normalized from zero to one. This temperature data further highlights the peak temperatures riding the hub and tip of the turbine inlet, but there was only a maximum 250 K change in temperatures between the hub (position 0.0) to the tip (position 1.0) of the turbine rotor inlet.

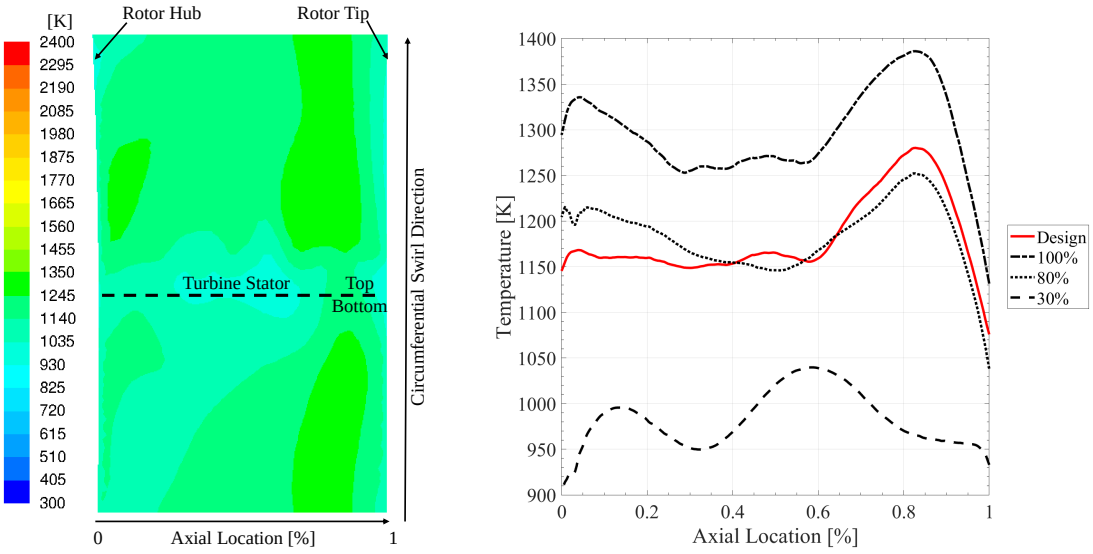

(a) Temperature Contours ($\Phi = 0.31$) (b) Circumferentially-Averaged Temperature

Figure 112. Temperature profiles on the exit plane for all conditions analyzed.

Pattern factor for the Disk-Oriented Engine, as defined by Equation 9, was determined to be 0.24 at the design condition. This marker of uniformity across the

exit plane was within the 0.2-0.45 range for traditional combustors suggested by Mattingly *et al.* [24]. Computational analysis extracts the maximum at any given cell, which is a much smaller measurement location than a temperature probe could take in a real engine. To compare this computational PF to one that would be taken experimentally, pattern factor was also calculated on a local-average basis, where the exit plane was divided into 49 bins to be averaged as pseudo-nodes, similar to the artificial area-averaged temperature measurements taken with a probe. The maximum exit temperature was then evaluated from these pseudo-nodes, resulting in an average pattern factor of 0.22, which is well within the desired range for traditional combustors. Real-world tests are necessary to corroborate these results prior to tests with rotating hardware. Pattern factor was also calculated for other operating conditions, presented in Table 9 between 0.24 and 0.29 across the operating envelope. All of these values are below the recommended maximum of 0.45, which indicates that the exit profile for the combustor should be turbine suitable for the entire flight envelope, from idle to max power. The variation in PF was likely caused by reallocation of air at different thrust conditions, where additional air entering the PZ increased combustion efficiency and therefore increased the maximum temperature at the exit. Additional air to the dilution holes would also impact this value, as they could drive down the average temperature at the exit, impacting PF as well.

4.4 Full-Scale Model Assembly

Many of the design decisions discussed in Section 4.2 led to the final design that performed as discussed in Section 4.3, but all of these results were based on computational analysis. Since one focus of the present research was to design and fabricate a testable combustor for a Disk-Oriented Engine, this section presents the hardware fabricated to house the key features already presented in Section 4.2. All parts are

referenced by their identification number in accordance with the assembly in Figure 51 (shown again in each of the following images).

The first pieces completed were the inlet and exit housings, including the turbine and compressor plugs shown in Figure 113. Since all of these parts were machined in stainless steel or aluminum, they were turned on a lathe in the AFIT Model Shop, significantly reducing their fabrication time compared parts that were machined on a five-axis mill. The plugs shown will eventually be replaced by a compressor and turbine to test the Disk-Oriented Engine with rotating hardware.

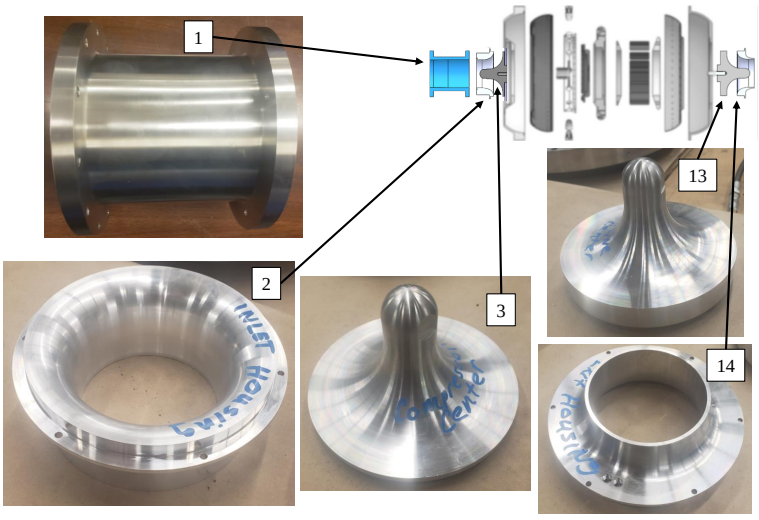

Figure 113. Inlet and exit hardware.

The inlet and exit housings mounted directly to the outer shell, shown in Figure 114. The rear shell (Part 12) is shown completed with the rear combustion liner (Part 11) and the turbine stator mount (Part 10) attached at their prescribed junction. The front shell (Part 4) is seen both mounted to the five-axis mill and finished with instrumentation ports. With diameters over 50 cm, these parts were too large for the AFIT Model Shop lathe, so they were produced entirely in the five-axis CNC mill. These parts were fabricated in stainless steel for the additional strength necessary to mount the combustor in this configuration. Initial estimates suggested that this entire assembly would weigh over 700 N, but reduction to a flight weight design could

exchange this shell for an aluminum one, assuming it is not exposed to excessive heat at its junction with the turbine stator in testing.

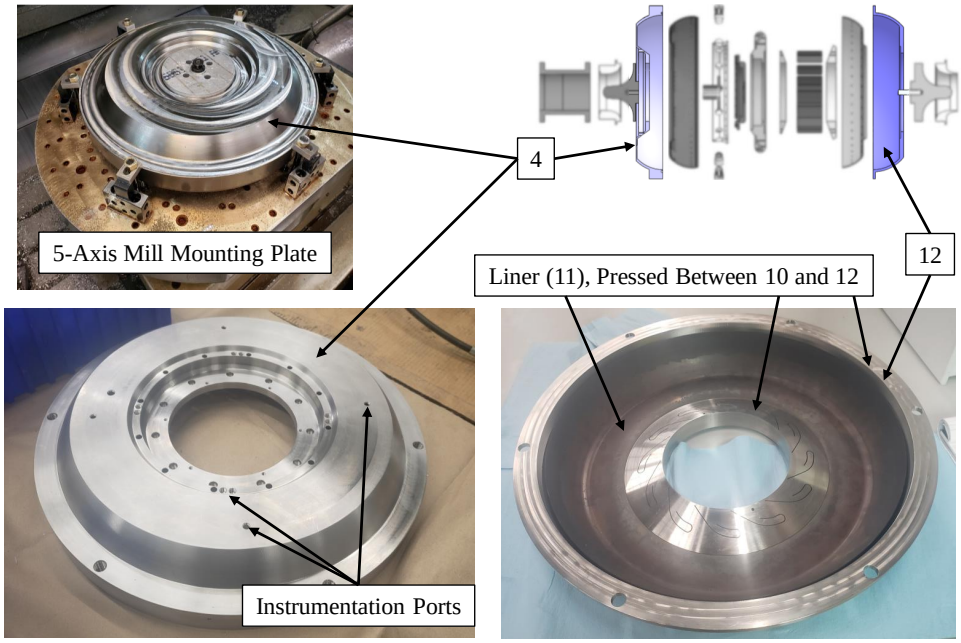

Figure 114. Outer clamshell housing.

Possibly the most complicated part of this assembly was the combustion liner. It is shown in Figure 115. Both the front (Part 5) and back (Part 11) liners had to be trimmed at their junctions with the rest of the assembly, as a scan of the heat-treated liners showed machining error at these fixture points. To accomplish this trimming, the liner sheets were fixed to the nests in which they were spun for stability purposes. These nests were retrieved from Lewark Metal Spinning after the liners were delivered.

Machined in Inconel for their anticipated exposure to high temperatures, the fuel body and center body (Parts 6 and 8) required lathe turning at low rotational speeds. The largest CNC lathe at the AFIT Model Shop was underpowered at these speeds, and these large Inconel parts pushed the limits of on-site machine capabilities. These two parts are displayed independently in Figure 116, as well as assembled within the engine. The twelve swirlers (Part 15) had yet to be printed, awaiting additional

swirler tests as mentioned in Section 4.5. Note that the fuel body ring was threaded, allowing for modular testing of various swirler designs in future research.

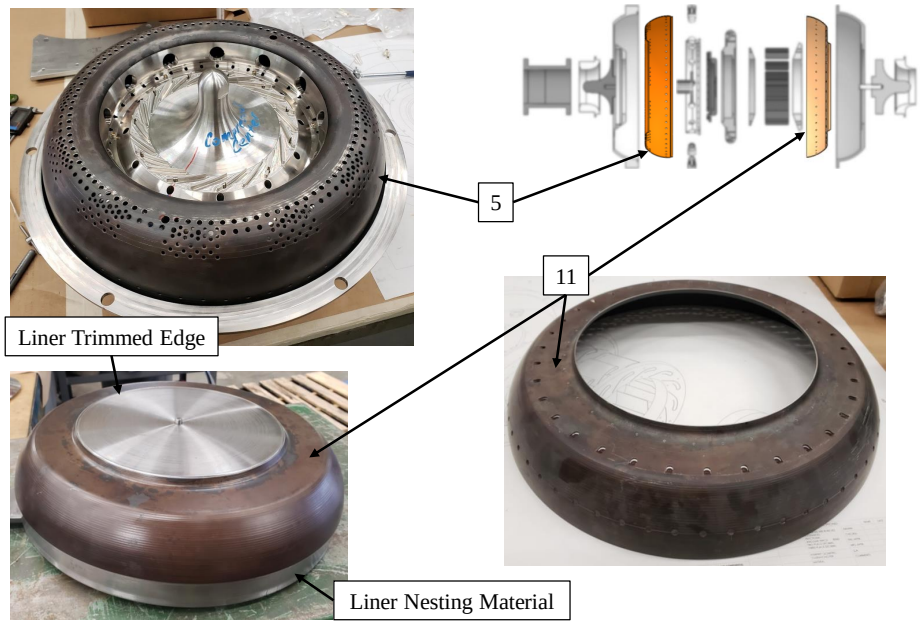

Figure 115. Combustion liner hardware.

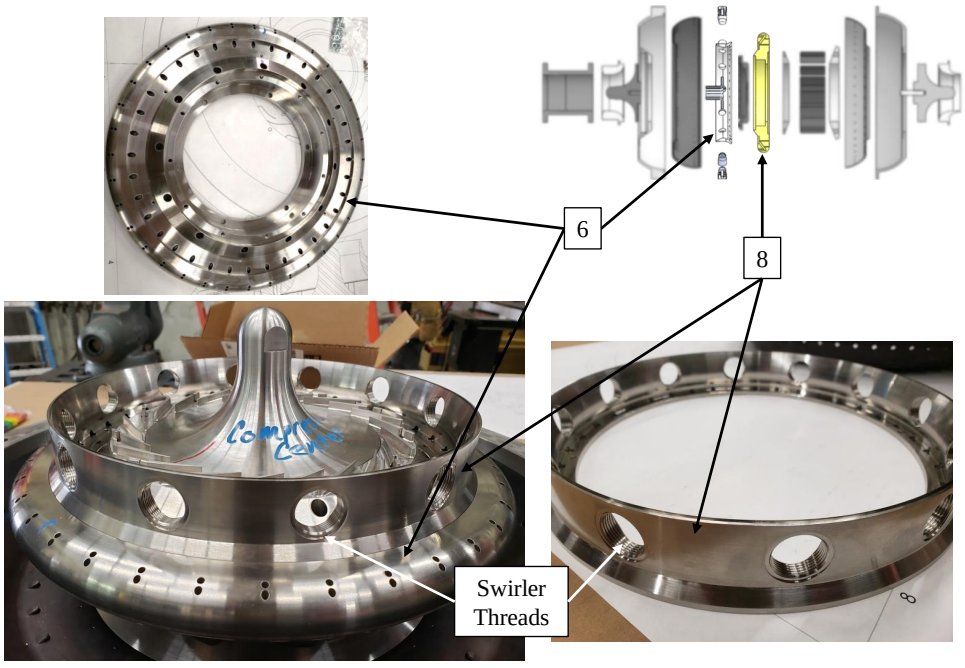

Figure 116. Center body and fuel injector hardware.

Integral to the Disk-Oriented Engine Combustor design was the incorporation of stators into the geometry. Figure 117 shows both the compressor and turbine stators. The mounting holes, which allowed bolts to pass through Part 7 to join Parts 4 and 8, were incorporated as a part of the stator. These holes were placed at the thickest point of the blade, hiding much of the bolt diameter from the passing flow. The compressor stator (Part 7) was machined in stainless steel, while the turbine stators (Part 17) and mounting plates (Parts 9 and 10) were fabricated in Inconel 718. Once again, the mounting plates pushed the limits of the lathe, requiring additional time to machine the slow-cutting Inconel. Each of these parts illustrates the time-intensive fabrication process that was required to build the proof-of-concept Disk-Oriented Engine combustor, but this process could be streamlined for mass production of a similar design.

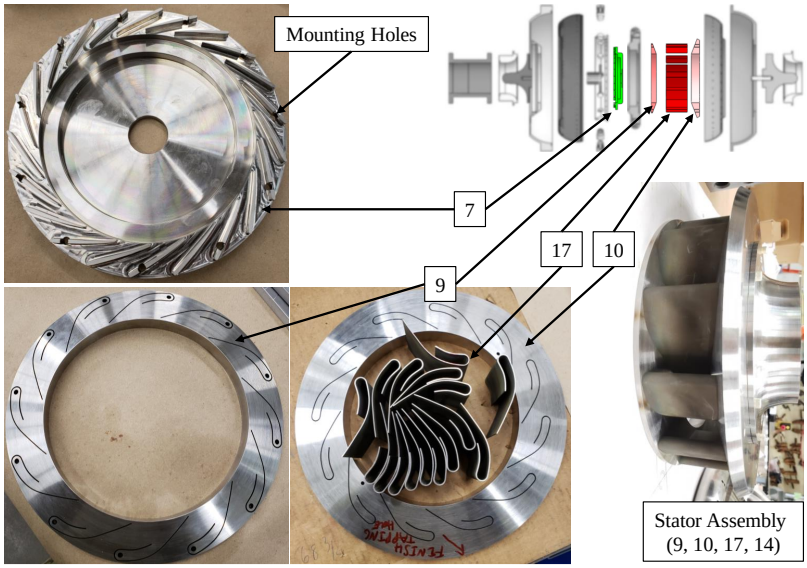

Figure 117. Compressor and turbine stator hardware.

For comparison to the CAD model, the finalized assembly of the Disk-Oriented Engine Combustor is shown in Figure 118. While this view only represents a few of the parts integral to this design, it does showcase the completeness of the build and readiness for experimental testing.

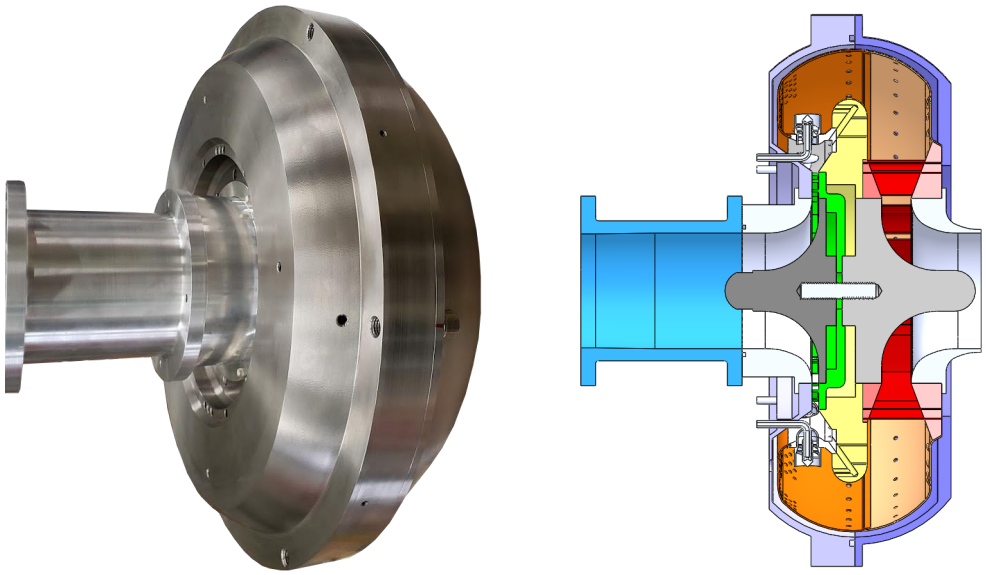

(a) Completed Assembly (b) CAD Assembly

Figure 118. Completed physical hardware, assembled for testing.

4.5 Swirler Experimental Results

With a final combustor and fuel-air injector designed in fulfillment of Objective 2 for the present research, it was important to fully understand the swirler operation prior to incorporating it into the engine. Although CFD predicted that the swirlers would maintain a stable flame at the design condition, as shown in Section 4.1, experimental testing on an individual swirler was necessary to understand how this design would operate across the operating envelope. Experimental testing on an individual swirler served two purposes: 1) the geometry was tested at various conditions to understand its limits with visual access that would be impossible to obtain once installed on an engine, and 2) the results obtained through testing on a single swirler were compared to CFD to better understand the error inherent in modeling these complex flow. The later purpose fulfilled Objective 3 of this research, quantifying the difference between experimental testing and CFD analysis to better understand how the combustor would perform in real-world testing.

4.5.1 Swirler Flame Holding

To understand the operability limits of the fuel-air swirl injector, an experimental test rig was built to visualize combustion on a single swirler, as outlined in Section 3.5.2. The swirler presented in Figure 78 was printed in Inconel 718 as a test bed for reacting flow observation. Based on CFD analysis, the mass flow rates targeted for these tests are shown in Table 10, where the single swirler matched the air and fuel mass flow rates seen computationally in a single swirler at the design, 80%, and 30% thrust conditions. A stable ignition point was found at an air mass flow rate of 0.0063 kg/s (28% of the design mass flow rate) and an air-propane equivalence ratio of 1.33. Since this equivalence ratio was between the 100% and 80% engine thrust conditions, the swirler was thought to operate in its most stable mode for $1.30 < \Phi < 1.35$.

Table 10. Swirler fuel and air mass flow rate settings for experimental analysis.

Thrust Settings	**Air [kg/s]**	**Fuel [kg/s]**	Φ_{PZ}
100%	0.023	0.0019	1.30
80%	0.021	0.0018	1.35
30%	0.014	0.0009	1.00

To test the equivalence ratio limits of the swirler design, fuel was varied at the ignition air setting (28% of design air) in an attempt to find the lean and rich blowout conditions. Figure 119 shows images of the flame structure for various Φ; it is important to note that the igniter is seen in these images, but it was rotated out of the flow path above the swirler. After ignition, the fuel flow was incrementally increased from 1.33 to 3.02, with Figures 119d, e, and f showing the resulting flame structure at three rich equivalence ratios. While the flame structures in Figures 119d and e were similar in shape to the light condition (Figure 119c), the height of the apparent flame structure grew from $\Phi = 1.33$ to $\Phi = 2.05$. As the amount of fuel introduced into the system increased, a longer distance was required for complete combustion.

Figure 119f shows the swirler in a state that would likely not be achieved in engine operation. At $\Phi = 3.02$, the primary combustion reaction is no longer attached to the high-shear region at the swirler exit where recirculation was expected to anchor, but it lifted to a secondary flame anchor point away from the swirler exit. Operation at $\Phi = 3.02$ was sustained in this fashion, but additional air provided by the exhaust system entrainment likely sustained the reaction.

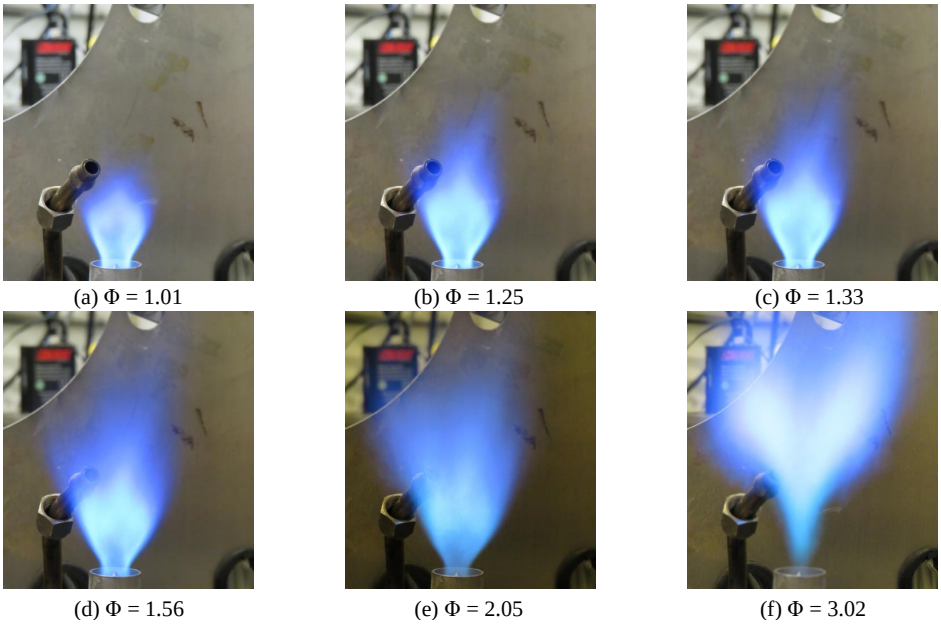

Figure 119. Visual comparison of the reaction zone above the swirler, varying Φ.

As the fuel setting was reduced to the lean side of the design condition, the length of the visible reaction also shrank. As the swirler Φ approached 1.0, the flame remained anchored in a smaller region, as shown in Figure 119a. The lean blowout test found flame extinction occurred below $\Phi = 0.93$, so the limits of flame stability at the light condition were $\Phi > 0.93$. Since rich blow out was not observed, a rich-end limit was not determined. Figure 120 shows high-speed imagery recorded over the last 24 ms prior to flame extinction. Blowout was determined to be the point at which no indication of flame radiation could be seen, and times listed in Figure 120 are in reference to the first frame without flame indication. Throughout this

progression, the intensity of the flame appears to decrease over the first three frames before growing in Figures 120e and f. After this initial instability, the flame relapses again over the last 12 ms leading up to extinction. While it was not unreasonable for the flame to blowout at an equivalence ratio of 0.85, the unsteady instability in Figure 120 shows where the flame anchor breaks up. In particular, the reaction front in Figure 120c shows how the reaction fronts in this initial instability are anchored to the swirling shear, rather than the swirl induced recirculation zones predicted by CFD. If the flame did not anchor to the recirculation zone at this ignition air flow rate, it would likely have issues maintaining stable combustion on the swirling shear as swirl velocities increased.

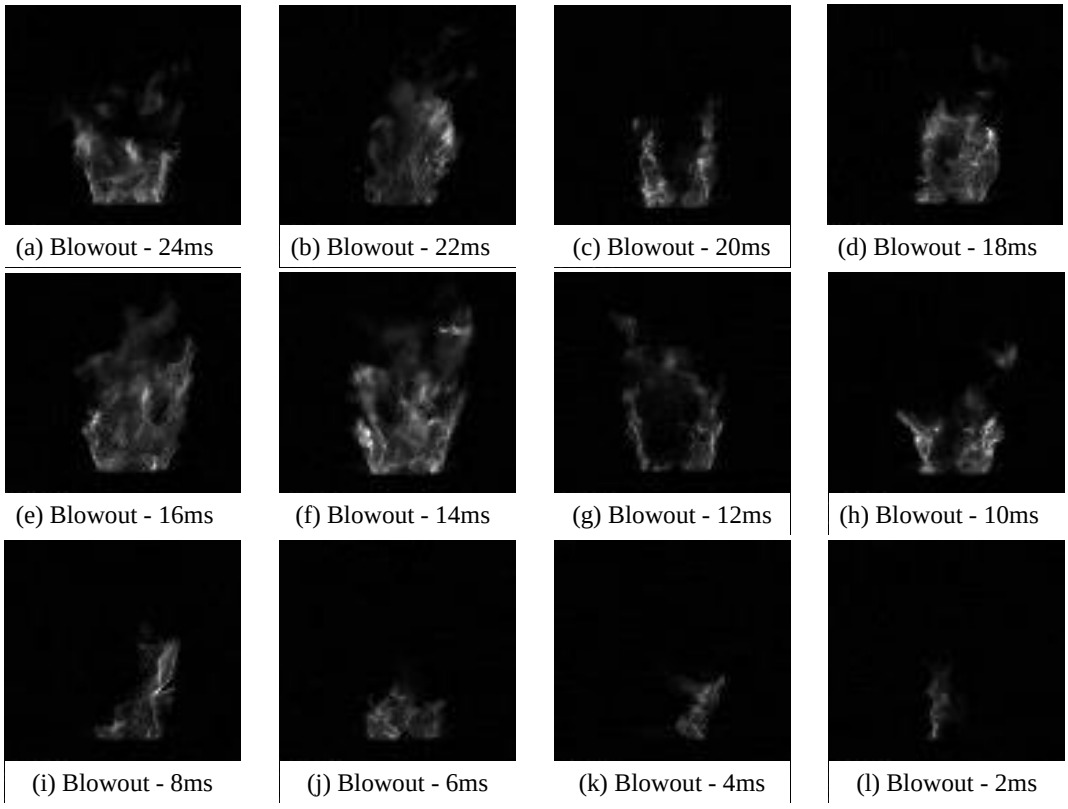

Figure 120. Lean blowout montage at swirler $\Phi = 0.85$.

To better understand the impact increasing the system mass flow had on swirler performance, Figure 121 compares combustion images for $\Phi = 1.33$ at various mass

flow settings (28%, 37%, and 46% of the design mass flow rates listed in Table 10). The highest flow rate shown is the 46% of design condition, as this was the highest mass flow rate of fuel and air capable of sustaining combustion. Of note in these images is the structure of the flame, which remains basically constant for the three conditions shown. As mass flow increased, a decrease in flame width was seen. This reduction in width was likely caused by increasing swirl velocities on the exit of the swirler. Higher swirl velocities required additional buffer between this swirling shear layer and the center where velocities were slow enough to combust.

Blowout also eventually occurred at 37% of the design mass flow rates, where an apparently stable flame quickly quenched without an outside disturbance. Figure 122 displays high-speed images captured prior to flame extinction at this elevated flow rate. Unlike the lean blowout scenario, this flame extinguished in approximately 25% of the time without any prior indication of instability. Rather than displaying a pulsed nature and slowly dying or lifting off due to increased mass flow rates, this flame appeared to be quenched of heat necessary to sustain the reaction, quickly extinguishing all signs of reaction.

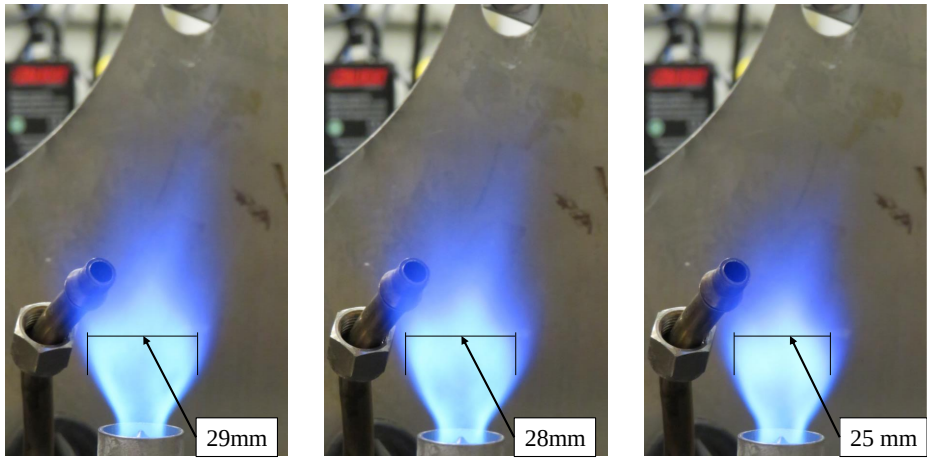

(a) 28% of Design Flow Rate (b) 37% of Design Flow Rate (c) 46% of Design Flow Rate

Figure 121. Visual comparison of the reaction zone above the swirler, varying system mass flow for $\Phi = 1.33$.

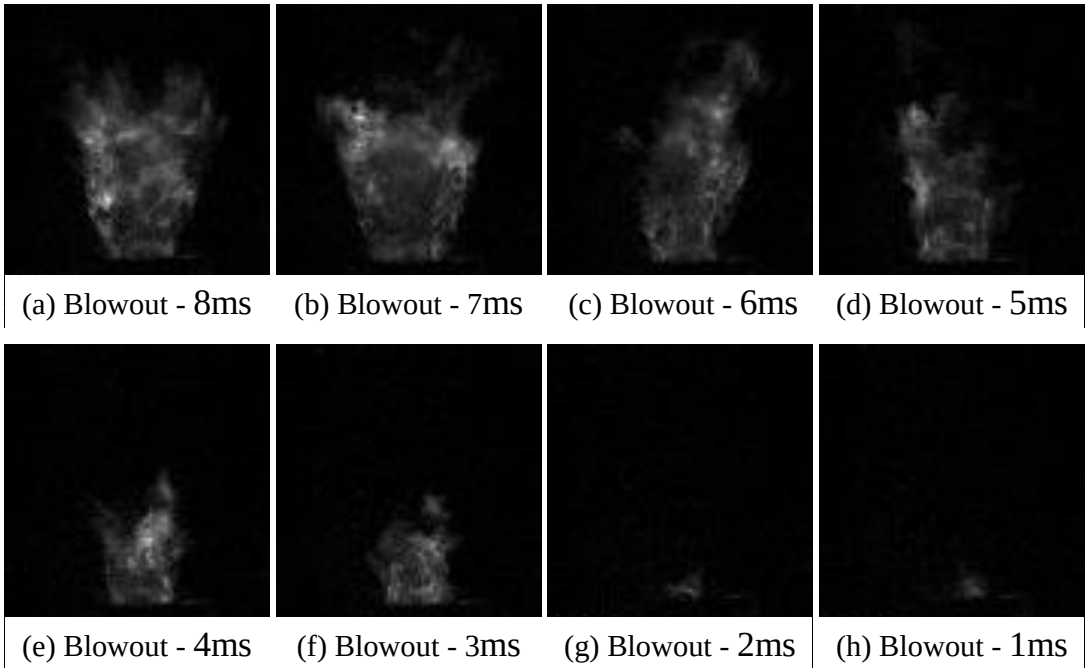

Figure 122. Swirled quenching montage at 37% of design flow rates, $\Phi = 1.30$.

Once again, the reason for this reaction instability was thought to be caused by location of the flame anchor. As noted previously in the discussion of Figure 120, if the reactions anchored to the shear layer between the highly swirled flow and the swirler center body, the reactions would likely not survive increased flow rates. To show the location of these primary reaction anchors, Figure 123 shows sums of maximum image intensities. Each of these images presents how the reaction changed over 50 ms, where bright sections of the sum indicate reaction regions that reoccurred over time. It is evident that the reactions were most prevalent along the edges of swirled air introduction. One may note that the edges are brighter as a result of the viewpoint, where a conical body in three dimensions appears the thickest at the boundary where the line of sight is tangent to the circumference. Acknowledging this, the flame was anticipated to anchor at the center of the swirling cone where the recirculation zones reside; this would produce the brightest region directly above the center of the swirler. Without a high-intensity image indicating a flame front that resided in these

recirculation zones, it can be assumed that the swirler was not anchoring combustion to the center of the swirl, but rather the edges of the swirling flow.

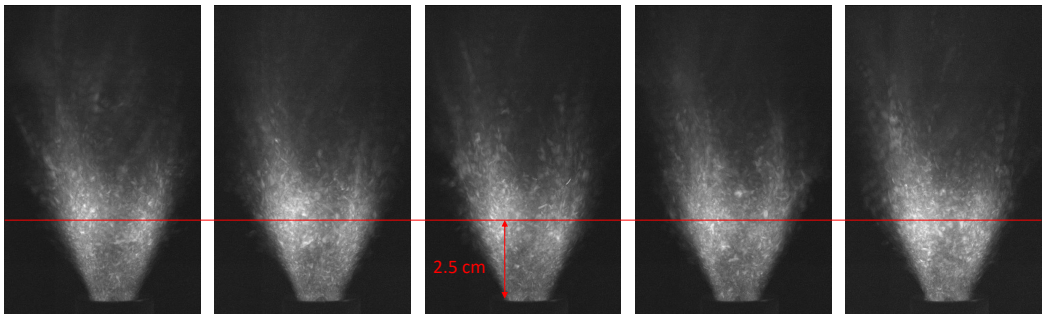

Figure 123. Reaction anchor locations shown by maximum intensities summed over 500 frames (50 ms), taken prior to blowout at 55% of design flow rates and $\Phi = 1.31$. Each image is 500 frames summed over 50ms, showcasing five separate samples over a 0.25 second time span.

To further investigate the cause of blowout, steady-state CFD analysis of reacting flow was conducted on a single swirler at ambient conditions. Figure 124 shows velocity vectors and equivalence ratios on a plane that dissects the swirler geometry. These images were taken at 60% of the design swirler mass flow rates to give an indication of what was causing flame out in conditions leading up to the design point. Similar to a previous AFIT compact combustion study [26], the computational model predicted sustained combustion that was not observed in experiment. This may point to a flaw in the partially-premixed combustion model recommended for UCC computations by Briones *et al.* [39] and used in other AFIT UCC studies [26, 48].

Focusing on other properties that rely less on the location of a modeled flame front for explanation of blowout, velocity vectors in Figure 124a show the recirculation zones adjacent to the highly swirled air at the swirler exit plane. These recirculation zones are similarly located to the regions of peak equivalence ratio in Figure 124b. Although it was anticipated that flame would anchor within these recirculations, it was apparent from CFD that the swirl-induced recirculation was the start of the mixing process.

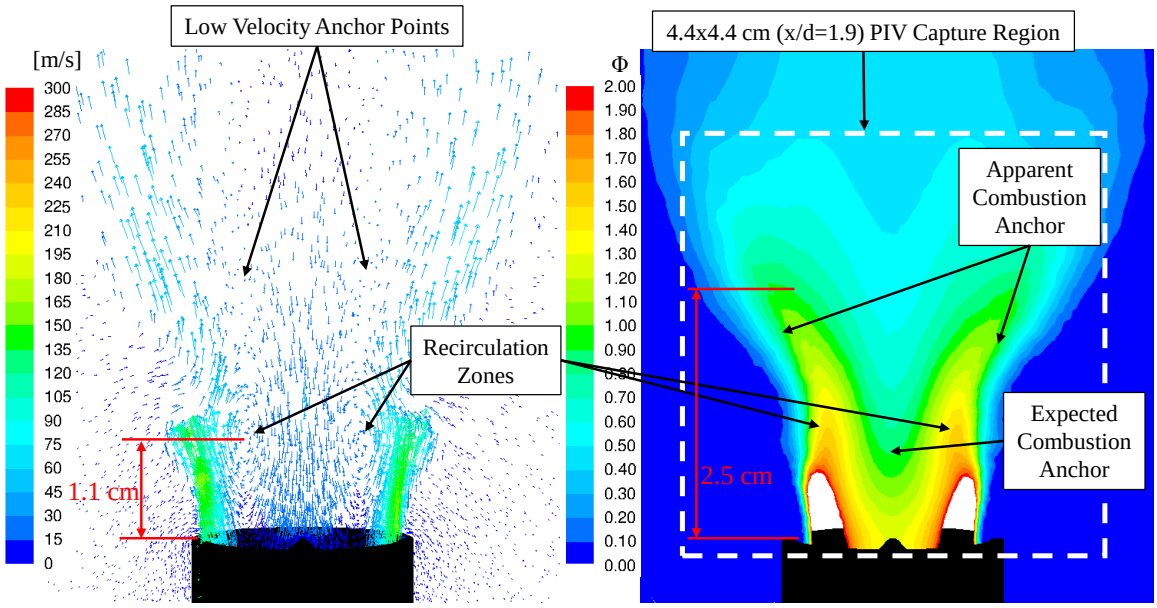

(a) Velocity vectors

(b) Contours of Equivalence Ratio

Figure 124. CFD results from ambient pressure, single swirler analysis at the 30% thrust condition (60% of the designed swirler mass flow rate).

Reaction fronts were expected to occur at or near local equivalence ratios of 1.0, as indicated in Figure 124b. The height of 2.5 cm is noted, as this was the same height that peak flame intensities were seen in Figure 123 for similar swirler conditions. Computational equivalence ratios and experimental images both suggest that the flame was anchored to the low velocity region above the main recirculation points, as noted in Figure 124a. While the low velocity provided a stable region for combustion of the already mixed products, this location's close proximity to high-velocity shear flow made it sensitive to velocity increases. This is what likely caused flame out at higher mass flow settings. The flame became unstable as the local flow velocity surpassed the turbulent flame speed of the propane-air reaction.

To combat this, the flame anchor point needed to be shielded from high-velocity swirling flow. It was anticipated that the flame would anchor to the center of the swirler if the local equivalence ratio there were to increase. This could be accomplished by allowing some fuel to enter through the recirculation body, being careful not to

disrupt the primary recirculation zones that conducted much of the mixing. If the flame were to anchor to the location noted in Figure 124b as the expected combustion anchor, the reaction would be less susceptible to blowout when increasing mass flow rates. Figure 125 shows how additional fuel was added to the center recirculation zone by the use of four holes at 0.5mm. The top of the recirculation body cone was also removed 1) to provide a flat face for machining holes and 2) to increase the separation and turbulence in the center of the swirler to provide a better flame anchor.

Figure 125 also shows the impact of this modification, moving that flame anchor to the center of the swirler jet. In doing so, this design was able to reach mass flow conditions representative of engine idle. This indicated that adding fuel to the center of the swirler would aide in stable combustion. This design was not able to achieve stable combustion to the design mass flow rates, so adjusting the fuel supply scheme further is a recommended next step for the current research, as the need for a stable flame anchor is apparent with the completion of all other components for the Disk-Oriented Engine Combustor.

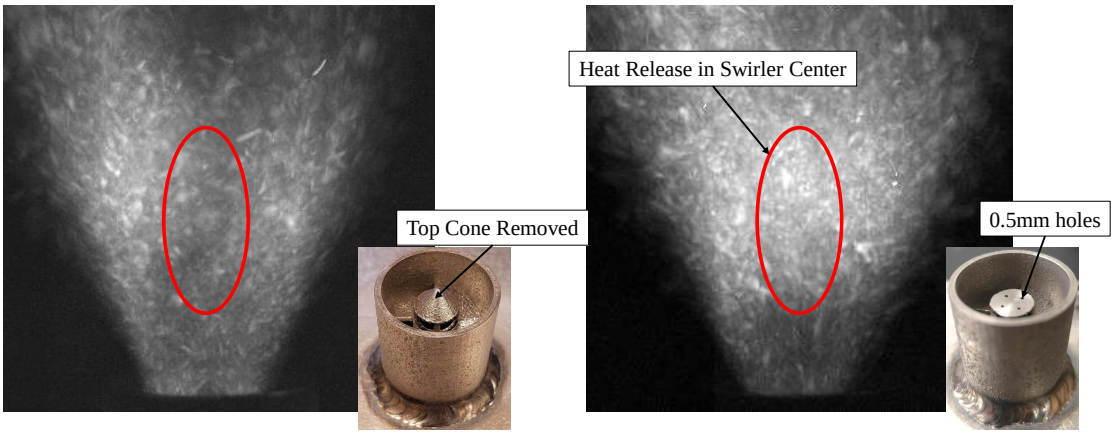

(a) Original Design

(b) New Recirculation Body

Figure 125. Reaction front comparison for new swirler fuel injection scheme. Images were created in the same way as Figure 123, summing 500 frames to highlight reaction front locations as a function of flame intensity.

4.5.2 Swirler PIV Testing

In order to understand and quantify the velocity above the actual swirler, and compare those velocity fields to those found in computational modeling, Particle Image Velocimetry (PIV) was used to measure velocity fields above the swirler center, in accordance with PIV methods outlined in Sections 2.5 and 3.5.2. Using this technique, two-dimensional velocity fields were measured in a 4.4 cm x 4.4 cm region above the swirler shown in Figure 60, and these experimental results were compared to atmospheric CFD analysis of an individual swirler. The CFD domain for comparison to experiment was not the entire domain used for Disk-Oriented Engine analysis; it was modeled after a single swirler issuing into atmospheric conditions (previously shown in Figure 56). This provided a direct comparison between CFD and experiment to quantify error in the computational results. The ambient swirler domain was modeled using the same solver settings and grid techniques discussed in Sections 3.2 and 3.3 so that it would produce results similar to those from the full Disk-Oriented Engine geometry.

Experimental testing and computational analysis of the swirler was done at three different air and fuel mass flow rates, listed in Table 10. While these tests were not conducted at engine pressures, the mass flow rates were matched to those expected in a single swirler at engine conditions. The mass flow rates for fuel and air for these tests were based on off-design CFD analysis of the entire combustor. Since the previous section discussed the inability to sustain reaction at operating conditions, PIV was captured at these flow rates in non-reacting cases.

Velocimetry data was taken on the capture region shown in Figure 126, which is highlighted in Figure 60 for the test setup and Figure 124 for CFD cases. The particle traces in Figure 126 are a compilation 10 frames, or 0.2 milliseconds, showing how individual seed particles move over time. In this plane, horizontal and vertical

velocities were calculated based on the auto-correlation between subsequent images. Not captured in Figure 126, or this method of planar PIV, is the rotational component of the flow (noted with the arrow about the swirler). With only a two-dimensional laser sheet, PIV could only detect velocities in the plane of interest. This meant that rotational velocities were not accounted for, and high rotational speeds would limit the amount of time a particle stayed in the laser sheet. Since PIV required two consecutive images for correlation analysis, these particles rotating about the swirler had to remain in the laser sheet for two frames, or 40 μs. The laser was not focused with a lens, allowing the sheet to be the full width of the beam diameter (approximately 2 mm).

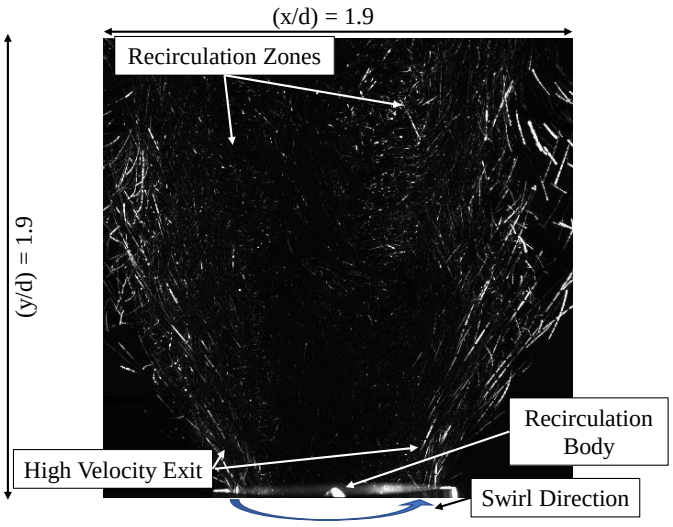

Figure 126. Example of image captured in swirler experimental testing.

Figures 127 and 128 show vertical and horizontal velocity magnitude contours taken on the plane from Figure 126 for engine conditions representative of 100%, 80%, and 30% thrust settings. These images represent average velocities over a 6000 frame (0.12 seconds) recorded time. Since the auto-correlation only relied on differences between two subsequent images to determine velocity, an average was obtained by comparing the two-frame velocities for various image pairs throughout the data set. For example, velocities were determined from Frames 1-2, 11-12, 21-22 and so on,

and these individual velocities were averaged to create a velocity plot representative of the data set. Next to the experimental results, steady-state CFD velocity fields are presented over the same region above the swirler for comparison. Evident in Figure 127, the experimental and computational results display the same general shape and rough magnitude for all operating conditions. While the computational results approximate the extrema of velocities to be greater than those shown in experimental data, it is likely that PIV did not capture all of the highest velocity flow while it was within the laser sheet. Likewise, it was possible that not enough seed particle reached the low velocity region to make accurate velocity measurements, as seen by the lack of particles in the recirculation zones of Figure 126.

Figure 128 shows the same general result for the horizontal velocities. Computations predicted much steeper gradients than those seen in experimental plots. Since seed was introduced with the fuel, seed density was likely not high enough to capture the gradients seen in CFD. Common between the two columns are the rough magnitude and velocities, as well as the shape of the velocity contours. Computational modeling predicted horizontal velocity to move outward from the swirler center upon exit, with a region of inward velocity as air was entrained above the swirling mass. Experimental results also showed this entrainment, as outward velocity is high at the exit plane, slows after the initial exit, and re-establishes radially outward near the upper edge of the domain. This phenomenon is more prevalent in Figures 128a and b, as the high velocity magnitudes entrain more flow back into the swirler.

To quantify the difference between velocities found by experiment and computations, Figure 129 shows a contour plot of the error between the two result types. This particular plot is for the 100% thrust case, as it was the design point that was of the most interest in this swirler investigation. The error is shown as a percentage, normalized by the maximum computational velocity on this domain. Computational

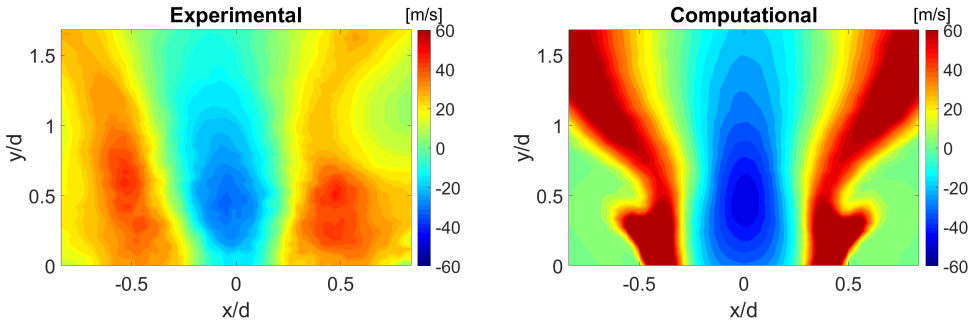

(a) 100% Thrust

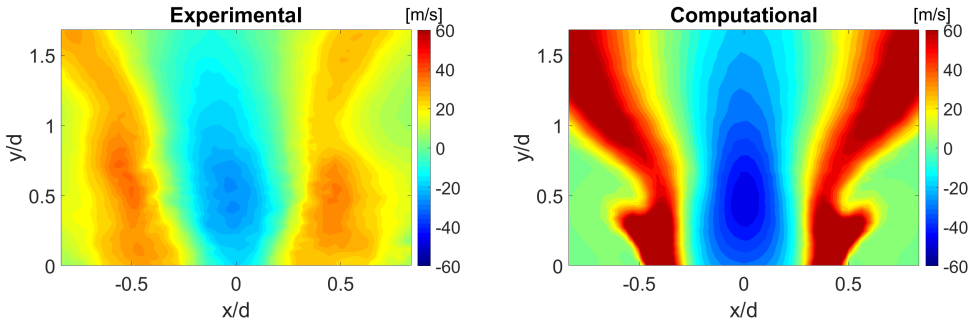

(b) 80% Thrust

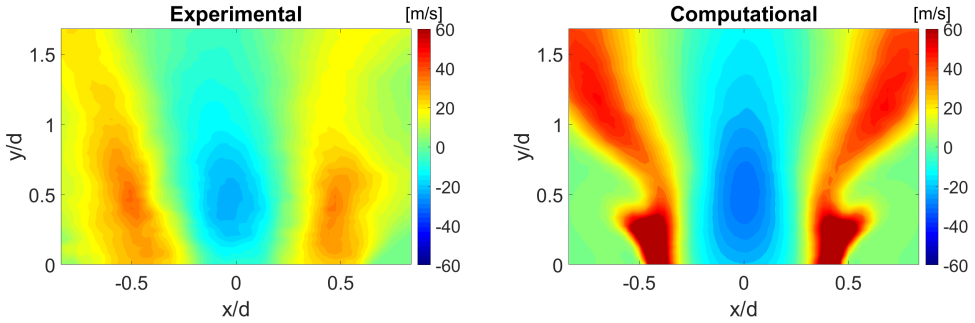

(c) 30% Thrust

Figure 127. Comparison of experimental and computational vertical velocities for non-reacting, ambient swirler tests

velocity was used for normalization as the maximum velocities were not thought to have been captured by PIV. The average error in Figure 129 was 12% in vertical velocities and 25% in horizontal velocities. For much of the plot, the vertical velocities seen in experiment and CFD were similar, with a maximum divergence of 97% near the exit of the swirler. This error at the swirler exit was expected to be a result of high swirl velocities, where the rotationality of the flow caused the highest velocities

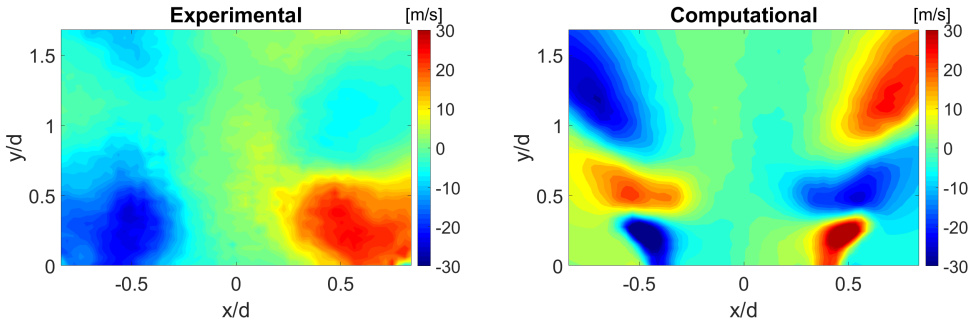

(a) 100% Thrust

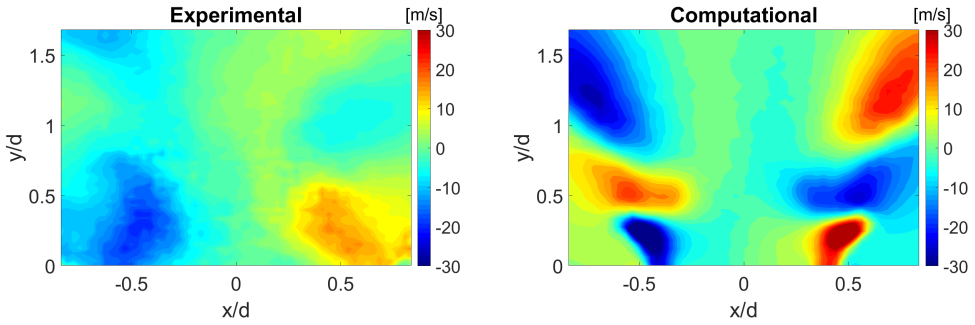

(b) 80% Thrust

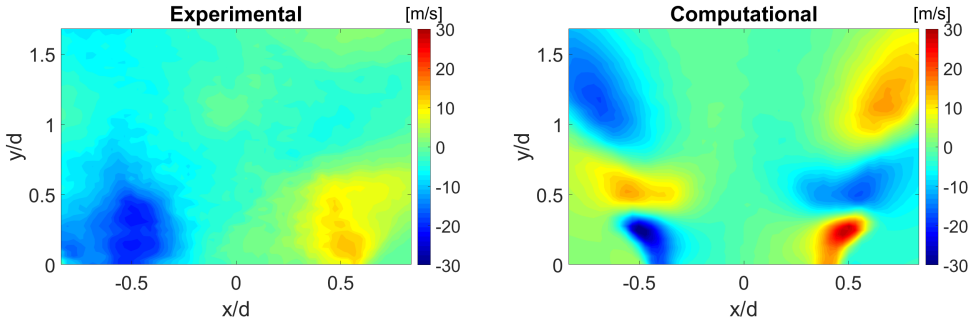

(c) 30% Thrust

Figure 128. Comparison of experimental and computational horizontal velocities for non-reacting, ambient swirler tests

to not be captured by two-dimensional planar PIV. The largest error in horizontal velocity was at the location of entrainment, where air external to the swirler was entrained by the high-speed swirl leaving the swirler. The maximum error in this location was 83% and was caused by a lack of seed particles in the entrained fluid. Computations estimated the shape of the swirler velocity profile well based on the visual similarity in Figures 127 and 128; the error shown in Figure 129 suggests that

there was an average difference of 12-25% between the experimental data and the CFD results. Knowing this, the computational approximation of the swirler flow was better understood, as the model predicted fluid structures similar to real-world effects and provided velocities on the same order as experimental findings.

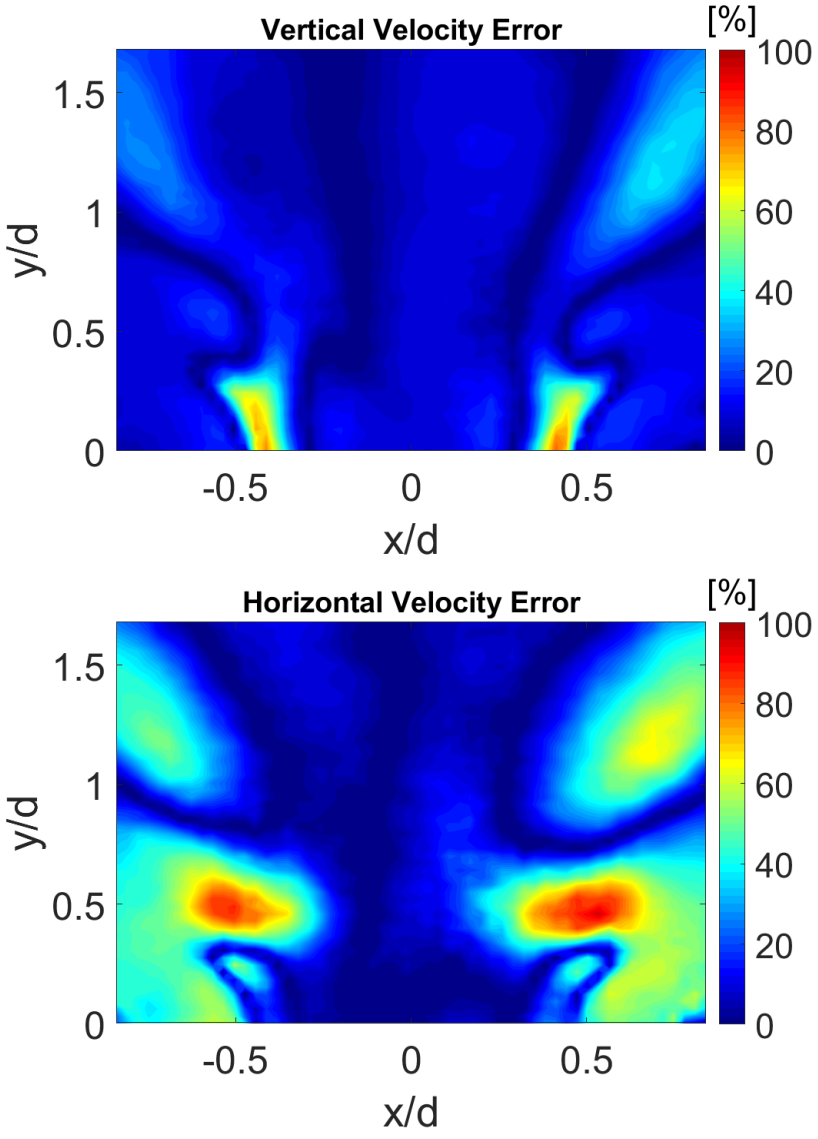

Figure 129. Contour plot of error between computational and experimental velocities of the swirler at the 100% thrust condition.

V. Conclusions

5.1 Motivation

The present research designed and built a combustor that served as a proof of concept for an entirely new gas turbine engine flow path. The Disk-Oriented Engine Combustor was designed to combine the inlet and exit conditions of a centrifugal compressor and radial in-flow turbine, while increasing residence time through circumferential combustion in 60% of the axial length of similar cycle gas turbine engines. Such a length reduction could be used to improve mobility of ground-based electric power generation, reducing the overall length of a power generation system. This length savings could also be used to provide power for distributive electric propulsion air vehicles, where the use of multiple electric thrust-producing fans increases the survivability of an aircraft over one with a single engine for thrust production. This research was focused on four objectives that led to the final design of a Disk-Oriented Engine Combustor.

5.2 Objectives and Results

As previously stated in Chapter I, the present research revolved around four separate objectives to guide the combustor design process for a Disk-Oriented Engine. These objectives included an engine cycle analysis, computational modeling, experimental comparison of select components, and physical hardware fabrication. Each of these specific objectives are reiterated for the discussion of results:

1. Perform an engine cycle analysis to determine operating conditions, station parameters, and sizing requirements for an engine operating at the target constraints: 668 N (150 lbf) of thrust at a compressor pressure ratio of 4.0.

2. Computationally investigate the combustion performance of various three-dimensional combustor geometries to determine a suitable design for sustained combustion at the target operating conditions.

    - Develop a fuel injection system appropriate for the flow path unique to a Disk-Oriented Engine, capable of anchoring a stable flame across the operating envelope, and adaptable between gaseous propane and future liquid jet fuel injection.

3. Compare velocity profiles and flame stability of focused experimental testing to CFD results to better understand the real-world operation of this design prior to full-engine tests.

4. Design a combustor geometry that is manufacturable, survivable, and testable at atmospheric and elevated conditions.

The following sections outline the approach taken in pursuit of each objective, while providing results from the present research.

5.2.1 Objective 1

Since an existing engine cycle was unavailable for the desired performance of the Disk-Oriented Engine, the first objective was to develop an engine cycle that would produce 668 N of thrust with a compressor pressure ratio of 4.0. Through the use of the AEDsys engine design software, a cycle producing 587 $\frac{N}{kg/s}$ of specific thrust at 39.6 $\frac{g/s}{kN}$ specific fuel consumption was selected based on comparison with other engines in the sub-1000 N thrust class. This selected cycle required an air mass flow rate of 1.14 kg/s to achieve 668 N at the design condition. Based on research into similarly performing engines and turbomachinery, the engine was sized to be within 0.5 m diameter, as set by the design constraints in Chapter I. The result of this cycle

analysis was an engine operating cycle that provided both an expected performance (specific thrust and specific fuel consumption) and fluid properties at various engine stations, which set the boundary conditions that were used in computational analysis of various combustor geometries.

5.2.2 Objective 2

Designing a geometry that would permit circumferential flow and sustain combustion in a shortened axial length was the focus of Objective 2, which investigated various geometries to find a solution where desired combustion performance characteristics were met. Performance goals based on similarly sized engines included sustained combustion with a combustor pressure drop below 5% and a turbine inlet pattern factor below 0.45. A feasible design was found after 48 systematic iterations of air partitioning strategies, coolant introduction methods, and flame stabilization techniques.

Rather than rely on centrifugal loading similar to Ultra-Compact Combustors that were the background for this research, the Disk-Oriented Engine Combustor utilized an increase in diameter and bulk-swirl circumferential combustion to create adequate residence time for complete combustion in a shortened axial length. This was accomplished by allowing air to maintain the bulk swirl imparted by the compressor throughout the entirety of the combustor. The bulk swirl within the combustor, created by the exit conditions of the compressor and maintained by the use of orifice holes rather than jets in the combustion liner, increased the swirling load in the entire combustor, achieving between 100 and 250*g_e m/s^2 in the primary combustion zone. The presence of bulk swirl increased the residence time within the Disk-Oriented Engine Combustor 67% compared to a non-swirling equivalent, improving reaction completion and combustion efficiency and helping to minimize aerodynamic pressure

losses. A focus on residence time rather than combustion loading resulted in a combustor volume increase of 720% compared to a UCC-like combustor scaled for the Disk-Oriented Engine. The final Disk-Oriented Engine was nearly the same diameter and length as the scaled UCC, but was designed to focus on combustion volume rather than circumferential loading.

The result of this computational investigation was a combustor geometry that could operate across the envelope developed in cycle analysis. The combustor was analyzed at the 100%, 80%, and 30% thrust conditions found through cycle analysis, as well as an additional condition (CPR = 4.0, Φ = 0.31) that isolated the effect of equivalence ratio at the design, 100% thrust condition. Computational analysis suggested that the engine would sustain stable and efficient combustion across the entire operating envelope, with combustor pressure losses between 3.5% and 4.2%, below the assumed loss of 5% from cycle analysis. The anticipated turbine inlet temperatures were between 980 and 1300 K (all conditions within 1% of cycle analysis), with pattern factors between 0.23 and 0.27. Since the largest pattern factor was 40% lower than the suggested maximum from literature [24], it stands to reason that this design will allow for sustained turbine operation without producing catastrophic hot spots at the turbine rotor inlet. With an adequately performing combustor designed and built, the next step in this research would be to test the combustor performance for comparison with computational findings.

Fundamental to the success of the Disk-Oriented Engine Combustor was the design of a fuel injection system that would provide a stable flame anchor. Through computational findings, a fuel-air swirl injector was designed unique to the flow path of the Disk-Oriented Engine. Unlike traditional axial swirlers, this design accepted swirling inlet air that was turned radial outboard while simultaneously being swirled to create the desired recirculation zones for stable combustion. At the design oper-

ating condition, computational analysis showed that the swirler anchored a steady, stable flame with a swirl number of 0.8 and a primary zone equivalence ratio of 1.3.

5.2.3 Objective 3

The third objective was to use the availability of a single swirler to compare velocity profiles and flame stability of focused experimental testing to CFD results to better understand the real-world operation of this design prior to full-engine tests. This experimental analysis consisted of reacting flow tests to establish the operating limits of a single atmospheric swirler, and Particle Image Velocimetry measurements above the non-reacting swirler to determine velocity fields and recirculation locations. Reacting flow tests showed stable operation of the swirler between equivalence ratios of 0.9 and 3.0 at a sub-idle condition, and elevated mass flow tests showed that modifications to the swirler fuel introduction provided flame stability up to the engine idle mass flow rates. Steady-state computational analysis suggested that an individual swirler showed stable combustion characteristics across the operating envelope, but experimental tests on a single swirler showed that the design was unable to sustain combustion at design mass flow rates. Additional investigations may be required to determine a suitable change in swirler geometry to sustain a physical flame at the design condition, as well as an explanation for the CFD model for flame stability that predicted success and failed to recognize the blowout conditions seen in experiments.

For comparison of velocity profiles, an individual swirler was modeled in CFD, and it was directly compared to velocity data obtained with PIV. Experimental findings corroborated both the velocity magnitudes (within an average of 12-25%) and swirler shapes anticipated by computation models, indicating that the numerical analysis for the entire combustor was likely realistic. This gave weight to back the Disk-Oriented Engine Combustor design for development and real-world testing.

5.2.4 Objective 4

As directed by the final objective, the combustor design was to be manufacturable, survivable, and testable at atmospheric conditions at AFIT and engine representative conditions at an AFRL facility. The design was machined in metal with the help of the AFIT Model Shop, Lewark Metal Spinning, and Wicked Welding, proving the manufacturability of the proof-of-concept design. Currently, many of the parts for this assembly are complete, but the need for additional testing on swirler designs has stalled the production process. Once a suitable adjustment to the swirler is found, the Disk-Oriented Engine Combustor will be completed and ready for assembly.

Traversing from a computationally derived geometry to a manufacturable one proved to be a tedious task. Once a design was found with desirable combustion characteristics in the computational model, the geometry was partitioned into 17 different parts, where each was manufactured in a material specific to the heating it would see in operation. Through additional computational analysis on this partitioned geometry, various changes were made to the swirler design, internal cooling, and air allocation to ensure the final design could be machined and would survive real-world engine tests. Of these changes, the most significant were the adaptation of cooling schemes to keep anticipated metal temperatures well below material failure points. Efforts to cool both the combustion liner and center body required multiple iterations based on CFD analysis, resulting in jet based coolant injections from both features.

5.3 Recommendations for Future Work

Based on these findings, recommendations for future research include testing of physical hardware to corroborate findings presented from computational analysis on the combustor. Additional investigation into blowout of the swirlers at sub-idle conditions is required before full combustor tests can be done. Further investigation to find

a suitable CFD combustion model may be required, as the present research revealed shortcomings in the partially-premixed combustion model which did not anticipate blowout conditions observed in experiment.

After a suitable swirler modification is found, experimentation beyond the fuel-air swirlers is necessary to prove the operability of this design. While sub-idle flow rates can be achieved in the AFIT COAL Lab, engine pressure tests will need to be conducted at AFRL facilities to determine performance characteristics above atmospheric conditions. As noted in the geometry design process, primary zone combustion may be dependent on the number of swirlers, as computational modeling may have over-predicted the success of this design. If issues arise in PZ flame stabilization, an experimental investigation into the number of swirlers may be required.

If experimentation shows similar results for exit temperatures and pattern factors to the computational analysis, it is recommended that this research progress to rotating hardware design. By incorporating a compressor and turbine, the Disk-Oriented Engine will be able to exhibit self-sustained operability. With operating turbomachinery and the ability to self-sustain combustion, the Disk-Oriented Engine could be redesigned to incorporate either flight-weight hardware for aircraft operation, or a secondary turbine stage and shaft could be designed to test the applicability of power production rather than thrust. Self-sustaining thrust or power production would allow the Disk-Oriented Engine to provide gas turbine power in a package up to 60% shorter than traditional engines of the same thrust class.

Appendix A. Fluent Settings

This appendix outlines the Fluent settings used to run on-condition test cases of the Disk-Oriented Engine Combustor. While many of these settings were taken from the test cases ran on the Version 3 rig setup, the settings required for k-ω SST turbulence modeling for Versions 1 & 2 are included in Figure A-5. Many of these settings were based on studies done by Bills [38] and Bohan [26], and settings not listed were left in their default state.

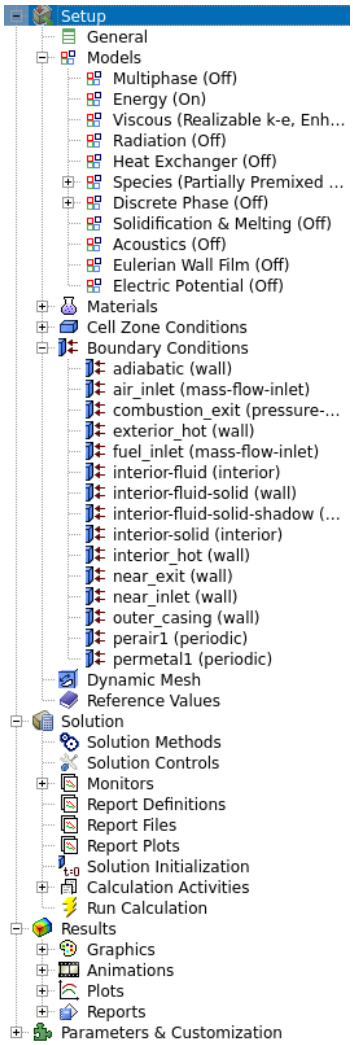

Figure A-1. Fluent Settings-Task Tree: Settings for Fluent were selected by stepping through the options on this selector tree, located on the left side of the Fluent GUI.

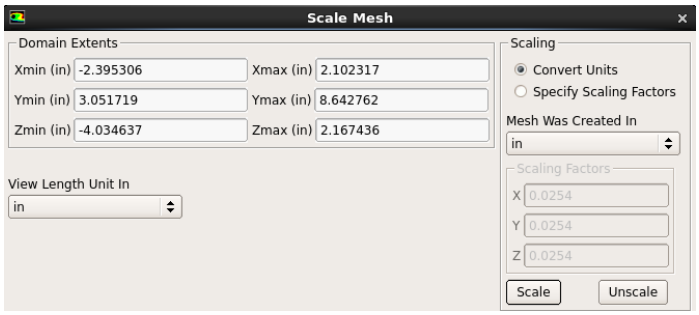

Figure A-2. Fluent Settings-Scaling: Mesh was scaled to the units (inches) used in SolidWorks and Pointwise.

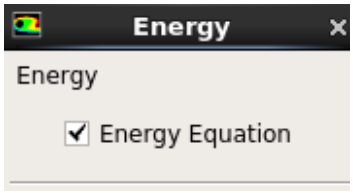

Figure A-3. Fluent Settings-Energy Model: Energy equation was turned on for heat transfer and combustion models.

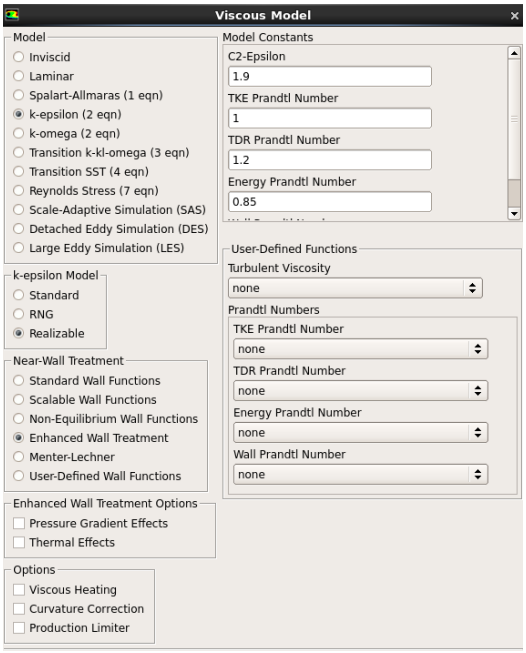

Figure A-4. Fluent Settings-Viscosity Model (k-ϵ): k-ϵ viscosity model settings, used for Version 3 testing. K-epsilon, realizable, and enhanced wall functions were selected.

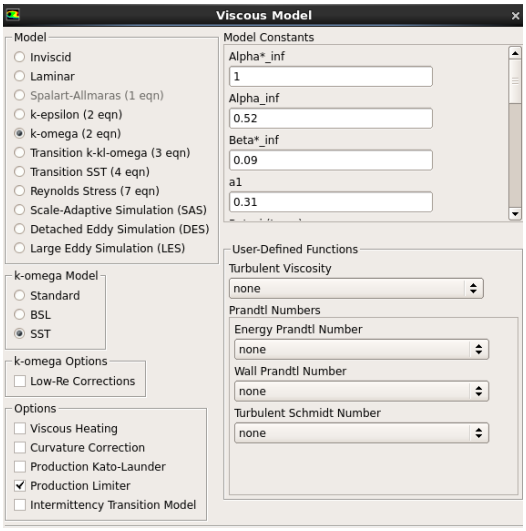

Figure A-5. Fluent Settings-Viscosity Model (k-ω): k-ω viscosity model settings, used for Version 1 & 2 testing. K-omega and SST were selected.

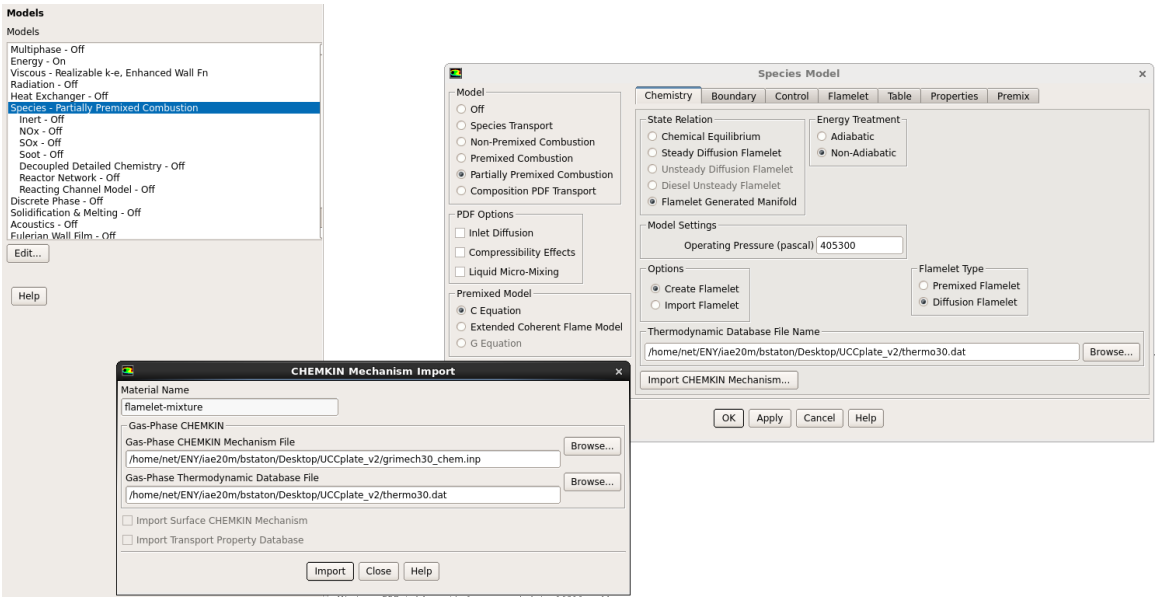

Figure A-6. Fluent Settings-Species Model Chemistry: The chemistry model selected was partially-premixed combustion. Operating pressure was set at 4 atm per the design cycle, Chemkin Mechanism was "grimech30_chem.inp" and thermodynamic database file was "thermo30.dat". Flamelet Generated manifold was selected.

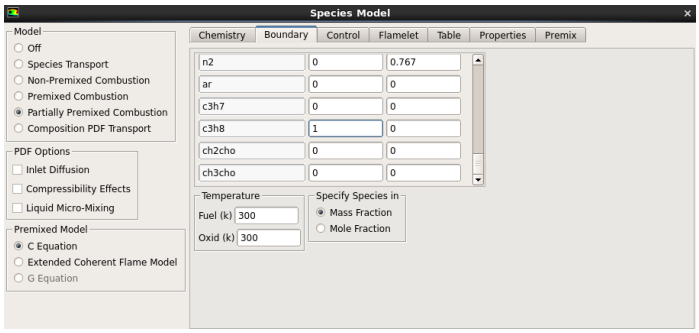

Figure A-7. Fluent Settings-Species Model Boundary: The mass fraction of fuel species was set 1.0 for propane.

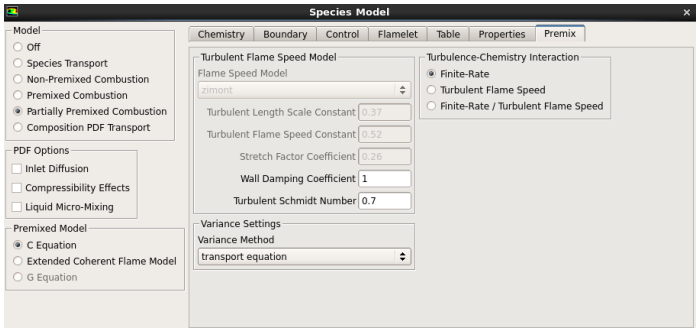

Figure A-8. Fluent Settings-Species Model Premix: Turbulence-Chemistry Interaction was set to "Finite-Rate".

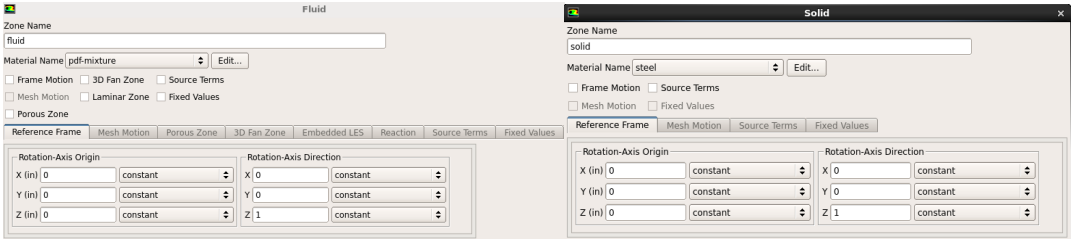

(a) Fluid Volume (b) Solid Volume

Figure A-9. Fluent Settings-Cell Zone Conditions: Volume conditions for fluid and solid bodies. Steel was chosen as a simpler, available material substitute for the stainless steel and Inconel to be incorporated into the experimental setup.

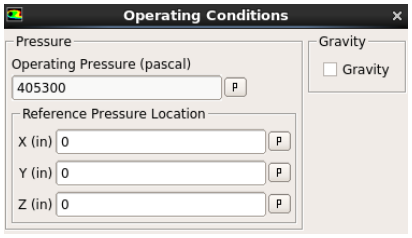

Figure A-10. Fluent Settings-Operating Conditions: Operating pressure defined for the combustor, based upon the selected cycle with overall pressure ratio of 4.0.

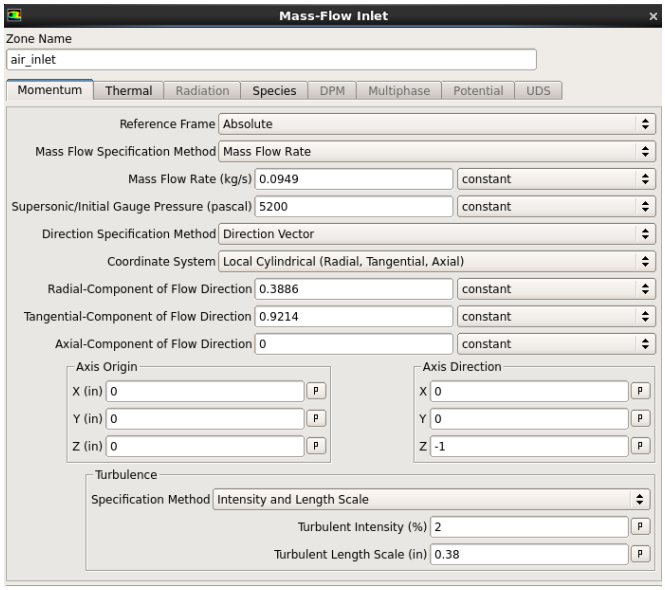

Figure A-11. Fluent Settings-Boundary Conditions (Air): Air inlet mass flow boundary conditions.

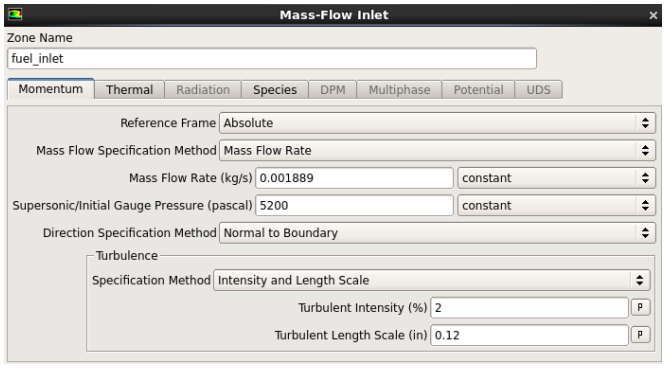

Figure A-12. Fluent Settings-Boundary Conditions (Fuel): Fuel inlet mass flow boundary conditions.

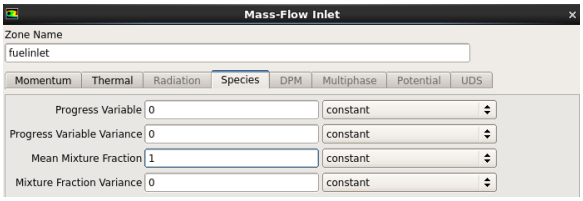

Figure A-13. Fluent Settings-Boundary Conditions (Fuel): Fuel inlet species boundary conditions, allowing for 100% propane to flow through the fuel inlet.

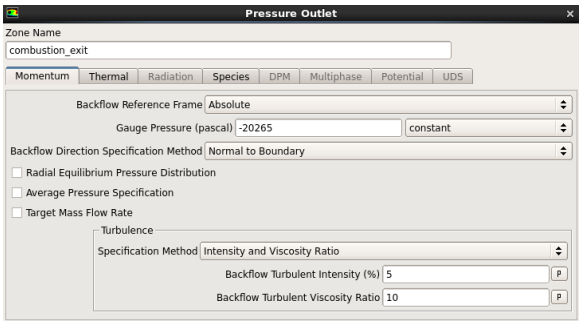

Figure A-14. Fluent Settings-Boundary Conditions (Exit): Combustor exit boundary condition, set as pressure outlet that assumes 5% static pressure loss from inlet condition.

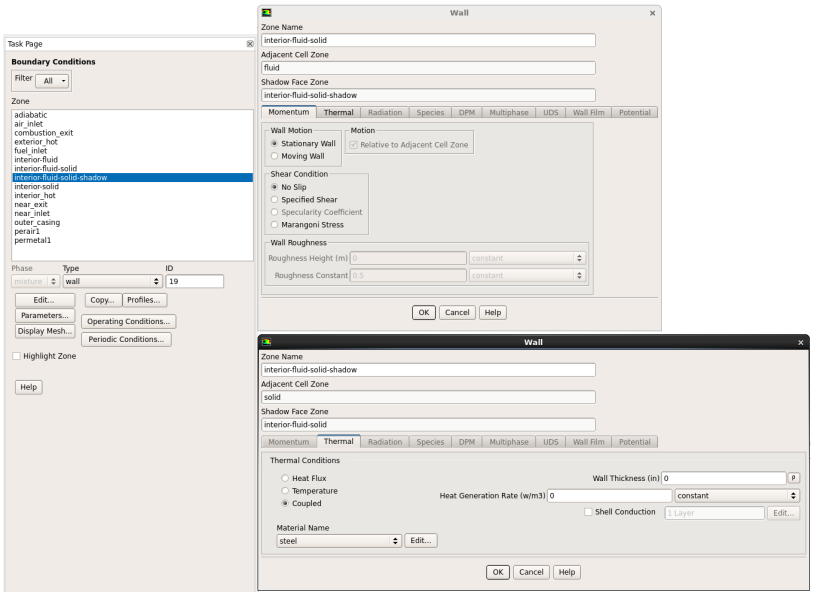

Figure A-15. Fluent Settings-Boundary Conditions (Coupled Wall): Coupled wall condition allowing for conjugate heat transfer between the fluid-solid interface.

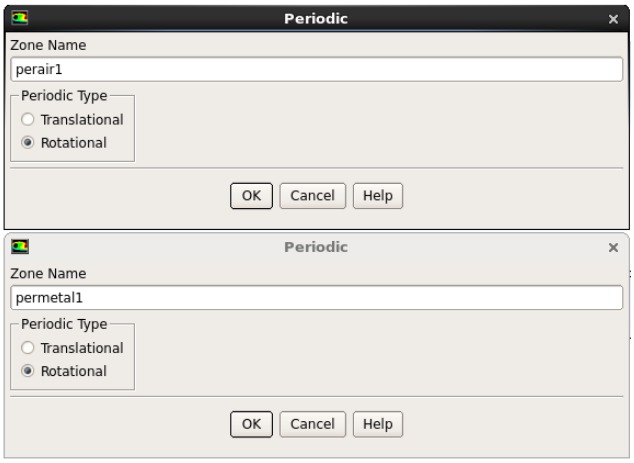

Figure A-16. Fluent Settings-Boundary Conditions (Periodic): Periodic boundary condition, allowing for reduction of the model to a 30° periodic sector.

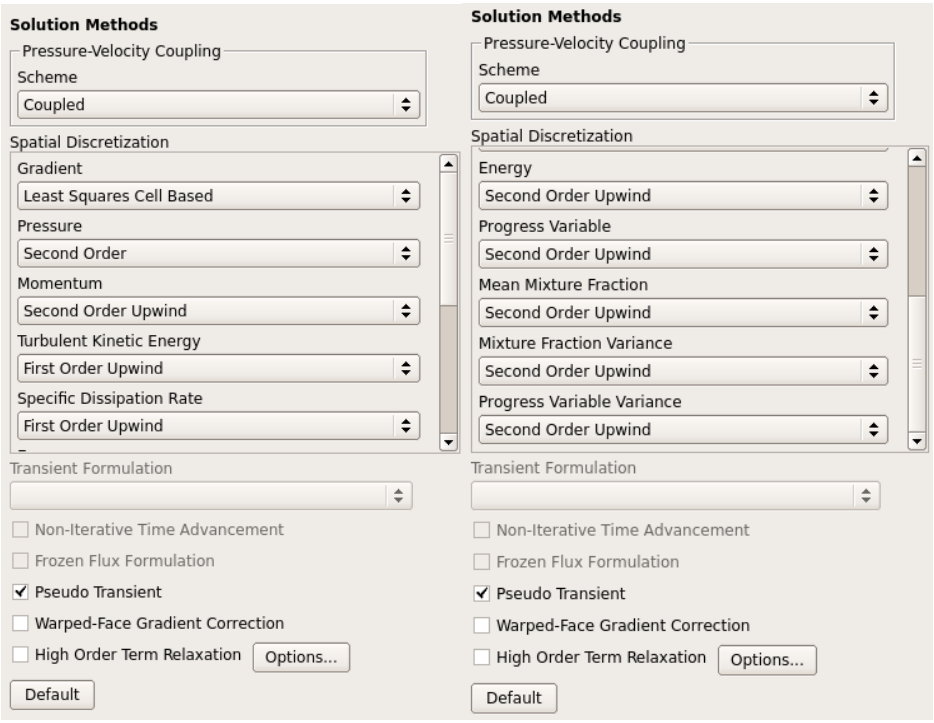

(a) (b)

Figure A-17. Fluent Settings-Solution Methods: CFD solver settings used to produce model simulation.

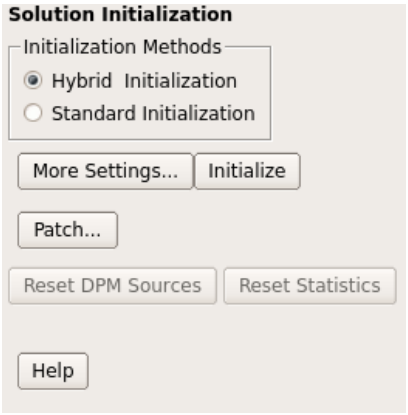

Figure A-18. Fluent Settings-Solution Initialization: Hybrid initialization was used to produce the first iteration of the computational solution.

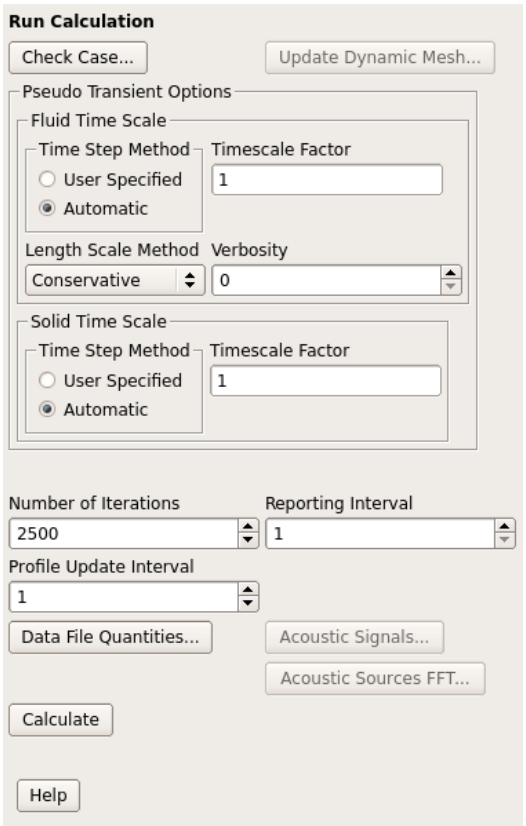

Figure A-19. Fluent Settings-Run Calculation: Run settings required to run a pseudo-transient solution. Convergence was generally seen within 2500 iterations, so this number was used for calculations.

Appendix B. AEDsys Engine Cycle Analysis Outputs

This appendix presents cycle analysis outputs, created by the methods outlined in Section 3.4. All analysis was done using the AEDsys program provided with Mattingly *et al.*'s Aircraft Engine Design text [9].

Table B-1. Engine station parameters at on-design conditions.

Design Interface Quantities (Version 4.100)

Station	m dot	Pt	Tt	P	T	Mach	Velocity	Area	Area*
	(kg/s)	(kPa)	(K)	(kPa)	(K)		(m/s)	(m^2)	(m^2)
0	1.14	101.33	288.16	101.32	288.15	0.0100	3.40	0.272	0.0047
1	1.14	101.33	288.16	66.48	255.46	0.8000	256.31	0.0049	0.0047
2	1.14	98.29	288.16	82.86	274.43	0.5000	166.04	0.0065	0.004
3.0	1.14	393.16	485.25	355.31	471.42	0.3815	166.04	0.0026	0.0016
3.1	1.09	393.16	485.25	355.31	471.42	0.3815	166.04	0.0025	0.0015
3.2	1.09	389.23	485.25	387.49	484.63	0.0800	35.30	0.0111	0.0015
MB fuel	0.0265								
4	1.12	373.51	1300.00	203.83	1130.43	1.0000	647.20	0.0027	0.0027
4.1	1.17		1264.49						
4.4	1.17	180.76	1105.92						
5	1.17	180.76	1105.92	143.92	1049.26	0.6000	374.12	0.0065	0.0054
8	1.17	180.76	1105.92	103.39	972.16	0.9577	574.82	0.0054	0.0054
9	1.17	177.14	1105.92	101.32	972.16	0.9577	574.82	0.0055	0.0055

Table B-2. ONX design condition engine inputs and outputs.

```
                Turbojet Engine - Single Spool
            using Modified Specific Heat (MSH) Model
**********************      Input Data      **********************
      Alt (m)   =      0               Pi c          =  4.000
      T0 (K)    = 288.15               Pi d (max)    =  0.970
      P0 (kPa)  =101.324               Pi b          =  0.950
      Density   = 1.2350990             Pi n          =  0.980
       (kg/m^3)                        Efficiency
      Cp c      = 0.9965 kJ/kg-K       Burner        =  0.980
      Cp t      = 1.2351 kJ/kg-K       Mechanical    =  0.980
      Gamma c   = 1.4000
      Gamma t   = 1.3000
      Tt4 max   = 1300.0 K             Compressor    =  0.760 (ec)
      h - fuel  =  41868 kJ/kg         Turbine       =  0.800 (et)
      CTO       = 0.0000               Pwr Mech Eff  =  0.980
      Cooling Air #1 =  4.000 %
      Cooling Air #2 =  0.000 %        Bleed Air     =  0.000 %
************************    RESULTS    ************************
      Tau r     =  1.000               a0 (m/sec)    =  340.3
      Pi r      =  1.000               V0 (m/sec)    =    3.4
      Pi d      =  0.970               Mass Flow     =    1.1 kg/sec
      TauL      =  5.592               Area Zero     =  0.271 m^2
      PTO       =   0.00 KW            Area Zero*    =  0.005 m^2
      Pi c      =   4.00               Tau m1        = 0.9727
      Tau c     = 1.6840               Tau m2        = 1.0000
      Eta c     = 0.7105
      Pi t      = 0.4839               Eta t         = 0.8132
      Tau t     = 0.8746
      Pt9/P9    =  1.748               M9            = 0.9577
      f         = 0.02422
      f o       = 0.02325
      F/mdot    =587.169 N/(kg/s)
      S         =39.5942 (mg/s)/N
      T9/T0     = 3.3738
      V9/V0     =169.613
      M9/M0     =95.7740
      A9/A0     = 0.0204
      A9/A8     = 1.0220
      Thrust    =    668 N
      Thermal Eff    =  22.50 %
      Propulsive Eff =   1.17 %
```

Table B-3. Throttle-hook data corresponding to plot in Figure 47.

Throttle Hook @ Mach = 0.00, Altitude = 0 m, T0 = 288.16 K, Standard Day

Thrust	S	mdot	mdotc2	Pic	Taut	M9	Tt4	Limit
666	39.76	1.14	1.17	3.996	0.8746	0.9570	1299.3	Thrust=Drag
652	39.77	1.13	1.17	3.950	0.8748	0.9474	1288.3	Thrust=Drag
638	39.78	1.12	1.16	3.904	0.8750	0.9375	1277.1	Thrust=Drag
628	39.79	1.12	1.15	3.871	0.8751	0.9300	1268.6	Thrust=Drag
614	39.82	1.11	1.14	3.824	0.8753	0.9201	1257.7	Thrust=Drag
602	39.86	1.10	1.13	3.780	0.8756	0.9108	1247.7	Thrust=Drag
588	39.91	1.09	1.12	3.732	0.8759	0.9004	1236.7	Thrust=Drag
575	39.97	1.08	1.11	3.686	0.8762	0.8906	1226.5	Thrust=Drag
561	40.04	1.07	1.10	3.636	0.8766	0.8798	1215.5	Thrust=Drag
548	40.12	1.06	1.09	3.589	0.8771	0.8696	1205.3	Thrust=Drag
535	40.21	1.05	1.08	3.541	0.8775	0.8592	1195.1	Thrust=Drag
522	40.32	1.04	1.07	3.492	0.8781	0.8488	1185.0	Thrust=Drag
508	40.44	1.03	1.06	3.443	0.8786	0.8382	1175.0	Thrust=Drag
494	40.58	1.02	1.05	3.390	0.8793	0.8266	1164.3	Thrust=Drag
481	40.73	1.01	1.04	3.340	0.8800	0.8157	1154.3	Thrust=Drag
468	40.90	1.00	1.03	3.289	0.8808	0.8046	1144.5	Thrust=Drag
455	41.09	0.99	1.02	3.238	0.8816	0.7934	1134.7	Thrust=Drag
442	41.30	0.98	1.01	3.186	0.8825	0.7819	1125.0	Thrust=Drag
429	41.53	0.96	0.99	3.133	0.8834	0.7704	1115.4	Thrust=Drag
414	41.80	0.95	0.98	3.075	0.8846	0.7577	1105.1	Thrust=Drag
401	42.08	0.94	0.97	3.021	0.8857	0.7457	1095.6	Thrust=Drag
388	42.39	0.92	0.95	2.966	0.8869	0.7335	1086.2	Thrust=Drag
375	42.74	0.91	0.94	2.909	0.8882	0.7211	1077.0	Thrust=Drag
362	43.12	0.90	0.92	2.853	0.8897	0.7084	1067.8	Thrust=Drag
349	43.54	0.88	0.91	2.795	0.8912	0.6955	1058.8	Thrust=Drag
334	44.05	0.87	0.89	2.731	0.8930	0.6814	1049.3	Thrust=Drag
321	44.57	0.85	0.88	2.671	0.8949	0.6680	1040.6	Thrust=Drag
308	45.16	0.83	0.86	2.610	0.8968	0.6542	1032.1	Thrust=Drag
295	45.81	0.82	0.84	2.548	0.8990	0.6402	1023.9	Thrust=Drag
282	46.54	0.80	0.83	2.484	0.9013	0.6257	1016.0	Thrust=Drag
268	47.38	0.78	0.81	2.419	0.9039	0.6109	1008.4	Thrust=Drag
255	48.31	0.76	0.79	2.352	0.9066	0.5958	1001.4	Thrust=Drag
242	49.39	0.74	0.77	2.284	0.9096	0.5802	994.9	Thrust=Drag
228	50.65	0.72	0.75	2.213	0.9130	0.5639	989.1	Thrust=Drag
215	52.15	0.70	0.72	2.138	0.9168	0.5468	984.3	Thrust=Drag
201	53.94	0.68	0.70	2.060	0.9210	0.5289	981.0	Thrust=Drag
Unable to converge on a solution for Pi t.								
249	48.84	0.75	0.70	2.007	0.9081	0.5289	979.6	Didn’t converge

Table B-4. Off-design analysis at 80% throttle.

```
80% THROTTLE TEST OUTPUT
AEDsys (Ver. 4.100)          Turbojet - Single Spool
   Input Constants
   Pidmax= 0.9700   Pi b  = 0.9500   Eta b = 0.9800   Pi n  = 0.9800
   cp c  = 0.9965   cp t  = 1.2351   Gam c = 1.4000   Gam t = 1.3000
   Eta c = 0.7105   Eta t = 0.8132   Eta m = 0.9800   Eta P = 0.9800
   PTO   =    0.0KW hPR   =  41868   Cool 1=   4.00%  Cool 2=   0.00%
   Bleed =   0.00%
   Control Limits:  Tt4   = 1300.0   Pi c  =   4.00
  ********************************************************************
   Parameter                        Reference**             Test**
   Mach Number @ 0                     0.0100              0.0100
   Temperature @ 0                     288.15              288.16
   Pressure    @ 0                     101324              101325
   Altitude    @ 0                          0                   0
   Total Temp  @ 4                    1300.00             1195.14
   Pi r  / Tau r              1.0001/ 1.0000      1.0001/ 1.0000
   Pi d                                0.9700              0.9700
   Pi c / Tau c               4.0000/ 1.6840      3.5408/ 1.6124
   Tau m1                              0.9727              0.9727
   Pi t / Tau t               0.4839/ 0.8746      0.4930/ 0.8775
   Tau m2                              1.0000              1.0000
   Control Limit                                       Thrust=Drag
   Spool RPM (% of Reference Point)   100.00               94.62
   Pt9/P9                              1.7483              1.5764
   P0/P9                               1.0000              1.0000
   Mach Number @ 9                     0.9577              0.8592
   Mass Flow Rate @ 0                    1.14                1.05
   Corr Mass Flow @ 0                    1.14                1.05
   Flow Area      @ 0                   0.272               0.251
   Flow Area*     @ 0                   0.005               0.004
   Flow Area      @ 9                   0.006               0.006
   MB - Fuel/Air Ratio (f)           0.02422             0.02128
   Overall Fuel/Air Ratio (fo)       0.02325             0.02043
   Specific Thrust  (F/m0)            584.39              508.10
   Thrust Spec Fuel Consumption (S) 39.7822              40.2130
   Thrust (F)                           666                 535
   Fuel Flow Rate                        95                  77
   Propulsive Efficiency (%)           1.17                1.34
   Thermal Efficiency    (%)          17.34               14.98
   Overall Efficiency    (%)           0.20                0.20
```

Table B-5. Off-design analysis at 30% throttle.

```
30% THROTTLE TEST OUTPUT
AEDsys (Ver. 4.100)          Turbojet - Single Spool
   Input Constants
   Pidmax= 0.9700   Pi b  = 0.9500   Eta b = 0.9800   Pi n  = 0.9800
   cp c  = 0.9965   cp t  = 1.2351   Gam c = 1.4000   Gam t = 1.3000
   Eta c = 0.7105   Eta t = 0.8132   Eta m = 0.9800   Eta P = 0.9800
   PTO   =    0.0KW hPR   =  41868   Cool 1=   4.00%  Cool 2=   0.00%
   Bleed =   0.00%
   Control Limits:  Tt4   = 1300.0   Pi c  =   4.00
  ********************************************************************
   Parameter                        Reference**            Test**
   Mach Number @ 0                     0.0100             0.0100
   Temperature @ 0                     288.15             288.16
   Pressure    @ 0                     101324             101325
   Altitude    @ 0                          0                  0
   Total Temp  @ 4                    1300.00             981.03
   Pi r  / Tau r              1.0001/ 1.0000     1.0001/ 1.0000
   Pi d                                0.9700             0.9700
   Pi c / Tau c               4.0000/ 1.6840     2.0603/ 1.3229
   Tau m1                              0.9727             0.9727
   Pi t / Tau t               0.4839/ 0.8746     0.4839/ 0.8746
   Tau m2                              1.0000             1.0000
   Control Limit                                       Thrust=Drag
   Spool RPM (% of Reference Point)    100.00              68.71
   Pt9/P9                              1.7483             1.1949
   P0/P9                               1.0000             1.0000
   Mach Number @ 9                     0.9577             0.5289
   Mass Flow Rate @ 0                    1.14               0.68
   Corr Mass Flow @ 0                    1.14               0.68
   Flow Area      @ 0                   0.272              0.161
   Flow Area*     @ 0                   0.005              0.003
   Flow Area      @ 9                   0.006              0.006
   MB - Fuel/Air Ratio (f)           0.02422            0.01669
   Overall Fuel/Air Ratio (fo)       0.02325            0.01602
   Specific Thrust  (F/m0)            584.39             297.01
   Thrust Spec Fuel Consumption (S) 39.7822             53.9447
   Thrust (F)                           666                201
   Fuel Flow Rate                        95                 39
   Propulsive Efficiency (%)           1.17               2.27
   Thermal Efficiency    (%)          17.34               6.62
   Overall Efficiency    (%)           0.20               0.15
```

Appendix C. Version Explanation

The following table outlines each Disk-Oriented Engine Combustor geometry analyzed through CFD. For each design, a small summary of changes from the previous design are listed, describing how the combustor changed over its design history. After each Version's section, a brief recap of takeaways from that design and a path forward is provided. The intent of this table is to supplement the discussion of the design process in Chapters III and IV.

Table C-1. Version explanation, highlighting key differences in the iterative design process.

Version	Changes From Previous Design
V1-1	Initial design, circumferential cavity size based on previous UCC work
V1-2	Scoop and cap were added to front-side plenum, forcing more air to the compressor-side driver holes
V1-2a	The location of the front-side scoop was clocked to align with PZ holes, and an L-bracket was added to the end of the scoop to catch air
V1-3	Additional scoop was added to bring air directly to PZ. This caused grid issues and was not analyzed
V1-4	Front-side scoop was enlarged about the circumference and dilution hole diameter was reduced to drive more air to the CC
V1-5	Front-side scoop extended, indicating that control of mass flow between front and back would be variable throughout design
V1-6	SZ hole diameter reduced to increase PZ air supply
V1-6a	Front-side scoop altered again
	Takeaways: V1 had too small of a PZ for complete combustion and fuel was introduced with too high of a velocity. This required an increase in CC area and fuel injector diameter.

V2-1	CC radial span was increased from 5.08 cm to 11.4 cm, and the front-side scoop was reduced from 15° to 10° to reduced compressor-side mass flow
V2-2	Scoop reduced to 7.5° and fuel injector diameter increased 50%
V2-3	Number of PZ holes doubled, holding hole area constant. All hole areas were increased 16.6% to reduce PZ velocities. Exit width was also reduced from 5.08 cm to 2.54 cm to increase exit velocity.
V2-4	Fuel injector area increased again, and holes were re-shaped to ellipses. PZ holes were turned normal to the CC to reduce PZ swirl
V2-5	12-step ring removed, and PZ holes injected 25° to induce PZ swirl
V2-6	PZ holes injected at 10° to reduce PZ swirl again. Front-side scoop was also reduced to 5°, with mass flow split providing 53% of air to the front and 47% to the back.
V2-7	PZ/SZ hole diameters were increased (0.51 cm/0.64 cm) to slow PZ flow, and back PZ was moved radially outward to tighten TVC swirl
V2-7a	Scoop was removed as front plate was extended into compressor flow to replace scoop. This did not work as well as scoop did
V2-8a	Fuel introduced on the back face in between back-side PZ holes. This attempted to increase time fuel spent in the PZ. This was the best working Version 2 design, holding a stable flame in the PZ
V2-8b	Fuel introduced on the front face in between front-side PZ holes. This was compared to the back-side introduction, attempting to maximize the time fuel spent in the PZ
	Takeaways: Version 2 was once again thought to be volume limited, leading to a non-UCC design used in V3. It was found that these designs (V1&V2) did not work as the combustor equivalence ratios were

	4.76 times too rich.
V3-1	Implementation of u-bend combustion path and forward dome PZ
V3-2	Center body air introduction into SZ was removed as it provided an easy path for diffuser air to follow, decreasing bypass air supply
V3-3	Center body convection cooling was removed, greatly reducing complexity for manufacturing. Turbine stator camber was added to account for new incidence angle. This design also used the first swirl injector
v3-4a	Swirler vanes were tilted 45°, sweeping 90° about the swirler, as designed through swirler-only testing
V3-4b	Bottom of swirler extended into the diffuser, acting as an air scoop for swirling air. Vane sweep increased to 135° to back pressure the additional air associated with the scooped swirler bottom
V3-4c	Fuel tubes modeled in the diffuser to see impact on swirler feed
V3-4d	Stator dilution hole feeds were clocked to occur between fuel lines. This helped lessen the impact tubes had on dilution air supply
V3-5a	Swirler vane sweep returned to 180°, and additional air supply holes were added to the PZ to reduce local Φ
V3-5b	First design to remove swirler tilt. This particular design was not analyzed as swirler was drastically different than previous designs
V3-5c	Swirler was turned radially outboard, but the 45° scoop in the diffuser remained to catch swirling flow.
V3-5d	The swirler cup was extended beyond the end of the vanes to prevent swirl jet from being lost to centrifugal acceleration. The bluff body was also added with the intent of strengthening the recirculation zone above the swirler
V3-5e	The swirler cup was extended out even further to maintain more swirl

V3-5f	A cone was added to the top of the bluff body to reduce separation behind the bluff body. The exit diameter of the swirler was also increased to reduce exit velocity while inlet diameter remained the same to keep air mass flow supply constant
	Takeaways: Once again, many of the V3 tests were realized to have run at too rich of an equivalence ratio, resulting in less than desirable combustion flame holding. The flow splits from the V3-5f design were thought to be reasonable for further iteration, so this design was the basis for the rig-ready test (RT) model. It was in the first RT model that the error in Φ was found, but Versions 1-6, 2-8a, 3-5e and 3-5f were re-run for comparison purposes at a corrected fuel flow rate.
RT-1	This geometry was identical to V3-5f, except the SZ slots were modeled as holes and the solid was partitioned into manufacturable sections
RT-2	In order to cool the center body, the stator dilution feed was necked down and that additional air was pushed radially outward in the center body
RT-3	The number of holes in the third secondary zone were reduced by 33% with the intent of allowing reactions to fill that area with less air forcing it away. The center body cooling was angled toward the back wall to reduce the turning angle of cooling flow.
RT-4	Scooped-louvers were added to the front face of the PZ liner to provide cooling from the PZ flame anchor. Additional branches were also added off of the center body cooling holes to provide additional internal cooling
RT-5	Scooped-louvers were added to the back wall to reduce temperature along the tip-side of the turbine stators. The front-side scooped

	louvers were stacked, not staggered, to create a shielding effect to prevent burning on these air injection points
RT-6	Center body cooling was changed to be fed directly from the diffuser, rather than the dilution supply. Additionally, the branching was removed and each hole was supplied individually, creating 48 cooling holes in the center body about the annulus
RT-7	A row of cooling holes, equal in number and area to the first SZ row, were added above the PZ to provide film cooling to the liner above the swirl injectors
RT-8	Center body cooling holes were redirected to the front side of the center body to push the swirler reaction from the surface. The hole area was maintained by increasing the number of holes and decreasing the diameter of each hole. The front-side scooped-louvers were also replaced by an impingement cooling plate that was supplied by air from holes equal in area to the scooped-louvers
RT-9	An additional hole was added to the back side of the center body, with the intent of supplying cool air to the hub-side of the turbine
RT-10	The back-side scooped-louvers and back-side center body dilution holes were moved radially outward to introduce dilution air earlier after the u-bend. An additional row of holes was added next to the first SZ row, increasing the air injected directly above the swirler
RT-10a	The 5 holes at 48 locations about the center body were reduced to 3 holes at 36 locations with the same hole area. This was done to improve manufacturability of the center body
RT-11	A third row of cooling holes directly above the swirler was added to cool the combustion liner.

RT-11a	The depth of the center body cooling supply hole was shorted to ensure that machining would not puncture the u-bend surface
RT-12	The 3 rows of cooling directly above the swirler were clustered to locations directly above each of the 12 swirlers. This resulted in additional cooling at the points of greatest heat release
RT-13	The spacing between these clustered holes was reduced, decreasing the likelihood that combustion would occur between air injection holes
RT-14	The two rows in the SZ liner after the cluster were swapped, supplying less air to the two that divided the rich and lean burns and supplying more air to the upper back end to complete the oxidation of CO
RT-14 (no plate)	The impingement cooling plate on the front liner was removed to reduce manufacturing complexity. Instead, the impingement holes were relocated to the top of where the plate was
	Takeaways: Based on the final RT-14 design, the Disk-Oriented Engine Combustor proceeded to the manufacturing stage of design.

Appendix D. Swirl Number Calculation

Table D-1. Matlab function for calculating swirl number (S) from velocity field at fuel-air swirl injection location.

```
function [S] = swirl_calc(filename,param)
%%%%%%%%%%%%%%%%%%%%%%%%%%%%%%%%%%%%%%%%%%%%%%%%%%%%%%%%%%%%%%%%%%%%%%%%%%%%%%%
%swirl_calc.m calculates the swirl number on a plane using(x,y,z)
%position and velocity vectors, obtained from CFD .csv exports.
%
%Inputs:
%   filename = ASCII based file name
%   param.P0 = swirler CL position vector [m]
%   param.Rh = swirler vane hub radius [m]
%   param.Rn = swirler vane tip radius [m]
%Outputs:
%   S = calculated swirl number based on
%   Huang and Yang (2009) eq. 3.1
%%%%%%%%%%%%%%%%%%%%%%%%%%%%%%%%%%%%%%%%%%%%%%%%%%%%%%%%%%%%%%%%%%%%%%%%%%%%%%%
[P1,V1] = PV_read(filename);

P0 = param.P0;
Rh = param.Rh;
Rn = param.Rn;

%postion relative to the swirler center, Cartesian coordinates
PR = P1-P0;

%normal vector is cross of two rand vectors in plane
n = cross(PR(150,1:3),PR(1,1:3));
n_hat = n/norm(n);

%angle of rotation about the z-axis is based on angle between
```

```
%[0,1] and x-y components of the swirl-exit unit vector
gamma  = acos(dot([0,1],n_hat(1:2))/dot(1,norm(n_hat(1:2))));

%since gamma is rotated clockwise about z-axis, the angle is
% negative in the standard rotation matrix
rotation_matrix = [cos(-gamma),sin(-gamma),0;...
                  -sin(-gamma),cos(-gamma),0;...
                       0            0      1];

PR_cartesian = rotation_matrix*PR';
VR_cartesian = rotation_matrix*V1';

%convert to cylindrical coordinates by eqns:
% P = (r,theta,y)
%       >r = sqrt(x^2+z^2)
%       >theta = atan(x/z)
%       >y = y
% V = (Vr,Vtheta,Vy), note that Vtheta is positive ccw about y,
% as this is the positive direction of the swirler
%       >Vr = rdot = (x*xdot+z*zdot)/sqrt(x^2+z^2)
%       >Vtheta = r*thetadot = r*(z*xdot-x*zdot)/(x^2+z^2)
%       >Vy = ydot
PR_cyl = nan(3,length(PR_cartesian));
VR_cyl = nan(3,length(PR_cartesian));
for i = 1:length(PR_cartesian)
    PR_cyl(1,i) = sqrt(PR_cartesian(1,i)^2+PR_cartesian(3,i)^2);
    PR_cyl(2,i) = atan2(PR_cartesian(1,i),PR_cartesian(3,i));
    PR_cyl(3,i) = PR_cartesian(2,i);
    VR_cyl(1,i) = (PR_cartesian(1,i)*VR_cartesian(1,i)+...
        PR_cartesian(3,i)*VR_cartesian(3,i))/...
        sqrt(PR_cartesian(1,i)^2+PR_cartesian(3,i)^2);
    VR_cyl(2,i) = PR_cyl(1,i)*(PR_cartesian(3,i)*...
```

```
61          VR_cartesian(1,i)-PR_cartesian(1,i)*VR_cartesian(3,i))/...
62          (PR_cartesian(1,i)^2+PR_cartesian(3,i)^2);
63      VR_cyl(3,i) = VR_cartesian(2,i);
64  end
65  PR_cyl = PR_cyl'; VR_cyl = VR_cyl';
66
67  i = length(PR_cyl);
68  while i>0
69      if PR_cyl(i,1) > Rn || PR_cyl(i,1) < Rh
70          VR_cyl(i,:) = []; PR_cyl(i,:) = [];
71      end
72      i = i-1;
73  end
74  %temporary assign to indiv. variables
75  R = PR_cyl(:,1);theta = PR_cyl(:,2);y = PR_cyl(:,3);
76  Vr = VR_cyl(:,1);Vtheta = VR_cyl(:,2);Vy = VR_cyl(:,3);
77  %reorder in terms of r for integration purposes
78  [PR_cyl(:,1),order] = sort(R);
79  theta = theta(order);
80  y = PR_cyl(order);
81  Vr = Vr(order);
82  Vtheta = Vtheta(order);
83  Vy = Vy(order);
84  %replace vectors
85  PR_cyl(:,2) = theta;PR_cyl(:,3) = y;
86  VR_cyl(:,1) = Vr;VR_cyl(:,2) = Vtheta;VR_cyl(:,3) = Vy;
87  %radially average quantities to be integrated from Rh to Rn
88  % sort into bins
89  n = 251; %number of buckets plus 1
90  dr = (Rn-Rh)/n; %bin size and step size for integration
91  i = 1; k = 1;
92  for j = 1:n-1
```

```
93      while PR_cyl(i,1) < dr*(j)+Rh
94          r_order(k,j) = i;
95          i = i+1;k = k+1;
96      end
97      k = 1;
98  end
99  %average in each bins
100 clear R
101 L = size(r_order);
102 for j = 1:n-1
103     for i = 1:L(1)
104         if r_order(i,j) < 1e-6
105             break
106         else
107             Vy(i) = VR_cyl(r_order(i,j),3);
108             Vtheta(i) = VR_cyl(r_order(i,j),2);
109             R(i) = PR_cyl(r_order(i,j),1);
110         end
111     end
112     Vy_avg(j) = mean(Vy);
113     Vtheta_avg(j) = mean(Vtheta);
114     R_avg(j) = mean(R);
115     clear R Vtheta Vy;
116 end
117 % integration
118 for j = 1:n-1
119     integrand_top(j) = Vy_avg(j)*Vtheta_avg(j)*R_avg(j)^2*dr;
120     integrand_bot(j) = Rn*Vy_avg(j)^2*R_avg(j)*dr;
121 end
122 S = sum(integrand_top)/sum(integrand_bot);
123 end
```

Bibliography

1. Mattingly, J. D. and Boyer, K. M., *Elements of Propulsion: Gas Turbines and Rockets*, AIAA Education Series, 2nd ed., 2016.

2. Mercure, R. A., "Small Gas Turbines for US Army Auxiliary Power Systems," *International Gas Turbine Converence and Exhibition, Dusseldorf, West Germany*, 1986, 86-GT-282.

3. "WEG Motor Specs: W50 500 HP 4P 5009," `https://www.weg.net/catalog/weg/US/en/Electric-Motors/Large-Induction-Motors/Cast-Iron-TEFC-Motors/W50-Line/W50-500-HP-4P-5009-10-3Ph-2300-4160-V-60-Hz-IC411---TEFC---Foot-mounted/p/13305337`, 2020, Accessed: 2020-02-05.

4. "PT6 Nation," `http://www.pt6nation.com/en/community/story/for-this-weeks-thursdayquiz-co/`, 2012, Accessed: 2020-02-05.

5. "Airbus and SAS Scandinavian Airlines sign hybrid and electric aircraft research agreement," `https://www.airbus.com/newsroom/press-releases/en/2019/05/airbus-and-sas-scandinavian-airlines-sign-hybrid-and-electric-aircraft-research-a` `html`, 2019, Accessed: 2020-02-05.

6. DeMarco, K. J., Bohan, B. T., Hornedo, E. A., Polanka, M. D., and Goss, L. P., "Design Strategy for Fuel Introduction to a Circumferential Combustion Cavity," *AIAA Sci Tech Forum, Kissimmee, Florida*, 2018, AIAA 2018-1876.

7. Turns, S. R., *An Introduction to Combustion Concepts and Applications*, McGraw Hill, 3rd ed., 2012.

8. Rathsack, T. C., Bohan, B. T., Polanka, M. D., and Goss, L. P., "Experimental Investigation of Flow Characteristics in an Ultra Compact Combustor," *AIAA Sci Tech Forum, San Diego, California*, 2019, AIAA 2019-0117.

9. Mattingly, J. D., Heiser, W. H., and Pratt, D. T., *Aircraft Engine Design*, AIAA Education Series, 2nd ed., 2002.

10. Huang, Y. and Yang, V., "Dynamics and Stability of Lean-Premixed Swirl-Stabilized combustion," *Progress in Energy and Combustion Science*, Vol. 35, 2009, pp. 293–364.

11. Cowell, L. H. and Smith, K. O., "Development of a Liquid-Fueled Lean-Premixed Gas Turbine Combustor," *Journal of Engineering for Gas Turbines and Power*, Vol. 115, 1993, pp. 554–562.

12. Lefebvre, A. H., *Gas Turbine Combustion*, Taylor & Francis Group, 2nd ed., 1998.

13. Yilmaz, I., "Effect of Swirl Number on Combustion Characteristics in a Natural Gas Diffusion Flame," *Journal of Energy Resources Technology*, Vol. 135, 2013, Web. JERT-12-1294.

14. Lewis, G. D., "Swirling Flow Combustin - Fundamentals and Application," *9th AIAA/SAE Propulsion Conference, Las Vegas, Nevada*, 1973, AIAA 73-1250.

15. Briones, A. M., Sekar, B., and Erdmann, T., "Effect of Centrifugal Force on Turbulent Premixed Flames," *Journal of Engineering for Gas Turbines and Power*, Vol. 137, 2015, pp. 011501 (1–10), DOI: 10.1115/1.4028057.

16. Sirignano, W., Delplanque, J. P., and Liu, F., "Selected Challenges in Jet and Rocket Engine Combustion Research," *33rd Joint Propulsion Conference and Exhibit, Seattle, Washington*, 1997, AIAA 1997-2701.

17. Zelina, J., Shouse, D. T., and Handcock, R. D., "Ultra-Compact Combustors for Advanced Gas Turbine Engines," *49th ASME International Gas Turbine And Aeroengine Congress and Exposition, Vienna, Austria*, 2004, GT2004-53155.

18. Bohan, B. T. and Polanka, M. D., "Analysis of Flow Migration in an Ultra-Compact Combustor," *Journal of Engineering for Gas Turbines and Power*, Vol. 135, 2013, pp. 051502 (1–11), DOI: 10.1115/1.4007866.

19. Conrad, M. M., Wilson, J., and Polanka, M. D., "Integration Issues of an Ultra-Compact Combustor to a Jet Turbine Engine," *49th AIAA/ASME/SAE/ASEE Joint Propulsion Conference, San Jose, California*, 2013, AIAA 2013-3711.

20. Cottle, A. E., Gilbert, N. A., and Polanka, M. D., "Mechanisms for Enhanced Flow Migration from an Annular, High-g Ultra Compact Combustor," *AIAA Sci Tech Forum, San Diego, California*, 2016, AIAA 2016-1392.

21. DeMarco, K. J., Bohan, B. T., Polanka, M. D., and Goss, L. P., "Performance Characterization of a Circumferential Combustion Cavity," *2018 Joint Propulsion Conference, Cincinnati, Ohio*, 2018, AIAA 2018-4922.

22. Damele, C. J., Polanka, M. D., Wilson, J. D., and Rutledge, J. L., "Characterizing Thermal Exit Conditions for an Ultra Compact Combustor," *AIAA Sci Tech Forum, National Harbor, Maryland*, 2014, AIAA 2014-0456.

23. Bohan, B. T. and Polanka, M. D., "A New Spin on Small-Scale Combustor Geometry," *Journal of Engineering for Gas Turbines and Power*, Vol. 141, 2018, pp. 011504 (1–10), DOI: 10.1115/1.4040658.

24. Mattingly, J. D. and Boyer, K. M., *Elements of Propulsion: Gas Turbines and Rockets*, AIAA Education Series, 1st ed., 2006.

25. Hendricks, R. C., Shouse, D. T., Roquemore, W. M., Burrus, D. L., Duncan, B. S., Ryder, R. C., Brankovic, A., Liu, N. S., Gallagher, J. R., and Hendricks, J. A., "Experimental and Computational Study of Trapped Vortex Combustor Sector Rig with High-Speed Diffuser Flow," *International Journal of Rotating Machinery*, Vol. 7, 2001, pp. 375–385.

26. Bohan, B. T., *Combustion Dynamics and Heat Transfer in an Ultra Compact Combustor*, Ph.D. thesis, Air Force Institute of Technology, 2018, AFIT-ENY-DS-18-S-057.

27. Mair, W. A., "The Effect of a Rear-Mounted Disc on the Drag of a Blunt-Based Body of Revolution," *Aeronautical Quarterly*, Vol. 10, 1965, pp. 350–360.

28. Little Jr., B. H. and Whipkey, R. R., "Locked Vortex Afterbodies," *Journal of Aircraft*, Vol. 16, No. 5, 1979, pp. 296–302.

29. Hsu, K.-Y., Goss, L. P., and Roquemore, W. M., "Characteristics of a Trapped-Vortex Combustor," *Journal of Propulsion and Power*, Vol. 14, No. 1, 1998, pp. 57–65.

30. Huellmantel, I. W., Ziemer, R. W., and Cambell, A. B., "Stabilization of Premixed Propane-Air Flames in Recessed Ducts," *Jet Propulsion*, Vol. 27, 1957, pp. 31–43.

31. Zelina, J., Anderson, W., Koch, P., and Shouse, D. T., "Compact Combustion Systems Using a Combination of Trapped Vortex and High-G Combustor Technologies," *ASME Turbo Expo 2008: Power for Land, Sea and Air, Berlin, Germany*, 2008, GT2008-50090.

32. Ariatabar, B., Koch, R., Bauer, H. J., and Negulescu, D.-A., "Short Helical Combustor: Concept Study of an Innovative Gas Turbine Combustor With Angular Air Supply," *Journal of Engineering for Gas Turbines and Power*, Vol. 138, 2016, pp. 031503 (1–10), DOI: 10.1115/1.4031362.

33. Norgren, C. T., Mularz, E. J., and Riddlebaugh, S. M., "Reverse-Flow Combustor for Small Gas Turbines with Pressure-Atomizing Fuel Injectors," Tech. rep., National Aeronautics and Space Administration, 1978, NASA TR 78-22(PL).

34. Tirres, L., DiCicco, L., and Nowlin, B., "Experimental Evaluation of a Cooled Radial-Inflow Turbine," *AIAA/SAE/ASME/ASEE 29th Joint Propulsion Conference and Exhibit, Monterey, California*, 1993, AIAA 93-1795.

35. Aungier, R. H., *Turbine Aerodynamics: Axial-Flow and Radial-Inflow Turbine Design and Analysis*, ASME Press, 1st ed., 2006.

36. Cummings, R. M., Mason, W. H., Morton, S. A., and McDaniel, D. R., *Applied Computational Aerodynamics: A Modern Engineering Approach*, Cambridge University Press, 1st ed., 2015.

37. ANSYS, INC., *FLUENT User Guide*, 12th ed., 2009.

38. Bills, J. D., *Liquid Fuel Film Cooling: A CFD Analysis with Hydrocarbon Fuel*, Master's thesis, Air Force Institute of Technology, 2016, AFIT-ENY-MS-16-M-199.

39. Briones, A. M., Sekar, B., Shouse, D. T., Blunck, D. L., Thornburg, H. J., and Erdmann, T. J., "Reacting Flows in Ultra-Compact Combustors with Combined-Diffuser Flameholder," *Journal of Propulsion and Power*, Vol. 31, 2015, pp. 238–252.

40. Patankar, S., *Numerical Heat Transfer and Fluid Flow*, Taylor & Francis Group, LLC, 1st ed., 1980.

41. Incropera, F. P., Dewitt, D. R., Bergman, T. L., and Lavine, A. S., *Principles of Heat and Mass Transfer*, Wiley, 7th ed., 2000.

42. ANSYS, INC., *FLUENT User Guide*, 12th ed., 2009.

43. Pope, S. B., *Turbulent Flows*, Cambridge University Press, 1st ed., 2000.

44. Menter, F. R., "Two-Equation Eddy-Viscosity Turbulence Models for Engineering Applications," *AIAA Journal*, Vol. 32, No. 8, 1994, pp. 1598–1605, AIAA 93-2906.

45. Wilcox, D. C., "Reassessment of the Scale-Determining Equation for Advanced Turbulence Models," *AIAA Journal*, Vol. 26, No. 11, 1988, pp. 1299–1310.

46. Menter, F. R., "Influence of Freestream Values on $k - \omega$ Turbulence Model Predictions," *AIAA Journal*, Vol. 30, No. 6, 1992, pp. 1657–1659.

47. Cottle, A. E., Gilbert, N. A., Polanka, M. D., Goss, L. P., and Goss, C. Z., "Optical Diagnostics in a High-g Combustion Cavity," *AIAA Propulsion and Energy Forum, Salt Lake City, Utah*, 2016, AIAA 2016-4560.

48. Cottle, A. E., *Flow Field Dynamics in a High-G Ultra-Compact Combustor*, Ph.D. thesis, Air Force Institute of Technology, 2016, AFIT-ENY-DS-16-S-057.

49. Gas Research Institute, *GRI-Mech Project*, 3rd ed., 2000.

50. Adrian, R. J., "Twenty Years of Particle Image Velocimetry," *Experiments in Fluids*, Vol. 39, 2004, pp. 159–169.

51. LeBay, K. D., Drenth, A. C., Thomas, L. D., Polanka, M. D., Branam, R. D., and Schmidt, J. B., "Characterizing the Effects of G-Loading in and Ultra Compact Combustor via Sectional Models," *ASME Turbo Expo 2010: Power for Land, Sea and Air, Glasgow, UK*, 2010, GT2010-22723.

52. DeMarco, K. J., *Control, Characterization, and Cooling of an Ultra-Compact Combustor*, Master's thesis, Air Force Institute of Technology, 2018, AFIT-ENY-MS-18-M-250.

53. "Rolled Alloys: Full Alloy Listing," https://www.rolledalloys.com/alloys/, 2011, Accessed: 2019-11-26.

54. "Jet Cat: RC-Hobby Engines," https://www.jetcat.de/en/products/, Accessed: 2019-11-01.

55. "Garrett Motion: GTX5544R GEN II Turbocharger," https://www.garrettmotion.com/racing-and-performance/performance-catalog/turbo/gtx5544r-gen-ii/, Accessed: 2019-11-06.

56. "American Metals Co.: tehcnical Information for 321," https://www.metalshims.com/t-321-Stainless-Steel-technical-data-sheet.aspx, 2019, Accessed: 2019-12-10.

REPORT DOCUMENTATION PAGE

Form Approved
OMB No. 0704–0188

1. REPORT DATE *(DD–MM–YYYY)*	2. REPORT TYPE	3. DATES COVERED *(From — To)*
26-03-2020	Master's Thesis	1 October 2018 - 26 Mar 2020

4. TITLE AND SUBTITLE

DESIGN AND ANALYSIS OF A DISK-ORIENTED ENGINE COMBUSTOR

5a. CONTRACT NUMBER

5b. GRANT NUMBER

5c. PROGRAM ELEMENT NUMBER

6. AUTHOR(S)

Bennett M. Staton, 2d Lt

5d. PROJECT NUMBER

5e. TASK NUMBER

5f. WORK UNIT NUMBER

7. PERFORMING ORGANIZATION NAME(S) AND ADDRESS(ES)

Air Force Institute of Technology
Graduate School of Engineering and Management (AFIT/EN)
2950 Hobson Way
WPAFB OH 45433-7765

8. PERFORMING ORGANIZATION REPORT NUMBER

AFIT/ENY

9. SPONSORING / MONITORING AGENCY NAME(S) AND ADDRESS(ES)

Armament System Development Division (EBZ)
Air Force Life Cycle Management Center
207 West D Ave, Suite 300
Eglin AFB, FL 32542
COMM 850-883-4934
Email: Joseph.Rapa.1@us.af.mil

10. SPONSOR/MONITOR'S ACRONYM(S)

AFLCMC

11. SPONSOR/MONITOR'S REPORT NUMBER(S)

12. DISTRIBUTION / AVAILABILITY STATEMENT

DISTRIBUTION STATEMENT A:
APPROVED FOR PUBLIC RELEASE; DISTRIBUTION UNLIMITED.

13. SUPPLEMENTARY NOTES

14. ABSTRACT

In a novel approach to gas-turbine power production for aircraft or ground power, a disk-shaped engine was designed to combine a centrifugal compressor with a radial in-flow turbine. A circumferential flow combustor was wrapped around the turbomachinery, substantially decreasing the axial length of the burner. The configuration of the combustion cavity was evaluated iteratively using computational fluid dynamics. The result of this design process was a computational combustor model that accepted swirling inlet flow, dispersed that air and fuel about a unique u-bend circumferential combustion cavity, and exhausted in the radial direction to feed a radial in-flow turbine. Sustained combustion was simulated at design conditions, indicating that such a design could operate a gas-turbine engine, while reducing axial length up to 60% compared to traditional systems. Computational results were corroborated by velocity fields obtained through experimentation on swirled fuel injectors. Based on these results, a test rig was fabricated for future research into bulk-swirl combustion for a Disk-Oriented Engine.

15. SUBJECT TERMS

Circumferential Combustion, Computational Fluid Dynamics, Small Gas Turbine Engines

16. SECURITY CLASSIFICATION OF:			17. LIMITATION OF ABSTRACT	18. NUMBER OF PAGES	19a. NAME OF RESPONSIBLE PERSON
a. REPORT	b. ABSTRACT	c. THIS PAGE			Maj Brian T. Bohan, AFIT/ENY
U	U	U	U	223	19b. TELEPHONE NUMBER *(include area code)* (937) 255-3636, x4773; brian.bohan@afit.edu